NASA Reference Publication 1054

Thunderstorm-Environment Interactions Determined With Three-Dimensional Trajectories

Gregory Sims Wilson

JANUARY 1980

NASA

NASA Reference Publication 1054

Thunderstorm-Environment Interactions Determined With Three-Dimensional Trajectories

Gregory Sims Wilson
George C. Marshall Space Flight Center
Marshall Space Flight Center, Alabama

National Aeronautics
and Space Administration

**Scientific and Technical
Information Office**

1980

ACKNOWLEDGEMENTS

The author expresses his sincere appreciation to Dr. James R. Scoggins for his support, guidance, and encouragement during the author's graduate studies and in the preparation of this report. Additional thanks are due to Dr. Kenneth C. Brundidge, Dr. A. M. Thompson, Dr. Dusan Djuric, Prof. John D. Cochrane, Dr. Jack A. Barnes, and Dr. Calvin E. Woods for their supervision and assistance in the final preparation of the manuscript.

The author also acknowledges the support and encouragement by members of the Atmospheric Sciences Division, Space Sciences Laboratory, NASA Marshall Space Flight Center, Alabama.

Finally, he thanks Dr. Henry Fuelberg for his suggestions and encouragement, and Mrs. Paula Ferguson and Mrs. Jackie Wilson for their help and cooperation in typing the manuscript.

TABLE OF CONTENTS

TABLE OF CONTENTS (Continued)

LIST OF FIGURES

LIST OF FIGURES (CONTINUED)

LIST OF TABLES

THUNDERSTORM-ENVIRONMENT INTERACTIONS DETERMINED WITH THREE-DIMENSIONAL TRAJECTORIES*

Gregory Sims Wilson**

1. STATEMENT OF THE PROBLEM

a. Introduction

The ultimate function performed by the ensemble of atmospheric circulation systems is that of redistributing atmospheric energy to produce the observed "macroclimate" of the earth. Fundamental to the understanding of this process is knowledge about the "scale interaction" between various-size atmospheric systems. Scale interaction processes determine, to a great extent, the nature and rate at which atmospheric air parcels undergo energy transformations and establish the exact means by which the general circulation transports, redistributes, and transforms energy.

Atmospheric eddy sizes range over the entire hydrodynamic spectrum from planetary waves down to small-scale turbulent eddies. The scale interaction process has been observed to transfer energy both up and down this spectrum. However, the dynamics and feedback mechanisms of scale interaction remain among the least understood processes in meteorology.

Interaction processes between convective storms (small mesoscale systems) and micro-, meso-, and synoptic-scale systems have attracted considerable research interest in recent years because of the established importance of moist convection in the general circulation. Tropical thunderstorms, in transporting heat upward into the upper troposphere, are largely responsible for maintaining the horizontal and vertical distributions of temperature and pressure that maintain large-scale tropical circulations. In addition, thunderstorms are important in both the angular momentum and moisture balances of mid-latitude circulation systems. Severe convective storms in middle latitudes are also responsible for creating phenomena such as tornadoes, hailstorms, and flash floods that destroy property and take lives. Tremendous success has been realized in parameterizing the scale interaction processes between macro- or synoptic-scale systems and severe convective systems as evidenced by the remarkably

* A portion of the research on which this report is based was supported by Contract NAS8-31773 to Texas A&M University.

** Universities Space Research Association Visiting Scientist at NASA Marshall Space Flight Center, Huntsville, Alabama 35812.

good severe weather forecasts that are made from the current synoptic weather observations.

These parameterized relationships indicate that the macroscale flow field exerts a strong controlling influence over the intensity as well as the spatial and temporal distributions of the small mesoscale convective circulations. However, they do not integrate in a complete dynamical theory capable of explaining the sequence of events which result in severe convection nor do they account fully for the feedback processes between the convective storms and their environment.

NASA's fourth Atmospheric Variability Experiment (AVE IV) was conducted from 0000 GMT, 24 April to 1200 GMT, 25 April 1975 primarily to further establish the variability and structure of the atmosphere in regions of convective storms, and to investigate the poorly understood interrelationships between these storms and their environment. AVE IV data provide a unique opportunity to evaluate these relationships and scale interactions since two severe lines of thunderstorms (one containing the Neosho tornado) occurred during the experiment. Special rawinsonde soundings were taken at 3- or 6-h intervals in AVE IV over the U.S. east of 105°W longitude. All available surface, radar (from Manually Digitized Radar (MDR) data (Foster and Reap, 1973)), and satellite data were used in the diagnostic analyses.

Specifically, this research presents results aimed at providing a better understanding of the interrelationships between synoptic- and convective-scale systems obtained by following individual air parcels, embedded within the macroscale flow pattern, as they traveled within the convective storm environment of AVE IV. A three-dimensional trajectory algorithm was used to objectively calculate parcel paths, while MDR data were used to locate convective activity of various intensities and to determine the proximity of trajectories to storms.

b. Previous studies

In trying to understand, predict, and modify convective storms, the scale interaction problem becomes extremely complex. Almost nowhere can convective storm formation be considered as either completely random or

completely organized. Over tropical oceans, where surface and synoptic-scale forcing are presumably weak, major convective clouds usually occur in "cloud clusters" apparently forced by weak macroscale disturbances. After cluster organization, the energy released by buoyancy overwhelms the initial forcing mechanisms and the large-scale meteorological characteristics of the cluster become products of the total fluxes of the convective elements (Reed and Recker, 1971).

In certain parts of the world and in some seasons, strong convection develops within the environment of moderate-to-strong large-scale disturbances. Under these conditions, the preconvective state includes a stable layer preventing moist, low-level air from rising into a conditionally unstable upper troposphere (Newton, 1963). When the stable layer is eliminated by large-scale or mesoscale uplift, the bouyant release occurs suddenly and violently. The large-scale conditions which favor this release have been known for many years and have been used in making 6-12 h forecasts of severe convection.

Miller (1972) has summarized the empirical relationships between macroscale conditions and severe convective storm development. They include: 1) a vertical temperature structure that is conditionally unstable; 2) large amounts of low level moisture; 3) strong mid- and upper-tropospheric jets; 4) a dynamical mechanism producing lifting and releasing convective instability; and 5) many times, dry air at mid-tropospheric levels. In addition, recent work by Whitney (1977) has shown the geometric relationships between severe thunderstorm formation and the positions of the polar and subtropical jet streams. His work reveals that most severe activity lies ahead of the surface front and between the two jet streams.

Endlich and Mancuso (1968) examined the relationships between objectively analyzed synoptic data and severe convective storms. They were able to identify accurately areas in which severe weather occurred by establishing those parameters that correlated best in space with the observed convection. A basic conclusion reached was that boundary layer fluxes of temperature and moisture appeared to be more directly related to severe storm occurrence than lapse rates of temperature or

parcel instabilities.

Probability forecasts of convection have been developed recently by Reap and Alaka (1969), Bonner et al. (1971), Reap and Foster (1975), and David (1973) using screening regression with forecast parameters from numerical models. Statistical correlations between observed convection and forecast parameters have helped in establishing the relationships between convective- and synoptic-scale systems, but the inability of the present models to resolve and forecast subsynoptic-scale systems has limited the accuracy of forecasts of convection. Even so, the best forecast parameters determined from the correlations of parameters with convective activity indicate that the layer of air between the surface and 3 km (10,000 ft) should be moist and convectively unstable with positive vertical motion occurring within the layer.

More quantitative relationships have been established by Hudson (1971), Ogura and Cho (1973), and Fritsch et al. (1976) where cumulus cloud formation and populations have been parametrically tied to macro-scale moisture convergence, vertical velocity, and heat and moisture budgets. Their work reveals that the amount of mass being processed by the severe convective clouds is several times larger than the synoptic-scale mass convergence, resulting in additional vertical circulations such as organized convective lifting and compensating downdrafts. These circulations suggest that convective transport rates may be strongly related to the existing potential buoyant energy, rather than to the rate at which energy is generated by the large-scale disturbance at the time of convection.

Research also indicates that areas of intense convection produce feedback effects on surrounding atmospheric volumes that can be detected using synoptic-scale data. Newton (1969) has shown that heat, moisture, and momentum, exchanged by convective processes between clouds and their environment, are often of comparable magnitude to those associated with the large-scale distribution.

Aubert (1957) indicated that latent heat release, associated with thunderstorms, produced increases in large-scale horizontal convergence below the level of maximum condensation and enhanced horizontal diver-

gence above that level. He found decreases in values of geopotential height in the lower troposphere and increases in the upper troposphere. Ninomiya (1971a and b), using satellite pictures, found that the pre-existing inflow at the cirrus level over tornado-producing thunderstorms changed into strong outflow as the thunderstorms developed. The existence of a mid-tropospheric warm core and a significant field of convergence below 700 mb was observed using synoptic-scale rawinsonde data, and the downward convective transport of horizontal momentum was shown to intensify the low-level jet stream. A primary conclusion reached was that convective systems interact with and modify the large-scale synoptic field through the release of latent heat. The resulting warm core observed by the author in the middle and upper troposphere above the convection area was apparently responsible for intensifying the horizontal temperature gradient that resulted in strong upper-level divergence over the convective area. An entire interaction model was developed to explain the formation and development of the convective system through the transfer of energy between the synoptic- and convective-scale systems.

Fuelberg (1977), Read and Scoggins (1977), and Scott and Scoggins (1977) have shown strong relationships between individual terms in the large-scale kinetic and potential energy, vorticity, and moisture budgets and thunderstorm formation. These budget studies consistently reveal the importance of sub-grid scale processes in residual term calculations. The large magnitudes of the residuals in convective areas indicate that strong interactions occur between the convective- and synoptic-scale systems as heat, momentum, and water are exchanged.

Finally, a new scale-interaction theory, based upon fundamental hydrodynamics, has been developed and numerically tested by Zack and Moore (1977), Paine and Kaplan (1974), and Paine and Kaplan (1977). This theory describes the cascade and generation of kinetic energy over the entire spectrum of atmospheric systems from Rossby waves to micro-scale weather systems. The development of large amplitude meso- and micro-scale systems is shown to occur when large accelerations exist in

a specific mass and momentum distribution at the macroscale. Numerical testing of the theory has shown remarkable skill in forecasting the development of severe convective systems and tornadoes from synoptic-scale initial conditions.

c. Objectives and Approach

Convective storm evolution depends on development and interaction of fields of motion, temperature, and humidity on scales ranging in size from that of mid-latitude cyclones down to the micro-meteorological scale involving turbulent eddies. The objective of this research was to examine the fundamental hypothesis that thermodynamic and hydrodynamic processes, produced by synoptic-scale circulation systems, exert a strong controlling influence upon the location, intensity, and duration of small mesoscale convective systems. Furthermore, that interaction processes between thunderstorms and their large-scale environment may alter the structure and dynamics of both the synoptic- and convective-scale systems as heat, mass, and momentum are exchanged between the convective storms and their immediate environment.

Specifically, this research attempts to provide more information on the interrelationships and "scale interactions" between synoptic- and convective-scale systems obtained by following individual air parcels, embedded and moving within the macroscale flow pattern, as they traveled within the convective storm environment. In accomplishing this objective, rawinsonde and surface data taken at 3- and 6-h intervals during AVE IV were used. These data allowed for the calculation of three-dimensional trajectories of air parcels traveling over the experiment area using a trajectory model developed specifically for this study. MDR data were used to locate convective activity of various intensities and to determine those trajectories that traversed the near-storm environment.

Since parcel trajectories represent the time-integrated three-dimensional motions of air parcels, total time derivatives mathematically express the atmospheric physical processes that occur following the air. Therefore, interactions between synoptic- and convective-scale systems were studies by calculating the total time derivatives of thermodynamic, kinematic, and energy quantities. The increased temporal resolution of

the AVE IV data over the standard synoptic data made these calculations possible.

Specific objectives of the research are listed below and encompass the use of the trajectory calculations to:

1) Establish the necessary and sufficient conditions for thunderstorm formation and intensity. This includes the horizontal and vertical distributions of wind, temperature, moisture, vertical velocity, stability, and variables associated with the trajectories to determine the synoptic-scale structure of the atmosphere during convective storm development.

2) Determine the thermodynamic and hydrodynamic physical processes that result in changes of atmospheric structure that finally lead to formation, maintenance, and dissipation of convective activity of various intensities.

3) After thunderstorm development, determine to what extent these convective storms interact with and modify the large-scale environment in changing its thermodynamic and kinematic structure through "feedback" processes.

2. THEORETICAL DEVELOPMENT

a. Dynamics of macro-scale flow and scale interaction

The net horizontal acceleration acting on an individual air parcel imbedded in synoptic-scale flow can be analyzed using

$$\frac{d\vec{V}}{dt} = -f(\hat{k}\times\vec{V}) \quad - \vec{\nabla}_p\phi + \vec{F}_2. \qquad \text{(x,y,p,t system)} \tag{1}$$

where $\frac{d\vec{V}}{dt}$ is the net horizontal acceleration imparted to an air parcel resulting from the imbalance between the coriolis force $-f(\hat{k}\times\vec{V})$, the pressure gradient force $-\vec{\nabla}_p\phi$, and the frictional force $\vec{F}_2$. Since the AVE IV data only allow complete resolution of synoptic-scale systems, all "subgrid-scale" processes must be considered as perturbation quantities that transfer momentum, heat, and water vapor to and from the synoptic-scale. Mathematically, this assumes the synoptic-scale to represent a mean flow about which perturbation velocities are superimposed. These perturbations occur as a result of scale interaction between the mean flow and all those systems whose eddy sizes are considerably below that of the synoptic-scale eddies (<1000 km) (Paine and Kaplan, 1974).

The first two terms on the right-hand side of (1) represent net horizontal forces per unit mass acting within the synoptic-scale flow while forces produced by perturbation velocities appear in the last term. From basic turbulence theory, $\vec{F}_2$ results from divergence of the covariance between perturbation velocities and mathematically appears in expanded component form in the x, y, z system as:

$$F_x = \frac{1}{\rho}\frac{\partial}{\partial z}(-\rho\overline{u'w'}) + \frac{1}{\rho}\frac{\partial}{\partial x}(-\rho\overline{u'u'}) + \frac{1}{\rho}\frac{\partial}{\partial y}(-\rho\overline{u'v'}) \tag{2}$$

$$F_y = \frac{1}{\rho}\frac{\partial}{\partial z}(-\rho\overline{v'w'}) + \frac{1}{\rho}\frac{\partial}{\partial x}(-\rho\overline{v'u'}) + \frac{1}{\rho}\frac{\partial}{\partial y}(-\rho\overline{v'v'}) \tag{3}$$

where primed velocities are turbulent perturbation quantities.

The largest of these turbulent eddies may be of the size which could be missed by the current network of observing points. Moreover, these

eddies may easily be of the order of 10 km in size and remain completely undetected with the present density of observing stations over the AVE area.

There are strong reasons to believe that the atmosphere contains eddies of the above-mentioned size when the flow field is highly accelerated and disturbed, but disturbances of the size of 10 to 100 km are usually damped (Godske et al., 1957). Direct measurements show a gap in this range of the turbulent kinetic energy spectrum (Lumley and Panofsky, 1964), but measurements reveal a distinct peak in the spectrum that corresponds to eddy sizes from 10 to 100 m and a characteristic velocity of about 1 m s^{-1} (Djuric, 1961). The effect of these eddies are not overlooked in this study, but turbulent eddies produced by convective activity are usually an order of magnitude larger and probably dominate the magnitude of $\vec{F}_2$ in the convective storm environment above the boundary layer (Newton, 1969).

Final calculation of the net parcel acceleration ($\frac{d\vec{V}}{dt}$) following the trajectories does not follow directly from a mathematical balance between computed terms in (1) as is usually done. Instead, the individual parcel trajectories are computed between each of the 3- and 6-h interval time periods of the AVE IV data, and $\frac{\Delta u}{\Delta t}\hat{i}$ and $\frac{\Delta v}{\Delta t}\hat{j}$ are determined for each trajectory. Then $\frac{d\vec{V}}{dt} \simeq \frac{\Delta u}{\Delta t}\hat{i} + \frac{\Delta v}{\Delta t}\hat{j}$ and interpretation of the acceleration must follow from (1) and the above discussion. This computing technique was used in determining all total derivatives of thermodynamic, kinematic, and energy quantities.

b. Spatial distribution of trajectory data and net vertical displacements

Reap (1972) has developed a technique for translating results from a trajectory model into an Eulerian framework. Specifically, a quantity called net vertical displacement (NVD) was developed by Reap which, when translated into the Eulerian grid, resulted in a spatial distribution of dp/dt for all air parcels ending their trajectories at all grid points in the grid array. The rate of pressure change along the parcel's path is actually calculated from $\Delta p/\Delta t$ where Δp represents the pressure change experienced by the parcel as it moved three-dimensionally

in space over a time period of 12 h (Δt). Reap and others have shown that NVD's correlate better with observed weather and precipitation than do instantaneous vertical velocities. They have also shown NVD's to be one of the most important predictors used in forecasting the probability of precipitation and thunderstorm activity since this parameter captures the time-dependent lifting and destabilizing processes that occur within the synoptic-scale flow prior to thunderstorm formation.

c. Static stability as measured by parcel energy indices

To accurately parameterize the static stability of the atmosphere in AVE IV, a method was developed to objectively calculate both the amount of buoyant energy (ergs g^{-1}) necessary to be added to a parcel to make it hydrostatically unstable (negative buoyant energy or NBE) and the amount available to be converted into kinetic energy of the upward vertical velocity (positive buoyant energy or PBE) or "updraft" if the parcel were to become unstable. Calculations of NBE and PBE follow the steps used in a one-dimensional, non-entrainment, cloud model without liquid water or "form" and "mixing" drag. An air parcel entering a "cloud" is lifted dry-adiabatically to its LCL and then moist-adiabatically to 100 mb. When the parcel virtual temperature (T_v') is warmer (colder) than T_v (the environmental virtual temperature) at a given pressure level, it will gain (lose) kinetic energy according to (Haltiner and Martin, 1957):

$$d\left(\frac{w^2}{2}\right) = -R_d(T_v' - T_v)\, d(\ln p). \tag{4}$$

Integrating (4) between two pressure levels gives

$$\Delta(KE_w) = \frac{w_2^2 - w_1^2}{2} = -R_d\int_1^2 (T_v' - T_v)\, d(\ln p) \tag{5}$$

or

$$\Delta(KE_w) = R_d(\overline{T}_v' - \overline{T}_v)\ln\frac{p_1}{p_2}$$

where bars are average temperatures for the layer and $\Delta(KE_w)$ is the parcel vertical kinetic energy change between levels p_1 and p_2. $\Delta(KE_w)$ is then determined for successive pressure layers of each sounding using (5) and NBE is calculated by summing all negative $\Delta(KE_w)$ values up to 500 mb over each sounding. PBE results from summing all positive values up to 100 mb. Smaller NBE should correlate with the increasing occurrence of thunderstorms while larger PBE should relate to the increasing intensity of convective activity since it is roughly proportional to the vertical kinetic energy of the maximum "updraft" velocity when NBE is small.

d. Parcel diabatic processes

Over short periods of time, air parcels will usually move isentropically so that $\frac{d\theta}{dt} = 0$. However, deviations from isentropic flow are the rule rather than the exception when condensation, evaporation, and radiation affect air parcels. Indeed, an essential job of the atmosphere is to transfer latent energy, stored in liquid water in the earth's oceans and lakes, into the atmosphere (through evaporation and horizontal and vertical transport), where it is finally realized as sensible heat during condensation. Thunderstorms are known to play an integral part in this process. In addition, the release of latent heat energy into the air alters the existing pressure and wind fields (Ninomiya, 1971a, 1971b) and affects the general circulation.

When diabatic effects and turbulent transfer of heat between synoptic- and subgrid-scale systems occur,

$$c_p \frac{d(\ln\theta)}{dt} = H_D + A_E \qquad (6)$$

where H_D is the diabatic heating rate (per unit mass) within the mean or synoptic flow (condensation, evaporation, radiation, etc.), and A_E is the divergence of the turbulent eddy flux of heat. A_E is probably a large term in the heat balance equation in areas where convection interacts with the synoptic flow and can be written as (Ninomiya, 1971a)

$$A_E = c_p \left[\frac{\partial(\overline{u'T'})}{\partial x} + \frac{\partial(\overline{v'T'})}{\partial y} + \frac{\partial(\overline{\omega'T'})}{\partial p}\right]. \qquad (7)$$

Primed quantities represent turbulent perturbations of velocity and potential temperature superimposed on a synoptic-scale flow defined by the AVE IV rawinsonde data.

e. Parcel accelerations

As discussed earlier, the total horizontal parcel acceleration vector per unit mass, $\frac{d\vec{V}}{dt}$, can be calculated along a trajectory and results transformed into a gridded output. $\frac{d\vec{V}}{dt}$ then represents the net horizontal force acting on the parcel as a result of an imbalance between the coriolis force, the pressure gradient force, and the turbulent eddy frictional force. These forces are mainly responsible for creating and altering atmospheric circulation systems.

The magnitude alone of the net force is not an easy quantity to use in determining changes in flow patterns since $\frac{d\vec{V}}{dt}$ is a vector quantity. Instead, changes in atmospheric flow patterns are usually studied by examining the changes in fields of vorticity or divergence in the fluid, both representable as scalar quantities. Changes in an air parcel's vorticity or divergence occur only when a net force acts on the parcel ($\frac{d\vec{V}}{dt} \neq 0$).

Equation 8 describes the rate of change of the vertical component of absolute vorticity (ζ_a) following an air parcel, and results from taking the horizontal curl of the acceleration vector and dotting this quantity with the vertical unit vector [$\hat{k} \cdot (\vec{\nabla}_p \times \frac{d\vec{V}}{dt})$]:

$$\frac{d\zeta_a}{dt} = -(\zeta + f)\vec{\nabla}_p \cdot \vec{v} - \hat{k} \cdot (\vec{\nabla}_p \omega \times \frac{\partial \vec{V}}{\partial p}) + \hat{k} \cdot (\vec{\nabla}_p \times \vec{F}). \qquad (8)$$

This familiar vorticity equation, when applied at the synoptic scale, relates $\frac{d\zeta_a}{dt}$ of the mean flow with the first term on the right-hand side which explains the production of vorticity through divergence, the second term on the right-hand side which represents the transfer of vorticity from other component axes into the vertical component, and the last term which explains the production of vorticity from the curl of the turbulent eddy frictional force. The second term on the right-hand side, usually called the twisting term, is normally an order of magnitude smaller than the following term, while the last term can,

in the vicinity of convective activity, be as large as the divergence term (Read and Scoggins, 1977). However, $\frac{d\zeta_a}{dt}$ should be positive (convergence) in the lower atmosphere and negative above (divergence) in the convective storm environment. As a result, upward vertical velocity is created from this pattern that can release potential instability and produce thunderstorms.

The turbulent eddy frictional force ($\vec{F}$) in the convective storm environment may be dominated by horizontal momentum exchange between thunderstorms and the environment. This is physically reasonable since low momentum surface air rises into convective clouds that are growing and mixing in an atmosphere with vertical shear, while high momentum air aloft enters precipitation downdrafts that plunge into the boundary layer. This complicated process alters the synoptic-scale flow since a net momentum transfer to or from the convective systems has occurred that changes the net horizontal acceleration at the macroscale through the turbulent eddy frictional force and affects the synoptic circulation pattern in the storm environment.

f. Parcel kinetic energy changes

When forces act upon air parcels, work is performed and energy transformations occur. Of particular interest in the atmosphere is the development of kinetic energy contained within the various size circulation systems.

From a Langrangian point of view, horizontal kinetic energy changes occur when the net horizontal vector force per unit mass acting upon the air parcel has a component along the velocity vector. Interpretation of the results may be obtained from (Haltiner and Martin, 1957):

$$\frac{d(KE)}{dt} = -\vec{V}\cdot\vec{\nabla}_p\phi + \vec{V}\cdot\vec{F} \qquad (9)$$

where KE is horizontal kinetic energy. Therefore, parcels change their horizontal kinetic energy during cross-contour flow and from kinetic energy imparted to or removed from the synoptic flow (last term in (9)) through "scale interaction." Under conditions that the momentum transfer between convective- and synoptic-scale systems alter the

large-scale acceleration vector field with respect to the direction of flow (through the last term on the right-hand side), horizontal kinetic energy at the synoptic scale is created or destroyed through this cloud-environment feedback process.

3. DATA ANALYSIS AND TRAJECTORY CALCULATIONS

a. AVE IV data

1) Rawinsonde data

The forty-two rawinsonde stations participating in the AVE IV experiment are shown in Fig. 1. Soundings were taken at nine times--24 April at 0000 GMT, 0600 GMT, 1200 GMT, 1500 GMT, 1800 GMT, 2100 GMT, and on 25 April at 0000 GMT, 0600 GMT, and 1200 GMT, 1975.

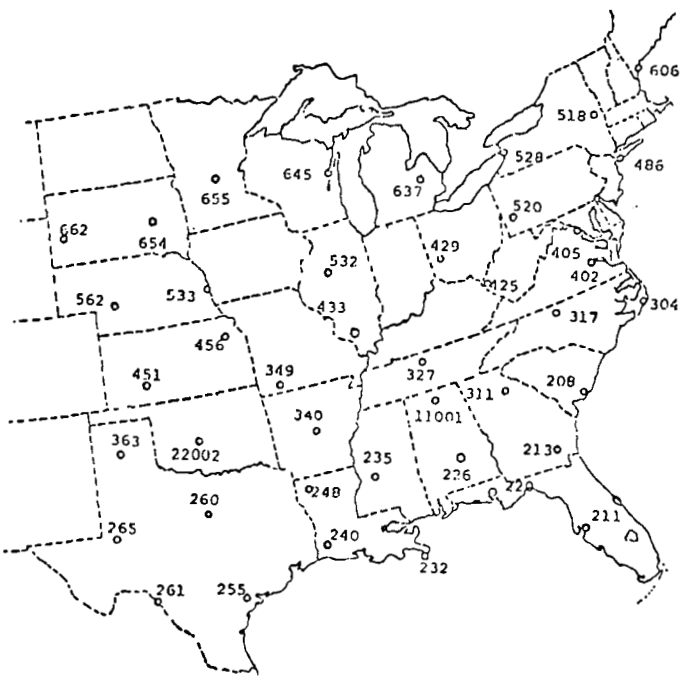

Fig. 1. Rawinsonde stations participating in the AVE IV experiment.

Data reduction procedures used to process the AVE IV rawinsonde data were designed to obtain the most accurate results possible (Fuelberg, 1974). The raw angle and ordinate data were checked for errors prior to calculating the soundings, and computed soundings were rechecked with corrections made as required. Data were given at 25-mb intervals by Fucik and Turner (1975). Estimates of RMS errors of the thermodynamic quantities are given in Table 1 (Scoggins and

Smith, 1973; Fuelberg, 1974). Recent studies have indicated that errors in the thermodynamic quantities may be even smaller than those given in Table 1 (Lenhard, 1973; Brousaides, 1975).

Table 1. RMS errors of thermodynamic quantities for the AVE IV data.

Parameter	Approximate RMS error
Temperature	1°C
Pressure	1.3 mb surface to 400 mb 1.1 mb between 400 and 100 mb 0.7 mb between 100 and 10 mb
Humidity	10%
Pressure Altitude	10 gpm at 500 mb 20 gpm at 300 mb 50 gpm at 50 mb

An error analysis conducted by Fuelberg (1974) gave RMS errors of scalar wind speed and wind direction for the AVE IV baroswitch contact data. Table 2 presents these RMS errors for elevation angles of 40° and 20°. RMS errors for the smoothed 25-mb data that were used in this study would be somewhat smaller.

Table 2. RMS errors of baroswitch contact wind data for the AVE IV data at elevation angles of 40° and 20°.

Level	Elevation Angle RMS Direction Error		Elevation Angle RMS Speed Error	
	40°	20°	40°	20°
700 mb	1.8°	3.8°	0.5 m s^{-1}	1.0 m s^{-1}
500 mb	2.5°	5.6°	0.8 m s^{-1}	2.0 m s^{-1}
300 mb	3.1°	7.5°	1.0 m s^{-1}	3.8 m s^{-1}
100 mb	6.2°	15.0°	2.0 m s^{-1}	5.7 m s^{-1}

Original strip charts from all rawinsonde soundings were checked carefully to determine if sondes entered thunderstorm updrafts or downdrafts. Data for four soundings were removed from the original data set because the sondes apparently had entered violent updrafts. The potential for distorted results due to nonhydrostatic accelerations was thereby considerably reduced.

2) Surface data

All available surface data for the AVE IV experiment were obtained from the National Climatic Center. Figure 2 shows locations of the 310 surface stations used. Vector wind, temperature, dew point temperature, and surface pressure were read, keypunched, and checked carefully for errors.

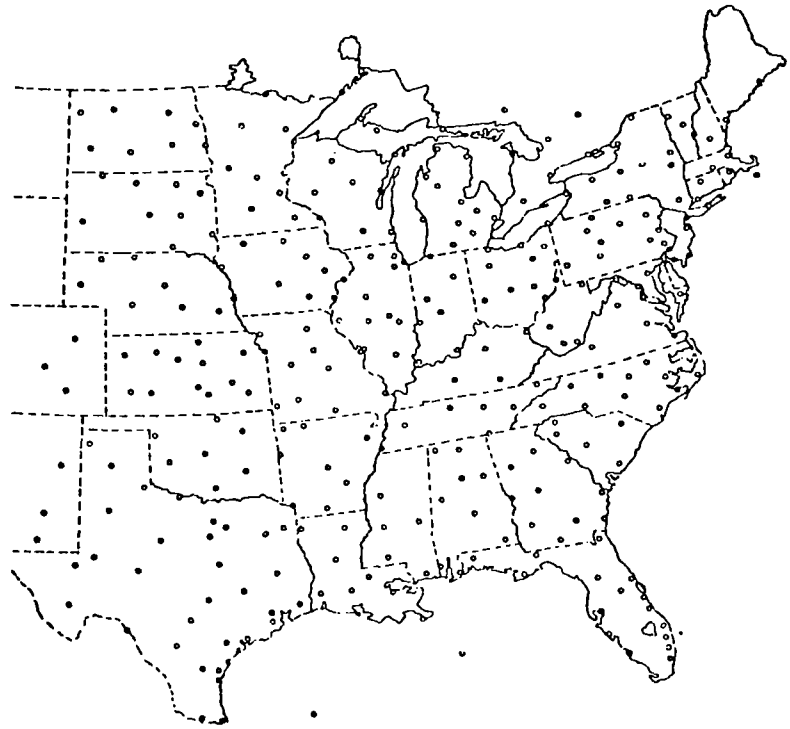

Fig. 2. Locations of surface stations for the AVE IV area.

3) Digital radar data

Manually Digitized Radar (MDR) data were obtained from NOAA's Techniques Development Laboratory to determine accurately the intensity and position of the radar-observed convection during the AVE IV experiment. The MDR grid network is shown in Fig. 3. MDR data are

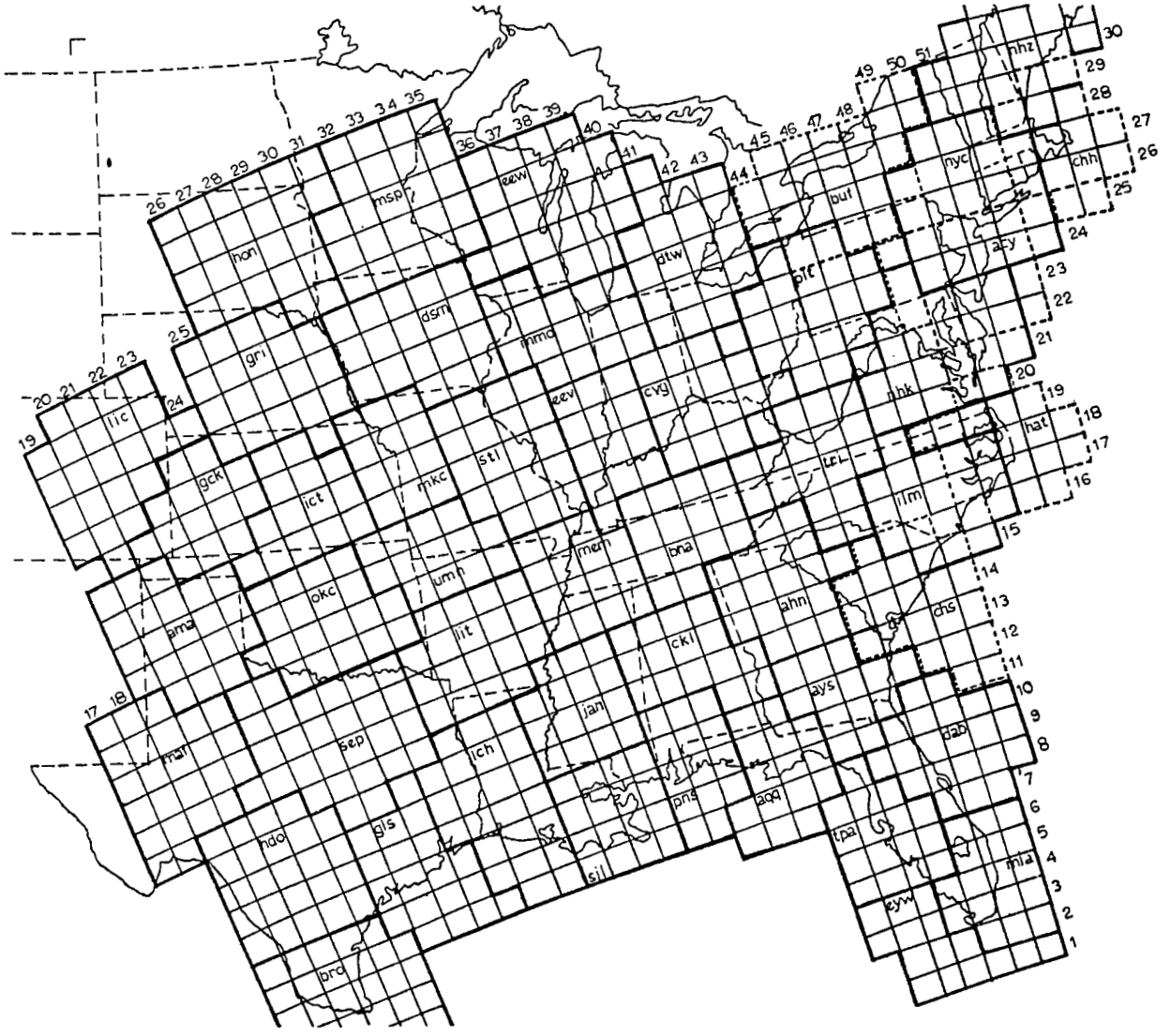

Fig. 3. Manually digitized radar (MDR) grid network.

coded with a single digit from 0 to 9 to indicate areal coverage and echo intensity within blocks that are approximately 83 km on a side. Table 3 is an explanation of the MDR code given by Foster and Reap (1973).

Table 3. Manually digitized radar (MDR) data code (Foster and Reap, 1973).

Code No.	Maximum Observed VIP[1] Values	Coverage In Box	Maximum Rainfall Rate (in h^{-1})	Intensity Category
0	No Echoes			
1	1	Any VIP1	<0.1	Weak
2	2	≤ 50% of VIP2	0.1-0.5	Moderate
3	2	> 50% of VIP2	0.5-1.0	Moderate
4	3	≤ 50% of VIP3	1.0-2.0	Strong
5	3	> 50% of VIP3	1.0-2.0	Strong
6	4	≤ 50% of VIP3 and 4	1.0-2.0	Very Strong
7	4	> 50% of VIP3 and 4	1.0-2.0	Very Strong
8	5 or 6	≤ 50% of VIP3, 4, 5, and 6	>2.0	Intense or Extreme
9	5 or 6	> 50% of VIP3, 4, 5, and 6	>2.0	Intense or Extreme

[1]Video Integrator Processor

Plots of the MDR data were made each hour for 3-h periods centered on each of the nine rawinsonde observation times. The three plots were then combined into a single chart for each of the nine times by using the highest coded value reported for each block.

b. Analytical procedures

Analytical procedures can determine the success or failure of an experiment and, therefore, must be considered carefully. This section

describes the procedures that were judged most advantageous for this study in relation to the available data, the trajectory model, and the objectives of the research.

1) Objective analysis and smoothing

The development and use of a trajectory model is simplified if data are interpolated from randomly-spaced rawinsonde stations to equally-spaced grid points. The grid network used (Fig. 4) is centered over the AVE IV data area and has a spacing of 158 km. Barr et al. (1971) have shown theoretically that a 169-km grid interval incorporates as much detail as is justified from the rawinsonde network over the United States.

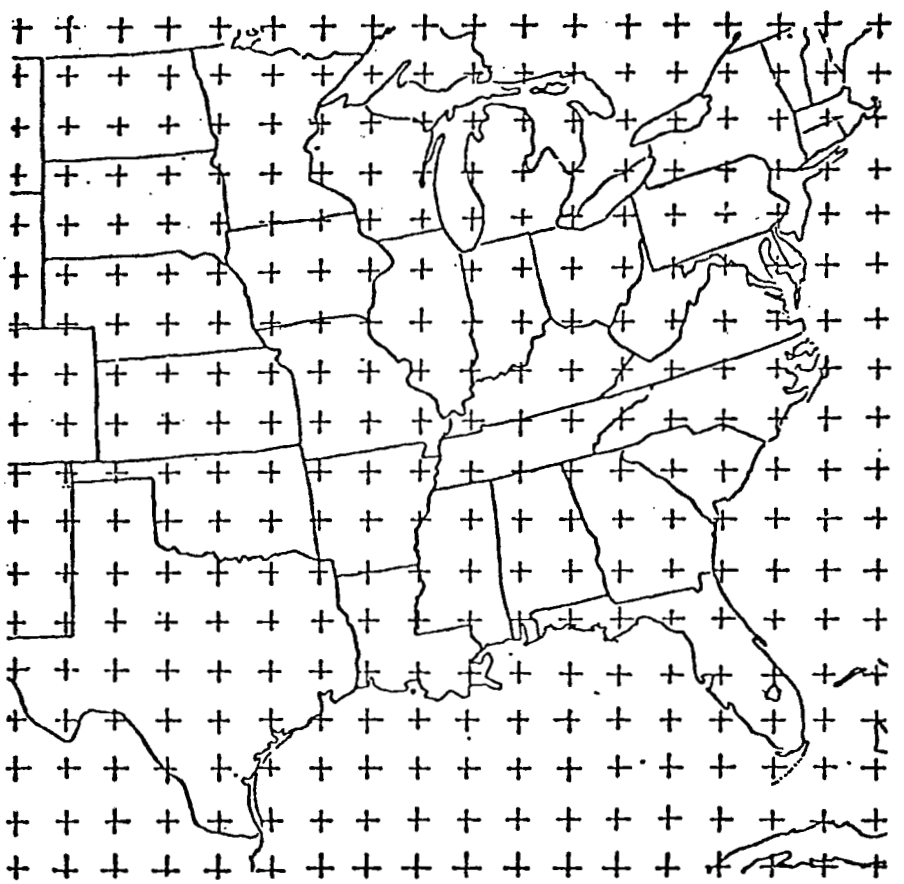

Fig. 4. Grid used for numerical computations.

Human analysis of data is still preferable to any objective scheme that has been devised, but the number of analyses required rendered hand analysis infeasible for this study. There were several considerations in the choice of an objective analysis and smoothing procedure from the several that are described in the literature. Such a procedure should interpolate data accurately from stations to the grid without creating fictitious waves or destroying real waves present in the data. Also, the desired results of the procedure should be considered carefully with respect to the input data density. Since the average spacing of rawinsonde stations over the eastern United States is about 350 km, features with wavelengths shorter than 1400 km can seldom be described completely by any objective analysis using this input data.

An objective analysis scheme by Barnes (1964) was used in this investigation. The procedure is referred to as successive corrections to a first-guess field. Data from each rawinsonde station were allowed to influence grid points within a scan radius of three grid distances while four iterations were allowed.

To suppress small waves which cannot be tracked consistently, as well as those which might arise due to the analysis scheme and random errors, a nine-point filter of the type used by Shuman (1957) was applied to the analyzed fields. The final result retained approximately 90% of the amplitudes of wavelengths of 1400 km, and appeared to contain as much detail as could be justified from the input data based on the agreement with hand analyses.

The surface data were analyzed using a scan radius of 2 grid distances with four iterations. This produced smooth fields from the high density surface data that meshed with the larger-scale rawinsonde data.

Gridded analyses of height, temperature, wind components, and moisture content were produced at 18 levels, i.e., the surface and at 50-mb intervals from 900 mb to 100 mb, for each of the nine time periods. Winds at the individual 18 levels were averaged over 50 mb layers which reduced random errors. These gridded values were stored on a computer disk and formed the working data set for all phases of the research.

2) Numerical evaluation of equations

In calculations not encompassing the trajectories, centered

finite differences were used to compute all horizontal and vertical derivatives except those at the surface and 100 mb where forward and backward differences were used for vertical derivatives. Time derivatives also were evaluated using centered differences where possible, but forward differences at the first period and backward differences at the last period were required. All computerized numerical calculations were performed on the Amdahl 470V/6 computer at Texas A&M University.

3) Computation of vertical velocities

Large-scale vertical motion cannot be measured directly, and no method currently available for determining vertical motion is completely accurate. The kinematic method was used in this research because it involved the least stringent assumptions and produced good results. Details of the procedures used are given by Wilson and Scoggins (1976) and Wilson (1976). Terrain-induced vertical motion was included, and a correction scheme by O'Brien (1970) was applied so the values of vertical motion at 100 mb would equal the values obtained by the adiabatic method. The adjustment factor significantly affects vertical motion in levels above about 500 mb. Application of an adjustment factor is necessary because the accuracy of wind data and resulting divergence calculations decrease with altitude. Adiabatic values at 100 mb were chosen because they are obtained independently of kinematic values and are more realistic than an assumption of zero at each grid point.

The kinematic method has been used widely in previous research. Vincent et al. (1976) suggested that it is better than the quasi-geostrophic form of the omega equation. Further support for the kinematic method has been given by such investigators as Chien and Smith (1973), Smith (1971), Fankhauser (1969), and Kung (1973). Moreover, Wilson (1976) indicated that values of kinematic vertical velocity related better to areal coverage and intensity of precipitation during the AVE IV experiment than did values of adiabatic vertical velocity. These results were based upon statistical comparisons between kinematic and adiabatic vertical velocities at various pressure levels and precipitation intensity categories determined from MDR data.

c. Trajectory Calculations

The main factors which hinder an exact evaluation of meteorological trajectories are the relative sparsity of observations in time and space, the inaccuracy of observations, and the fact that large-scale vertical velocities are impossible to observe and difficult to calculate (Djuric, 1961). The use of AVE IV data partially overcomes these difficulties so that the calculation of trajectories becomes both feasible and useful.

The input data for trajectories consisted of objectively gridded u, v, and ω components, potential temperature (θ), and geopotential height (ϕ) available at various pressure levels and at successive time periods. The gridded data set for AVE IV, which meets these criteria, has been described previously.

All trajectories in AVE IV were computed backward in time to insure that air parcels would terminate their paths exactly at a given grid point on a given pressure surface. The mathematical procedure used to calculate trajectories backward in time from wind fields defined in Eulerian space briefly is described below (Collins, 1970; Thomas, 1971).

Considering one grid point, in one dimension, "x", a first approximation to the displacement for one time step is given by

$$\Delta x_1 = u_i^t \Delta t \tag{10}$$

where Δx is the displacement, u is the wind component, Δt is the time step (3 or 6 h), i is the initial point, t is the initial time, and "1" is the iteration number. Figure 5 shows schematically the "first guess" displacement calculation for a hypothetical parcel trajectory when all three dimensions are included.

After initial displacement, "n" interations are performed using the expression

$$\Delta x_n = [(u_i^t + u_{n-1}^{t-\Delta t})/2]\Delta t \tag{11}$$

where $u_{n-1}^{t-\Delta t}$ is the wind component from the previous time step interpolated at the point x_{n-1} given by $x_{n-1} = x_i - \Delta x_{n-1}$. From the surface

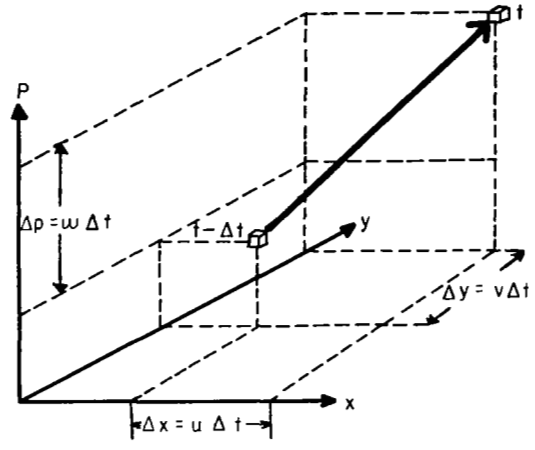

Fig. 5. Schematic diagram of the "first guess" three-dimensional (x,y,p system) parcel motion in the trajectory model between times "t" and "t-Δt".

to 100 mb, the three-dimensional wind is interpolated between levels and grid points using tri-linear interpolation for each component displacement. When $\Delta x_n - \Delta x_{n-1} < \xi$, Δx_n is accepted as the true backward displacement in the "x" direction. The 3-dimensional trajectory is determined by combining Δx_n, Δy_n, and Δp_n. Subsequently, air parcels can be traced backward in time and the total time derivative of a basic variable (say x) may be approximated by $\Delta x/\Delta t$. ξ had values of 0.5 km for the "x" and "y" directions, and 0.2 mb for the "p" direction.

Calculations were made along trajectories for the total derivatives of the u and v wind components ($\frac{du}{dt}$ and $\frac{dv}{dt}$), pressure ($\frac{dp}{dt}$), potential temperature ($\frac{d\theta}{dt}$) and horizontal kinetic energy $\{\frac{d(KE)}{dt}\}$ for the last eight consecutive times of AVE IV (backward displacement in time makes calculations impossible for the first time period). At each time period, gridded trajectory data were computed for 100-mb intervals between 900 and 100 mb and also at the 850-mb surface. In addition, individual air parcels were traced backward in time throughout the entire experiment by locating successive positions (x, y, p) of the parcels over the network. Computer-plotted trajectories displayed actual parcel paths during the experiment for those parcels starting at certain pressure levels and grid points of

the last observation period (25 April at 1200 GMT). All quantitative results from the trajectory calculations were stored on a computer disk to be used later, along with the basic gridded data in the statistical, synoptic, and dynamic analyses. This included calculation of average values of gridded trajectory data as a function of pressure level and various intensity categories of MDR data using data from all AVE IV time periods. The spatial variation of the quantities in relationship to the convective activity was also studied and the temporal variation examined during the formation, maintenance, and dissipation of areas of convective activity.

4. RESULTS

a. Synoptic structure and radar echo analysis (from MDR data) of AVE IV

Results in this section establish the temporal and spatial relationships between features in the synoptic structure and identified systems of precipitation and convective activity for all consecutive times of AVE IV excluding the first release time (24 April at 0000 GMT). Discussions will refer to these eight consecutive periods separately in Figs. 6(a-e) through 13(a-e) where analyzed spatial fields of radar, surface, and upper-level data are shown.

1) Radar (MDR) analysis of precipitation

Figures 6a-13a are composite MDR charts of precipitation intensity where each coded value represents the highest radar return intensity reported in an MDR block during a 3-h period surrounding the rawinsonde release times. All areas of reported precipitation in each chart have been outlined and "systems" of precipitation are identified from the spatial and temporal distribution of these areas as indicated by the letters A-E. All shower and thunderstorm activity (MDR$\geq$2) has been scalloped in each chart to identify better the location and movement of each storm system (all identified systems contained showers or thunderstorms).

Systems A, B, and C are shown in Fig. 6a. System A represents the first of two areas of severe thunderstorms (MDR$\geq$8) that occurred in AVE IV. This system moved consistently eastward through the network starting in the central Plains States at 0600 GMT 24 April. While moving eastward the system slowly dissipated by 0000 GMT 25 April so that (Fig. 11a) only light thunderstorms and rainshowers (maximum MDR=2) were located over the southern and middle Appalachians. By 1200 GMT 25 April, A was located off the North Carolina Coast (Fig. 13a).

System B was an area of light-to-moderate shower and thundershower activity (MDR$\leq$4) closely associated with and usually connected to System A. Separation of the two systems was done on the basis of precipitation intensity. This system also moved consistently eastward

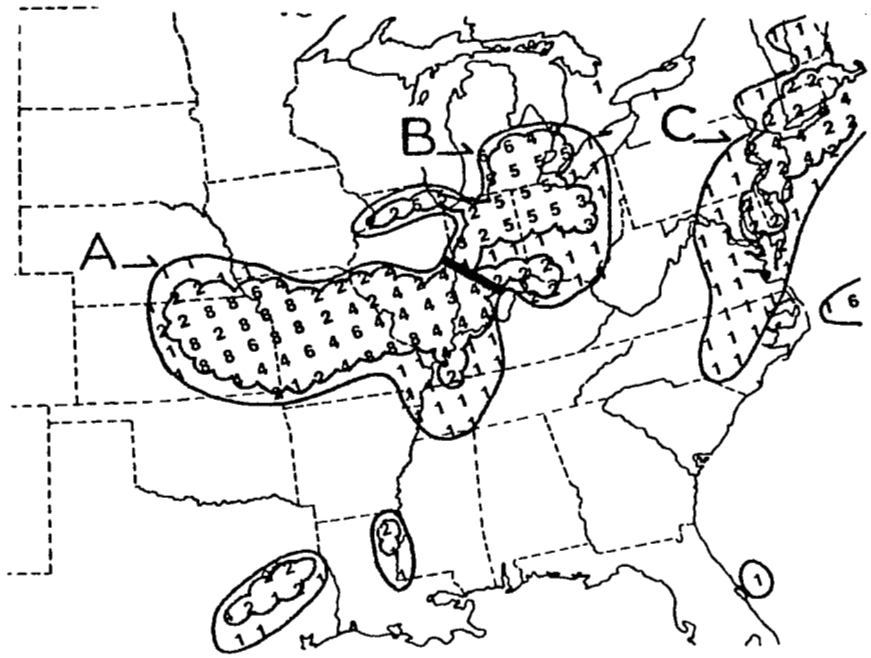

a. Composite MDR precipitation analysis

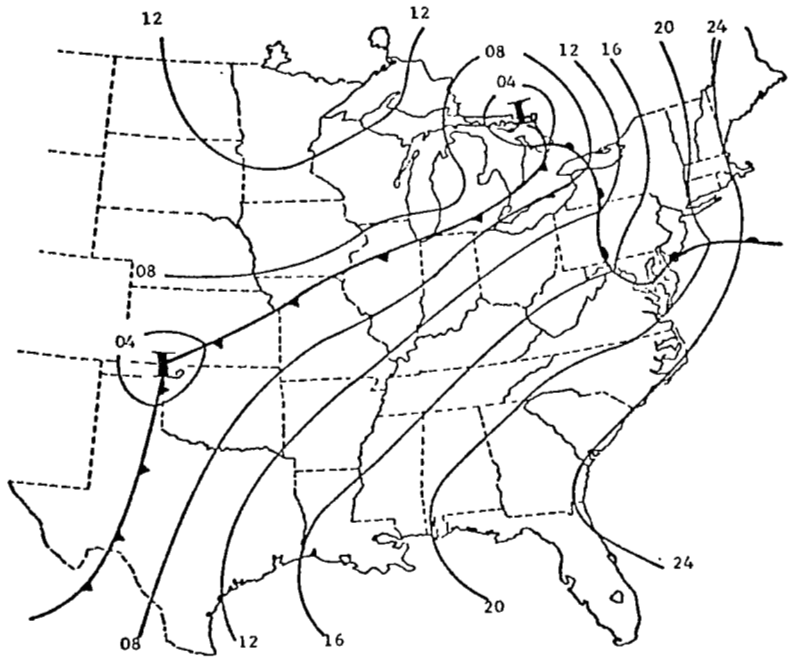

b. Surface pressure and frontal analysis

Fig. 6. Analyzed fields of (a) MDR precipitation systems, (b) surface pressure (fronts superimposed), (c) geopotential height, temperature, and wind at 850 and 500 mb, (d) vertical velocity at 850 and 500 mb, and (e) mixing ratio at 850 and 500 mb at 0600 GMT, 24 April 1975.

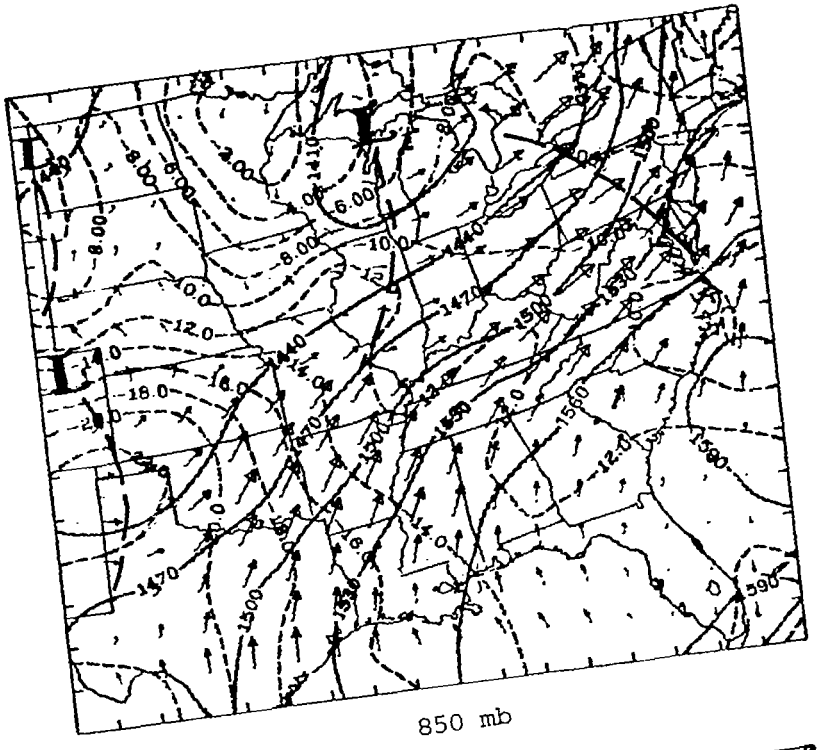

850 mb

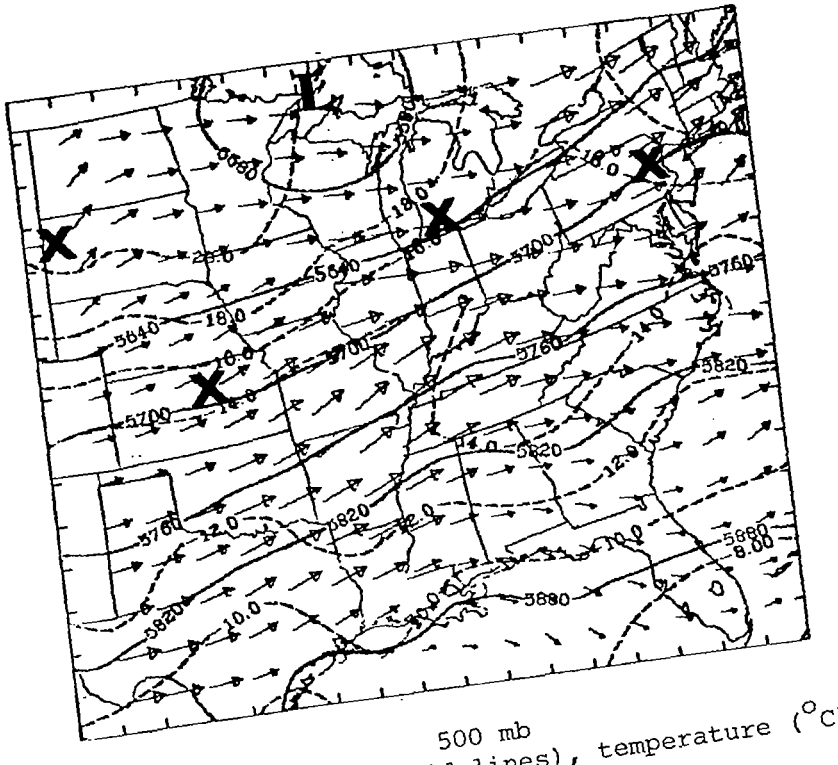

500 mb

c. Geopotential height (m)(solid lines), temperature (^{o}C)(dashed lines), and vector wind ($\rightarrow$=25 m s^{-1}).

Fig. 6. (Continued)

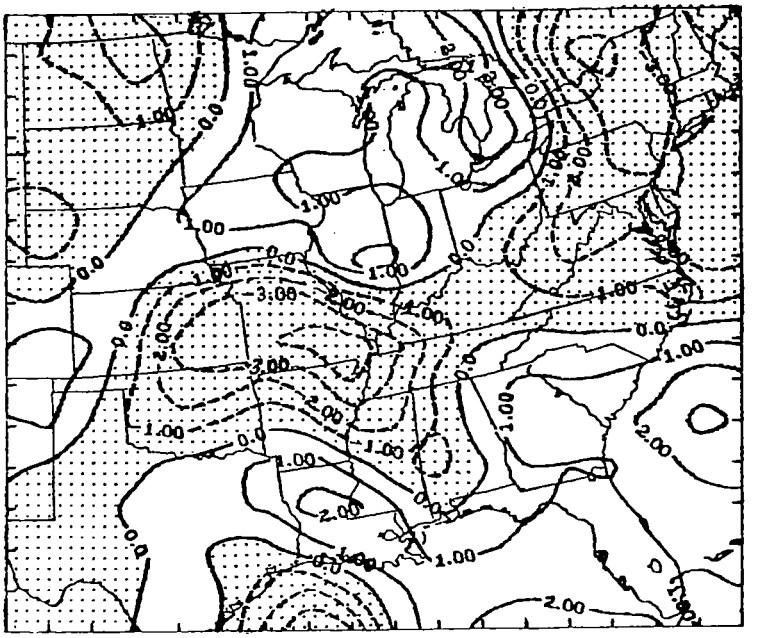

850 mb

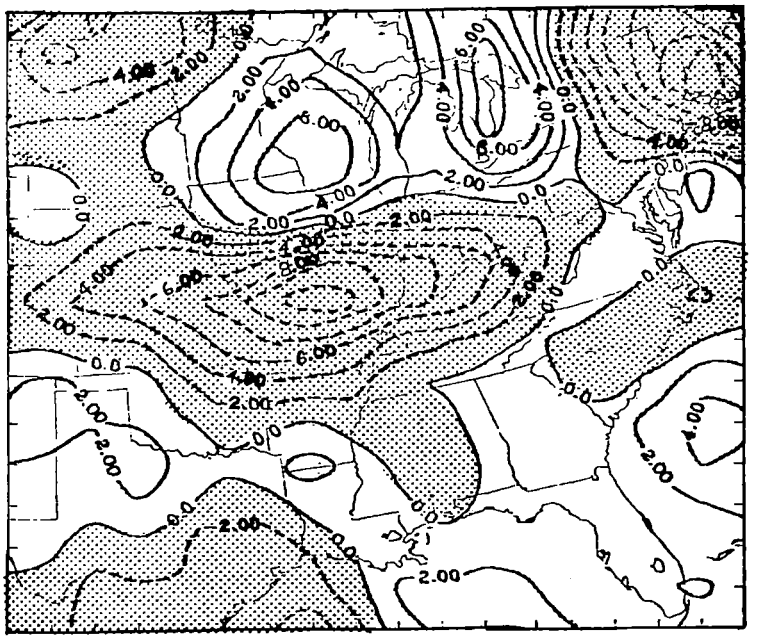

500 mb

d. Vertical velocity (μbars s^{-1}) (upward areas are shaded).

Fig. 6. (Continued)

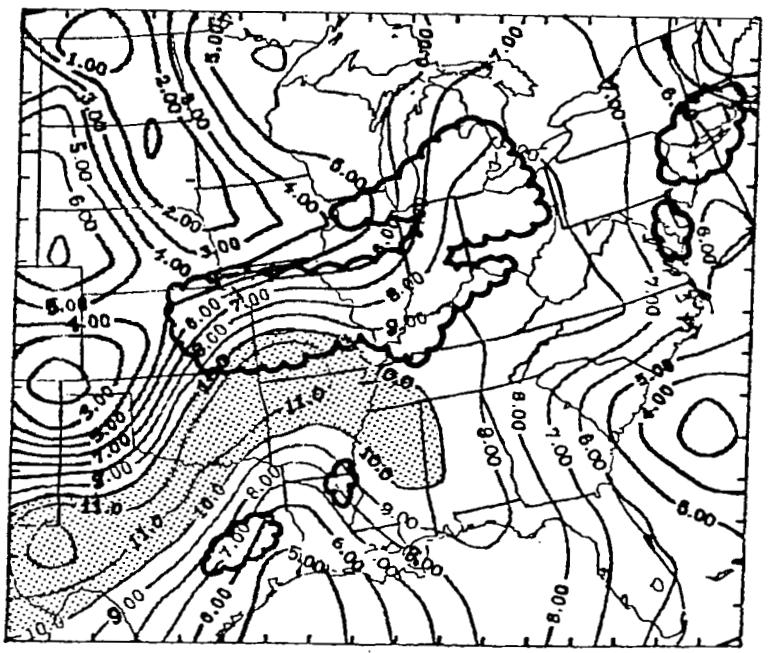

850 mb

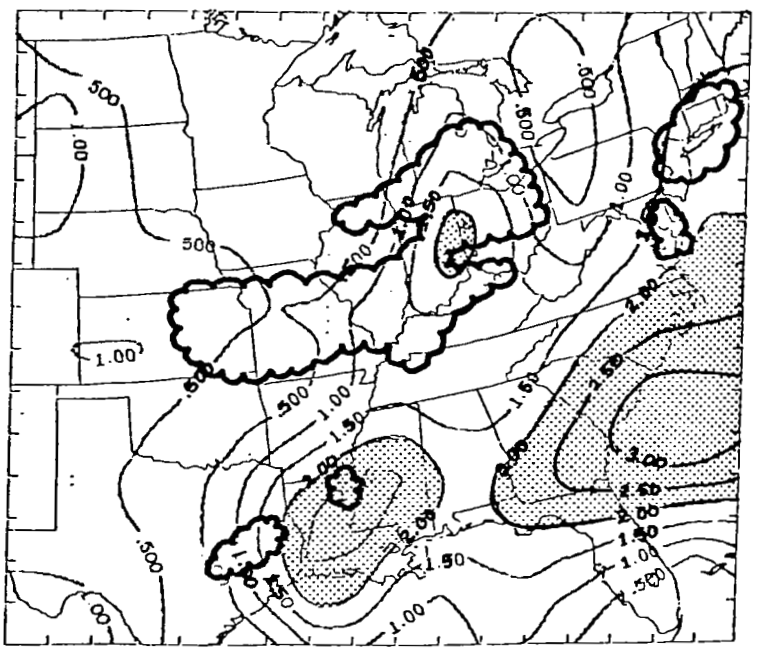

500 mb

e. Mixing ratio (g kg^{-1}) (areas of convection are scalloped). Values greater than 10 and 2 g kg^{-1} are shaded at 850 and 500 mb, respectively.

Fig. 6. (Continued)

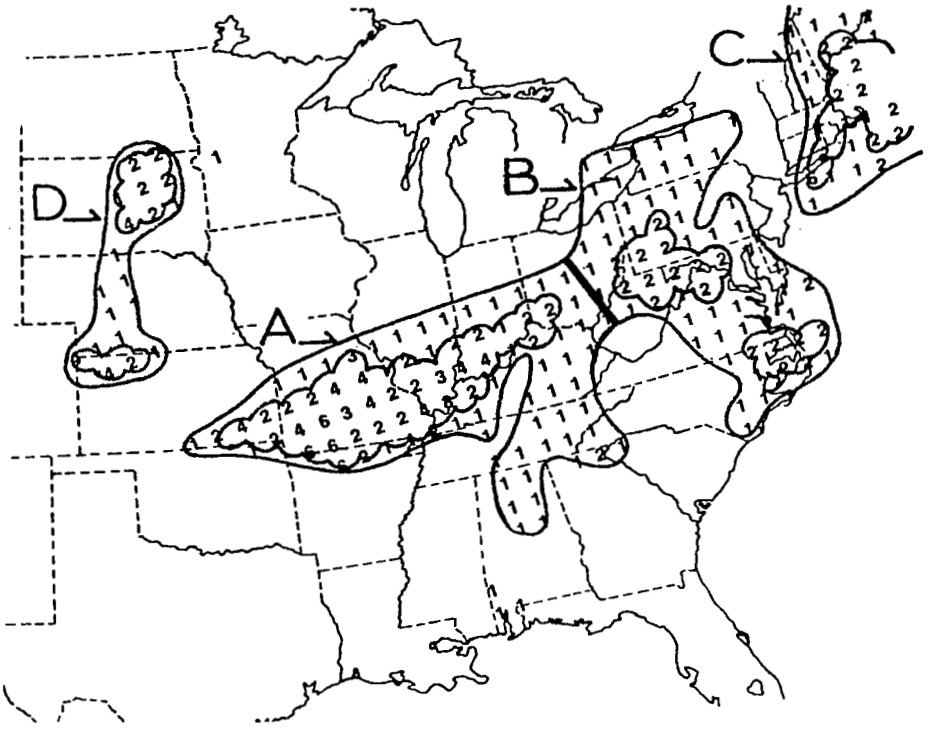

a. Composite MDR precipitation analysis

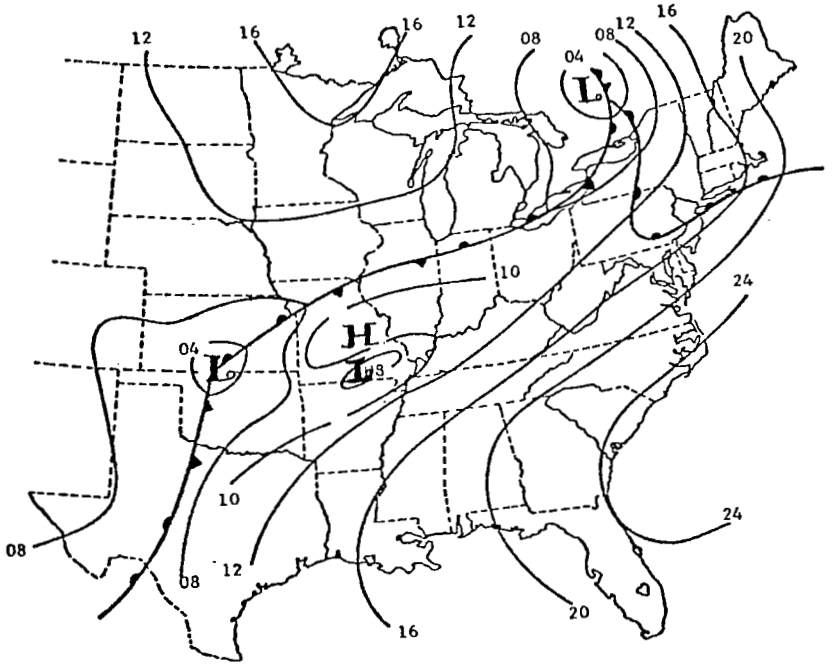

b. Surface pressure and frontal analysis

Fig. 7. Same as Fig. 6 except for 1200 GMT,24 April 1975.

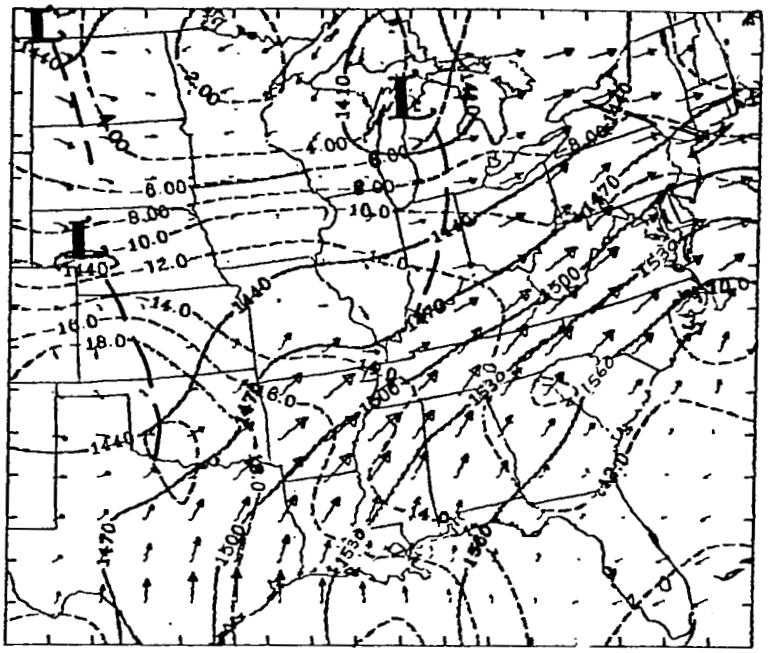

850 mb

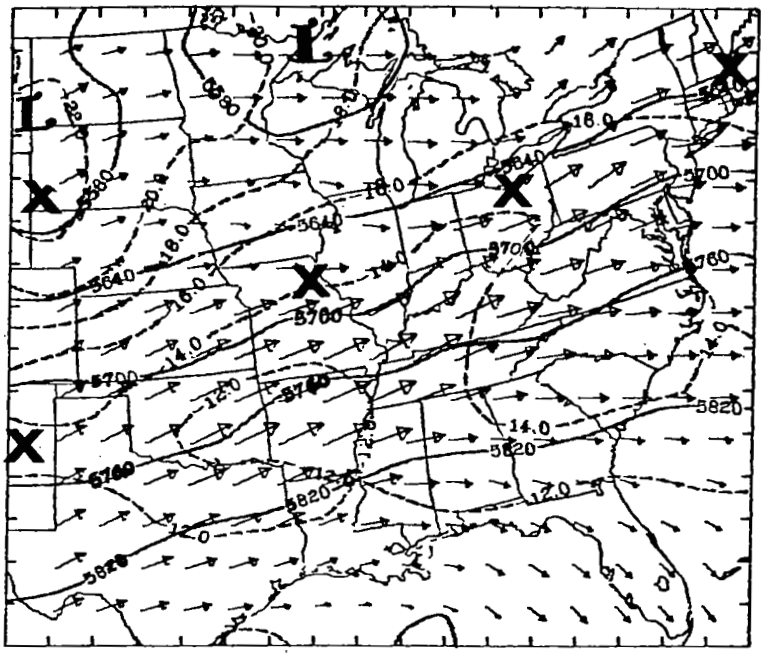

500 mb

c. Geopotential height (m) (solid lines), temperature (^{o}C) (dashed lines), and vector wind (→=25 m s^{-1}).

Fig. 7. (Continued)

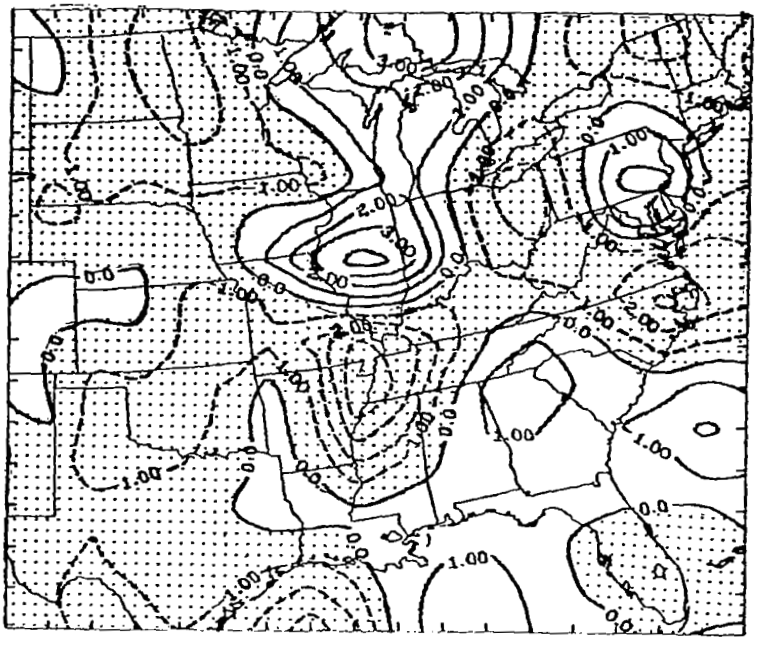

850 mb

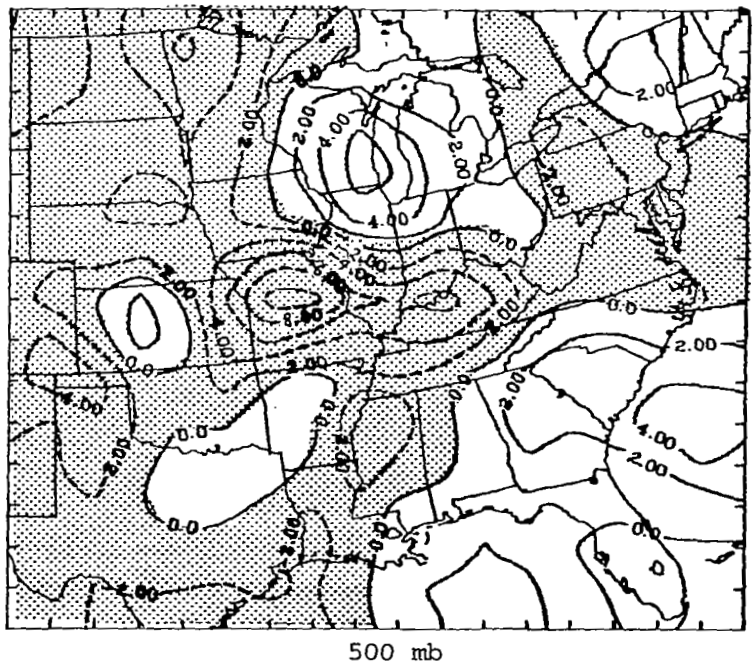

500 mb

d. Vertical velocity (μbars s^{-1}) (upward areas are shaded).

Fig. 7. (Continued)

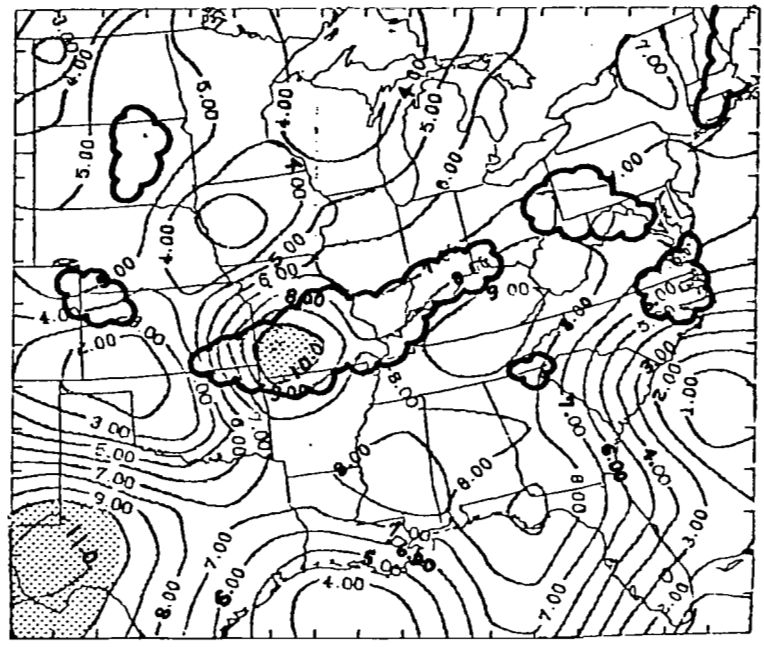

850 mb

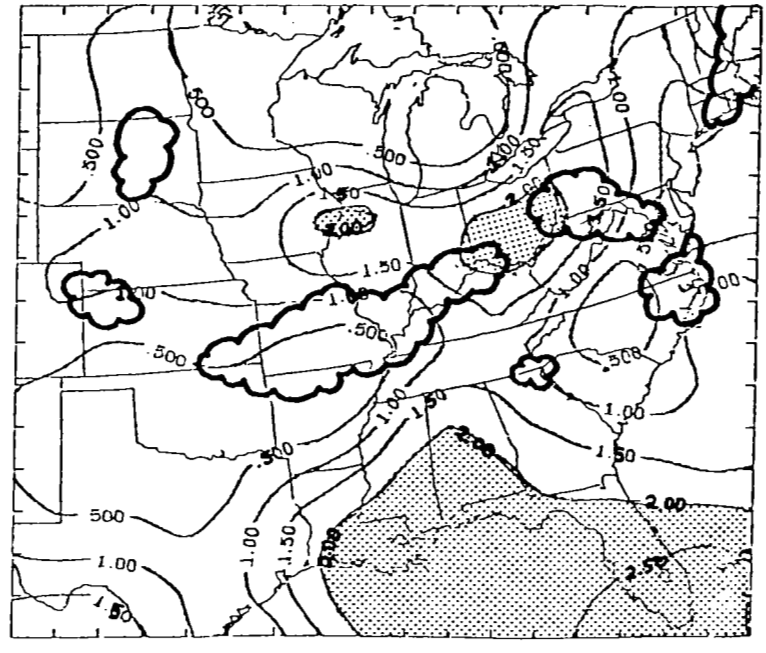

500 mb

e. Mixing ratio (g kg^{-1})(areas of convection are scalloped). Values greater than 10 and 2 g kg^{-1} are shaded at 850 and 500 mb, respectively.

Fig. 7. (Continued)

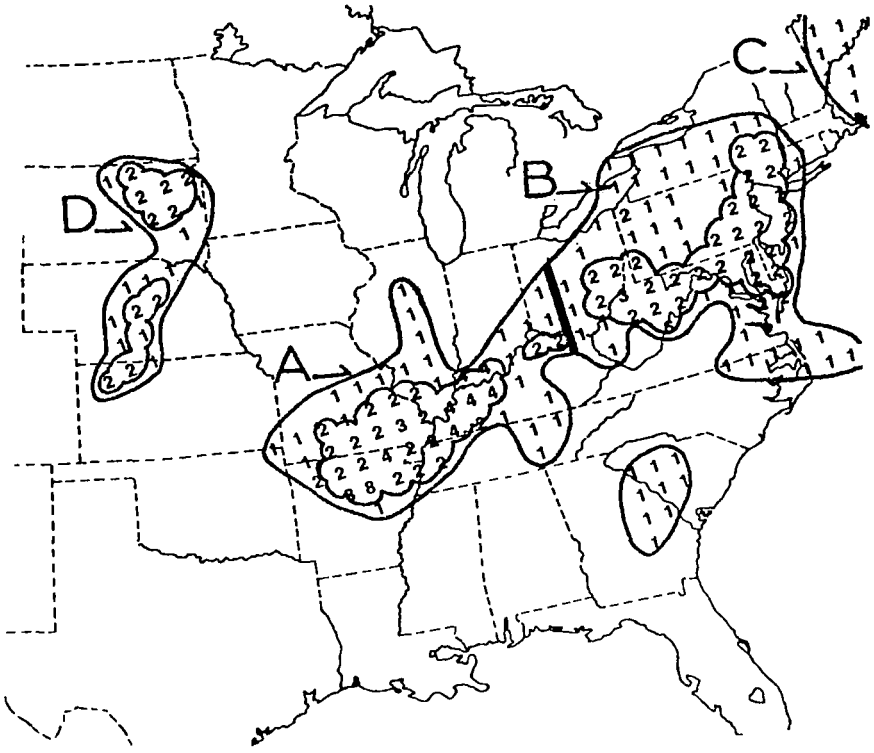

a. Composite MDR precipitation analysis

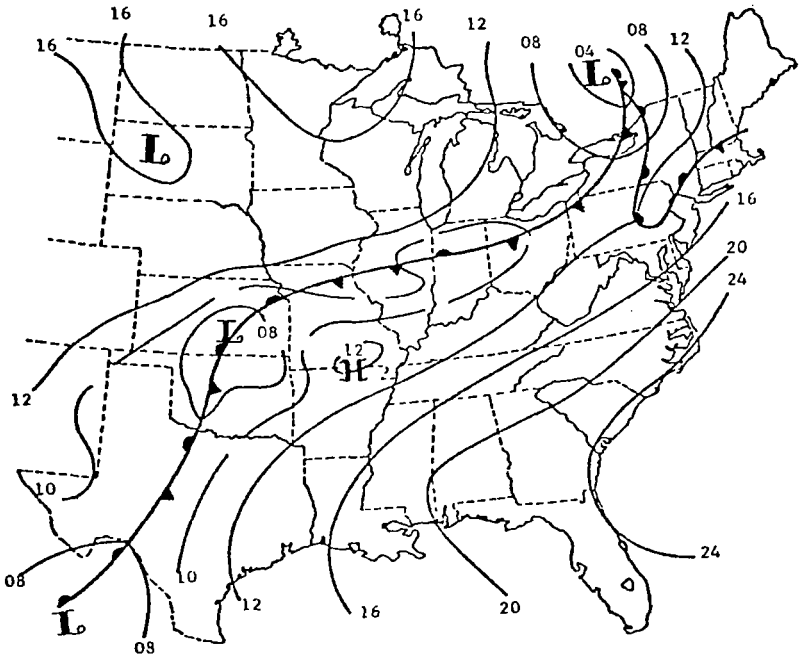

b. Surface pressure and frontal analysis

Fig. 8. Same as Fig. 6 except for 1500 GMT,24 April 1975.

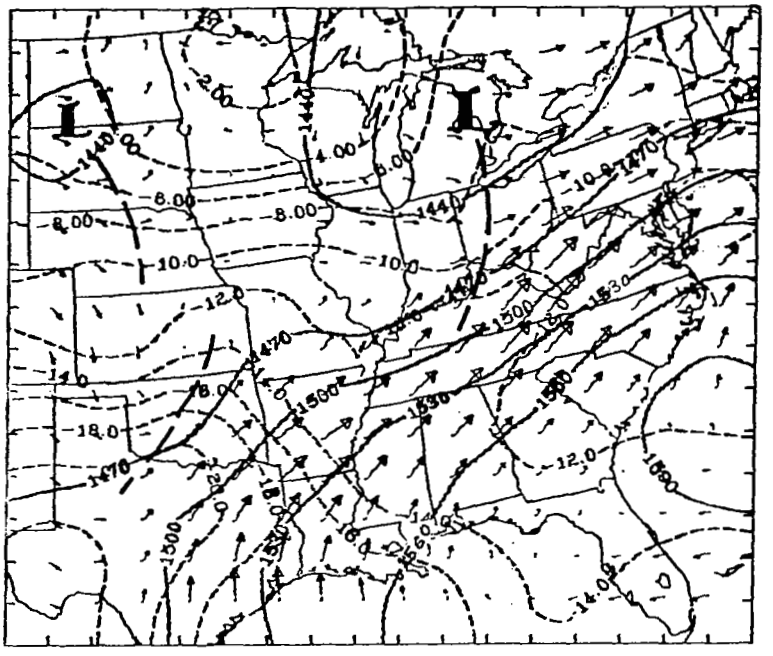

850 mb

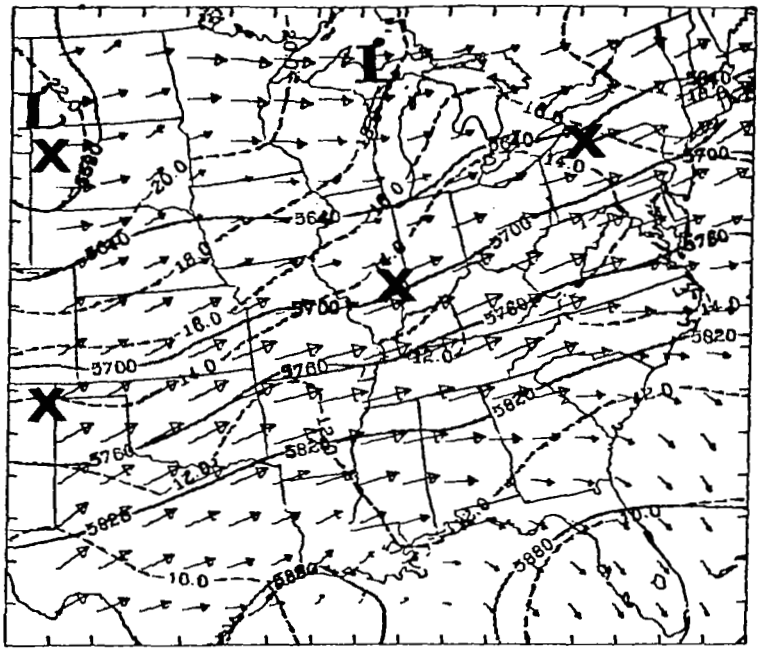

500 mb

c. Geopotential height (m)(solid lines), temperature ($^{\circ}$C)(dashed lines), and vector wind (→=25 m s^{-1}).

Fig. 8. (Continued)

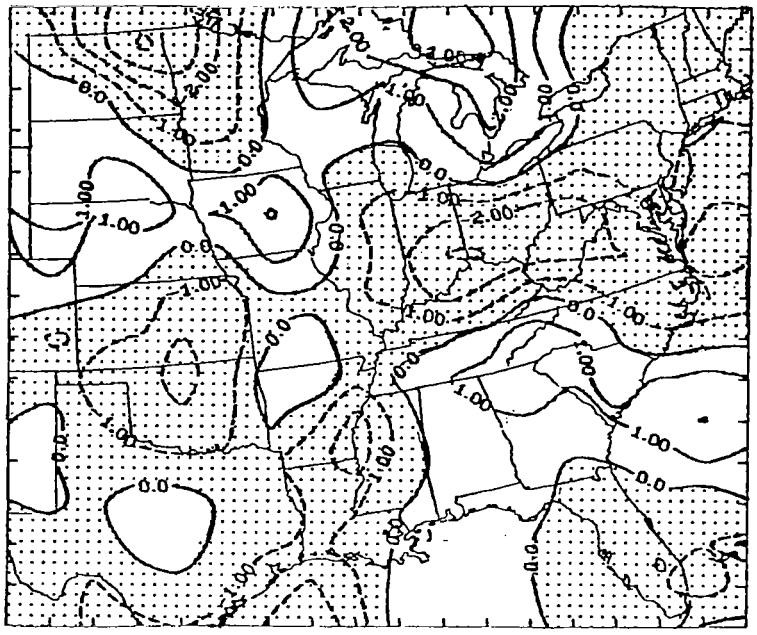

850 mb

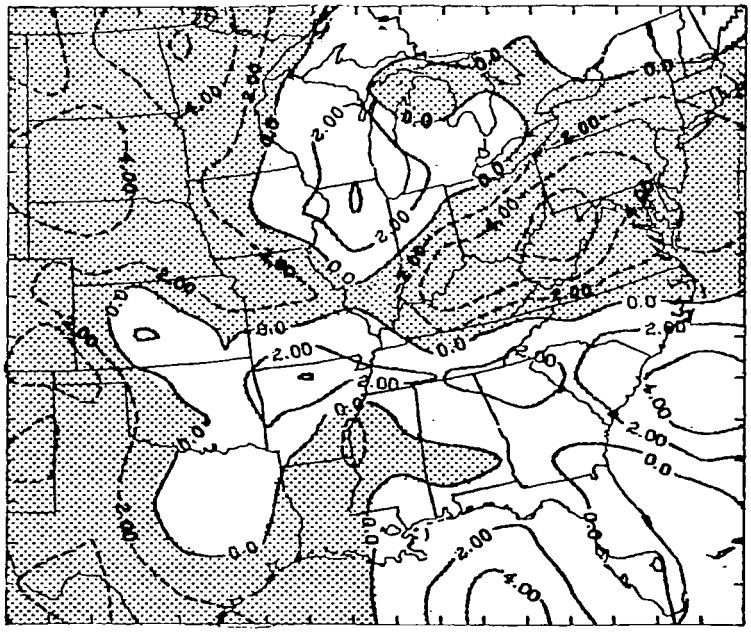

500 mb

d. Vertical velocity (μbars s^{-1}) (upward areas are shaded).

Fig. 8. (Continued)

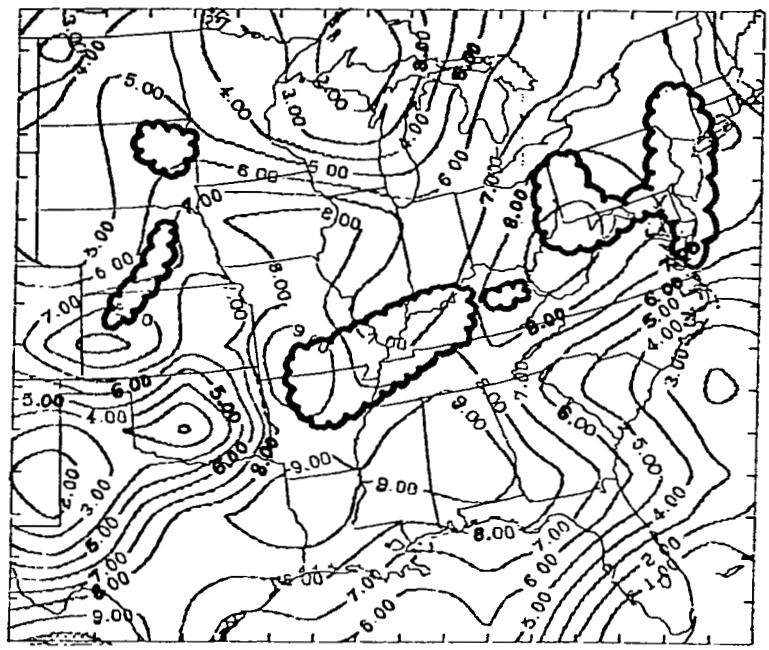

850 mb

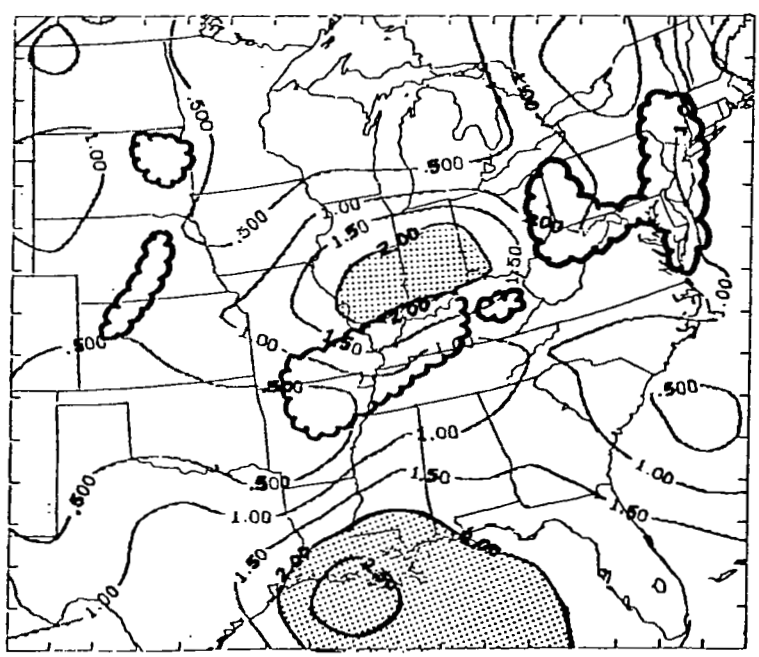

500 mb

e. Mixing ratio (g kg^{-1}) (areas of convection are scalloped). Values greater than 10 and 2 g kg^{-1} are shaded at 850 and 500 mb, respectively.

Fig. 8. (Continued)

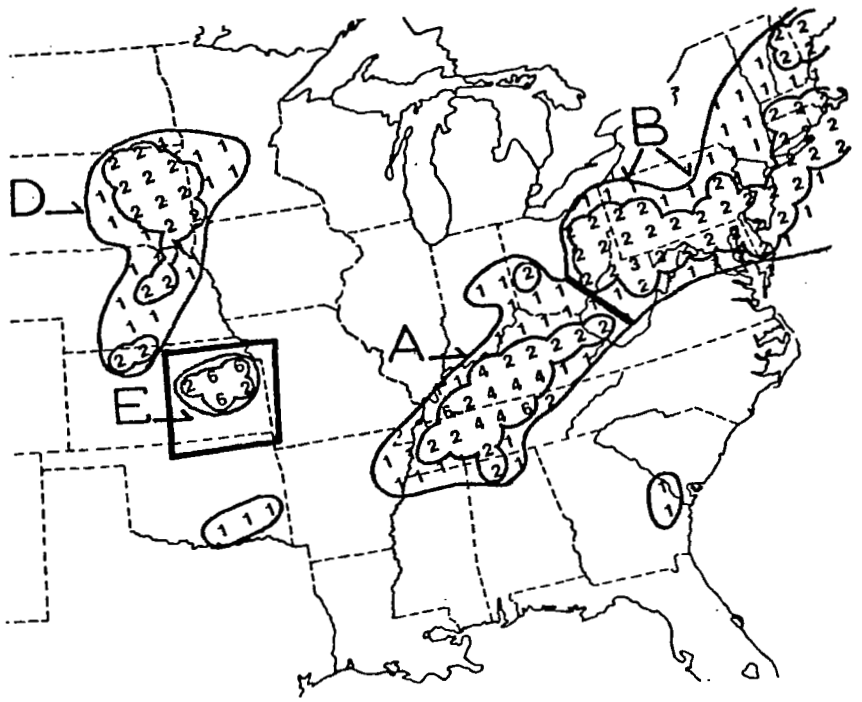

a. Composite MDR precipitation analysis

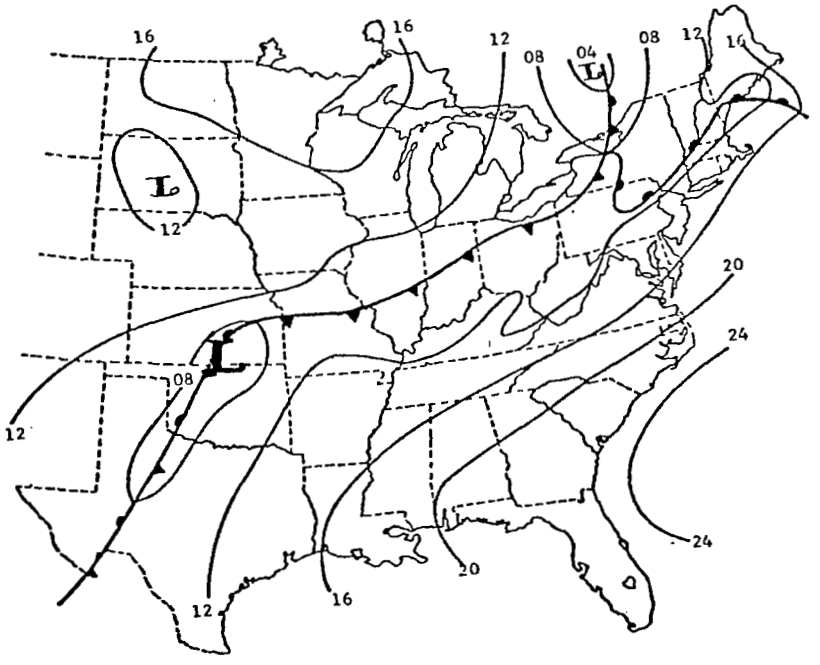

b. Surface pressure and frontal analysis

Fig. 9. Same as Fig. 6 except for 1800 GMT, 24 April 1975.

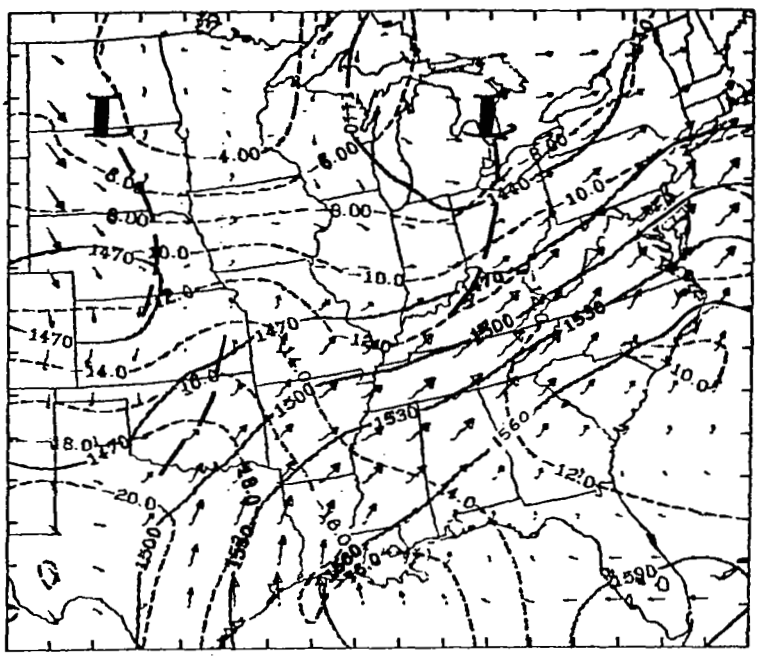

850 mb

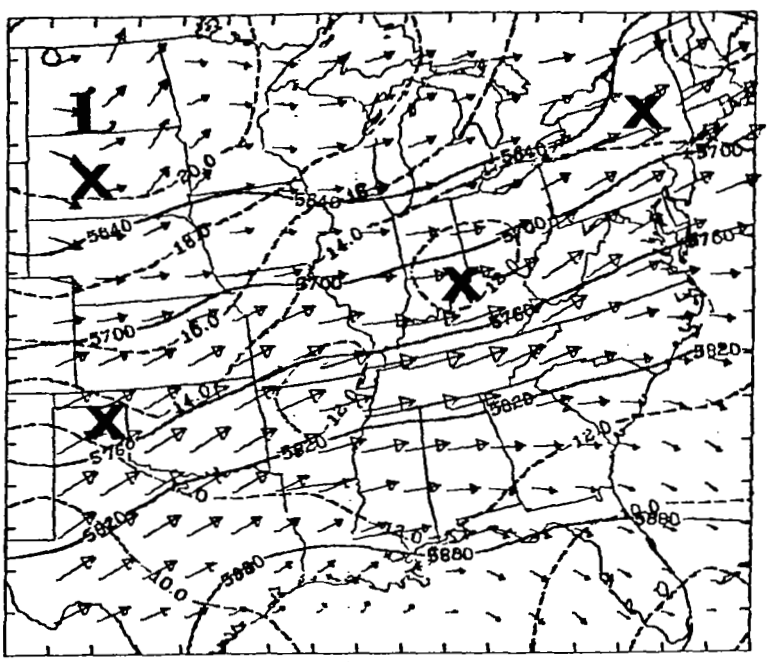

500 mb

c. Geopotential height (m)(solid lines), temperature (^{o}C)(dashed lines), and vector wind (→=25 m s^{-1}).

Fig. 9. (Continued)

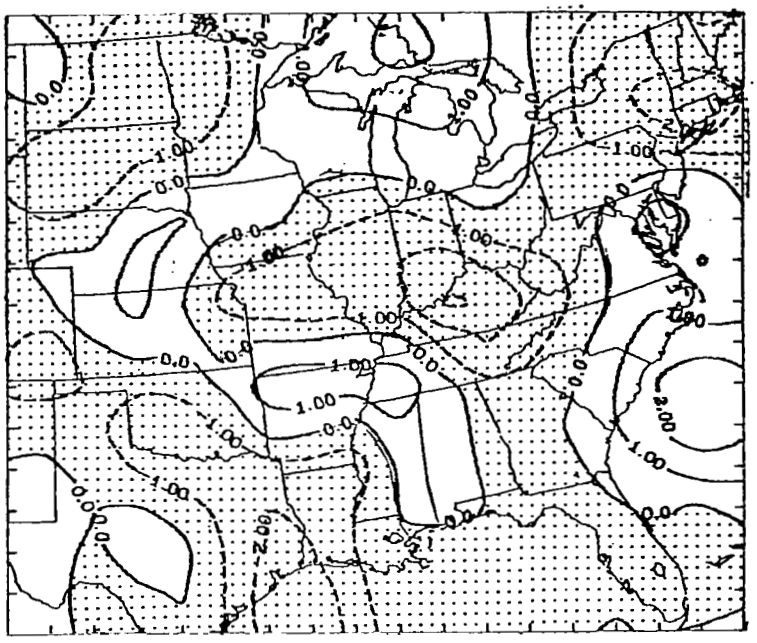

850 mb

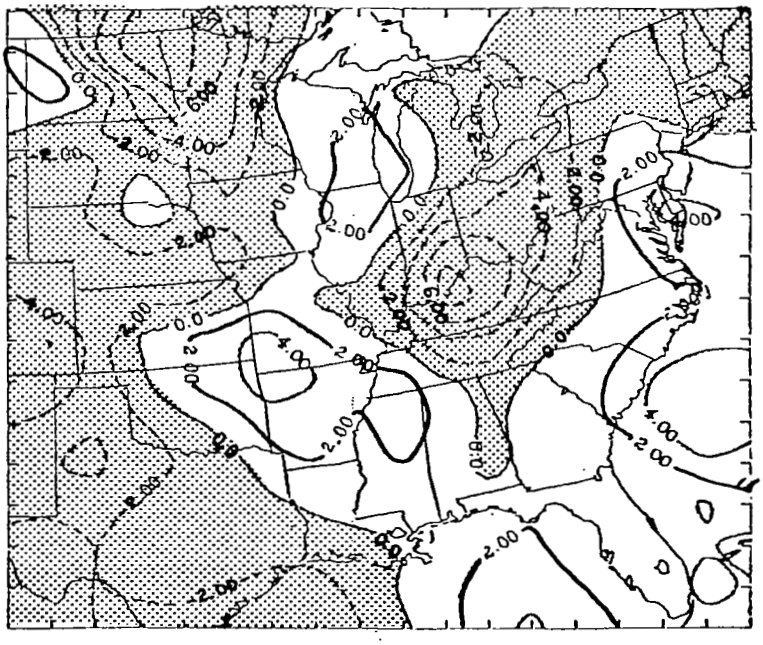

500 mb

d. Vertical velocity (μbars s^{-1}) (upward areas are shaded).

Fig. 9. (Continued)

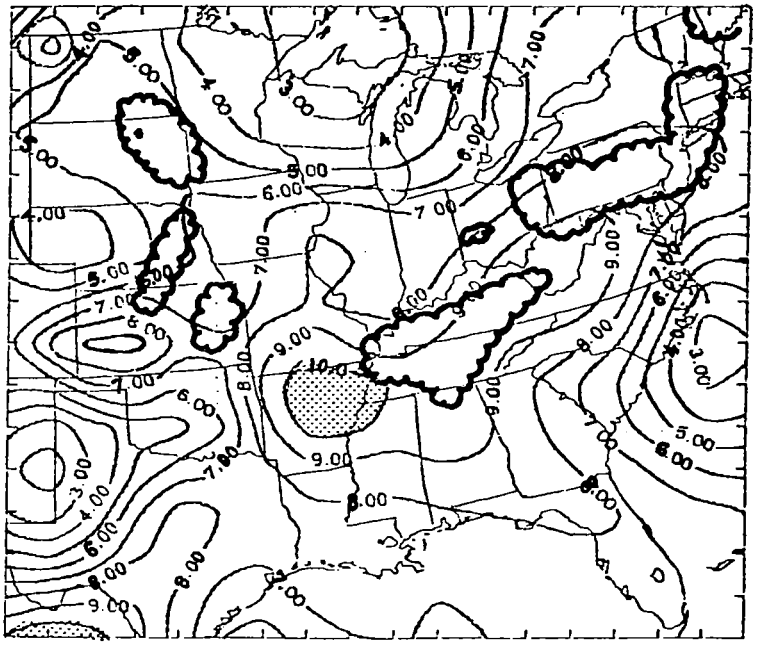

850 mb

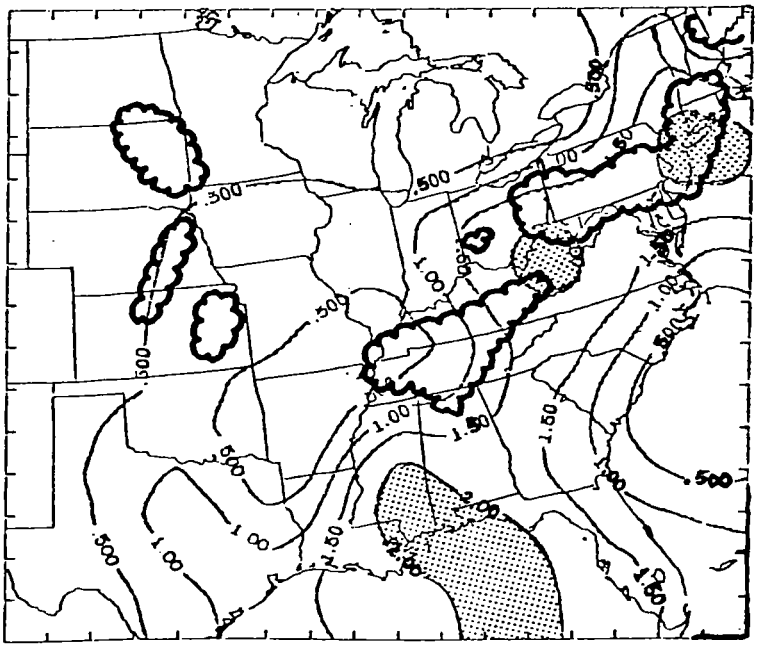

500 mb

e. Mixing ratio (g kg^{-1}) (areas of convection are scalloped). Values greater than 10 and 2 g kg^{-1} are shaded at 850 and and 500 mb, respectively.

Fig. 9. (Continued)

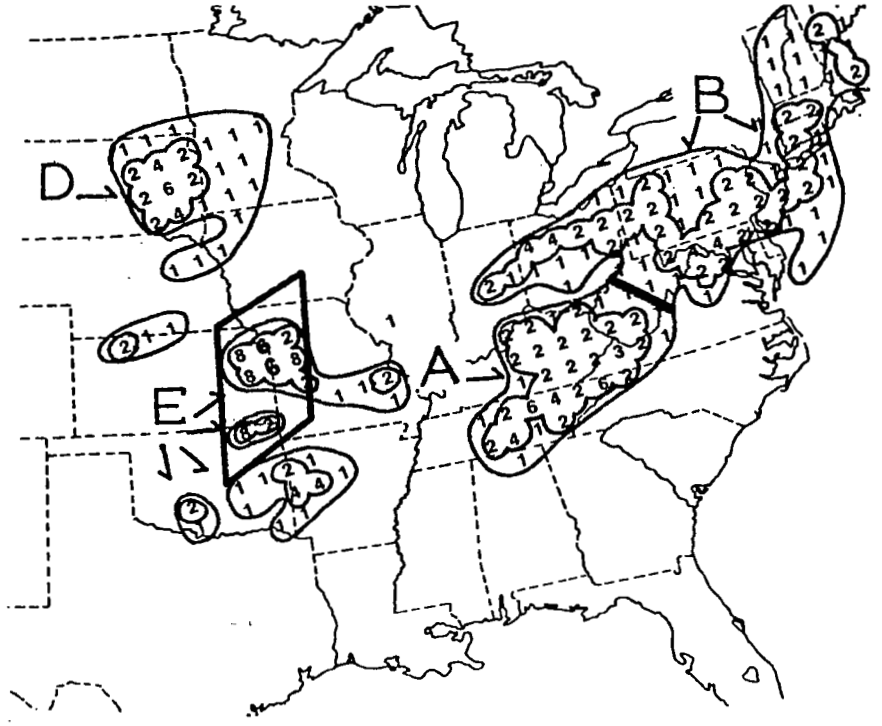

a. Composite MDR precipitation analysis

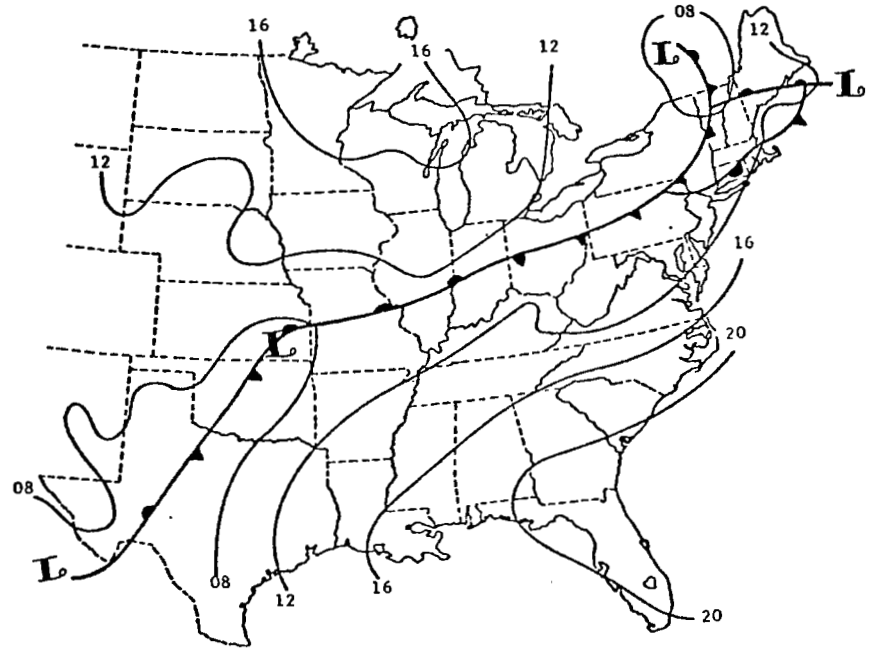

b. Surface pressure and frontal analysis

Fig. 10. Same as Fig. 6 except for 2100 GMT, 24 April 1975.

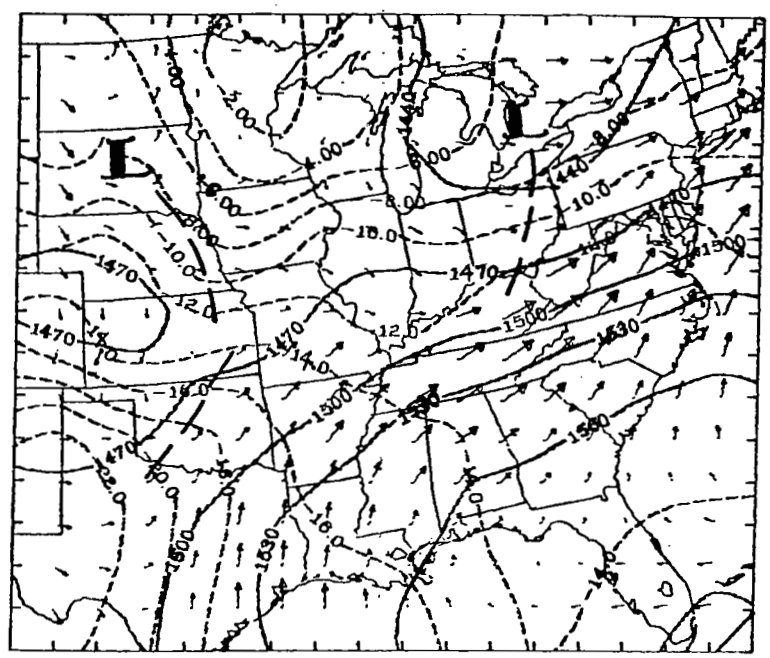

850 mb

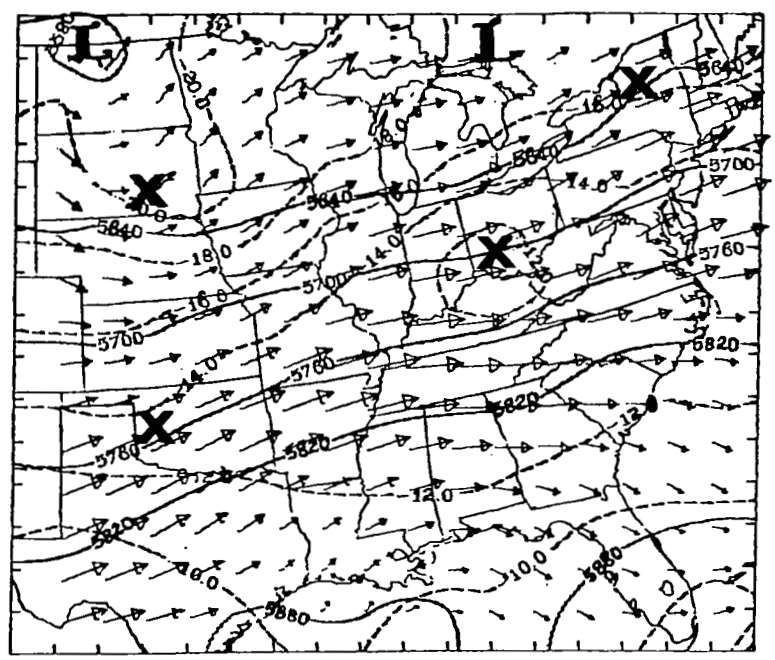

500 mb

c. Geopotential height (m)(soiild lines), temperature (^{o}C)(dashed lines), and vector wind (→=25 m s^{-1}).

Fig. 10. (continued)

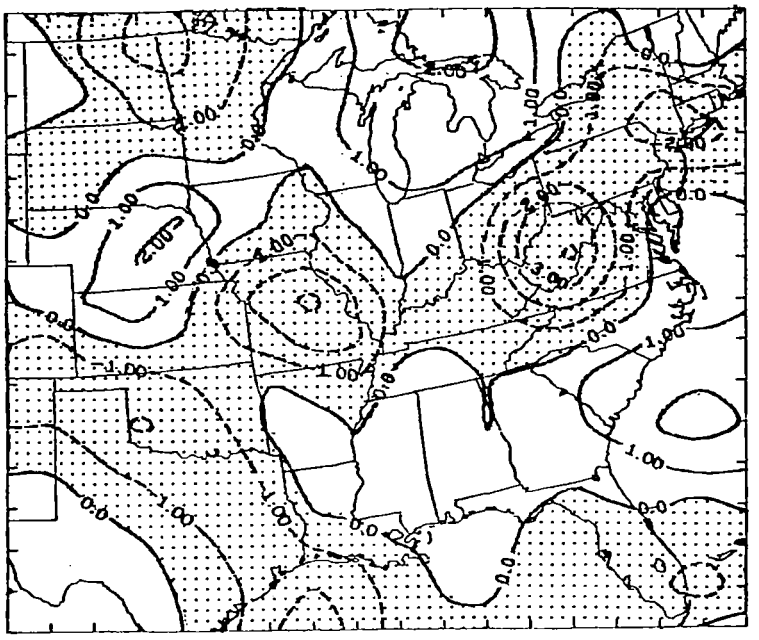

850 mb

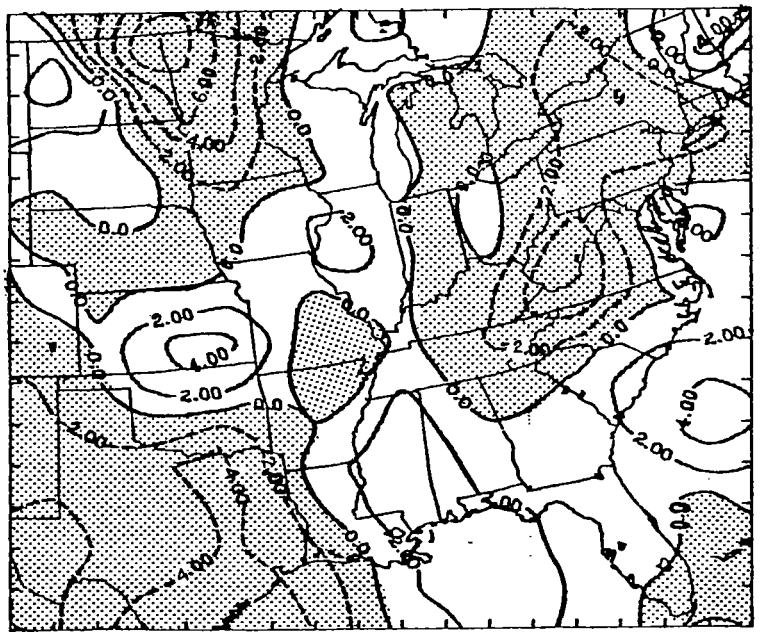

500 mb

d. Vertical velocity (μbars s^{-1}) (upward areas are shaded).

Fig. 10. (Continued)

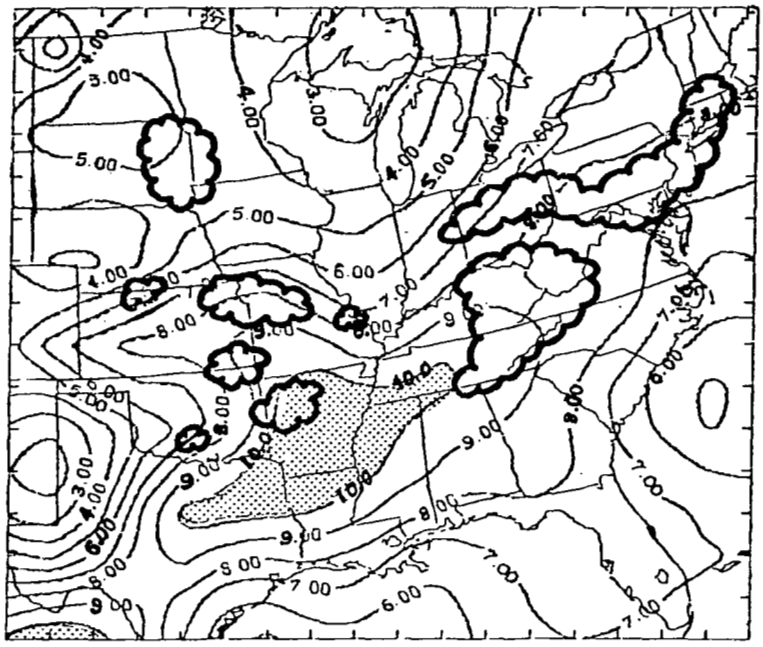

850 mb

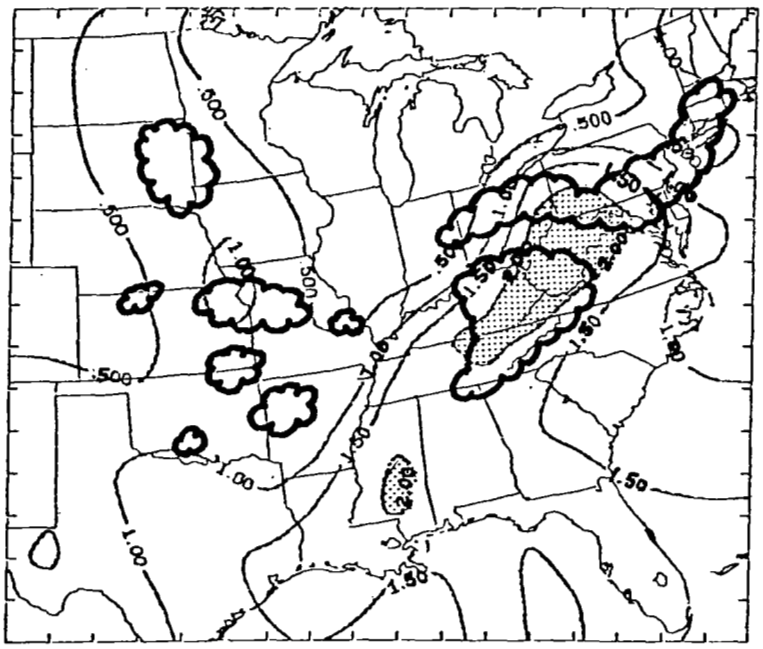

500 mb

e. Mixing ratio (g kg^{-1}) (areas of convection are scalloped). Values greater than 10 and 2 g kg^{-1} are shaded at 850 and 500 mb, respectively.

Fig. 10. (Continued)

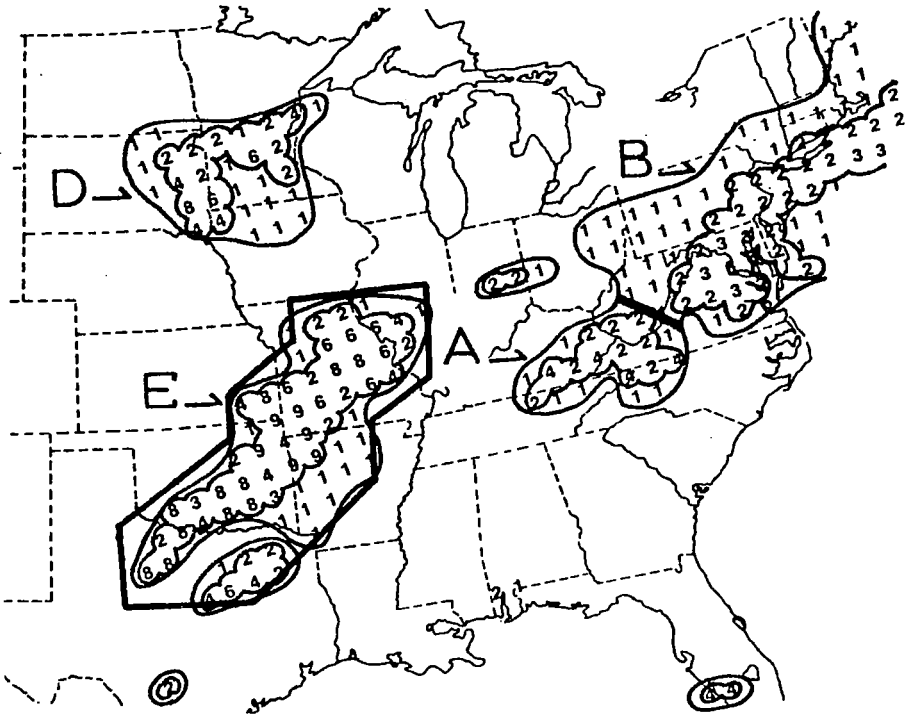

a. Composite MDR precipitation analysis

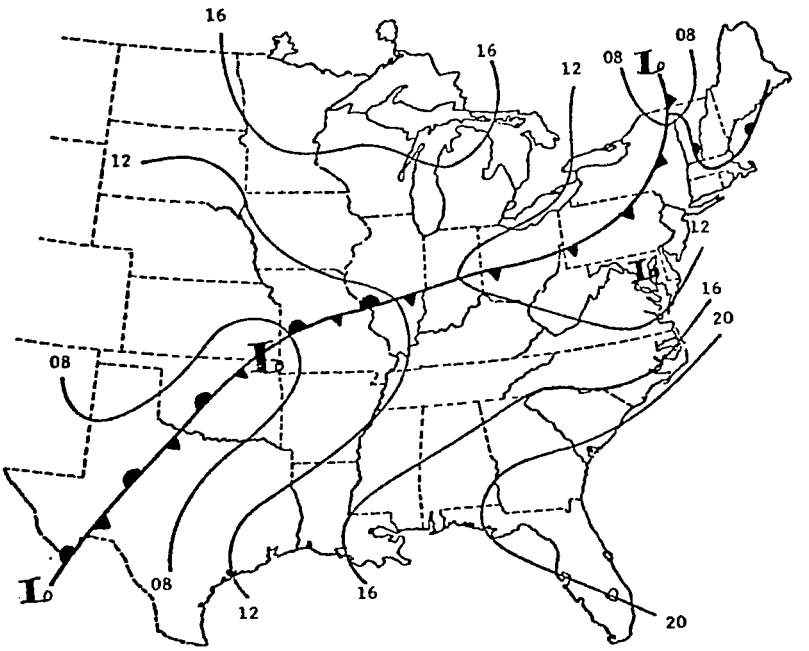

b. Surface pressure and frontal analysis

Fig. 11. Same as Fig. 6 except for 0000 GMT, 25 April 1975.

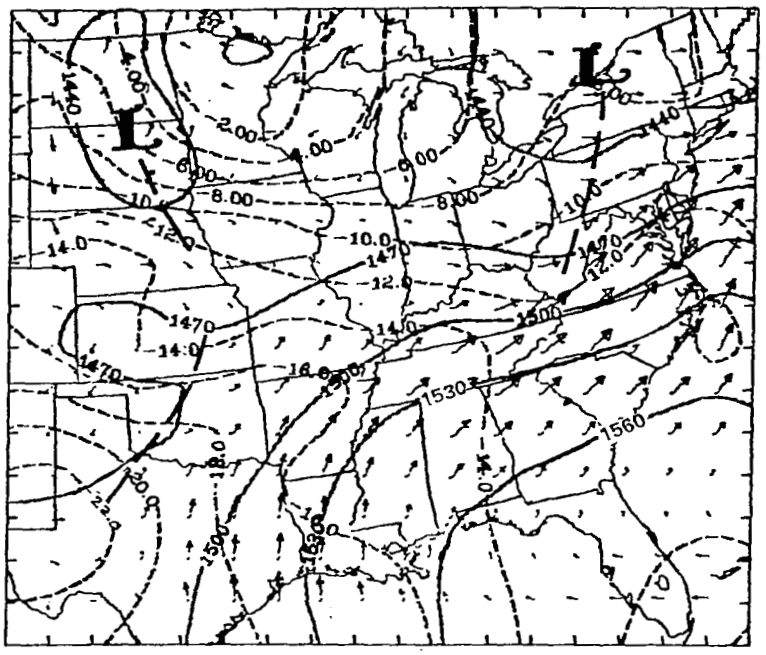

850 mb

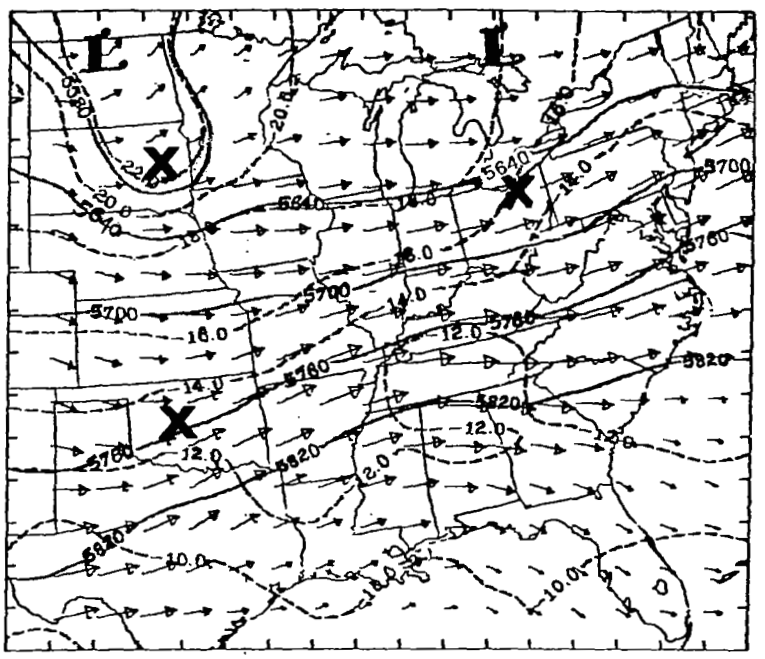

500 mb

c. Geopotential height (m)(solid lines), temperature (^{o}C)(dashed lines), and vector wind (→≈25 m s^{-1}).

Fig. 11. (Continued)

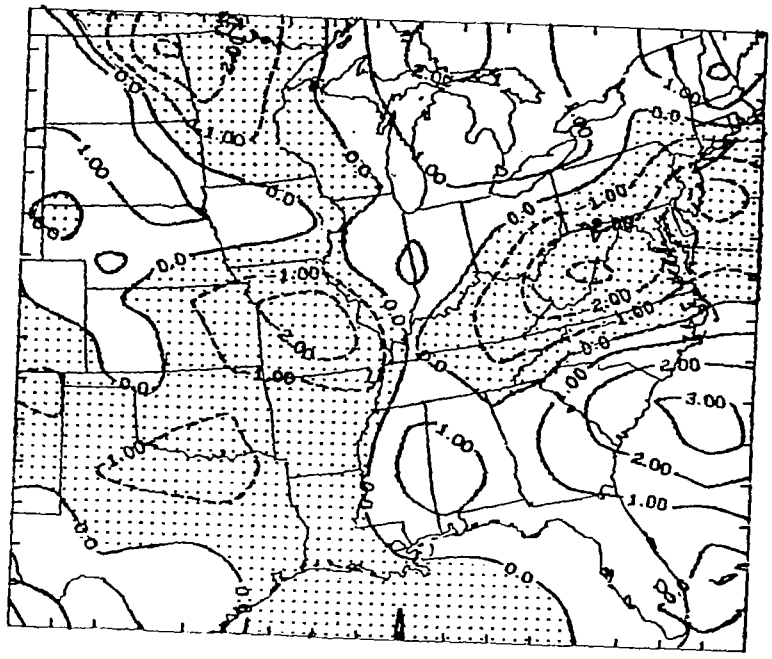

850 mb

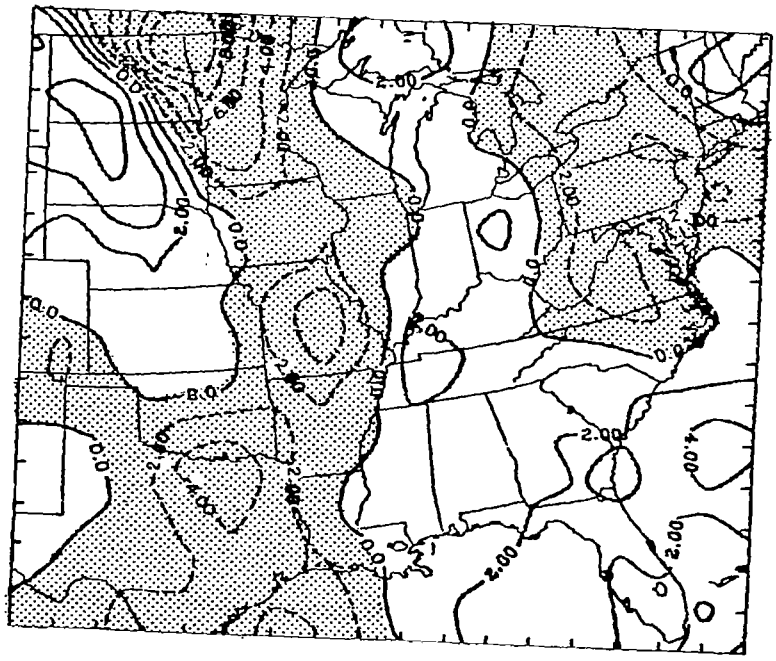

500 mb

d. Vertical velocity (μbars s^{-1}) (upward areas are shaded).

Fig. 11. (Continued)

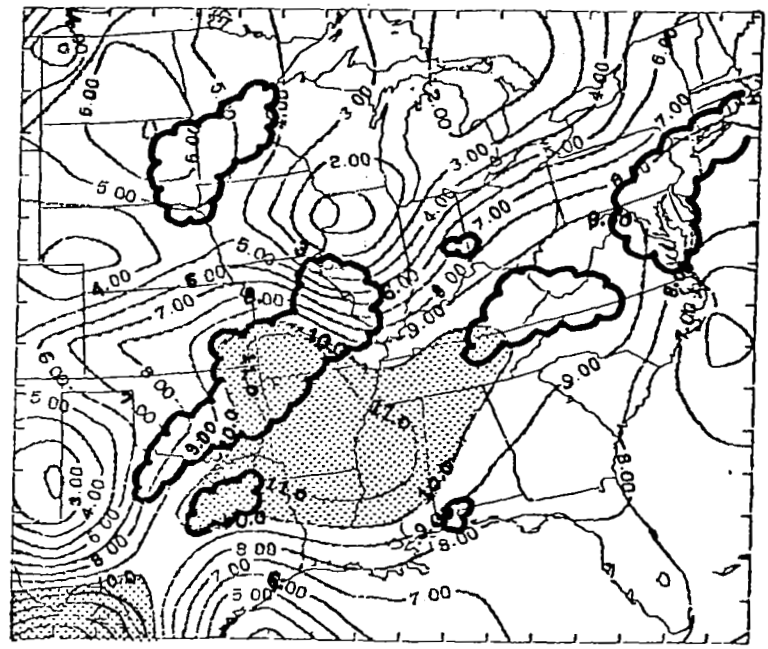

850 mb

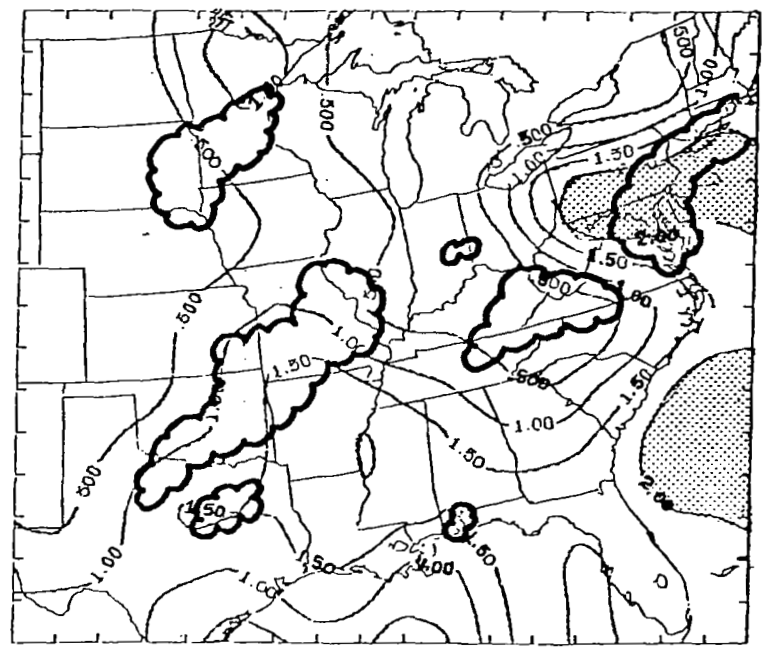

500 mb

e. Mixing ratio (g kg^{-1}) (areas of convection are scalloped). Values greater than 10 and 2 g kg^{-1} are shaded at 850 and 500 mb, respectively.

Fig. 11. (Continued)

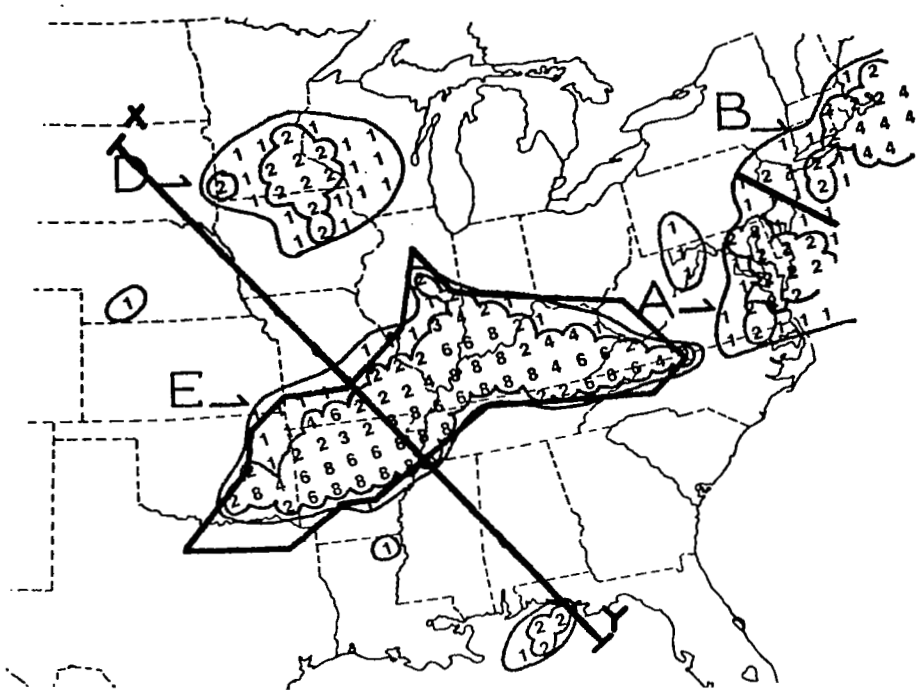

a. Composite MDR precipitation analysis

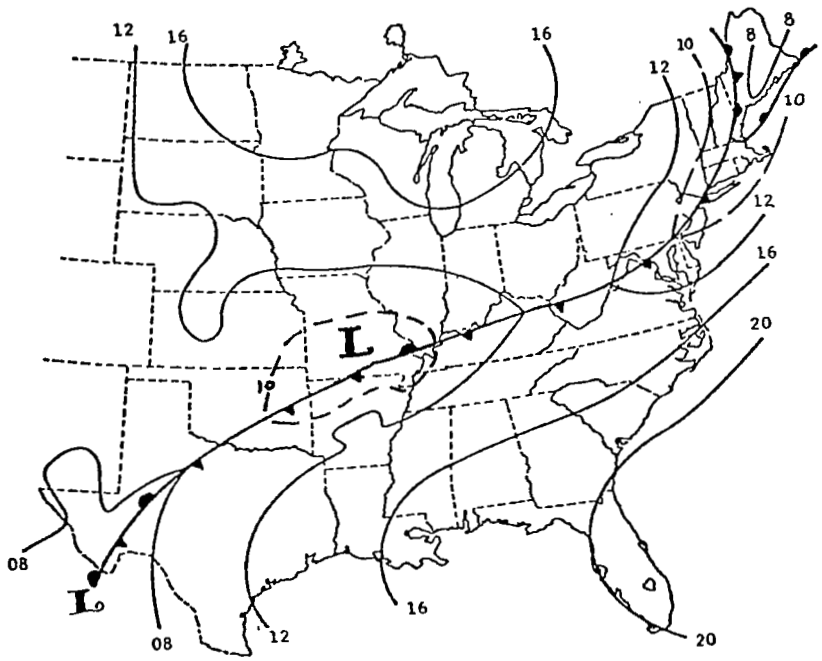

b. Surface pressure and frontal analysis

Fig. 12. Same as Fig. 6 except for 0600 GMT, 25 April 1975.

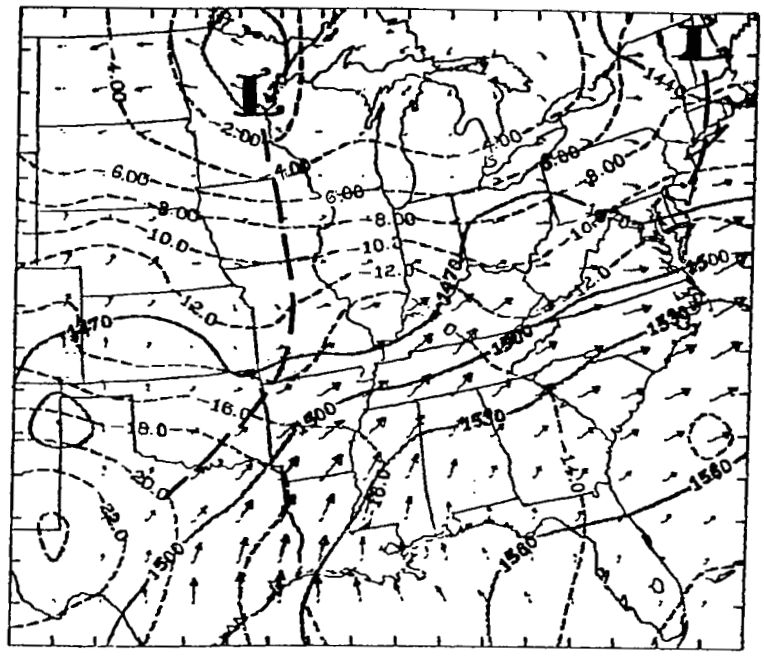

850 mb

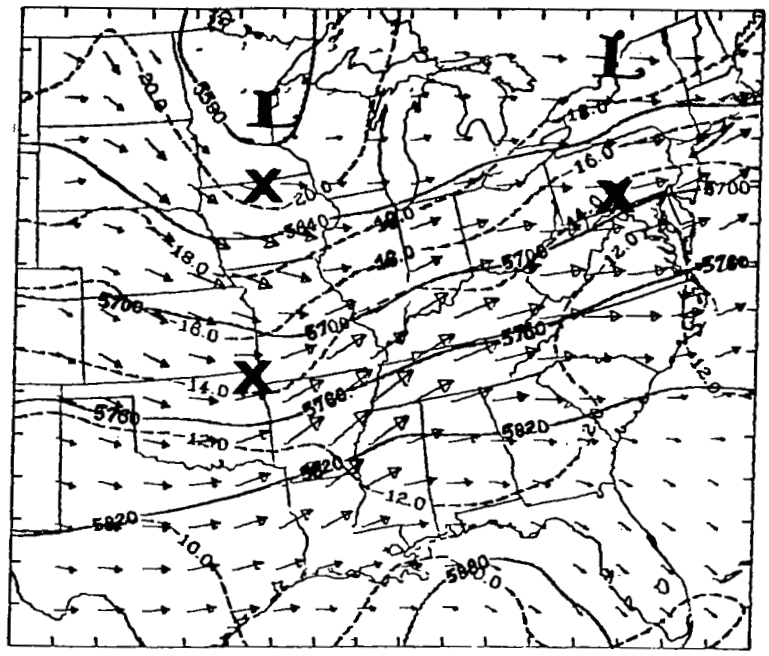

500 mb

c. Geopotential height (m)(solid lines), temperature (^{o}C)(dashed lines), and vector wind (→=25 m s^{-1}).

Fig. 12. (Continued)

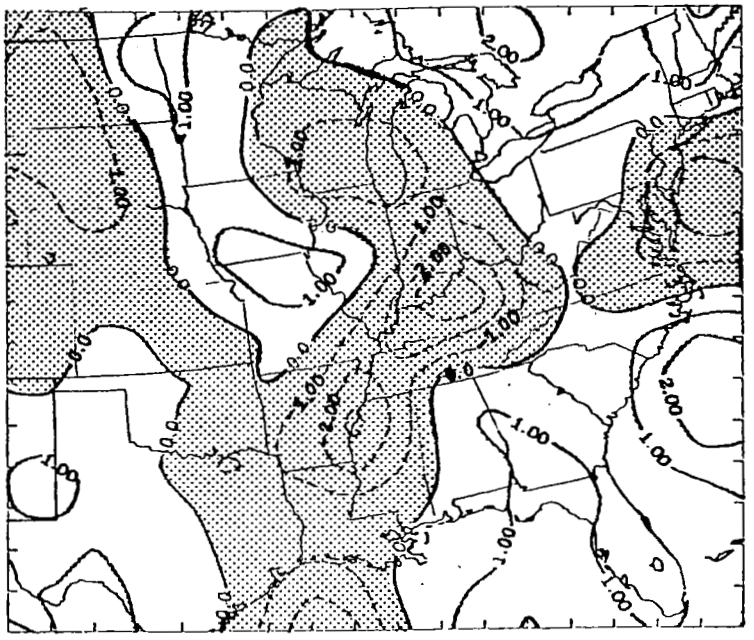

850 mb

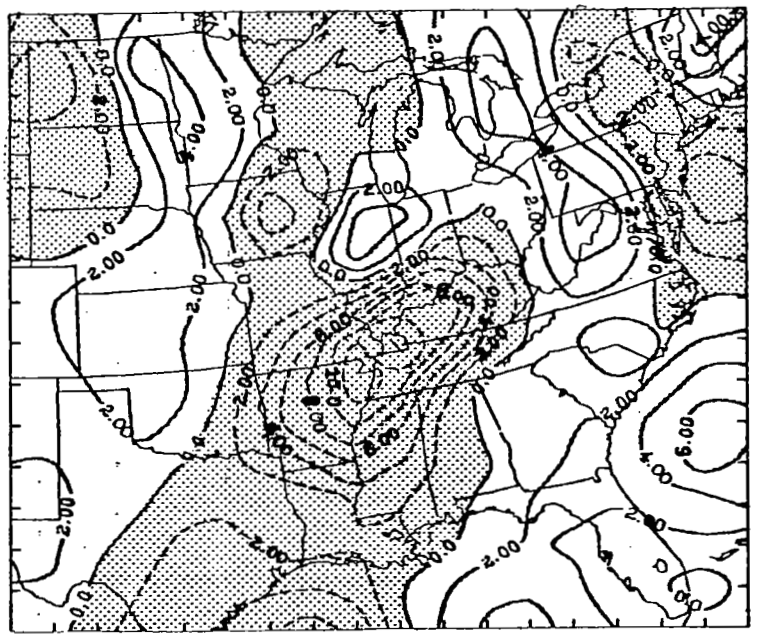

500 mb

d. Vertical velocity (μbars s^{-1}) (upward areas are shaded).

Fig. 12. (Continued)

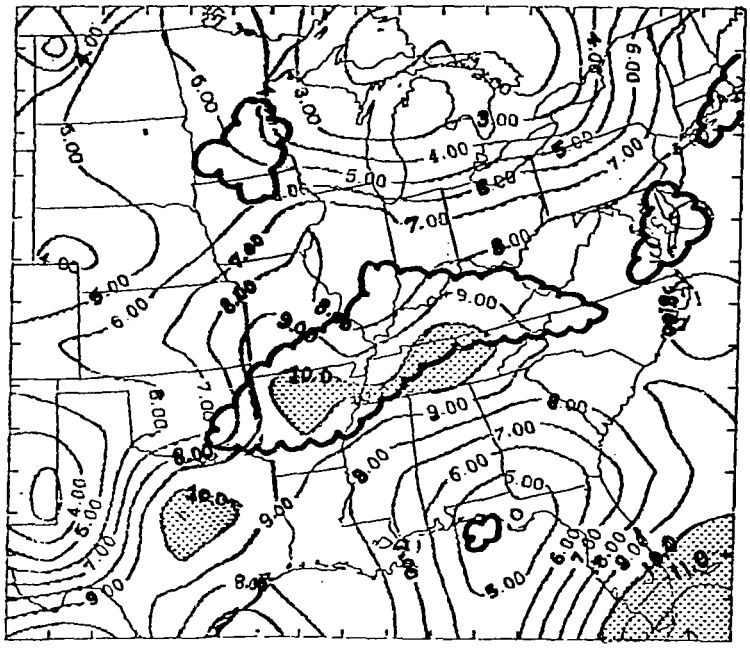

850 mb

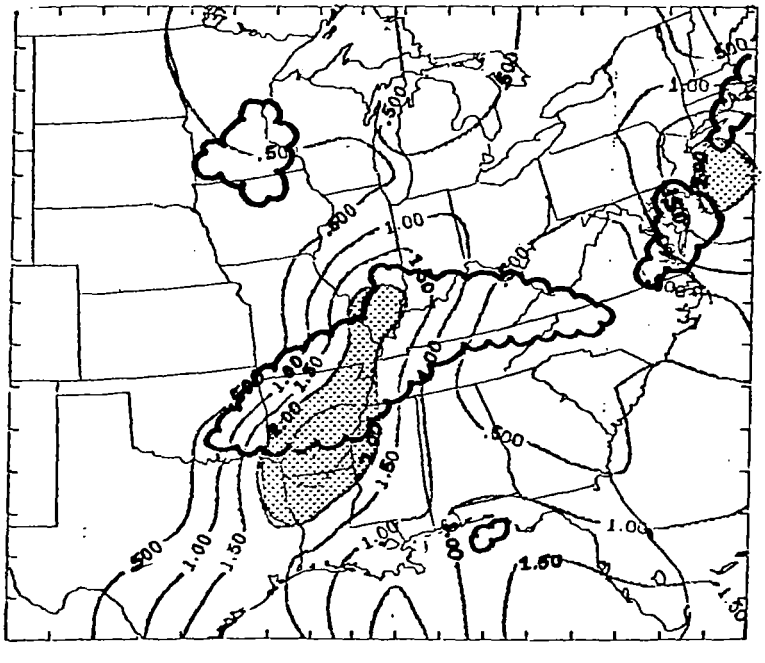

500 mb

e. Mixing ratio (g kg^{-1}) (areas of convection are scalloped). Values greater than 10 and 2 g kg^{-1} are shaded at 850 and 500 mb, respectively.

Fig. 12. (Continued)

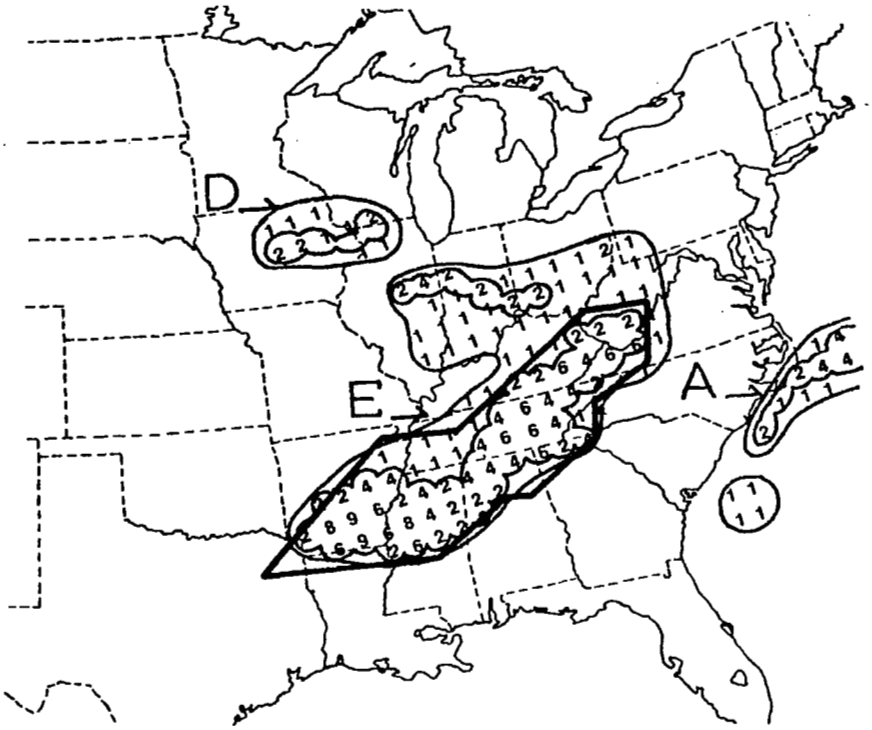

a. Composite MDR precipitation analysis

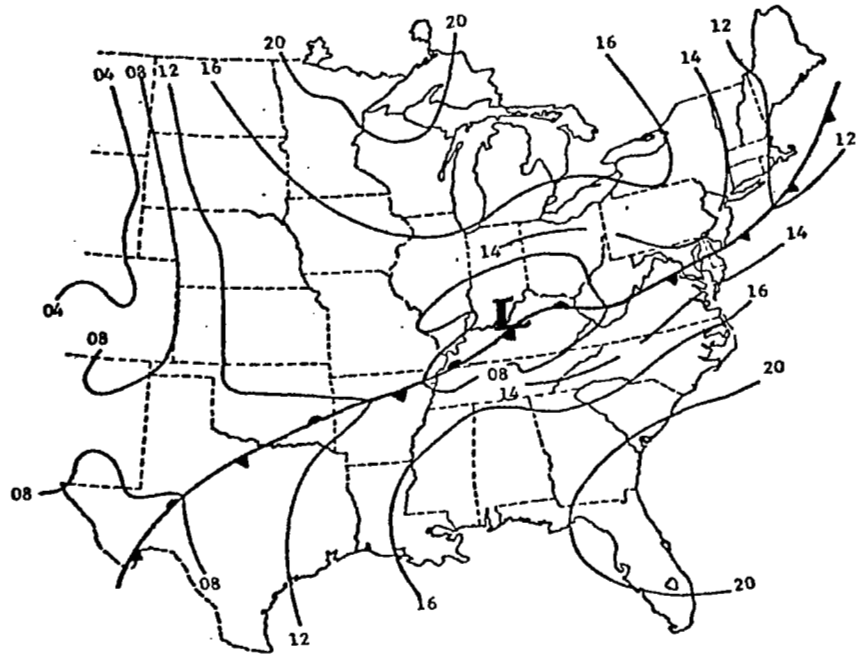

b. Surface pressure and frontal analysis

Fig. 13. Same as Fig. 6 except for 1200 GMT, 25 April 1975.

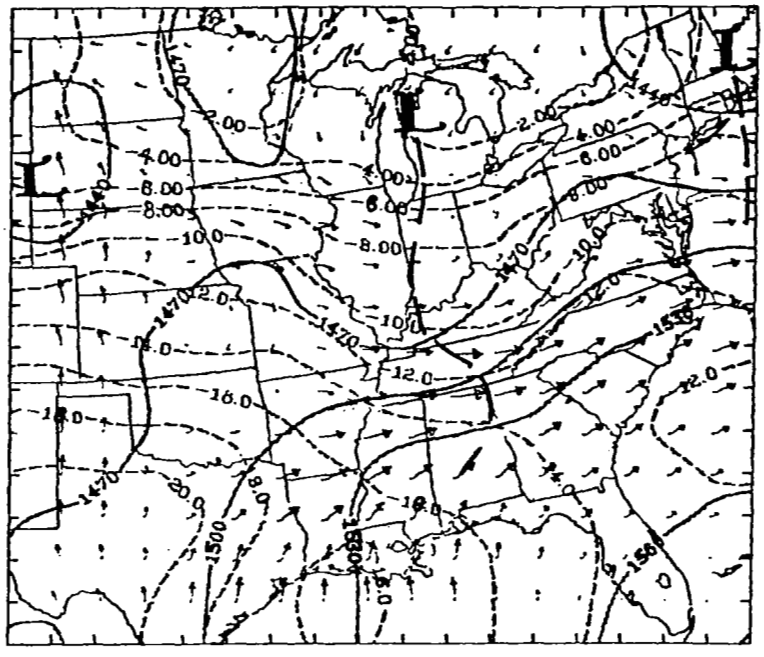

850 mb

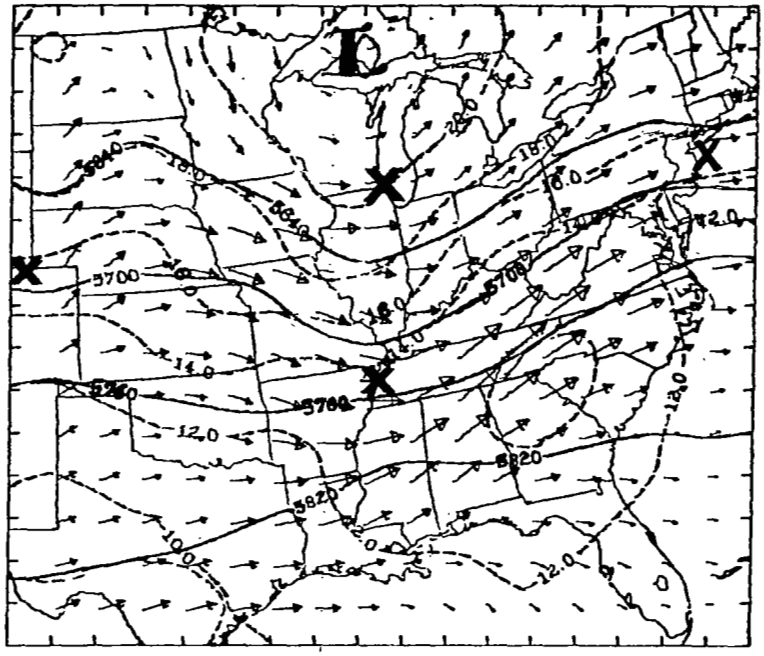

500 mb

c. Geopotential height (m)(solid lines), temperature (^{o}C)(dashed lines), and vector wind (→=25 m s^{-1}).

Fig. 13. (Continued)

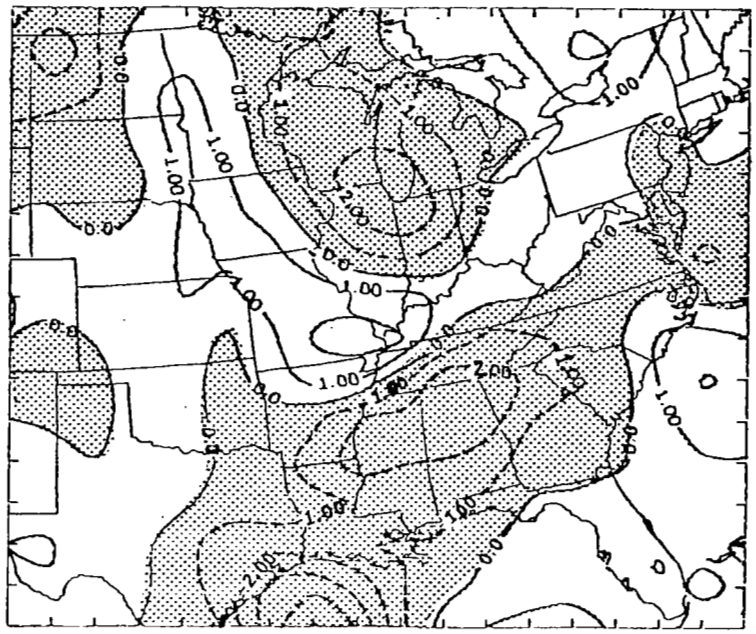

850 mb

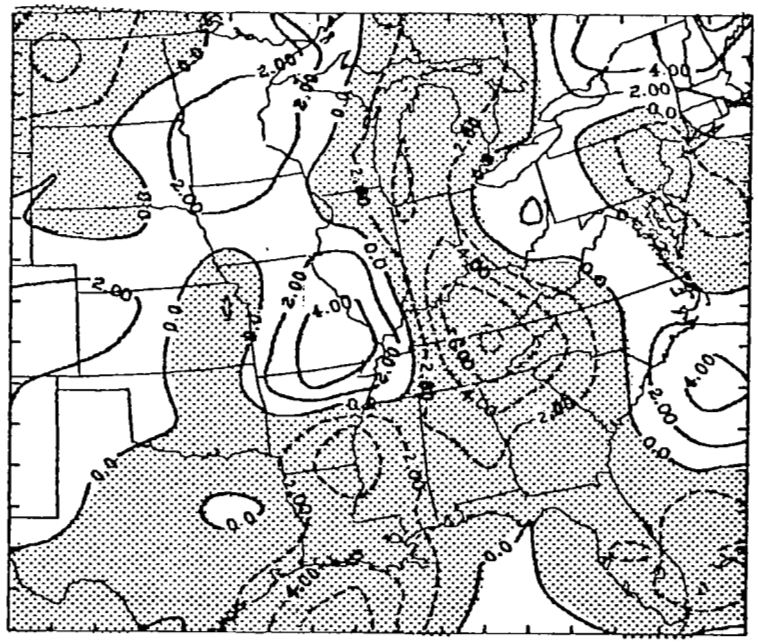

500 mb

d. Vertical velocity (μbars s^{-1}) (upward areas are shaded).

Fig. 13. (Continued)

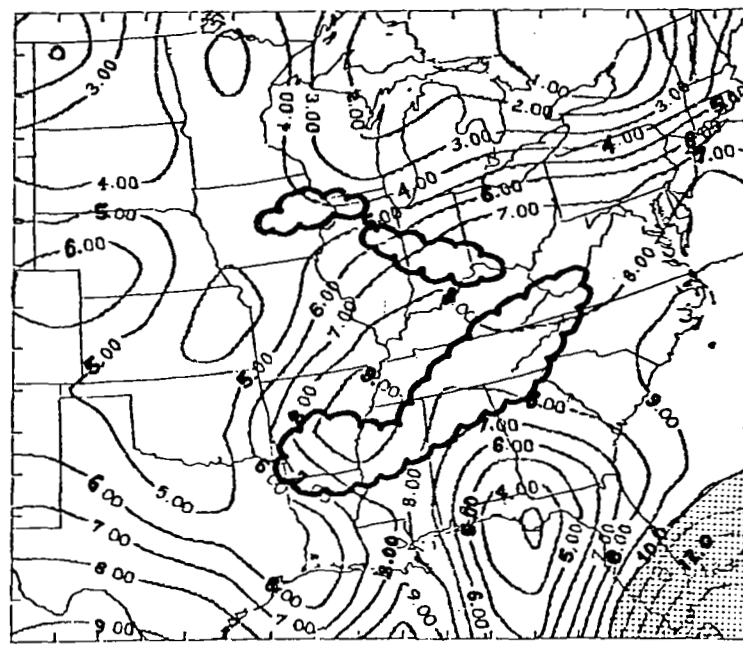

850 mb

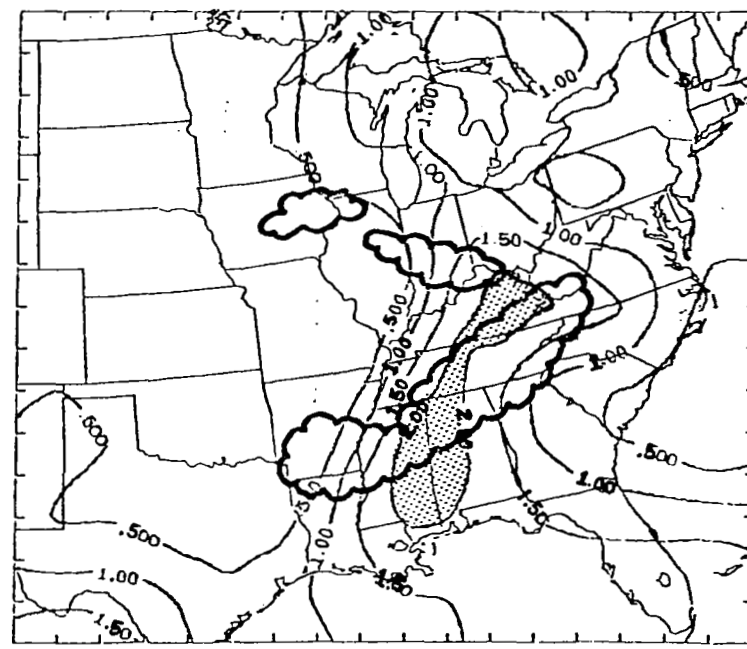

500 mb

e. Mixing ratio (g kg^{-1})(areas of convection are scalloped). Values greater than 10 and 2 g kg^{-1} are shaded at 850 and 500 mb, respectively.

Fig. 13. (Continued)

through the network from its initial location in the upper Ohio Valley (Fig. 6a) to a final position off the New England coast (Fig. 12a) while maintaining moderate intensity.

System C was also of light-to-moderate intensity and was located initially along the U. S. Atlantic coast from North Carolina to Maine (Fig. 6a). Movement of the system was eastward and by 1800 GMT 24 April (Fig. 9a) the precipitation was outside the network.

System D was first detected as an area of light-to-moderate shower activity extending from western Kansas into central South Dakota at 1200 GMT April 24 (Fig. 7a). Movement of the system was slowly eastward and the intensity of precipitation was increasing. By 0000 GMT April 25 (Fig. 11a) a few MDR values of 6 were detected over eastern South Dakota and Minnesota. Afterwards, D continued to move slowly eastward into Illinois while decreasing in areal coverage and intensity (Figs. 11a-13a).

System E was the second of two areas of severe thunderstorms to develop and move through the AVE IV network. It was initially detected in eastern Kansas at 1800 GMT 24 April (Fig. 9a) as a small area of moderate to strong thunderstorms. By 0000 GMT 25 April (Fig. 11a) this system had developed into a long line of severe thunderstorms from west Texas to central Illinois that moved rapidly eastward into the southeastern states (Figs. 11a-13a) by 1200 GMT 25 April. Over 30 reports of severe weather at the surface were logged during the life cycle of the storm system including the Neosho, Missouri tornado that caused 3 deaths, 22 injuries, and $10.5 million in property damage.

In the following sections of the report, the precipitation system codes established above (i.e., A-E) will be used when referring to the relationships between atmospheric structure and formation, maintenance, and dissipation of convective activity.

2) Surface analysis

At the beginning of the experiment (Fig. 6b), three air mass types were distinguishable at the surface over the AVE IV network. A moist and warm maritime tropical air mass was moving northward over the

network with strong southerly flow around a high pressure center (1030-mb central pressure) located about 500 km off the coast of the Carolinas. Maritime tropical air covered almost two thirds of the network extending from central Texas and Oklahoma eastward through all of the Gulf Coast and Middle Atlantic States and northeastward into the Ohio Valley.

A cold front, extending southwestward into Kansas from a moderately strong cyclone (1000-mb center) over northern Michigan, separated the maritime tropical air from the cooler and drier continental polar air moving southward over the northern Plains State, while a warm front, extending southeastward from the cyclone into Pennsylvania, separated continental polar air over New England from maritime tropical air over the Ohio Valley. A second cyclone (1000-mb center) was located over the Kansas-Oklahoma border with a cold front or dry line extending southward into west Texas separating the very dry continental tropical air from the maritime tropical air over east Texas. A third and weaker cyclone was just entering the network in western Nebraska and South Dakota.

Temperatures over the AVE IV network ranged from 25°C along the Gulf Coast to 5°C in the northern Plains States, and dew point temperatures ranged from 20°C to -10°C between the tropical and polar air masses.

The cyclone in northern Michigan moved slowly eastward during the experiment and was located off the Maine coast at the last time period (Figs. 6b-13b). The associated warm front also moved off the coast while the trailing cold front moved slowly southeastward and passed through most of the New England and Mid-Atlantic States.

The second low pressure center over the Kansas-Oklahoma border also moved slowly eastward through the middle Mississippi Valley into Kentucky. This pushed the associated cold front slowly southeastward through most of Oklahoma and Missouri while the southern end of the front remained anchored in western Texas in close association with the "dry line".

The low pressure center, initially over the northern plains, was very weak and poorly defined at the surface. Only at 1500 and 1800 GMT

24 April (Fig. 8b and 9b) did a closed low pressure center exist, although a weak pressure trough could be seen moving slowly eastward into Wisconsin and Illinois during the last two time periods.

Two high pressure centers, one located east of the Carolinas and the other north of Minnesota (Fig. 6b), moved eastward about 400 km during the 36 hours of the experiment in response to the eastward movement of the surface cyclones.

Clear relationships exist between the location and movement of surface features and areas of precipitation (see Figs. 6a and b through 13a and b). System A developed ahead of the cold front in the central Plains States and moved as a pre-frontal squall line until it dissipated into light showers east of the North Carolina coast. System B developed along the northern edge of the same front and moved eastward ahead and along the frontal surface as it passed through the North Atlantic States. System C was located along and north of the warm front in New England in Fig. 6b and moved off the coast as its associated cyclone traveled eastward into Canada (Fig. 8b). The light precipitation in System D was clearly associated with the surface low and pressure trough in the Northern Plains, while E formed along the cold front and dry line in Oklahoma, Kansas, and Texas (Fig. 10b) and moved eastward as another pre-frontal squall line.

3) Upper-air analysis of geopotential height, temperature, wind, moisture, and vertical velocity

Figures 6c through 13c are analyzed fields of geopotential height (m) (solid lines), temperature (°C) (dashed lines), and vector wind for the 850- and 500-mb levels. The length of each wind vector is proportional to the wind speed (m s^{-1}) where the length of one grid interval (distance between two adjacent tick marks that surround each figure) is 25 m s^{-1}. Figures 6d through 13d are fields of vertical velocity (μbars s^{-1} where shaded is upward motion) at the 850- and 500-mb levels. Figures 6e through 13e are the mixing ratio analyses (g kg^{-1} where values greater than 10 g kg^{-1} and 2 g kg^{-1} are shaded at 850 mb and 500 mb, respectively) for the same levels and time periods previously described. All fields are from the basic gridded data set.

Examination of the vector wind and height fields show the flow pattern to be nearly zonal over the experiment area with several weak-to-moderate strength short-wave perturbations (half wavelengths < 1000 km) moving rapidly eastward across the central and north sections of the network. These troughs (shown as wide dashed lines at 850 mb in Figs. 6c-13c) usually extended in the southward direction from three slowly moving low pressure centers shown in the height analyses. The lows aloft were the upper-air reflections of the three surface cyclones discussed earlier as revealed by the spatial and temporal continuity of the systems. However, the stable short-wave troughs that moved rapidly eastward along a moderately strong baroclinic zone (containing the polar jet) running southwest-northeast through the center of the network, were directly responsible for the development and movement of each precipitation system previously described (500-mb relative vorticity centers, marked with X's in Figs. 6c-13c, more clearly define these short waves). In addition, the vertical velocity and mixing ratio fields also contain features closely associated with trough positions and movements.

Superimposed on the mixing ratio analyses are scalloped zones outlining all convective precipitation areas determined in the MDR analysis. Spatial and temporal comparisons between these coded precipitation areas (A-E) and atmospheric structural features contained in Figs. 6c, d, and e through 13c, d, and e reveal some of the relationships between the synoptic structure and convective activity. These relationships (discussed below) are clearly established at any given time period in AVE IV and good time continuity between successive 3- and 6-h periods gives credibility to those results.

From Fig. 6, it is evident that systems A, B, and C are all located east or southeast of short-wave troughs at 850 mb that generally slope west or northwest to troughs or vorticity centers at 500 mb (Fig. 6c). East and southeast of the troughs, strong upward vertical velocity occurred at both 850 and 500 mb (Fig. 6d) and tongues of higher moisture content also existed at both levels. West of each trough, precipitation failed to develop, air was subsiding, and zones

of lesser moisture content were evident. Systems D and E were also associated with the eastward movement of troughs aloft as seen in Figs. 7c and 9c. The temporal continuity of each trough (and its associated vertical velocity and moisture distribution) is excellent in relationship to the development and movement of all precipitation systems. This is particularly clear in Figs. 11, 12, and 13 where a strong and developing trough moves eastward through the center of the network producing System E. However, surface reflections of the troughs are seldom seen as developing cyclones during AVE IV so that the relationships between surface frontal systems and storm development are not exceedingly strong. Instead, these short-wave systems move rapidly eastward along a rather broad baroclinic zone, advecting (horizontally and vertically) moisture ahead of the systems while strong upward vertical velocity releases potential instability to produce thunderstorms. Large horizontal temperature advection is impossible within these waves since system speeds are large and wavelengths are small. This suppresses amplification of the waves into long-wave troughs while stable system movement is dictated by the rapid adiabatic cooling and warming within the large vertical velocity centers associated with the waves. These vertical velocities are capable of quickly releasing instability already present in the path of wave propagation and suppressing it after wave passage (Holton, 1972).

b. Individual plotted trajectories

Analysis of the results from trajectory calculations is somewhat difficult to present since air parcels move three-dimensionally in space. One method for presenting a trajectory is to plot a horizontal map showing the previous positions (x and y) of a given air parcel along with its vertical position (z or p). All trajectories were computed and plotted backward in time from grid points located at various (x, y, p) positions.

Figures 14a-14e are five examples of this plotting technique for air parcel trajectories passing over the AVE network in proximity to System E and terminating their paths at 1200 GMT 25 April at 850,

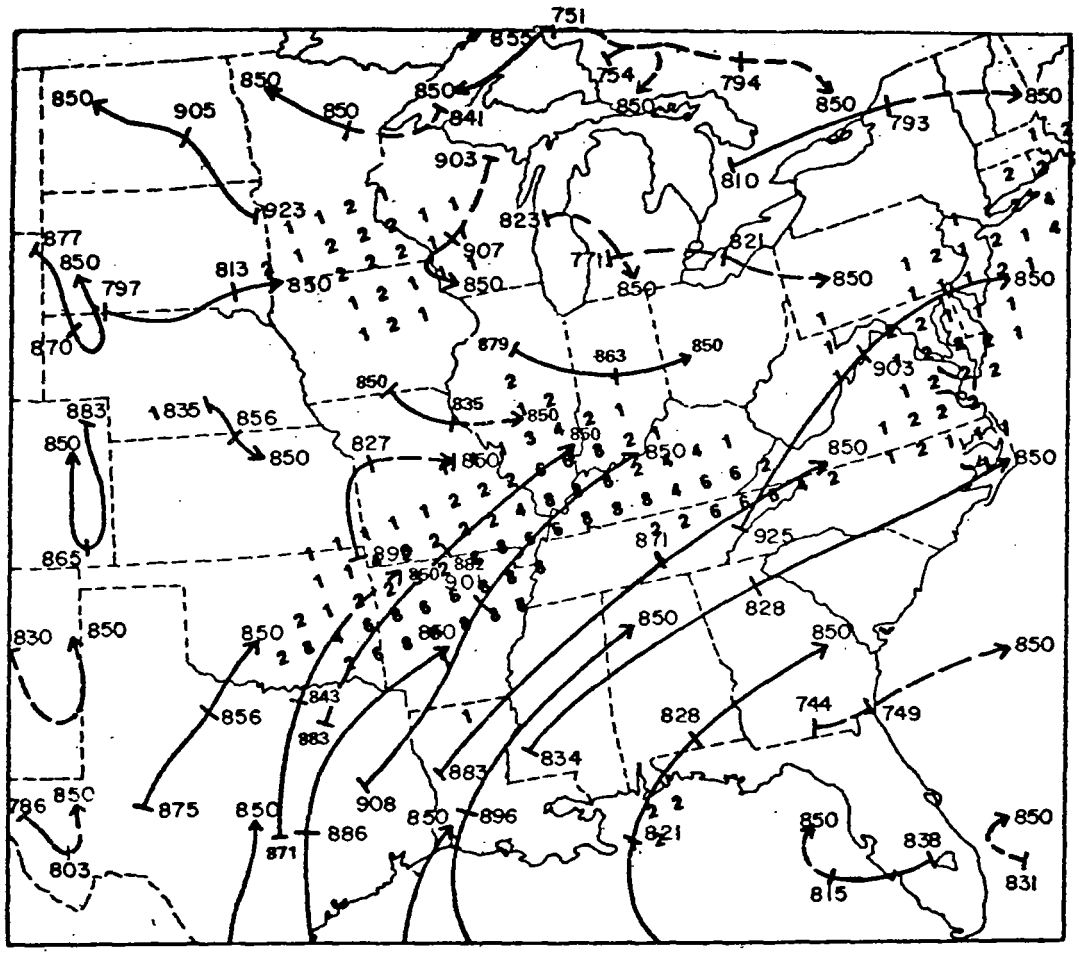

a. Parcel terminating at 850 mb. (tick marks at successive 12-h positions along the trajectories).

Fig. 14 Trajectories of air parcels passing through the AVE IV network. All parcels terminate their paths at grid points on the pressure levels indicated at 1200 GMT, 25 April. The vertical location (pressure in millibars) is shown beside tick marks placed on each trajectory at successive 3-h positions except where noted. Rising and sinking air is denoted by solid and dashed lines, respectively. Thin solid lines between tick marks of some trajectories connect points along trajectories having the same date and time as indicated. The MDR composite data for 0600 GMT, 25 April are superimposed in each chart.

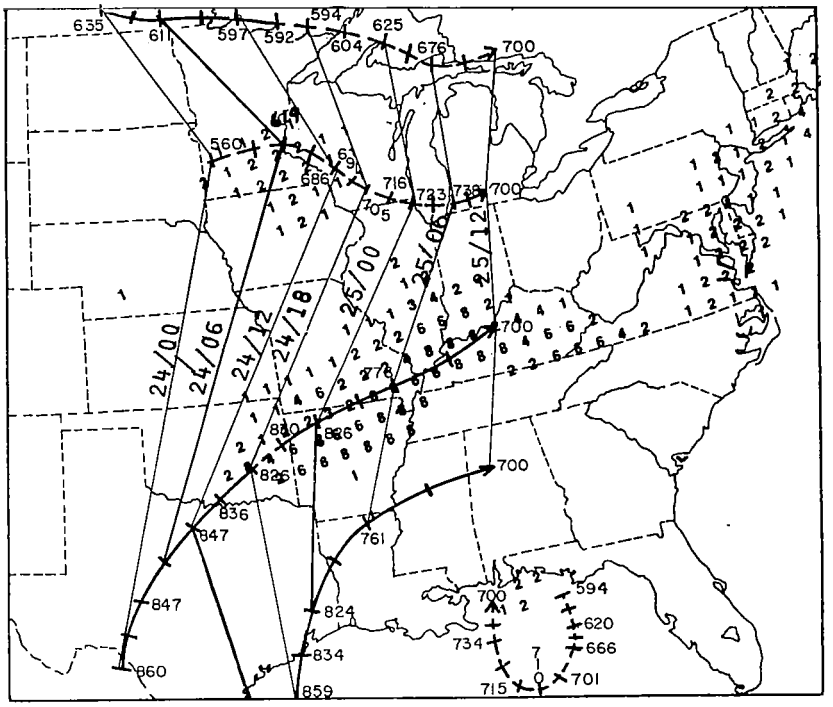

b. Parcels terminating at 700 mb.

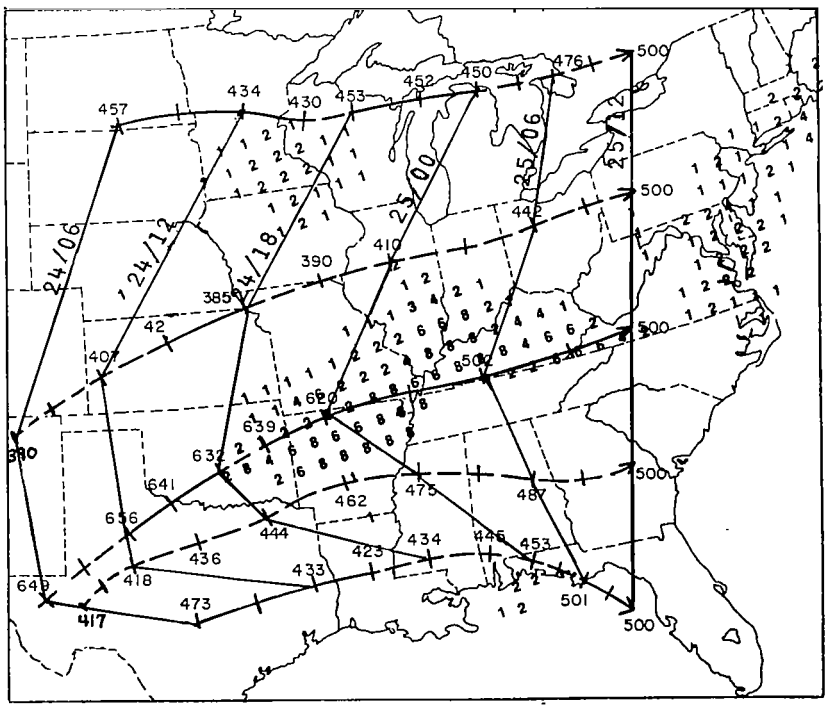

c. Parcel terminating at 500 mb.

Fig. 14. (Continued)

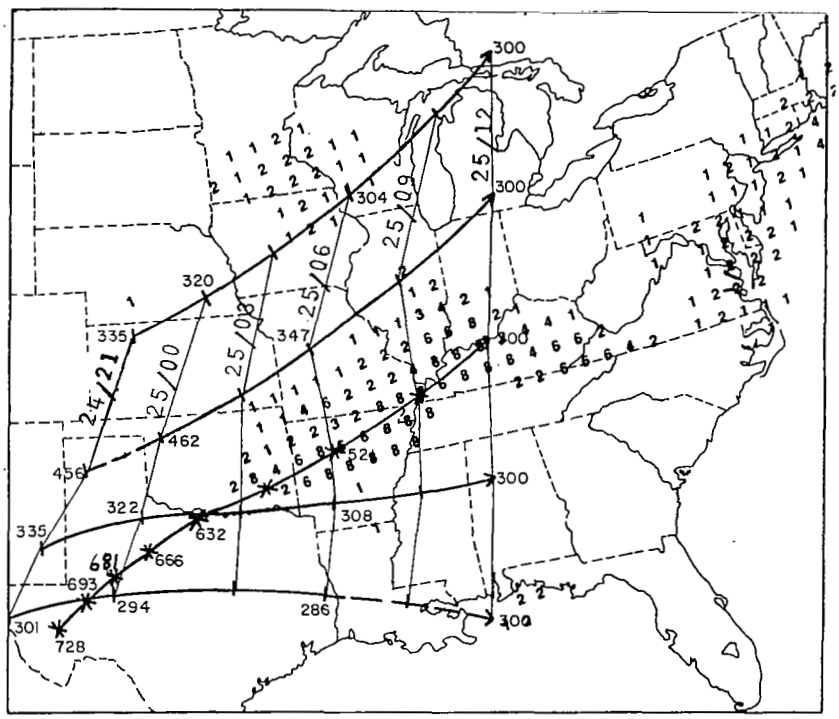

d. Parcels terminating at 300 mb.

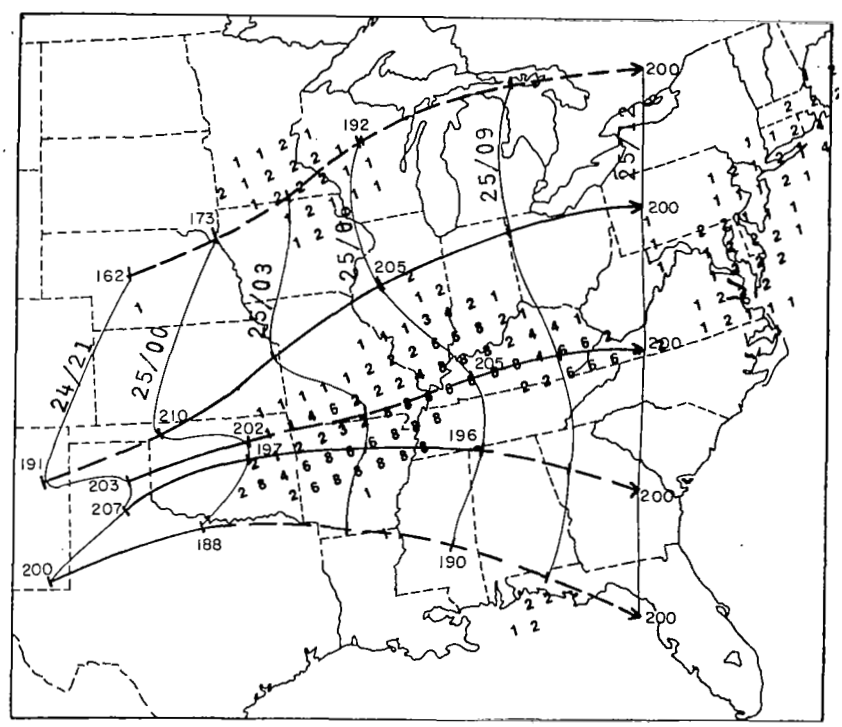

e. Parcels terminating at 200 mb.

Fig. 14. (Continued)

700, 500, 300, and 200 mb, respectively. The vertical location of each parcel is listed beside "tick" marks denoting the parcel's pressure at successive time periods of the experiment, while solid and dashed lines show rising and sinking air, respectively. Thin solid lines connect tick marks of some trajectories having common dates and times for air parcels that remain within ±150 mb of their final pressure positions. By observing the changing area of rectangles outlined by these thin solid lines and trajectory paths a qualitative estimate of the quasi-horizontal velocity divergence can be made. Parcels that move vertically in excess of ±150 mb are denoted by placing "stars" along the trajectories at successive time periods. Trajectories are plotted for all time periods in which each parcel remained inside the grid network. The MDR composite chart for 0600 GMT April 25 is superimposed on each chart.

Figures 14a and 14b show the quasi-horizontal converging of air at 850 and 700 mb within the immediate thunderstorm environment of System E. Parcels moving ahead and within the storm area originated in the southern and western sections of the network and rose in excess of 25 and 100 mb before ending their paths at 850 and 700 mb, respectively. Behind and north of the thunderstorms, air parcels were sinking and moving toward the storms from westerly directions.

For parcels ending their paths at 500 mb (Fig. 14c) very little convergence or divergence is evident. Sinking air, in excess of 75 mb, occurs both north and south of the thunderstorms as air parcels move zonally across the experiment area. The air parcel passing through the immediate storm environment rises from 632 to 500 mb between 1800 GMT 24 April and 1200 GMT 25 April while moving from Oklahoma to Virginia.

In the upper troposphere (Figs. 14d and 14e) air parcels terminating at 300 and 200 mb show strong quasi-horizontal divergence around and over the storm environment while remaining within ±30 mb of their final pressure positions. The only exception occurs in Fig. 14d where the air parcel moving over the center of the storm area rises from 728 to 300 mb in response to extreme divergence aloft. This vertical displacement occurs between 1200 GMT 24 April and 1200 GMT 25 April while moving from southwest Texas to Kentucky (an upward displacement of 372 mb in 24 h).

A four-dimensional assimilation of air flow in the storm environment shows lower tropospheric air to be convergent while supplying moisture and heat from southern and southwestern source regions into the leading edge of the storm system. This air undergoes upward displacements of between -50 and -150 mb in 12 h while moving into the pre-storm environment. Air in the post-storm environment is subsiding at about the same rate.

The mid-troposhere is primarily nondivergent with trajectories usually bringing air from dryer western and southwestern areas into the storm environment (see Figs. 6-13 for moisture distributions). Upward displacement of mid-tropospheric air (at the rate of about -50 mb/3h) occurs within the radar-observed storm area while subsidence at the rate of about 30 mb/3h exists northwest and southeast of the convective storm system.

The upper-troposphere is highly divergent over and surrounding the convective storm system with relatively small net vertical displacements (±30 mb in 12 h) occurring in most areas. However, very strong upward vertical velocity, created by low-level convergence and upper-level divergence, causes air parcels within the radar-observed storm area to rise large vertical distances in short time periods (as much as -300 mb in 12 h). This results in tremendous vertical stretching and lifting of layers of air originating in the warm and moist regions of the lower troposphere as they move into the area of the storm system. Because of veering winds ahead of the convective storm system, mid-level dry air overrides moist low-level air to produce large convective instability, while continued lifting and stretching of this air finally releases the available potential instability. Continuous air motion into the storm environment supplies the atmosphere with new potential instability and maintains the "fuel" for the convective system for periods in excess of 12 h, even though individual clouds in the system usually require less than 1 h to realize existing instability in their updrafts.

The above description does not, however, consider the effects of the convective system transferring heat, momentum, and water vapor into the synoptic flow and possibly modifying these relationships. These so called "feedback" effects are discussed in subsections d-f.

c. Parcel energy indices, net vertical displacements (NVD's), and convective storm delineation

To parameterize accurately the static stability of the atmosphere in AVE IV, a method was devised to calculate objectively both the amount of buoyant energy (ergs g^{-1}) necessary to be added to a parcel to make it hydrostatically unstable (negative buoyant energy or NBE), and the amount available to be converted into kinetic energy of the upward vertical velocity (positive buoyant energy or PBE) or "updraft" if the parcel were to become unstable. For each time period, the basic gridded temperature and moisture fields were used to establish an environmental virtual temperature (T_v) sounding (from 900 mb to 100 mb) "above" each grid point with data available at 50-mb intervals. Each sounding was then scanned from 900 to 700 mb to determine the value and pressure level of the maximum θ_e. $\Delta(KE_w)$ was then determined for all 50-mb layers for each sounding using (5) and techniques previously discussed. NBE was calculated by summing all negative buoyant energy up to 500 mb over each grid point while PBE resulted from summing all positive energy up to 100 mb. As stated earlier, smaller NBE should correlate with the increasing occurrence of thunderstorms while larger PBE should relate to the increasing intensity of convective activity.

Figures 15a through 22a present the NBE and PBE spatial fields (units of 10^4 ergs g^{-1}) for the last eight consecutive time periods of AVE IV. A spatial comparison between the NBE fields and areas of convective precipitation (MDR$\geq$2) for all time periods has shown that convection usually occurred in areas where NBE values were $<200 \times 10^4$ ergs g^{-1} while moderate and severe convection was associated with values $<100 \times 10^4$ ergs g^{-1}. For individual comparisons, Figs. 15c through 22c contain scalloped areas enclosing observed convective activity, while Figs. 6a through 13a present actual fields of MDR values.

While the general locations of storms are accurately delineated with the NBE index fields, PBE fields relate well to the intensity with most MDR$<$6 occurring in areas of PBE values $<500 \times 10^4$ ergs g^{-1}.

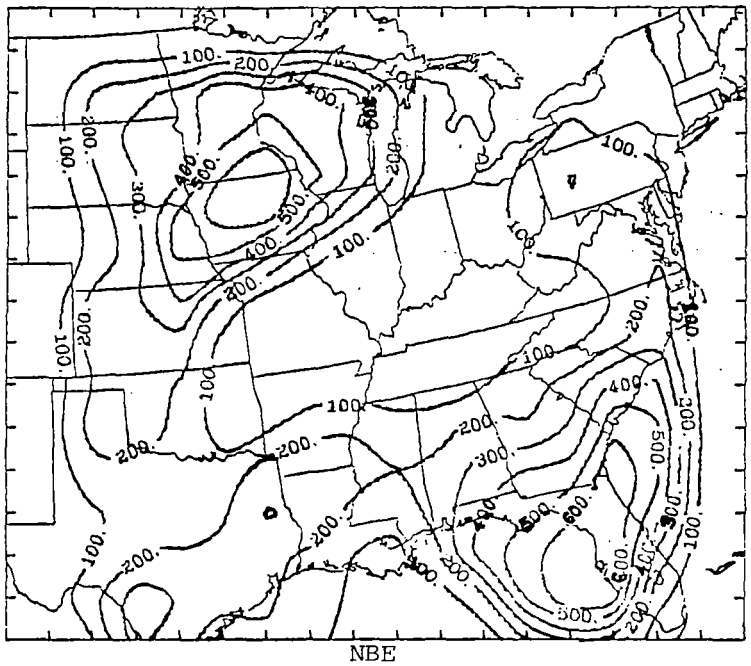

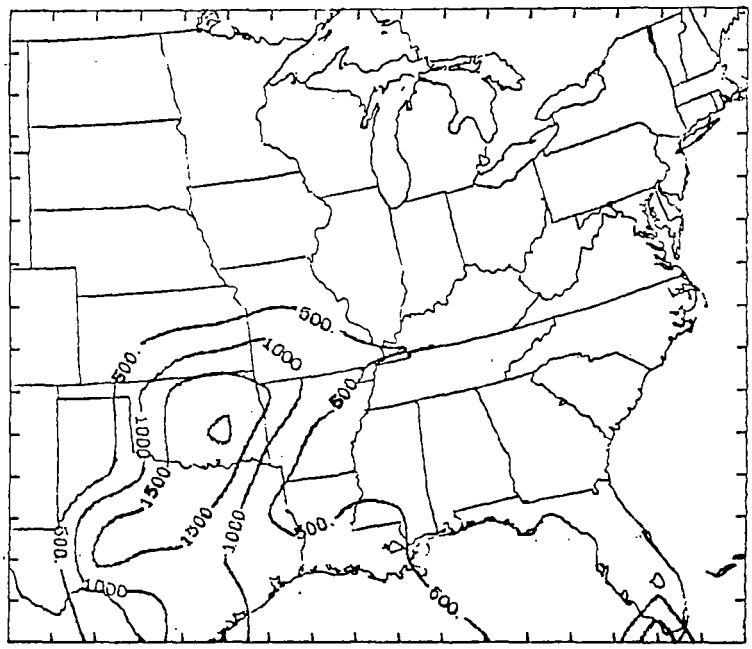

a. Parcel energy indices (10^4 ergs g^{-1}).

Fig. 15. Analyses of a) parcel energy indices, b) net vertical displacements, and c) diagnostically determined intensity categories of convection for 0600 GMT, 24 April 1975. In (c), radar observed values of MDR ≥ 2 are shown by scalloped areas. Lines labelled *in thunderstorm intensity categories* actually apply to those areas in (c) lying on the more intense side of the isolines separating categories of thunderstorm intensity.

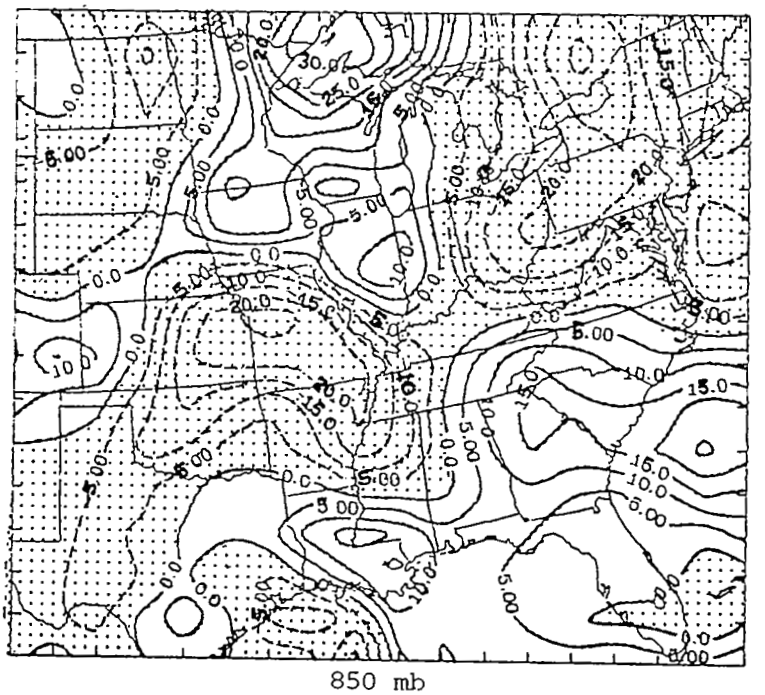

850 mb

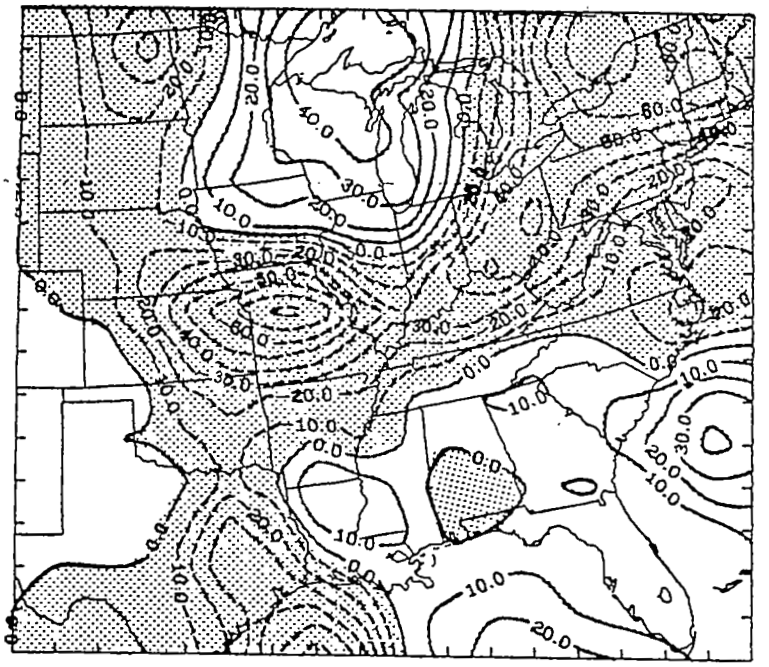

500 mb

b. Net vertical displacements (mb/3h).

Fig. 15. (Continued)

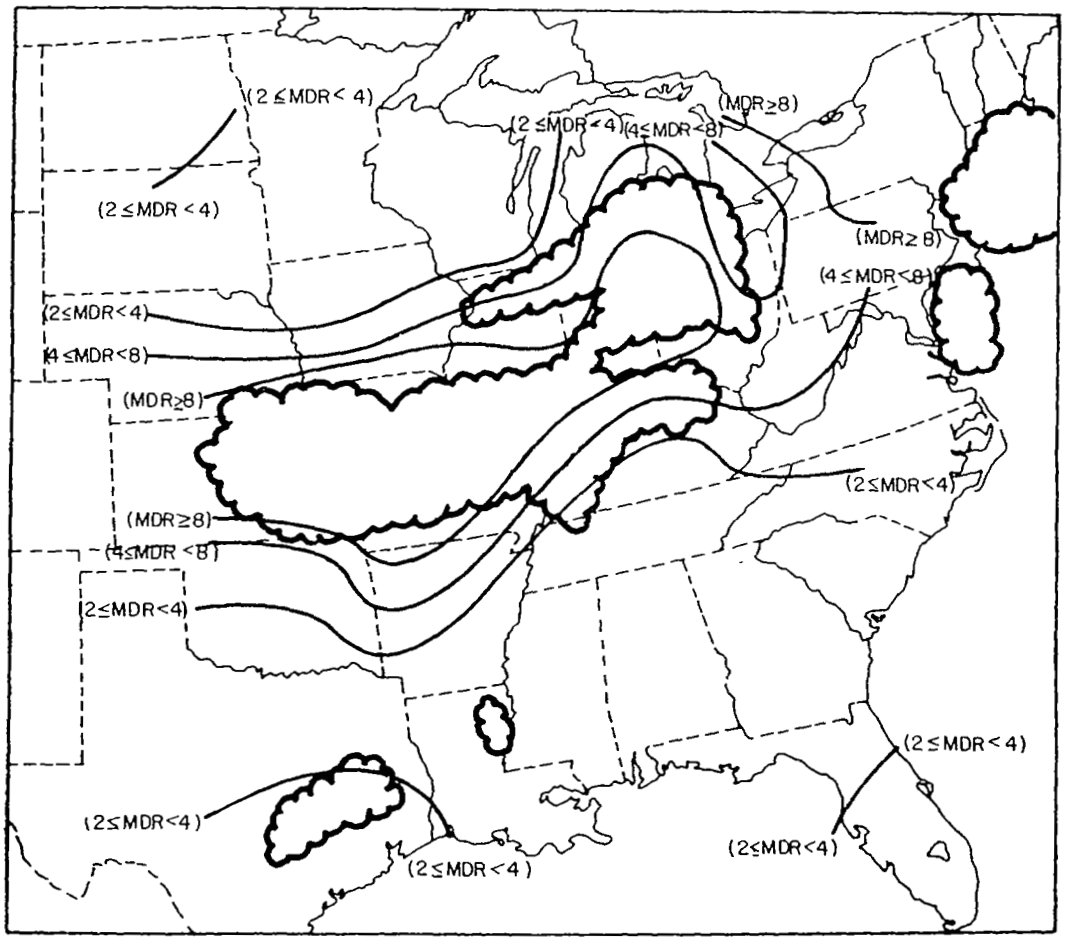

c. Diagnostic delineation of convective storm location and intensity.

Fig. 15. (Continued)

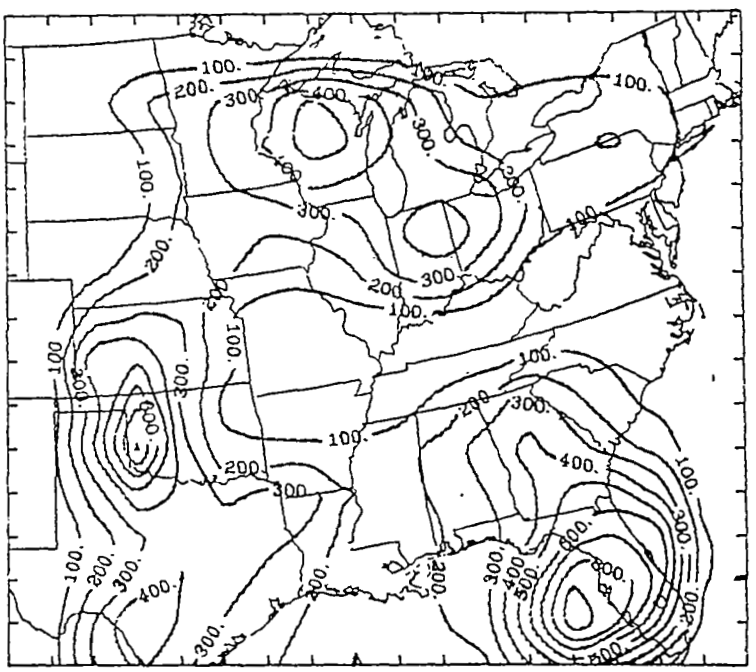

NBE

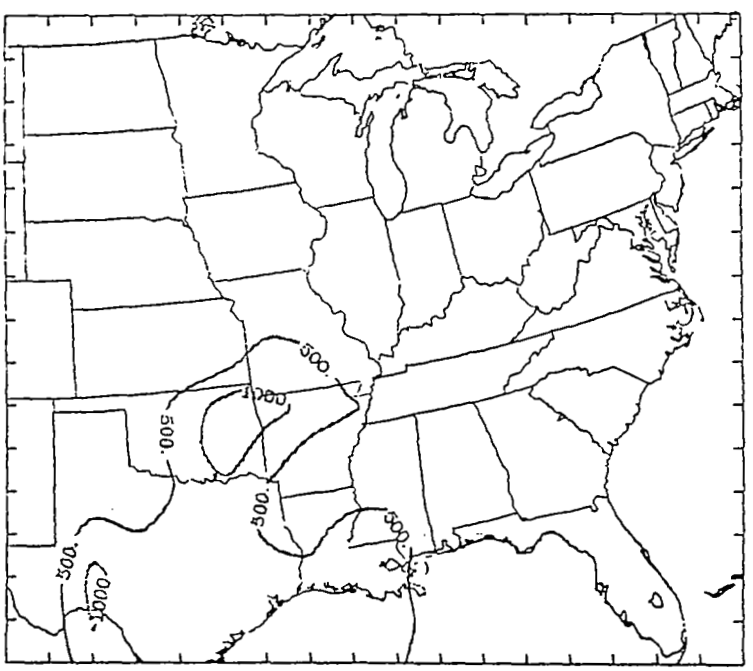

PBE

a. Parcel energy indices (10^4 ergs g^{-1}).

Fig. 16. Same as Fig. 15 except for 1200 GMT, 24 April 1975.

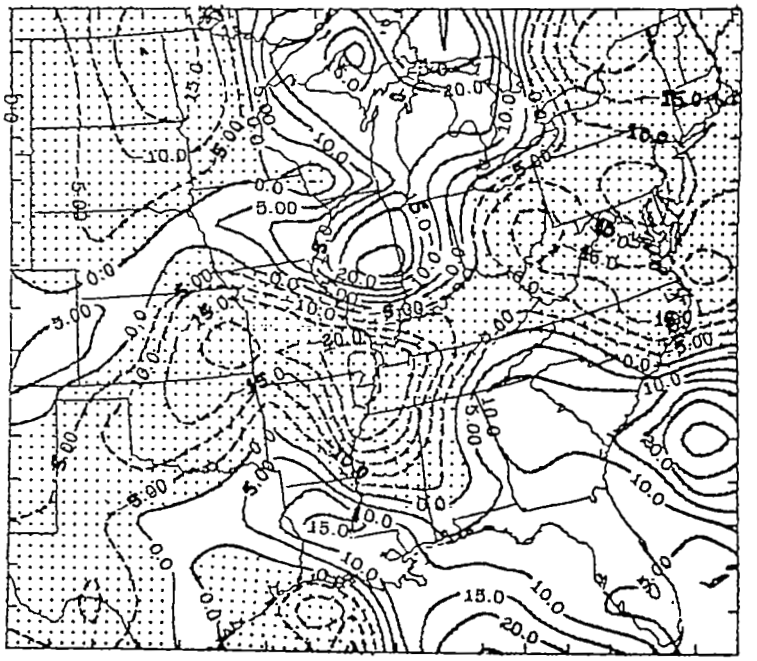

850 mb

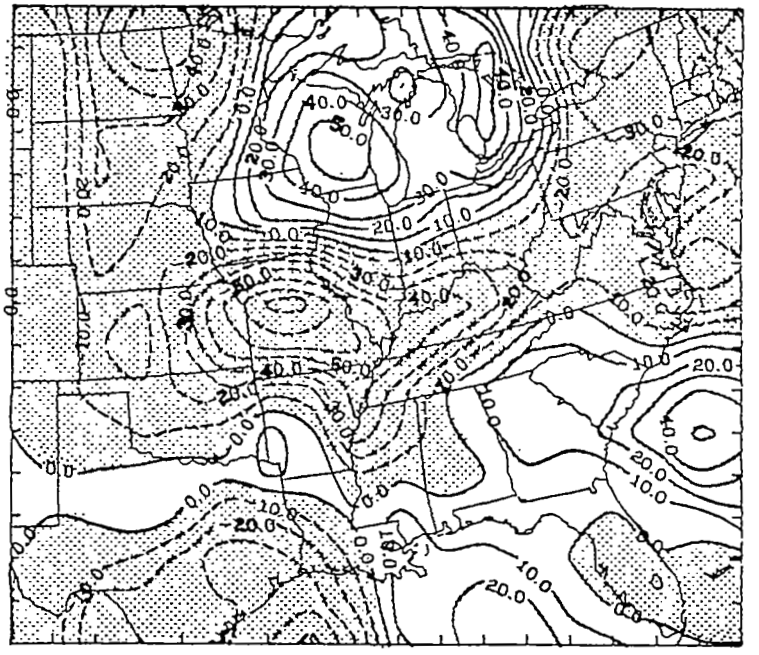

500 mb

b. Net vertical displacements (mb/3h).

Fig. 16. (Continued)

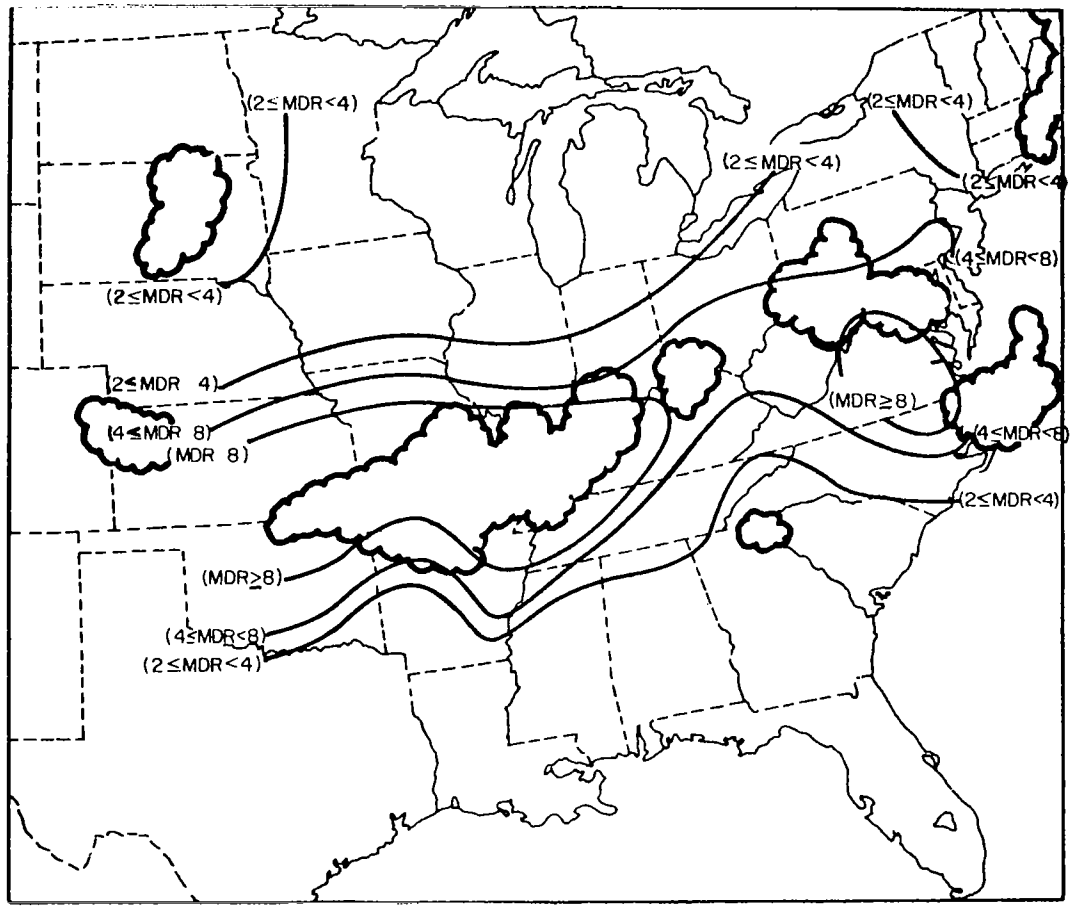

c. Diagnostic delineation of convective storm location and intensity.

Fig. 16. (Continued)

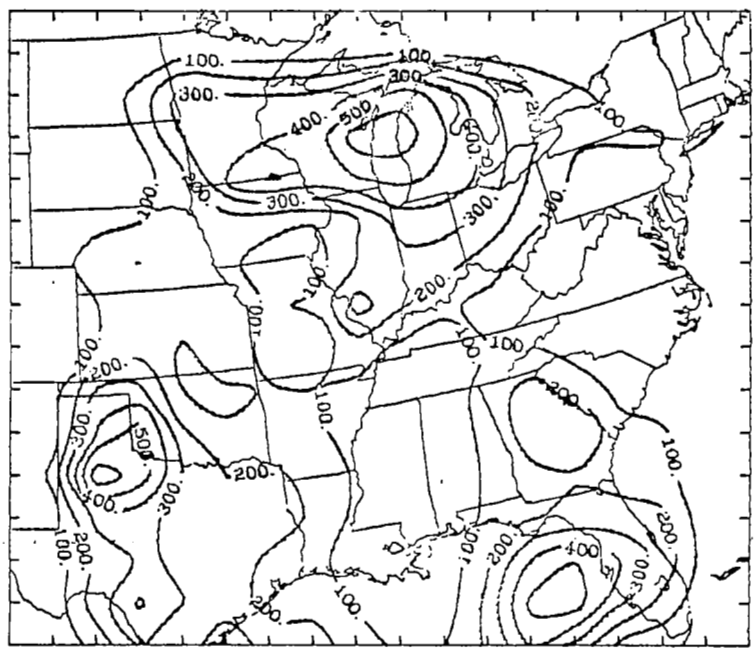

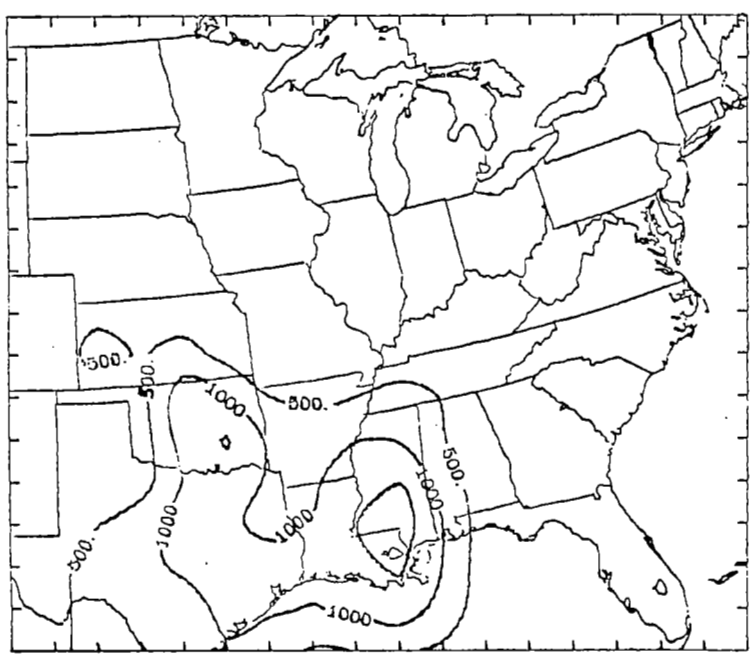

a. Parcel energy indices (10^4 ergs g^{-1}).

Fig. 17. Same as Fig. 15 except for 1500 GMT, 24 April 1975.

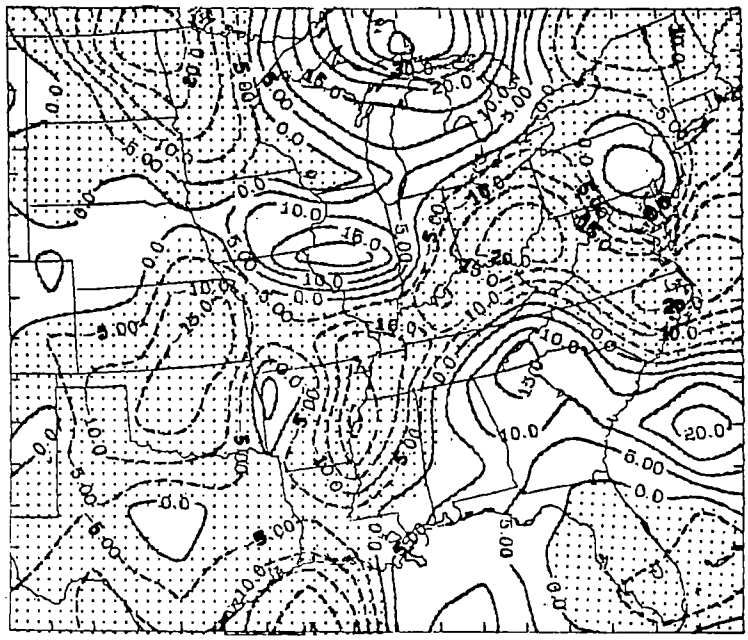

850 mb

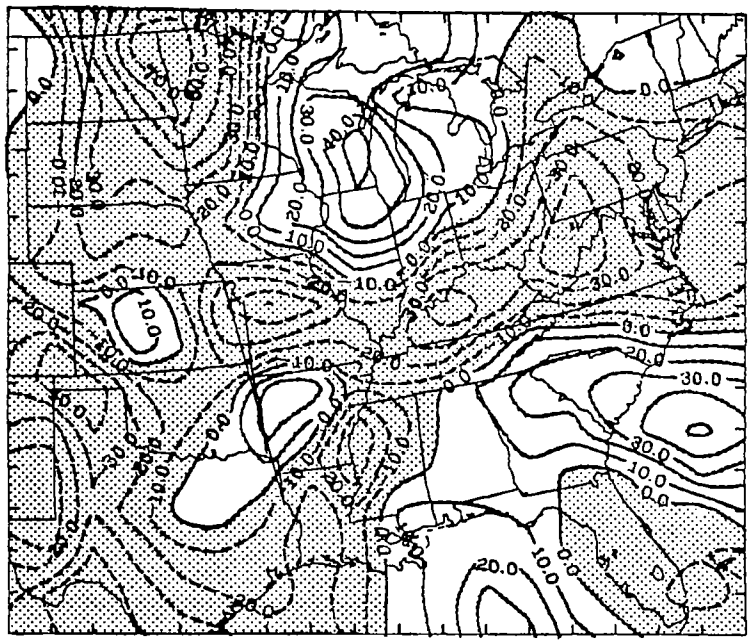

500 mb

b. Net vertical displacements (mb/3h).

Fig. 17. (Continued)

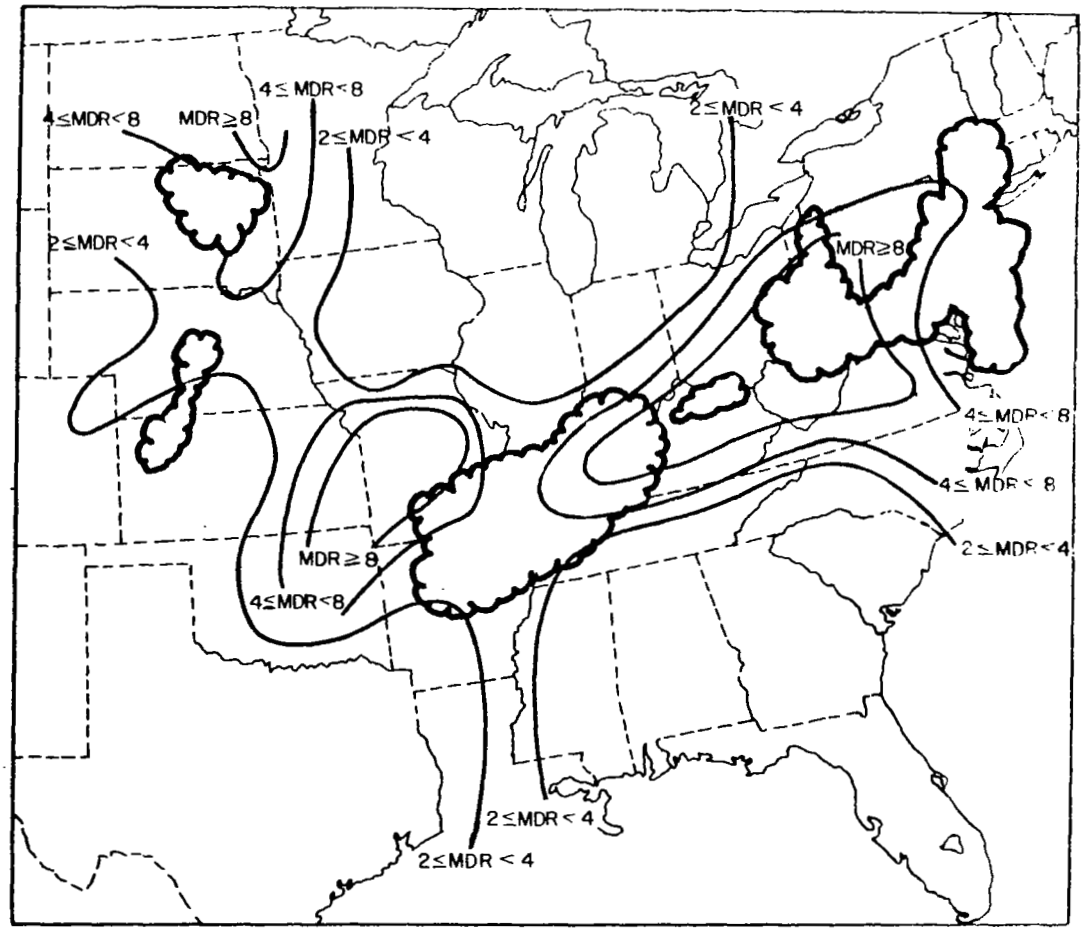

c. Diagnostic delineation of convective storm location and intensity.

Fig. 17. (Continued)

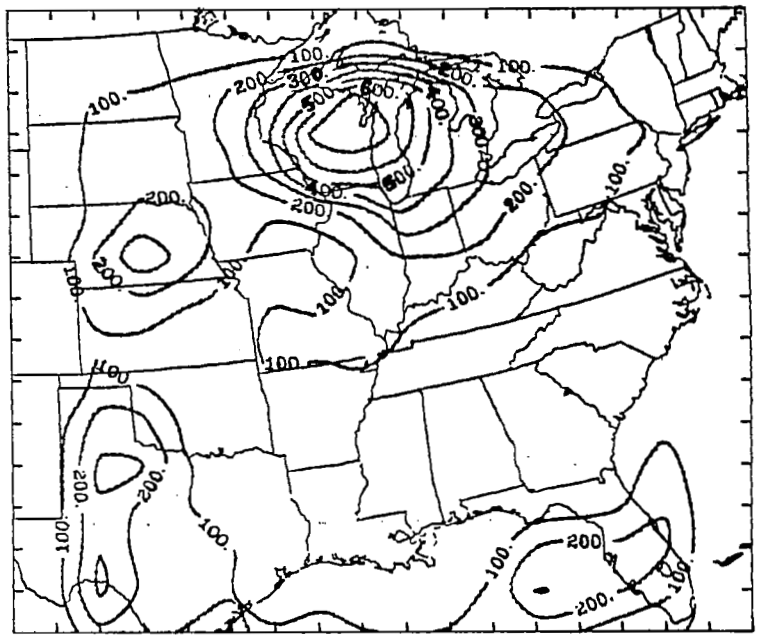

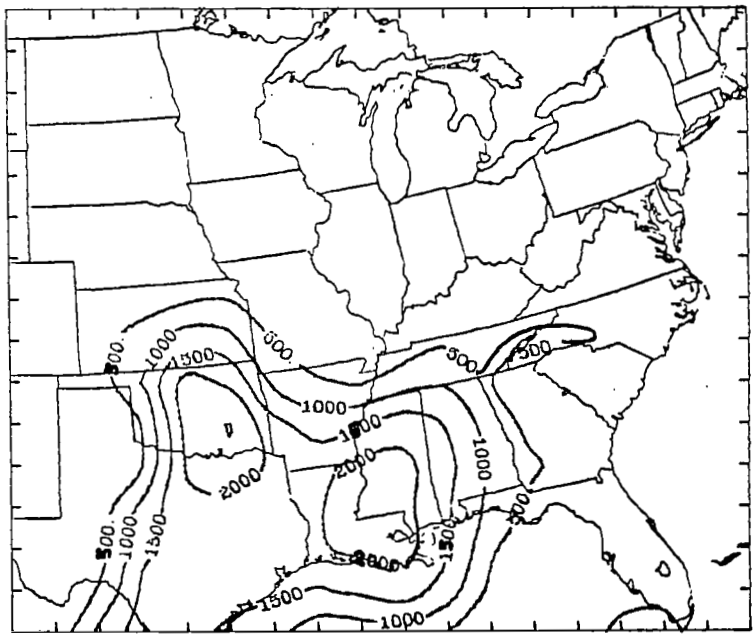

a. Parcel energy indices (10^4 ergs g^{-1}).

Fig. 18. Same as Fig. 15 except for 1800 GMT, 24 April 1975.

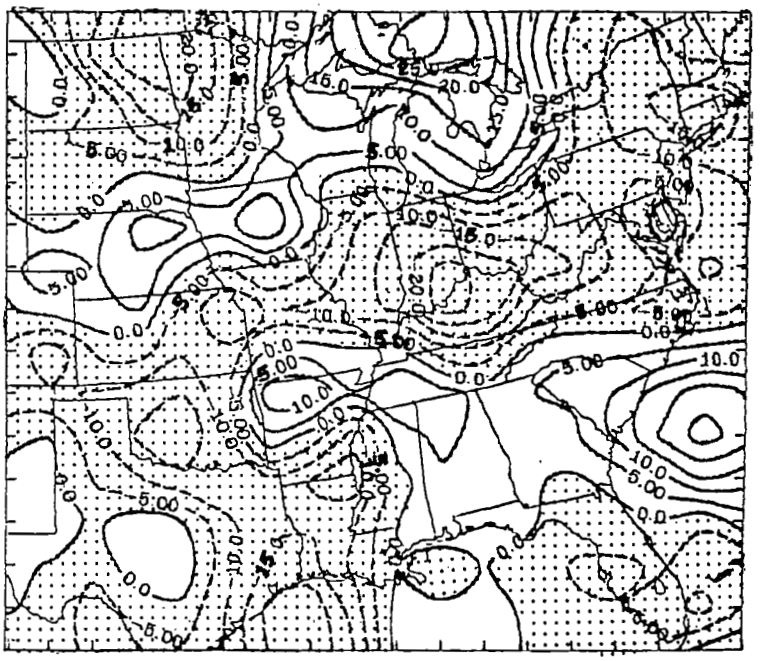

850 mb

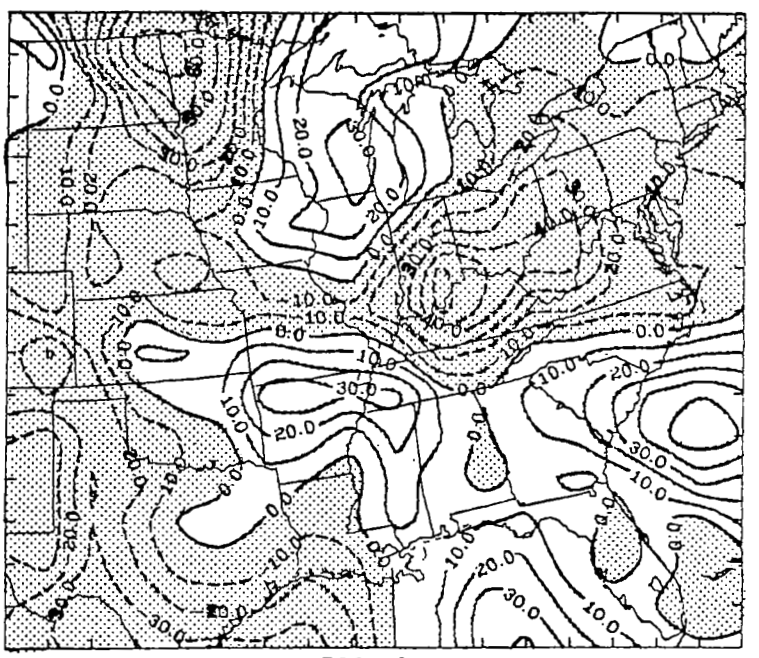

500 mb

b. Net vertical displacements (mb/3h).

Fig. 18. (Continued)

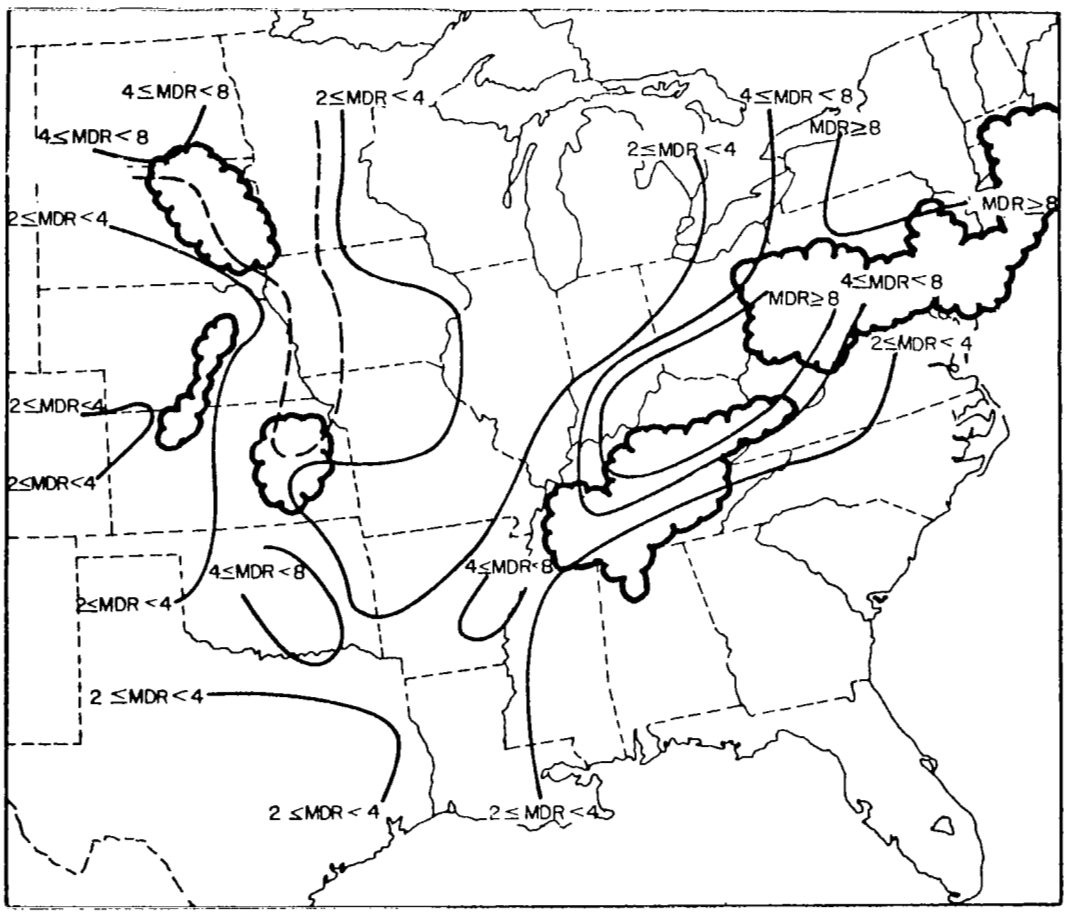

c. Diagnostic delineation of convective storm location and intensity.

Fig. 18. (Continued)

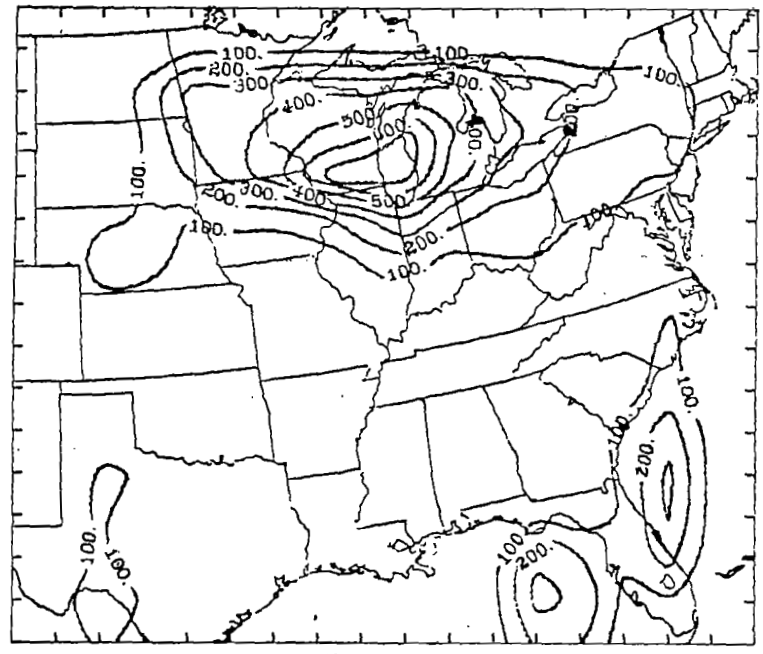

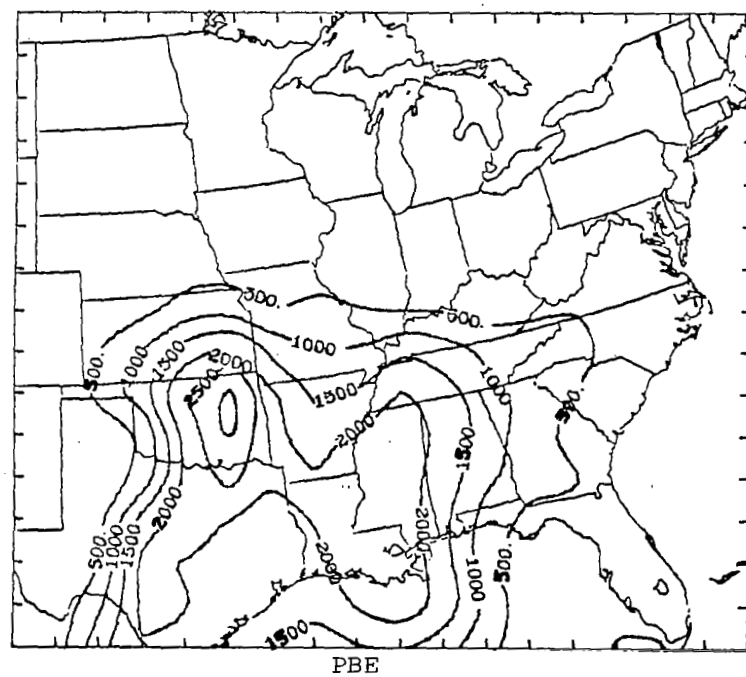

a. Parcel energy indices (10^4 ergs g^{-1}).

Fig. 19. Same as Fig. 15 except for 2100 GMT, 24 April 1975.

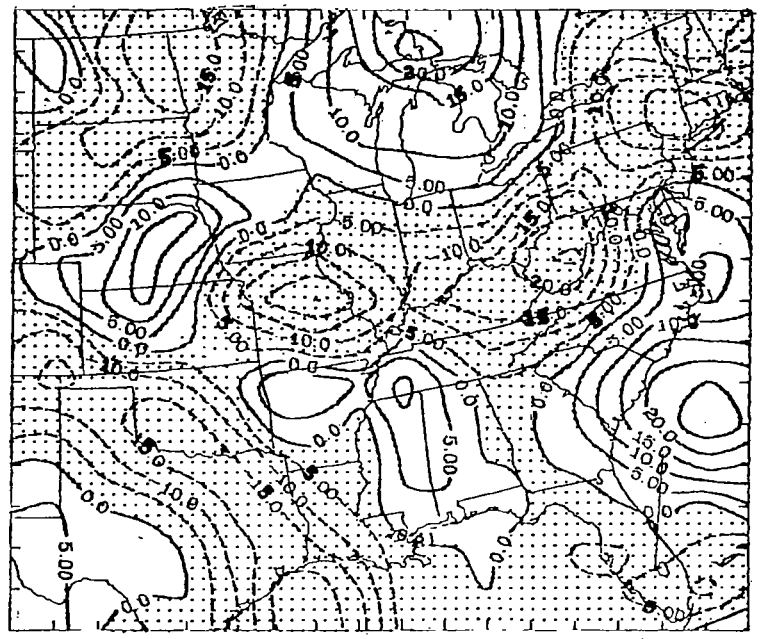

850 mb

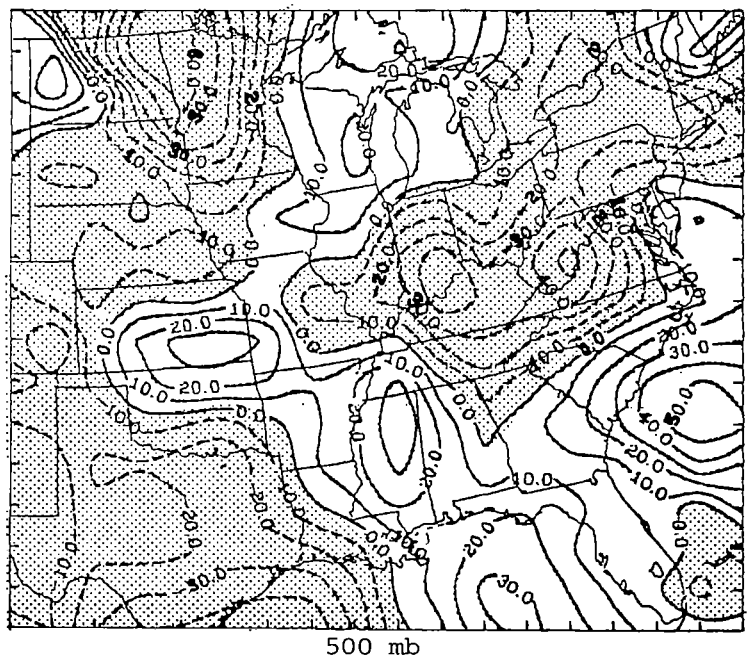

500 mb

b. Net vertical displacements (mb/3h).

Fig. 19. (Continued)

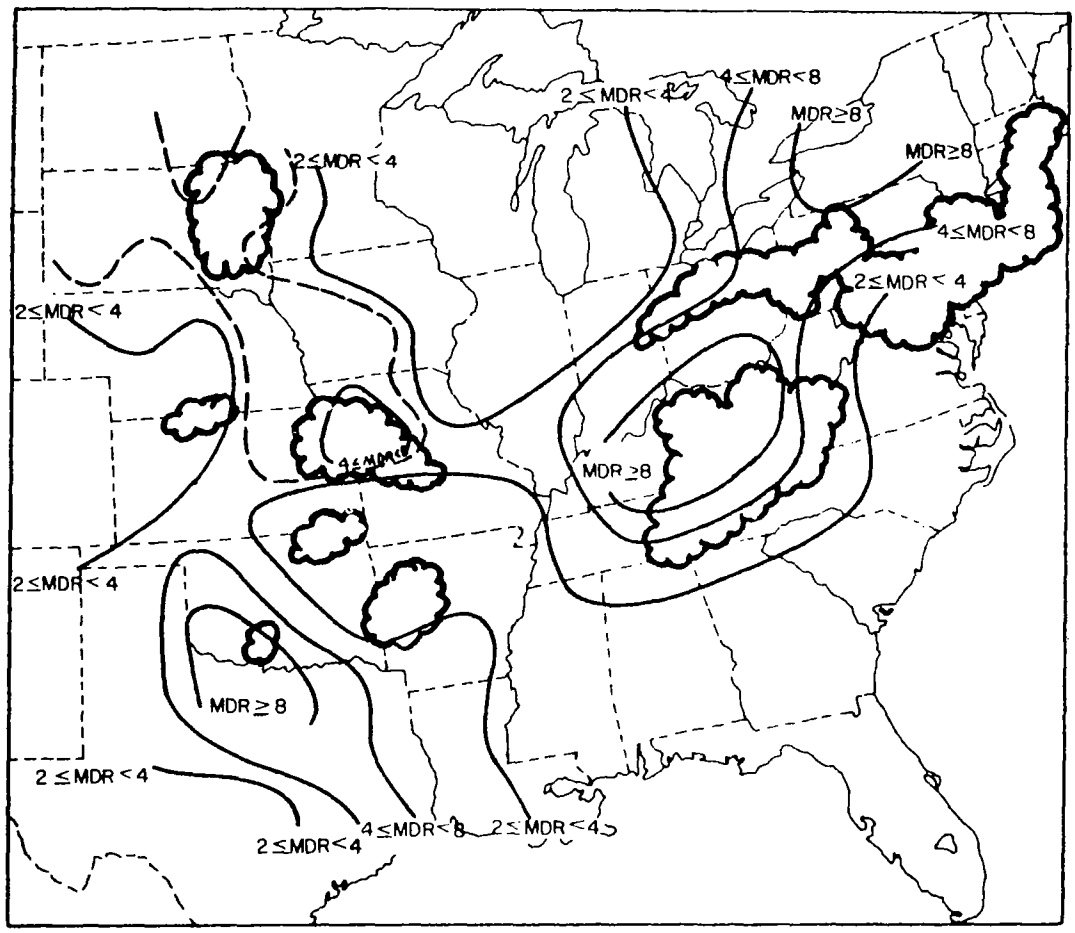

c. Diagnostic delineation of convective storm location and intensity.

Fig. 19. (Continued)

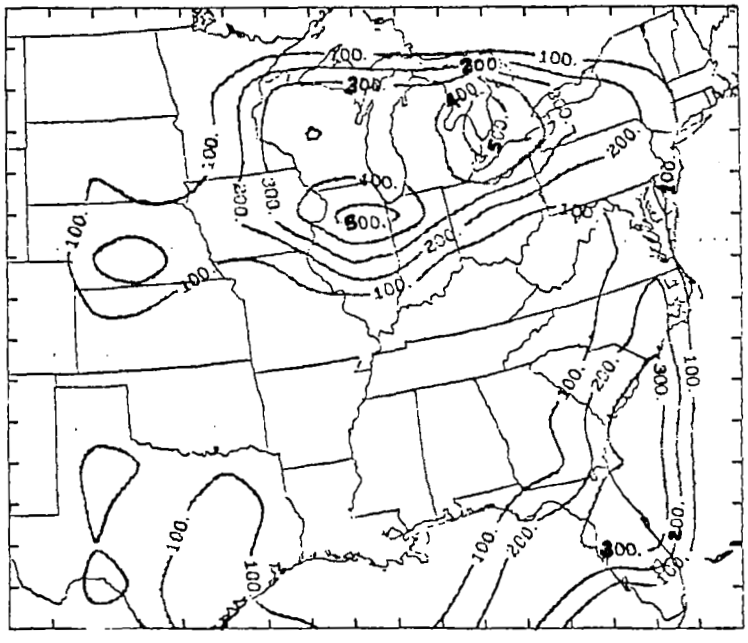

NBE

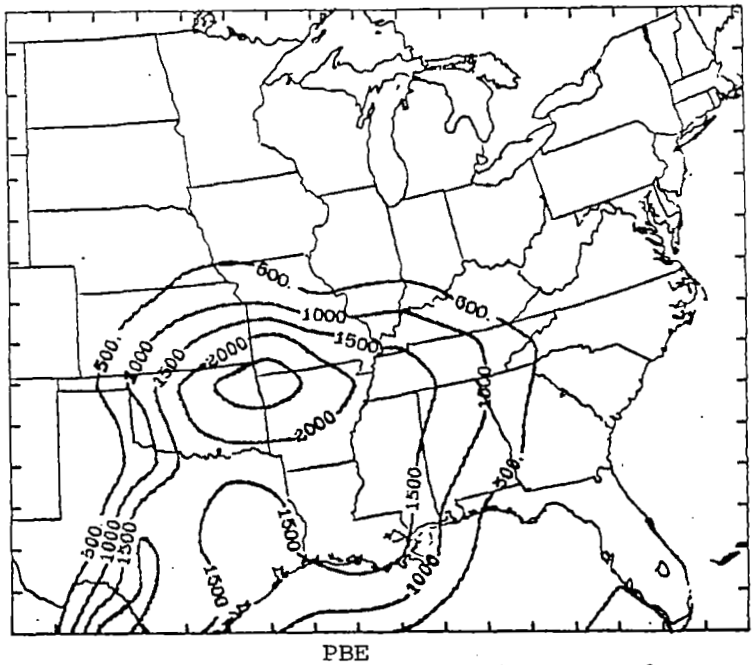

PBE

a. Parcel energy indices (10^4 ergs g^{-1}).

Fig. 20. Same as Fig. 15 except for 0000 GMT, 25 April 1975.

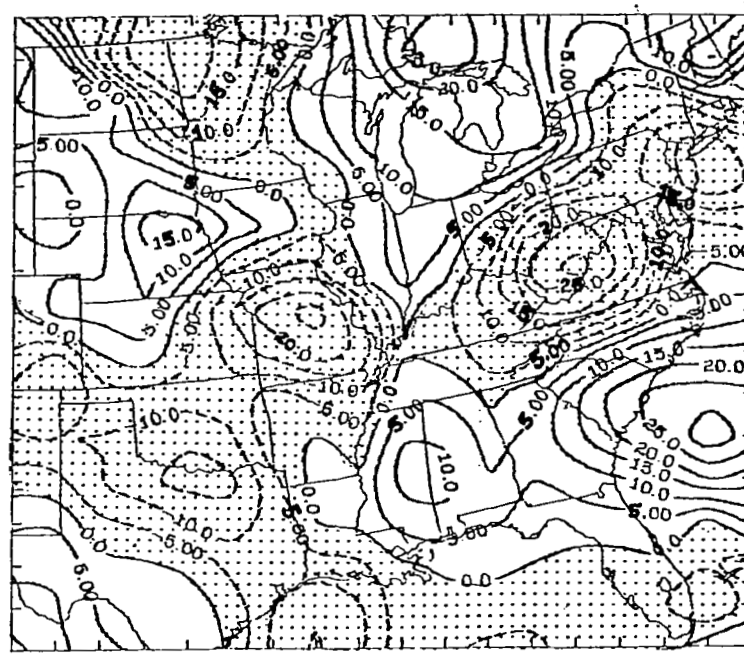

850 mb

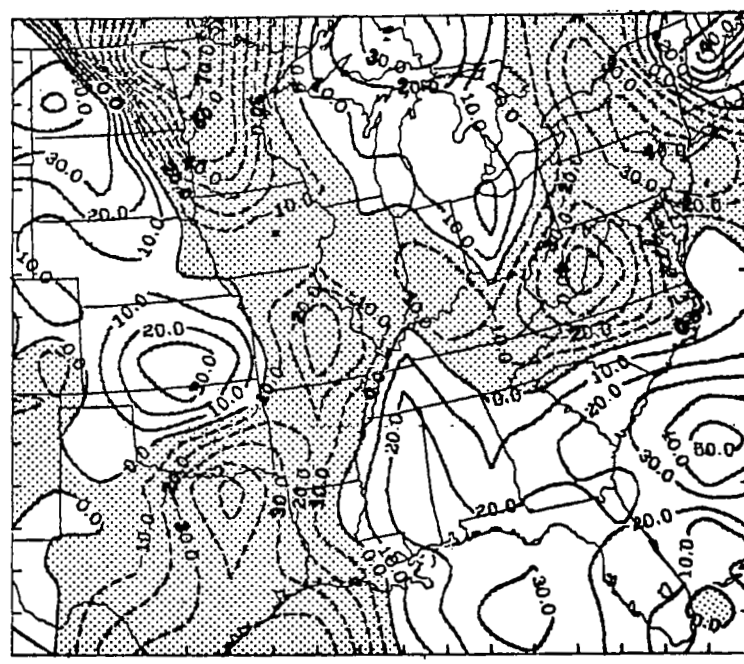

500 mb

b. Net vertical displacements (mb/3h).

Fig. 20. (Continued)

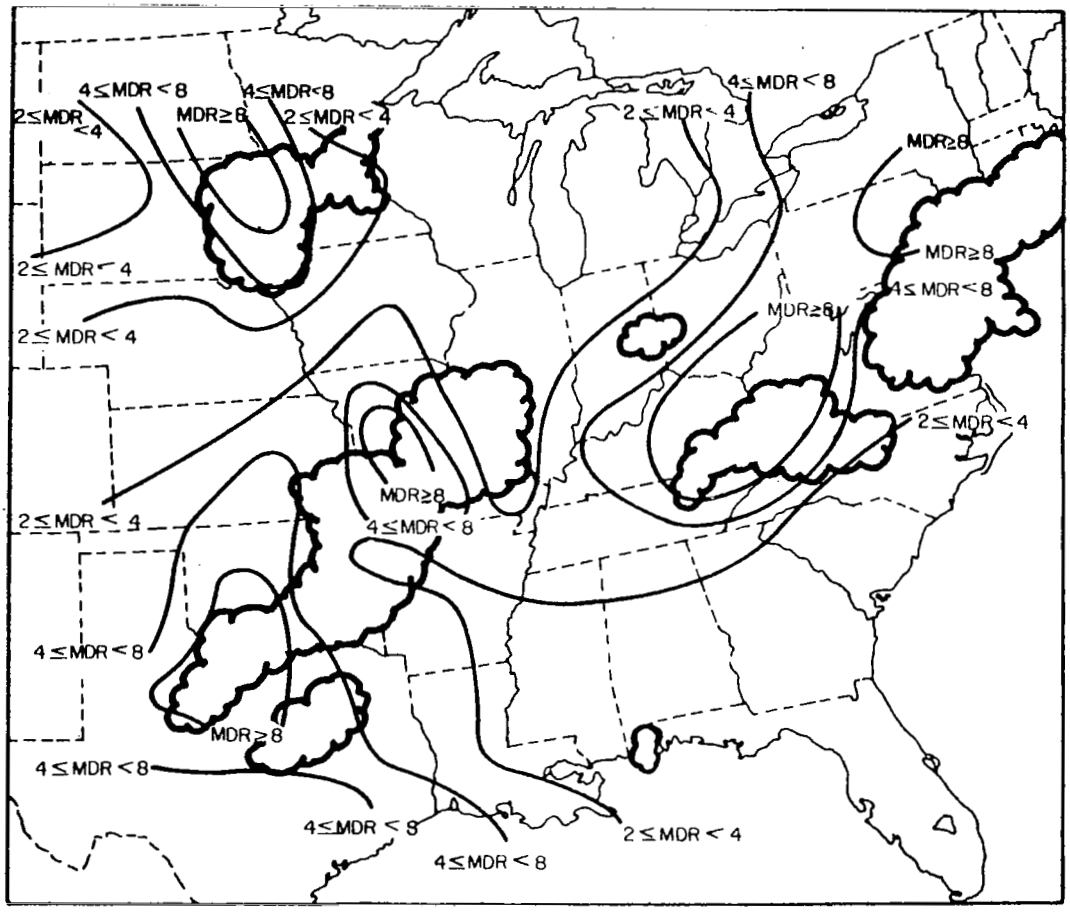

c. Diagnostic delineation of convective storm location and intensity.

Fig. 20. (Continued)

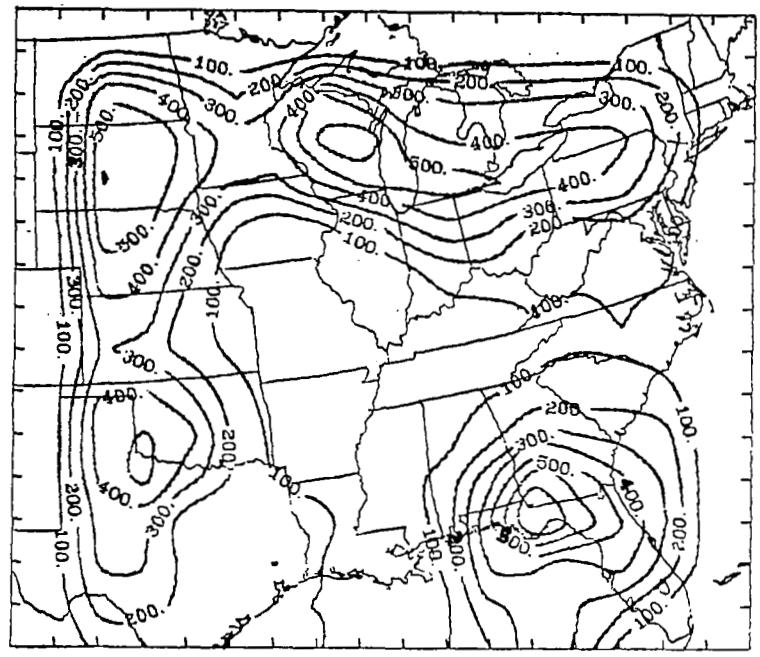

NBE

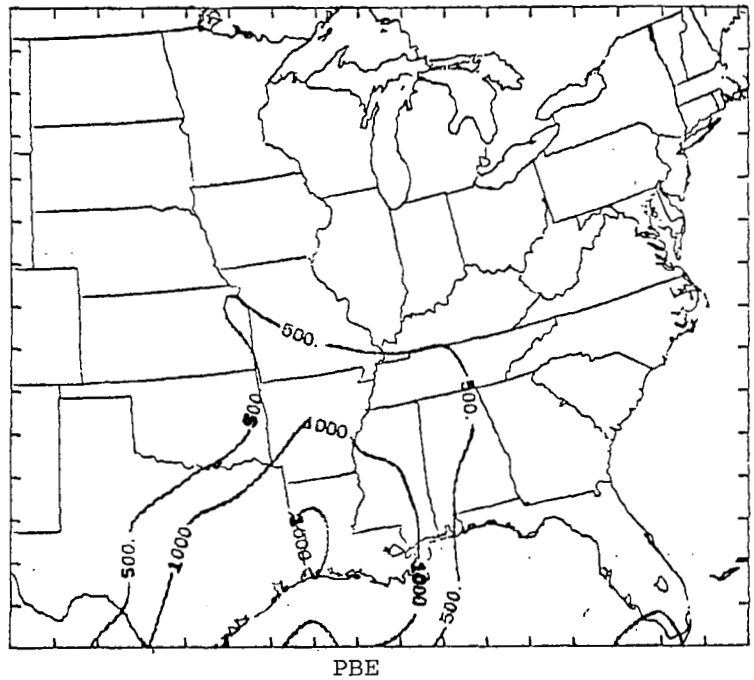

PBE

a. Parcel energy indices (10^4 ergs g^{-1}).

Fig. 21. Same as Fig. 15 except for 0600 GMT, 25 April 1975.

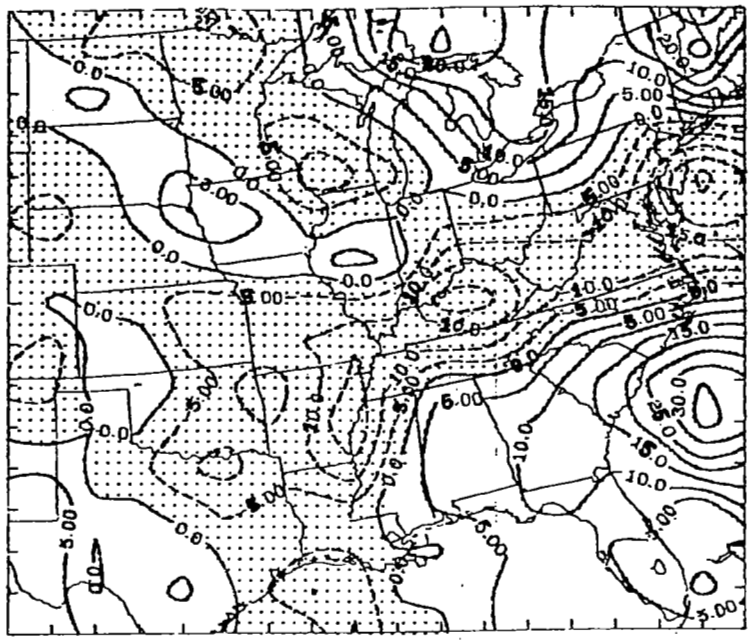

850 mb

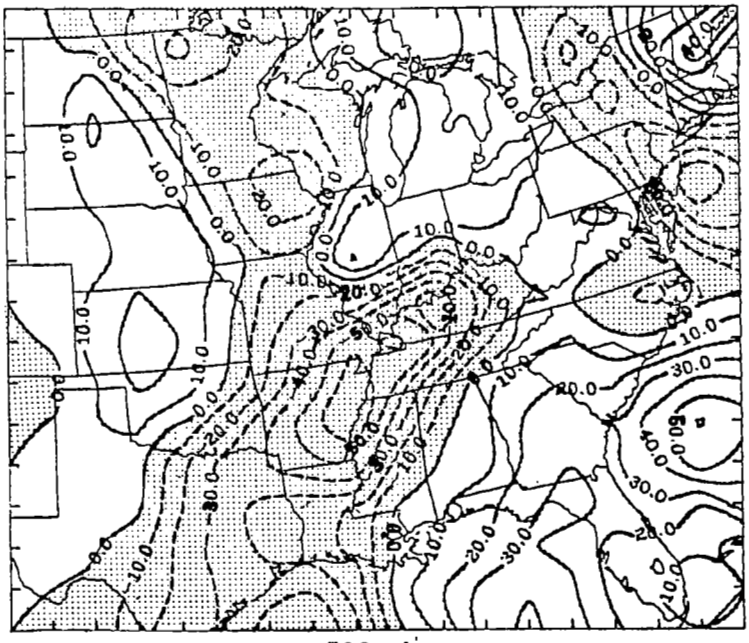

500 mb

b. Net vertical displacements (mb/3h).

Fig. 21. (Continued)

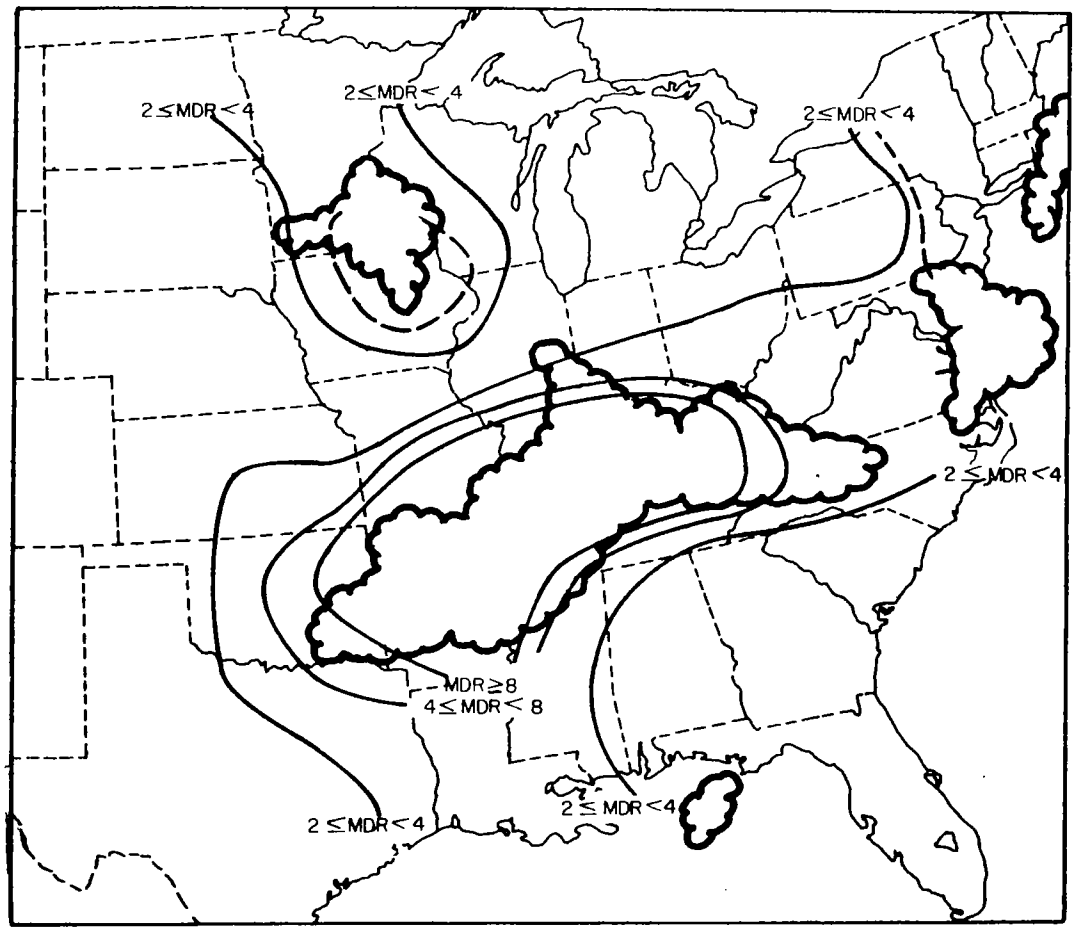

c. Diagnostic delineation of convective storm location and intensity.

Fig. 21. (Continued)

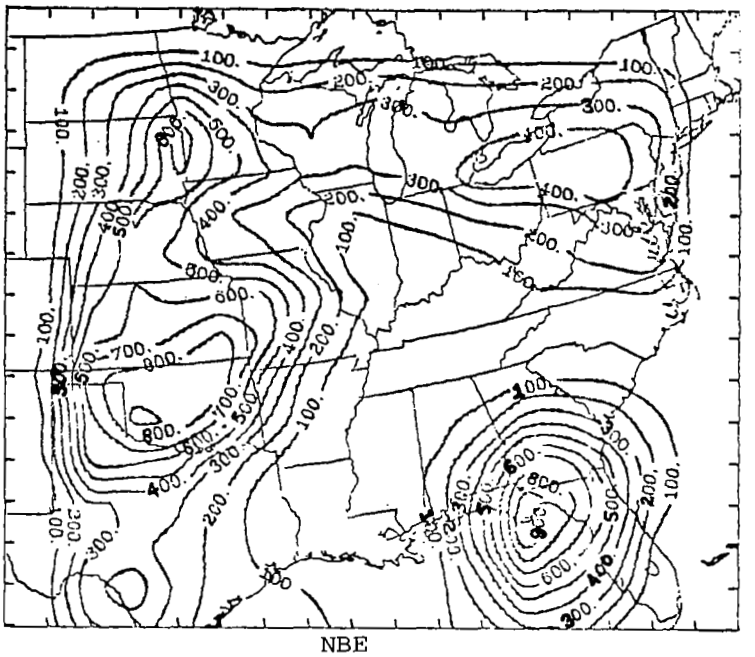

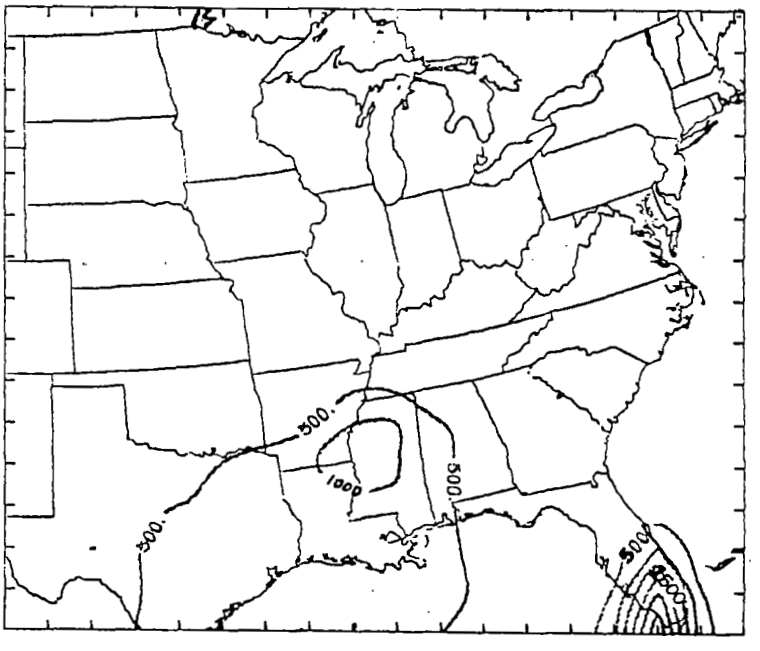

a. Parcel energy indices (10^4 ergs g^{-1}).

Fig. 22. Same as Fig. 15 except for 1200 GMT, 25 April 1975.

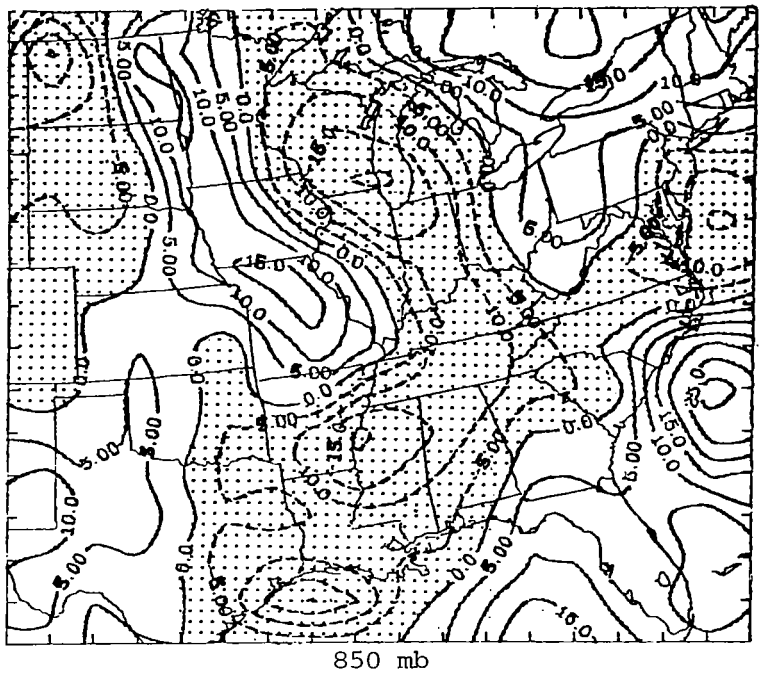

850 mb

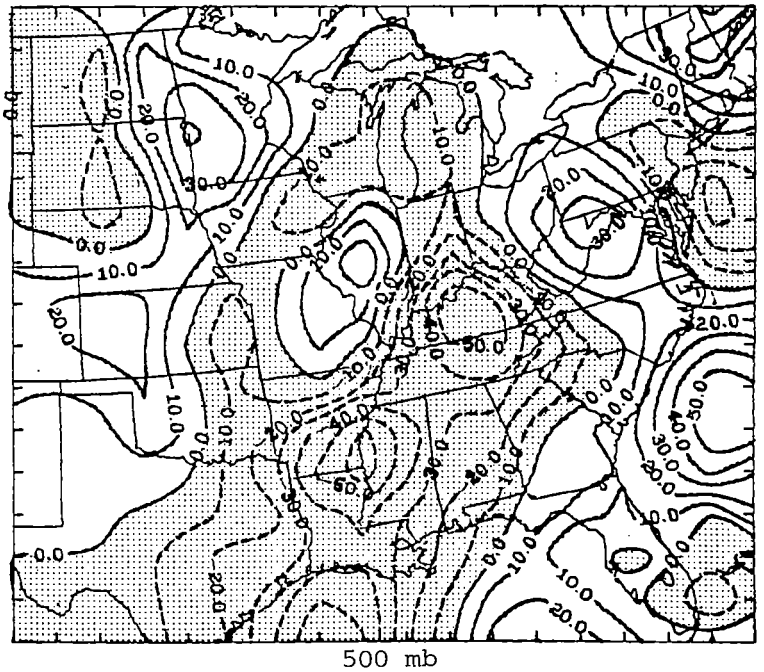

500 mb

b. Net vertical displacements (mb/3h).

Fig. 22. (Continued)

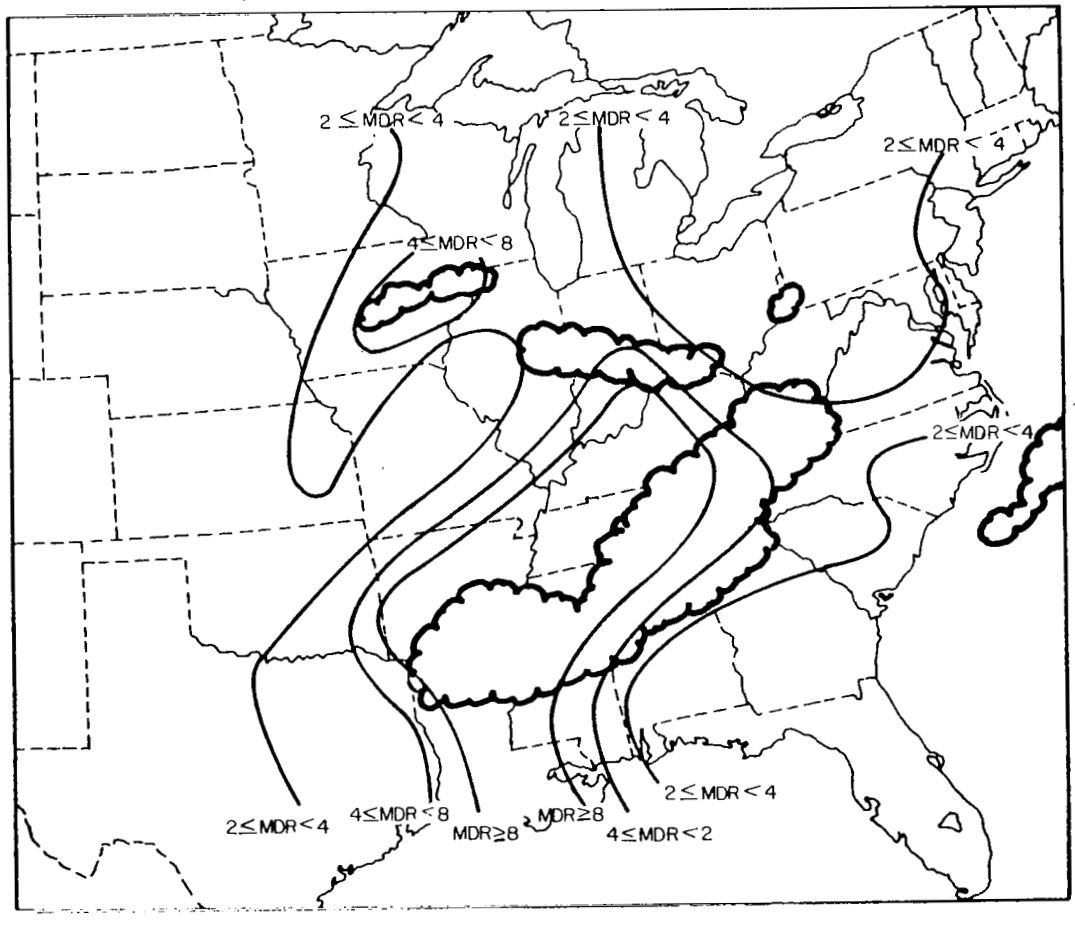

c. Diagnostic delineation of convective storm location and intensity.

Fig. 22. (Continued)

In contrast, heavy and severe thunderstorms (MDR>6) are located in higher PBE areas with the two lines of severe thunderstorms (systems A and E) moving and developing into regions of PBE values exceeding 500 x 10^4 ergs g^{-1}. Areas in excess of this value occurred only in the southern and central portions of the network coincident with the strong influx of moisture and heat below 700 mb seen in the synoptic structure and trajectory plot analyses. This influx contributed, in part, to decreasing NBE and increasing PBE values before and during storm development. However, surface and boundary layer heating as well as dynamic lifting associated with short-wave trough movement aloft, also changed the energy index values in the same manner. In general, NBE values are clearly smaller and PBE values higher during the daylight hours (Figs. 17a through 20a) coincident with strong radiational warming in the lower troposphere during the Spring season.

However, a dynamic lifting mechanism and weak static stability (low NBE values) are both usually needed for convective storm development. As discussed earlier, the gridded trajectory fields of dp/dt or net vertical displacement (NVD in mb/3h) have been successfully used to indicate those areas undergoing the time-dependent lifting and destabilizing processes needed for thunderstorm formation and maintenance. The increased temporal resolution of the AVE IV data was clearly able to identify an NVD distribution that related extremely well to the location and intensity of convective activity as described below.

Figures 15b through 22b are the NVD fields (mb/3h at 850 and 500 mb) for the last eight consecutive time periods of the experiment. Upward (negative) displacements are shaded in each chart. Major areas of negative and positive NVD's are closely associated with the eastward movement of the short-wave troughs located earlier where air parcels ascend ahead and descend behind each system while moving quasi-horizontally through the vertical motion fields created by the short-wave perturbations. In all cases, convection is located within a negative NVD area either at 850 or 500 mb or at both levels while no precipitation is present in the subsiding (positive) areas behind

the troughs. Qualitative comparison generally indicates that the spatial correlation between NVD's and convection is higher than that between instantaneous vertical velocities and thunderstorms (see Figs. 6d-13d). Moreover, large negative NVDs can quickly destabilize the atmosphere, creating the smaller NBE and larger PBE values (depending upon the resulting vertical temperature and moisture structure) favorable for thunderstorm formation.

Under sufficiently small NBE conditions, possibly created by diabatic heating, advection of heat and moisture, and destabilizing lifting, the intensity of the resulting convection is controlled, in part, by the PBE available to be converted into the vertical velocity of the cloud updraft from non-hydrostatic accelerations. These conditions are clearly evident in Fig. 20 where the synoptic conditions associated with the Neosho tornado in southwestern Missouri included: 1) NBE$<100 \times 10^4$ ergs g^{-1}; 2) a very large PBE center exceeding 2500 ergs g^{-1}; and, 3) strong upward NVD centers at both 850 and 500 mb.

To objectively compare the spatial correlation between all NVD fields and the location and intensity of convective activity, biserial correlation coefficients were computed. This correlation coefficient measures the ability of a particular parameter (NVD) to delineate in space between convective and non-convective areas as a function of convection intensity determined from MDR data. These coefficients are shown in Fig. 23 as a function of pressure and MDR intensity along with the coefficients for the instantaneous vertical velocities computed by the adiabatic and kinematic techniques (from Wilson, 1976). In every case, the NVD's are more highly correlated to precipitation location and intensity than are the instantaneous vertical velocities, indicating the high correlation between the time-dependent macroscale lifting process (releasing potential instability) and the location and intensity of convective activity.

To summarize the relationship between NVD's and the location and intensity of convective activity, Fig. 24 shows the average vertical profiles of NVD (mb/3h) as a function of precipitation intensity (from MDR data) using data from all eight time periods of AVE IV. "No precipitation" areas had small positive NVD's at most levels while

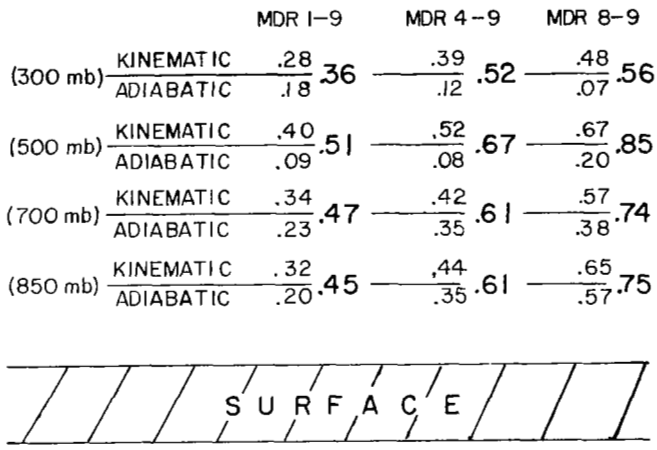

Fig. 23. Biserial correlation coefficients for the kinematic and adiabatic vertical velocities (from Wilson, 1976) and NVD's (bold type) for various pressures and MDR coded precipitation intensities.

negative values (upward vertical motion) occured in precipitation areas with the maximum upward values located around 500 mb. The magnitudes of the average values of NVD's were larger at all pressure levels in areas containing more intense convective activity so that an average value of -70 mb/3h was associated with severe thunderstorms in AVE IV.

Since both a dynamic lifting mechanism and weak static stability are usually needed for convective storm development, NVD's (at 9 pressure levels from 900 mb to 100 mb) and the NBE and PBE stability measurements were combined, using multiple linear regression, in an attempt to delineate spatially the location and intensity of convection for all AVE IV time periods. Correlations were computed with grid point data where the predictand was MDR intensity categories ($MDR < 2$, $2 \leq MDR < 4$, $4 \leq MDR < 8$, $MDR \geq 8$) calculated in the manner explained in Fig. 24. A linear correlation coefficient of 0.6 was obtained for these increasing intensity categories of convection with the most important parameters (in order) being NVD (500 mb), NVD (850 mb), NBE, and PBE (these parameters account for 98% of the total explained variance). This linear regression delineates (with 80% accuracy)

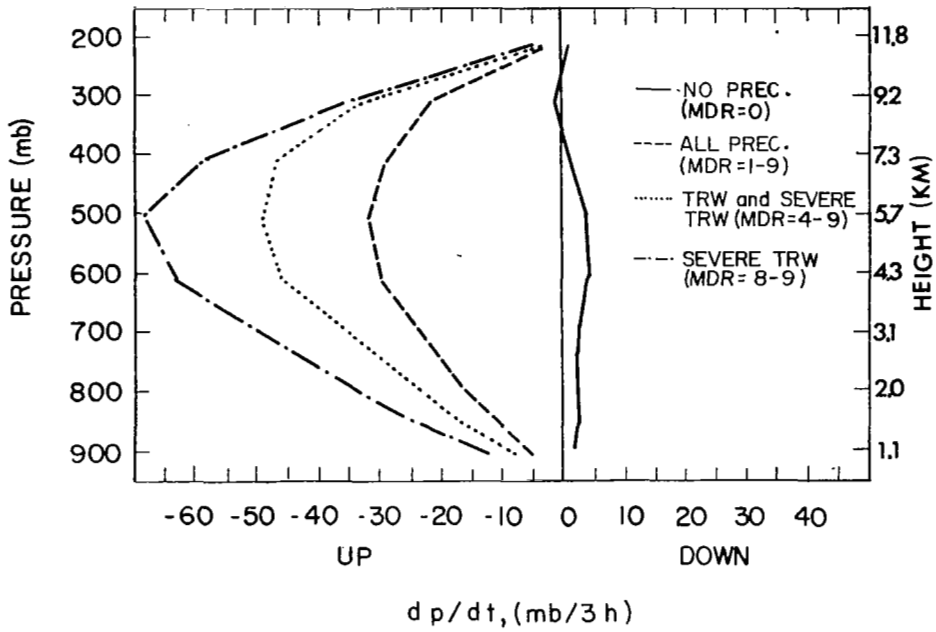

Fig. 24. Average profiles of dp/dt or NVD as a function of pressure and MDR coded precipitation intensity. (Maximum MDR value was assigned to a grid point within 1/2 grid distance (≈80 km) from MDR 3-h composite charts).

between non-convective (MDR<2) and convective areas (MDR>2), but it only determines the correct intensity category 50% of the time.

Figures 15c through 22c present spatial fields of the diagnostically determined intensity categories derived from multiple linear regression techniques (Figures 15a and b through 22a and b are analyses of the primary variables used in the final regressions). Grid point MDR intensity categories (predictand) were computed by applying the linear regression equation to the values of the primary variables (predictors) found in the multiple linear regression analysis at each grid point. These results reveal that synoptic-scale variables can accurately locate areas with and without convection, while delineation of convective storm intensity is also possible but with somewhat less accuracy. Even so, the strong controlling influence of synoptic scale systems over the temporal and spatial distribution of thunderstorm location and intensity is explicitly shown.

In looking specifically at the Neosho storm development and System E's formation and movement (Figs. 20c-22c), an intensity category for MDR

values ≥8 (severe convection) was computed over southwestern Missouri and western Texas and Oklahoma coincident with severe thunderstorms and reported tornadoes and hail at 0000 GMT 25 April. In the 12 hours that followed, System E moved eastward as an area of severe thunderstorms while an intensity category for MDR ≥8 was consistently computed with this storm system at both 0600 and 1200 GMT 25 April.

d. Parcel diabatic processes

Diabatic effects reflected in the AVE IV data were examined by calculating $\frac{d\theta}{dt}$ ($\simeq \frac{\Delta\theta}{\Delta t}$) along air parcel trajectories at all points in a grid array at various pressure levels and times as discussed previously. In interpreting the results, non-zero values of $\frac{d\theta}{dt}$ result physically from the combination of all diabatic processes in the mean or synoptic flow (condensation, evaporation, radiation, etc.) plus the net turbulent eddy flux of heat as shown in (6). Since the turbulent flux term is possibly large in thunderstorm areas, of particular interest was the determination of the heating rate experienced by the macroscale flow as a result of scale interaction between thunderstorms and their environment.

Figure 25 presents the average profiles (from all AVE IV periods) of $d\theta/dt$ (°C/3h) as a function of pressure and MDR coded precipitation intensity. In precipitation areas, diabatic warming occurs between about 800 mb and 250 mb and cooling occurs above 250 mb and below 800 mb. In addition, more intense precipitation results in larger diabatic effects, especially above 500 mb, with maximum heating (an average of 2.0°C/3h at 400 mb) associated with severe thunderstorms. Only small diabatic cooling was calculated in the "no precipitation" areas possibly associated with evaporation of liquid cloud water.

These results are similar to those obtained by Fuelberg (1977), Ninomiya (1971a) and others. Diabatic cooling (below 800 mb) is assumed to result for evaporation of precipitation (mostly convective in AVE IV) and surface radiative effects, while above 250 mb radiative cooling from thunderstorm cirrus shields is thought to occur. Large diabatic heating at mid- and upper-tropospheric levels results mostly

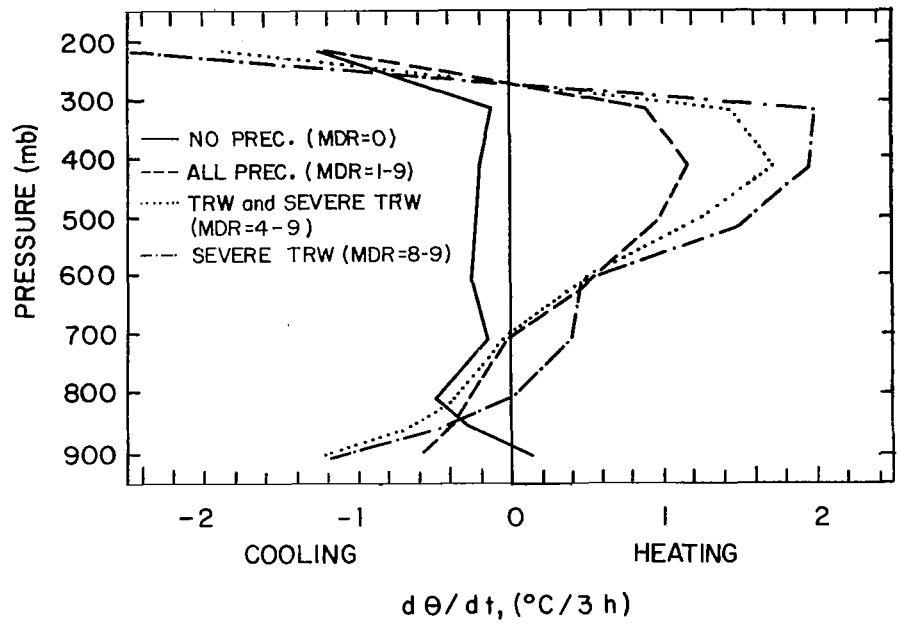

Fig. 25. Average profiles of $d\theta/dt$ as a function of pressure and MDR coded precipitation intensity. (Maximum MDR value was assigned to a grid point within 1/2 grid distance (≈80 km) from MDR 3-h composite charts).

from the turbulent interaction between the macroscale environment and convection where sensible heat is transferred into the synoptic-scale flow after condensation develops inside the convective turrets.

Figures 26 and 27 are analyzed fields of $\frac{d\theta}{dt}$ ($^{\circ}$C/3h) at a) 900mb, b) 600 mb, and c) 300 mb for the first and last two consecutive time periods of trajectory data. These time periods were chosen to show the spatial and temporal distribution of diabatic heating associated with the development and movement of the two areas of severe thunderstorms (Systems A and E) in AVE IV. Areas of diabatic heating greater than 1°C/3h are shaded while areas of convection are scolloped in each chart.

As inferred in Fig. 25, diabatic effects relative to the thunderstorm Systems A and E of Figs. 26 and 27 generally show cooling at 900 mb and diabatic warming (usually <2°C/3h) at 600 mb within the

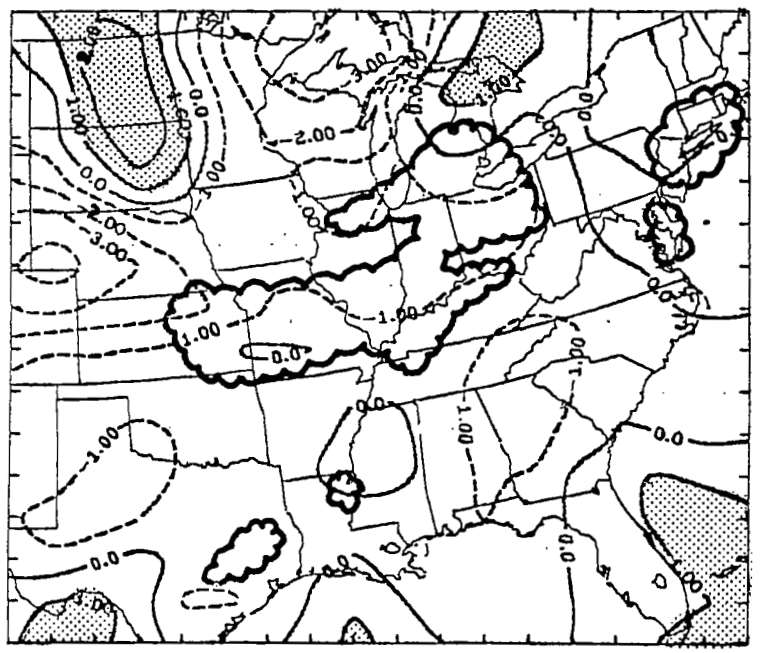

0600 GMT, 24 April

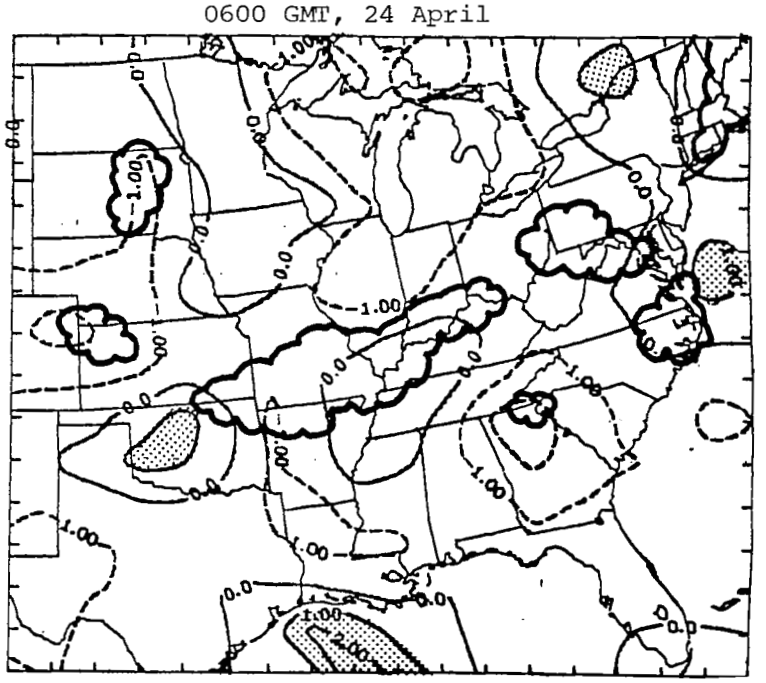

1200 GMT, 24 April

a. 900 mb

Fig. 26. Spatial fields of $\frac{d\theta}{dt}$ (^{o}C/3h) for the first two analyzed time periods of AVE IV at a) 900 mb, b) 600 mb, and c) 300 mb. Shaded areas are $\frac{d\theta}{dt} > 1.0^{o}$C/3h and scalloped areas are regions of convective activity.

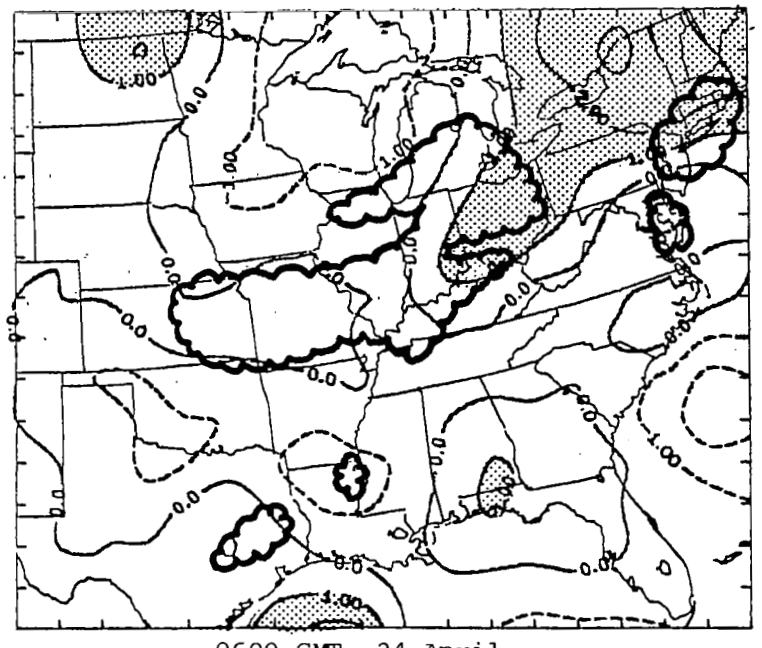

0600 GMT, 24 April

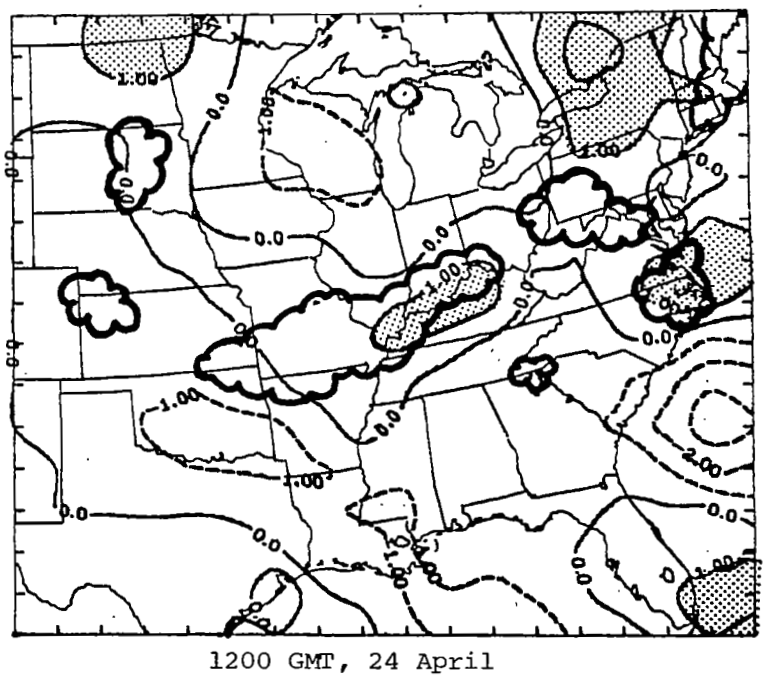

1200 GMT, 24 April
b. 600 mb

Fig. 26. (Continued)

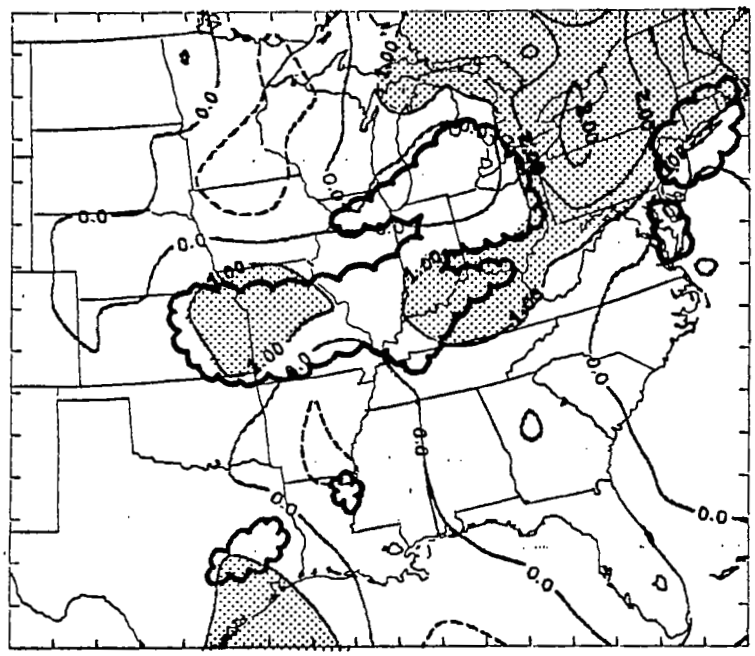

0600 GMT, 24 April

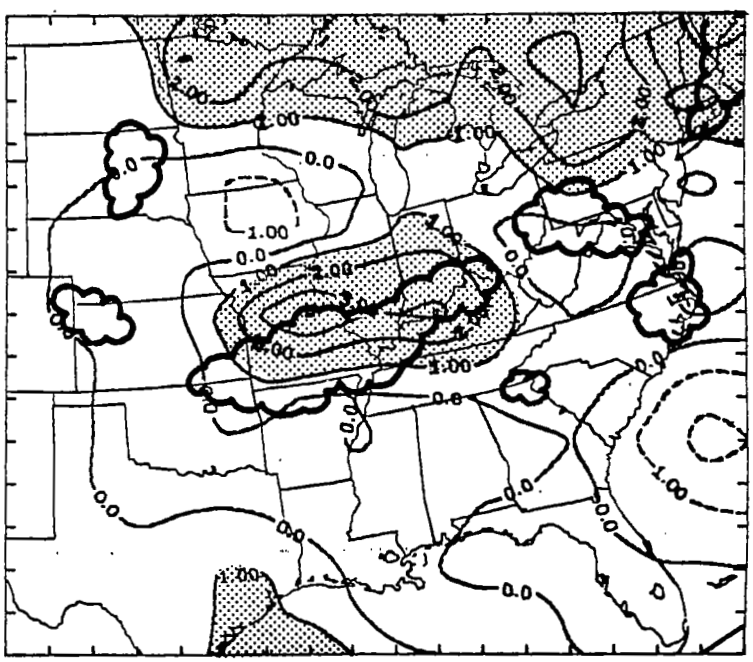

1200 GMT, 24 April

c. 300 mb

Fig. 26. (Continued)

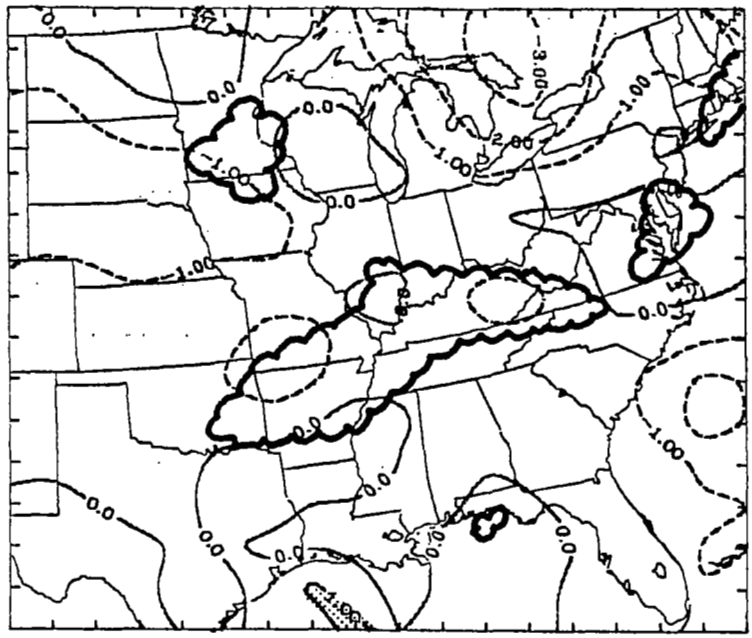

0600 GMT, 25 April

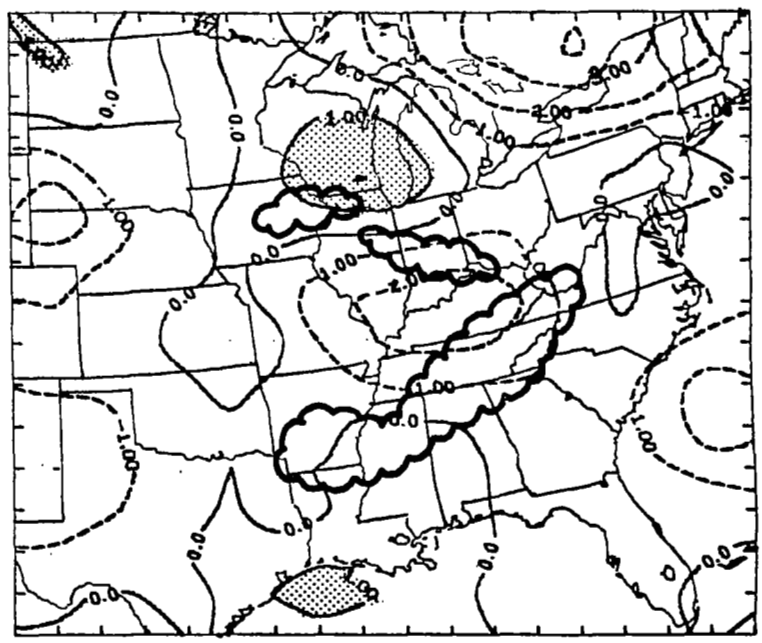

1200 GMT, 25 April

a. 900 mb

Fig. 27. Same as Fig. 26 except for the last two analyzed time periods.

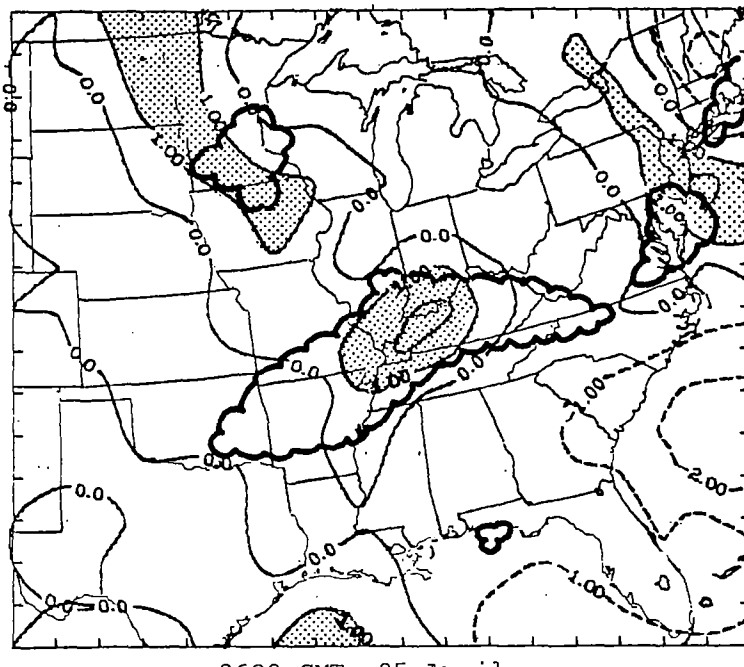

0600 GMT, 25 April

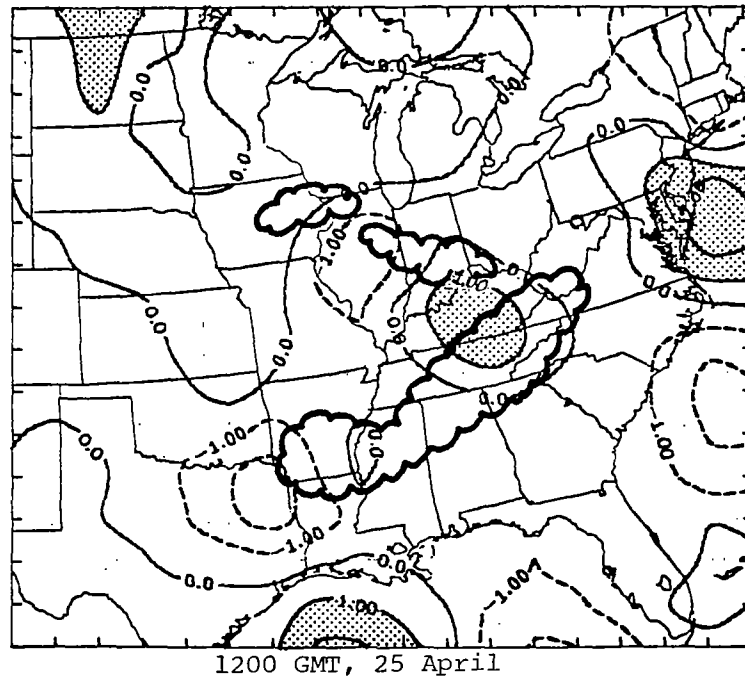

1200 GMT, 25 April

b. 600 mb

Fig. 27. (Continued)

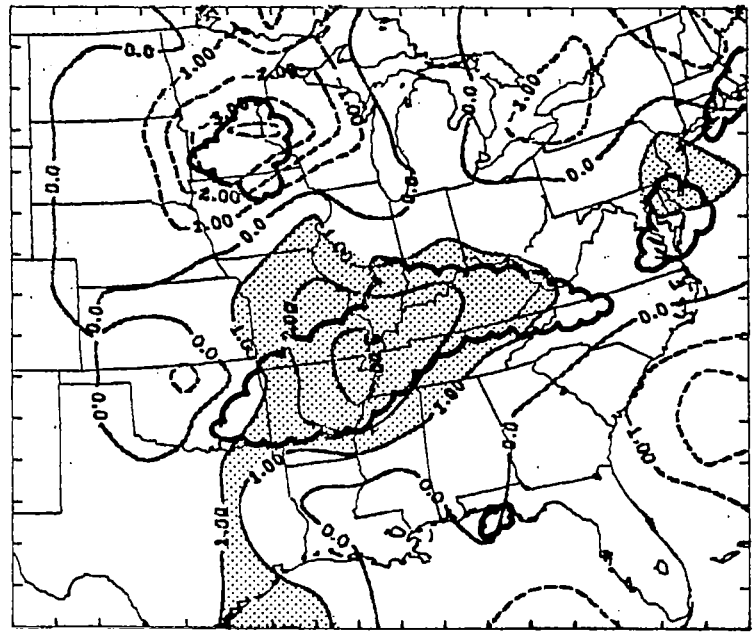

0600 GMT, 25 April

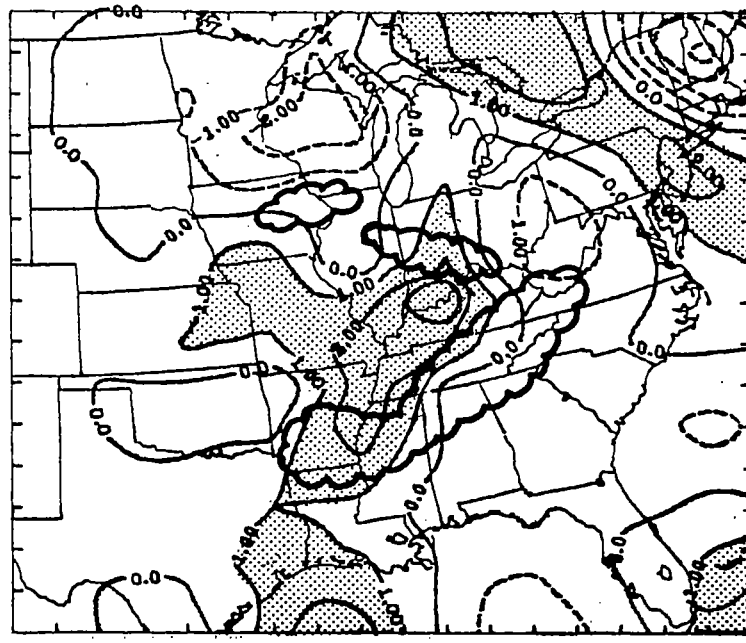

1200 GMT, 25 April
c. 300 mb

Fig. 27. (Continued)

synoptic-scale environment of the storms. At 300 mb, areas of heating, sometimes in excess of $3^{o}C/3h$, are located over and slightly northwest of the storms. Thunderstorm systems covering smaller areas than those of Systems A and E are generally associated with diabatic patterns of cooling in the lower troposphere and heating in the middle and upper levels, but magnitudes of $d\theta/dt$ are significantly smaller and rarely exceed $\pm 1^{o}C/3h$. At 600 and 300 mb, moderate diabatic cooling ($>-2^{o}C/3h$) is found both southeast and northwest of Systems A and E. Otherwise, large $d\theta/dt$ values were not calculated in other regions of the experiment area (excluding boundary regions) with the exception of the large diabatic cooling ($<-2^{o}C/3h$) found at 900 mb in the Northern Plains (Figs. 26a and 27a), and the cooling computed at 300 mb over and north of System D in Iowa and Wisconsin (see Fig. 27c). These areas are thought to be related to radiational processes where nocturnal cooling along the high terrain in the Plains affects the 900-mb temperatures and radiational cooling associated with cirrus clouds (discussed further below) lowers the temperature in the vicinity of System D around the 300-mb level.

These results clearly indicate that large diabatic processes are associated with the convective storm systems as heat is possibly exchanged between the many convective cells and the immediate environmental flow around the storms since $\frac{d\theta}{dt}$ values in non-convective areas are usually small. In the net, however, the synoptic flow experiences cooling in the lower troposphere and warming in the mid- and upper-levels, even though both evaporation and condensation in the mean flow and both positive and negative net turbulent heat transfers probably occur at some levels. Moreover, the resulting static stability of the atmosphere is increased and the thunderstorms have accomplished the important process of vertical heat transfer needed in the overall maintenance of the general circulation and global heat balance. Still, the hydrodynamic aspects of the diabatic heating and cooling of the synoptic scale must be examined.

The hypothesis that radiative cooling from the top of thu ³erstorm cirrus (or any cirrus cloud deck) causes large diabatic cooling is supported by Figs. 28a and 28b. These figures show the spatial field

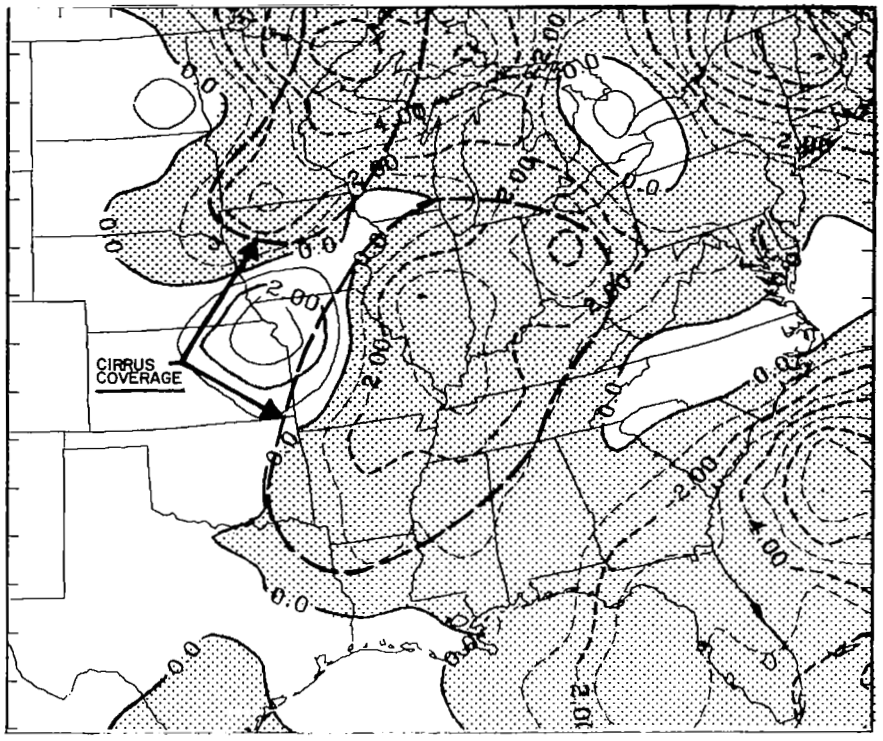

a. dθ/dt(°C/3h) at 200 mb at 0600 GMT 25 April.

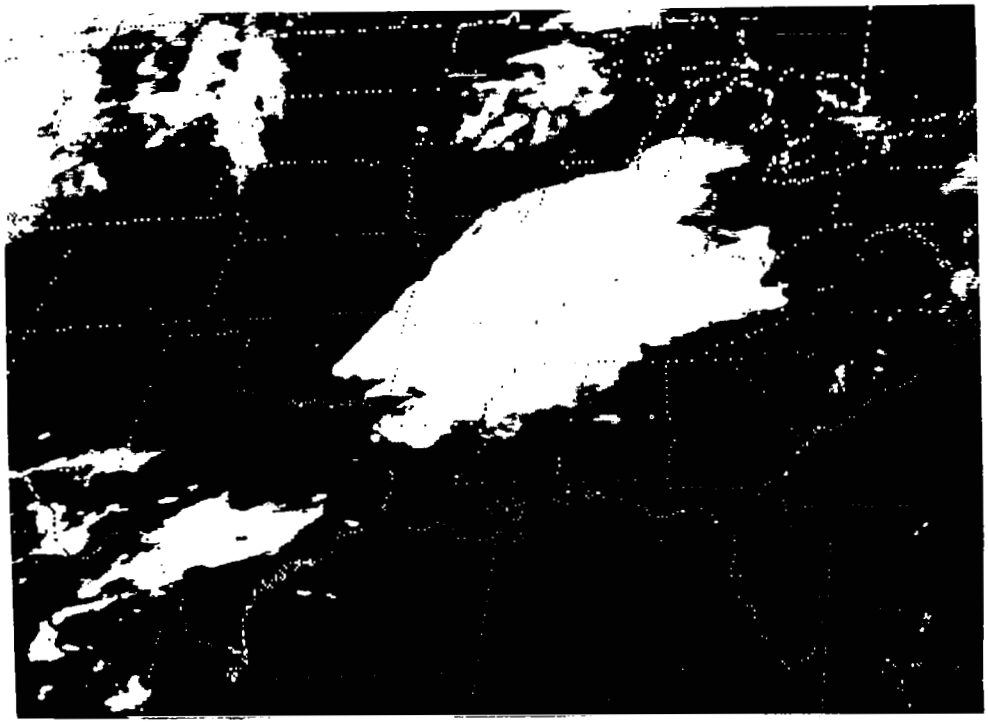

b. Infrared satellite picture at 0600 GMT 25 April.

Fig. 28. Spatial field of a) dθ/dt (°C/3h) at 200 mb, and b) infrared satellite picture, both for 0600 GMT, 25 April.

of $d\theta/dt$ at 200 mb and the IR satellite picture, respectively, for 0600 GMT 25 April. The two areas of cirrus in Fig. 28b lie essentially over the large negative zones of $d\theta/dt$ in Fig. 28a (exceeding $-3^{o}C/3h$), both over the squall line in the Mississippi Valley and the precipitation area in the northern Plains. Weak diabatic warming separates the two areas from Kansas northeastward into southern Wisconsin.

Large radiational cooling could conceivably change the vertical and horizontal temperature structure in the upper troposphere and thereby alter flow patterns, including jet stream location and intensity, over and surrounding the storms. Without question, however, these large cirrus shields alter the net radiative processes associated with incoming solar radiation and the outgoing long-wave radiation (emanating from cloud and earth sources), thereby affecting the overall heat budget of the atmosphere.

e. Parcel accelerations

As discussed earlier, the total horizontal parcel acceleration vector per unit mass, $\frac{d\vec{V}}{dt}$, can be calculated along a trajectory and results transformed into a gridded output. $\frac{d\vec{V}}{dt}$ then represents the net horizontal force acting on the parcel as a result of an imbalance between the coriolis force, the pressure gradient force, and the turbulent eddy frictional force. These net forces are mainly responsible for creating and altering atmospheric circulation systems.

The rate of change of the vertical component of relative vorticity (ζ) following an air parcel results from taking the curl of the horizontal acceleration vector and dotting this quantity with the vertical unit vector. The term $\frac{d\zeta}{dt}$ should be proportional to horizontal velocity divergence in the convective storm environment when computed from synoptic-scale measurements. Read and Scoggins (1977) have verified this approximation in their vorticity budget analysis of AVE IV. As a result, upward vertical velocity can be created from a pattern of low-level convergence (cyclonic or positive curl of $\frac{d\vec{V}}{dt}$) and upper-level divergence (anticyclonic or negative curl of $\frac{d\vec{V}}{dt}$) that can release potential instability and produce thunderstorms.

The three pairs of Figs. 29a-30a, 31a-32a, and 33a-34a show the

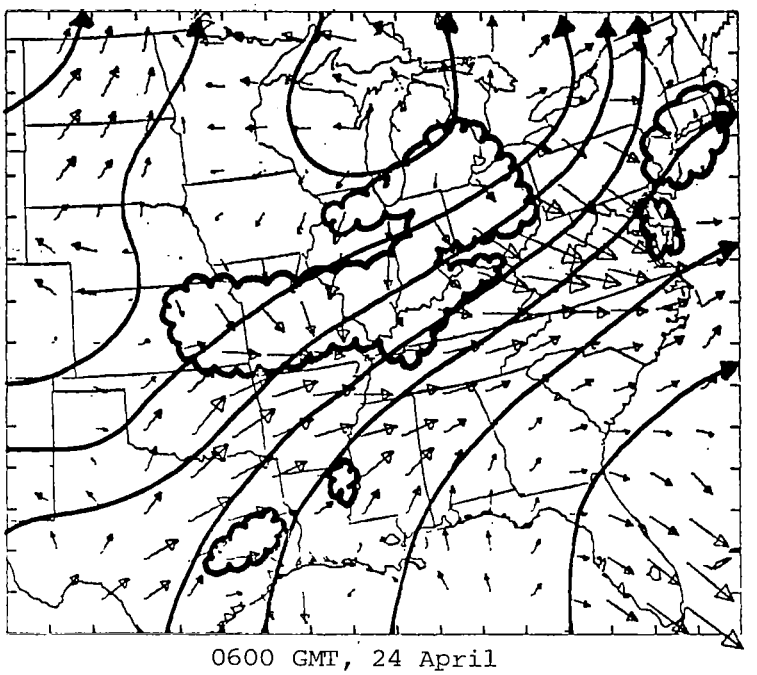

0600 GMT, 24 April

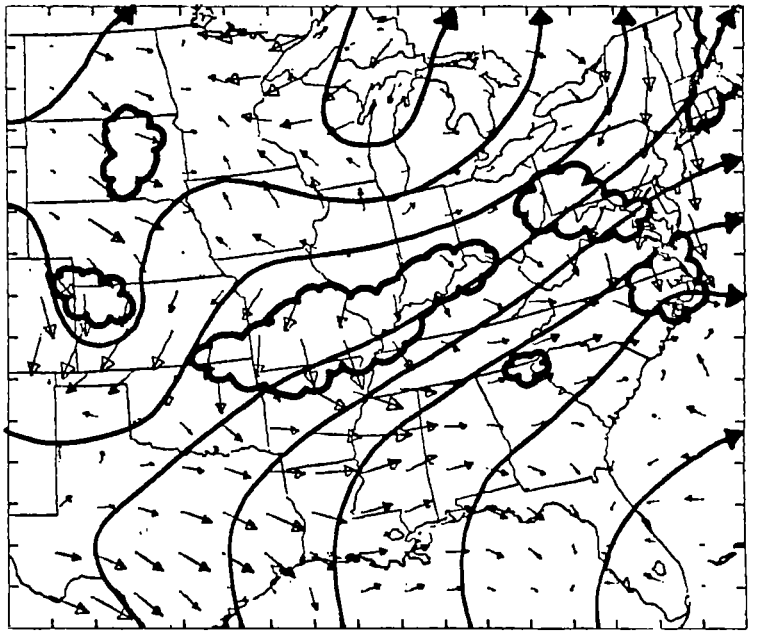

1200 GMT, 24 April

a. Horizontal acceleration vector fields (10^{-5}m s^{-2}) (→=50 x 10^{-5}m s^{-2}). Convection is scalloped and actual wind streamlines are superimposed.

Fig. 29. Spatial fields of a) vector acceleration $(\frac{d\vec{V}}{dt})$, b) $\{\hat{k} \cdot (\vec{V}p \times \frac{d\vec{V}}{dt})\}$, and c) $\frac{d(\overline{KE})}{dt}$ at 900 mb for the first two analyzed time periods of AVE IV.

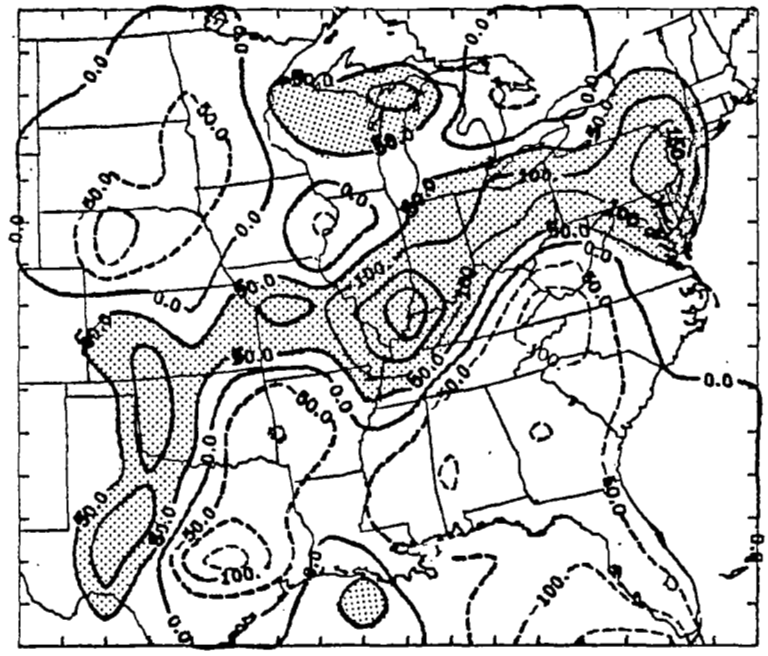

0600 GMT, 24 April

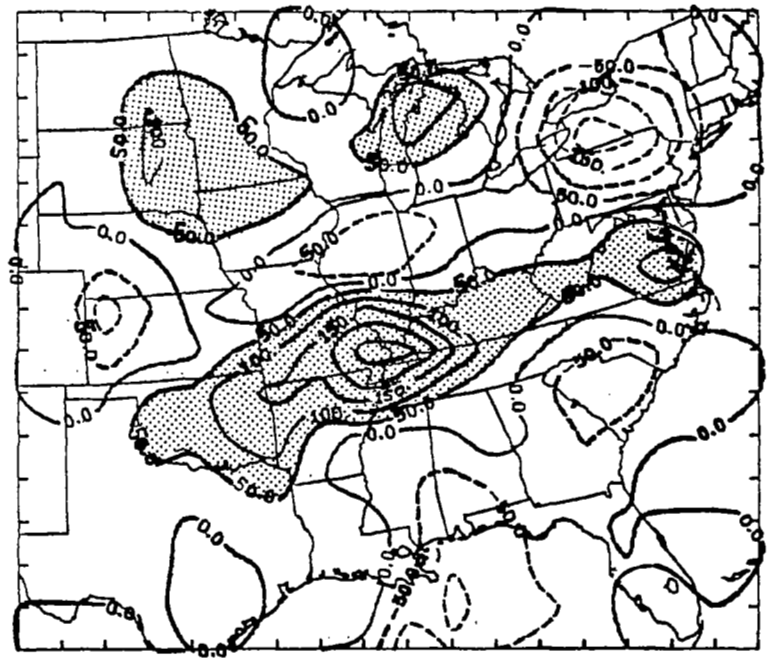

1200 GMT, 24 April

b. Horizontal curl of acceleration vector fields in (a)(10^{-11} s^{-2}). Values greater than 50 are shaded.

Fig. 29. (Continued)

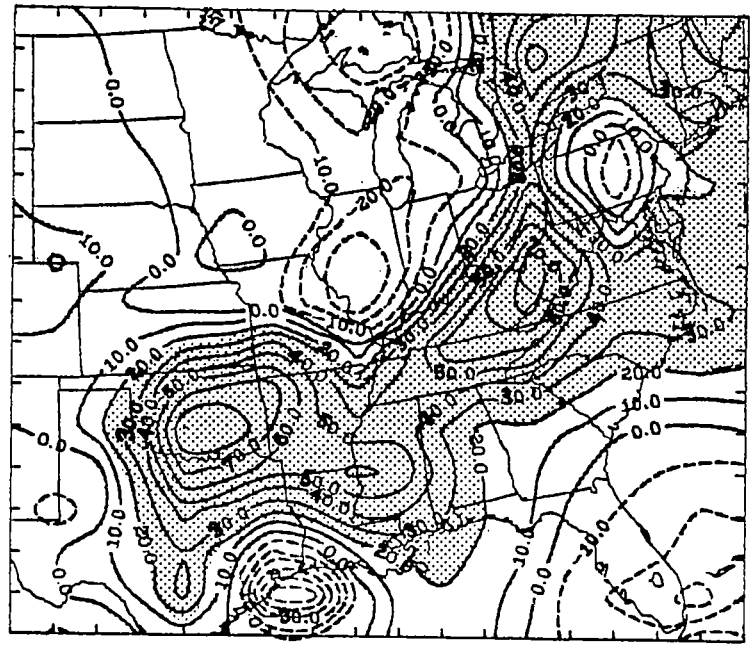

0600 GMT, 24 April

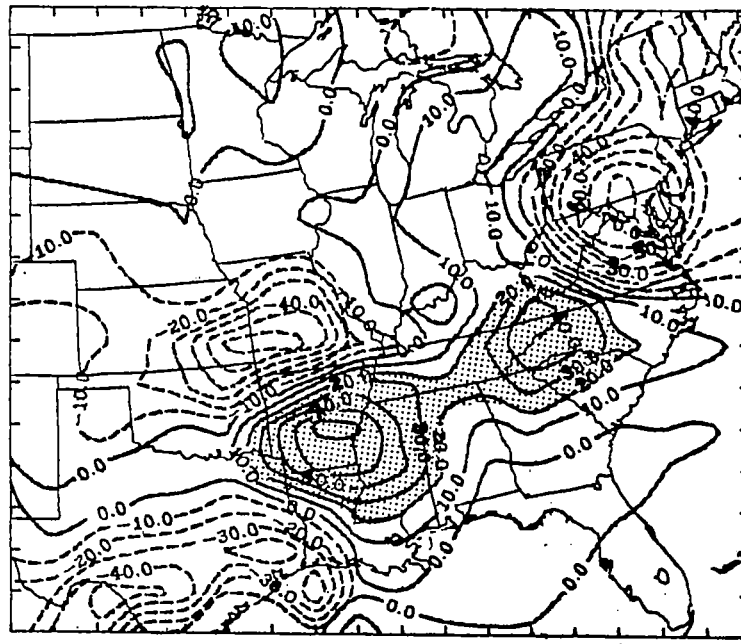

1200 GMT, 24 April

c. Rate of change of parcel kinetic energy $(\frac{d(KE)}{dt})$ (ergs g^{-1} s^{-1}). Values greater than 20 are shaded.

Fig. 29. (Continued)

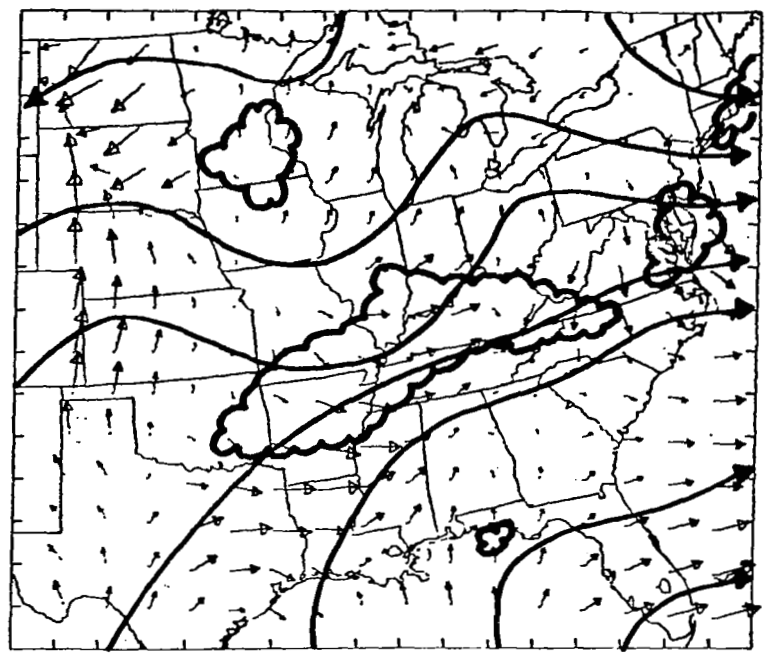

0600 GMT, 25 April

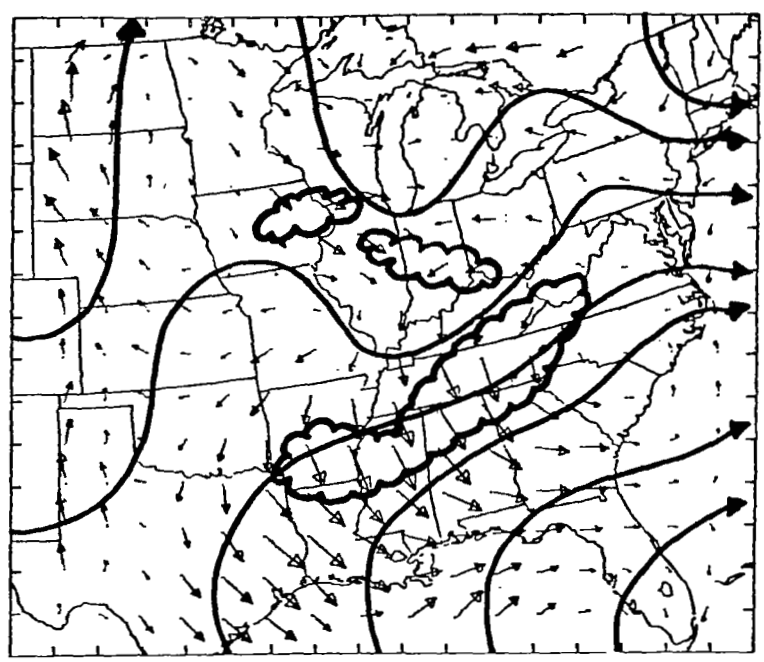

1200 GMT, 25 April

a. Horizontal acceleration vector fields (10^{-5} m s^{-2}) ($\rightarrow$=50 x 10^{-5} m s^{-2}). Convection is scalloped and actual wind streamlines are superimposed.

Fig. 30. Spatial fields of a) vector acceleration $(\frac{d\vec{V}}{dt})$, b) $\{\hat{k}\cdot(\vec{\nabla}p \times \frac{d\vec{V}}{dt})\}$, and c) $\frac{d(KE)}{dt}$ at 900 mb for the last two analyzed time periods of AVE IV.

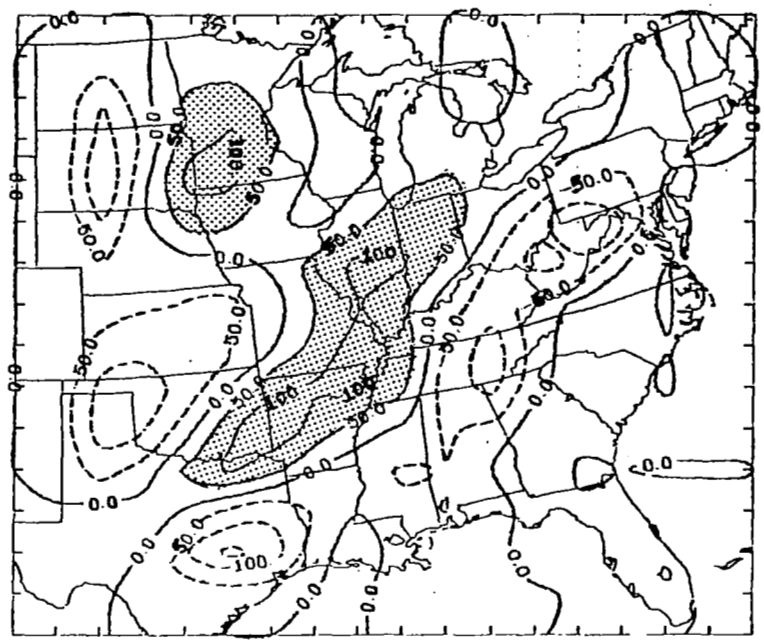

0600 GMT, 25 April

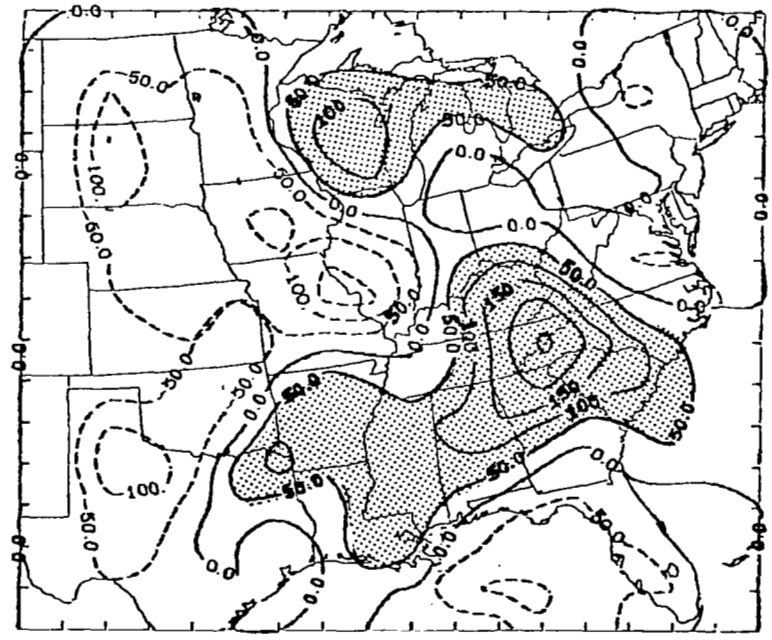

1200 GMT, 25 April

b. Horizontal curl of acceleration vector fields in (a)(10^{-11} s^{-2}). Values greater than 50 are shaded.

Fig. 30. (Continued)

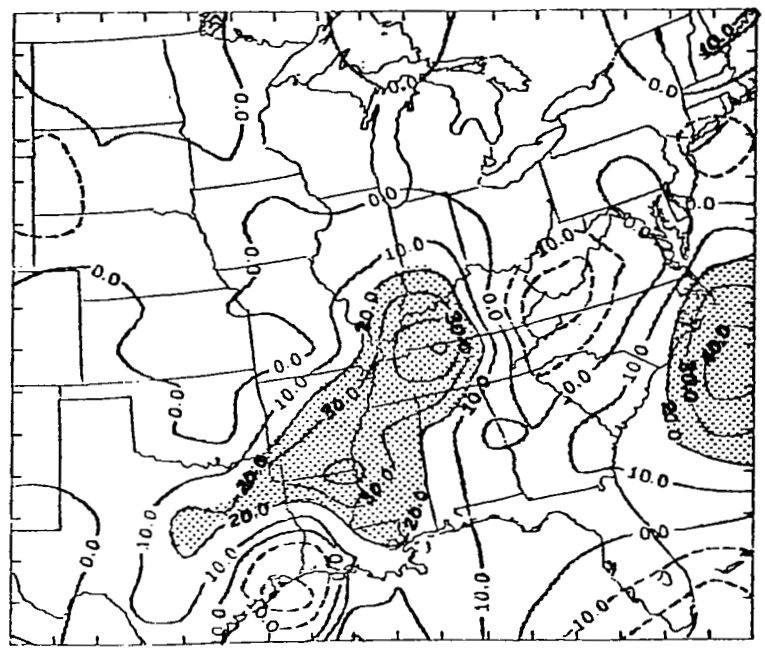

0600 GMT, 25 April

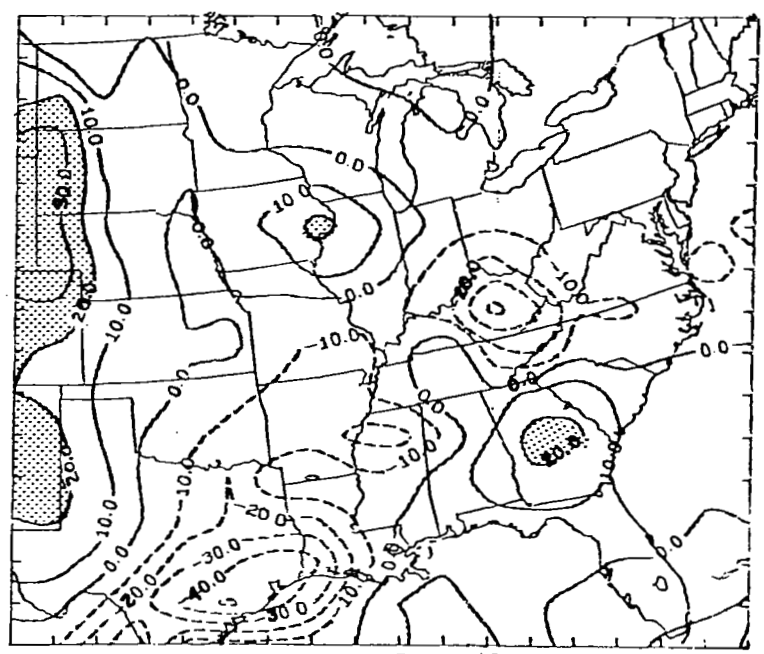

1200 GMT, 25 April

c. Rate of change of parcel kinetic energy $(\frac{d(KE)}{dt})$ (ergs g^{-1} s^{-1}). Values greater than 20 are shaded.

Fig. 30. (Continued)

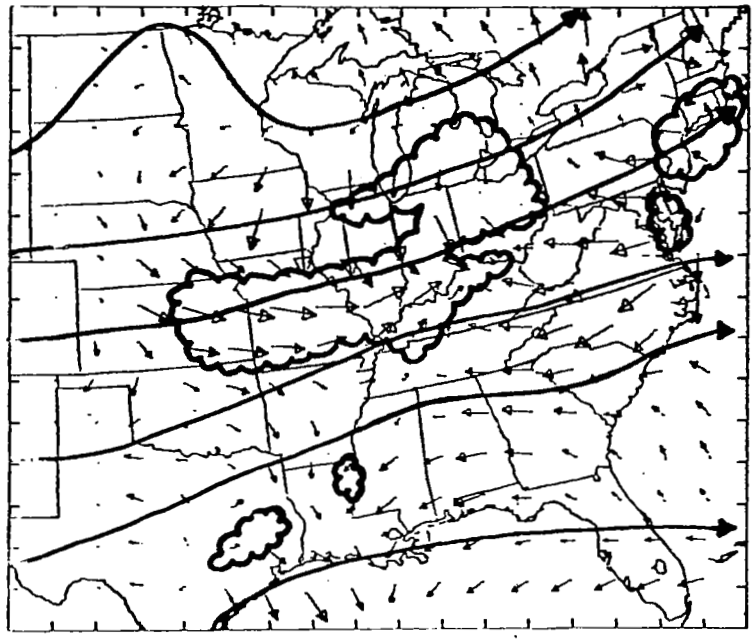

0600 GMT, 24 April

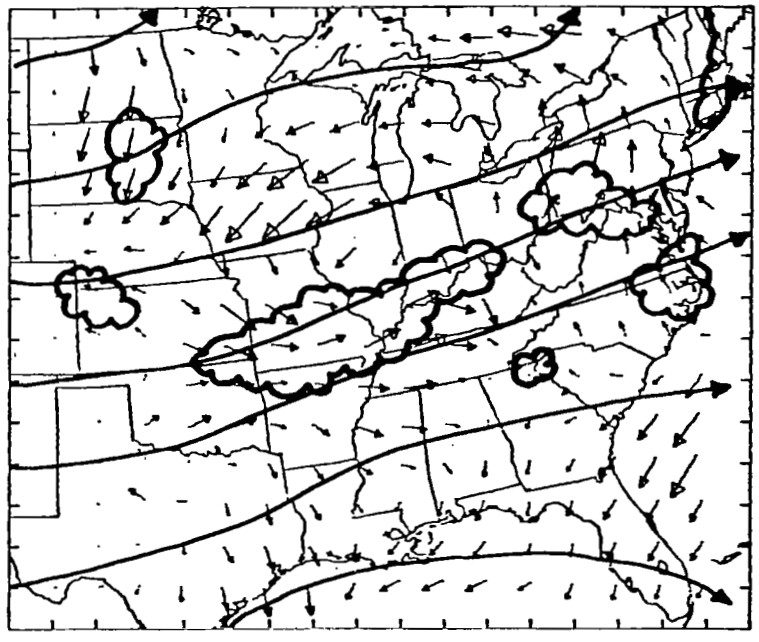

1200 GMT, 24 April

a. Horizontal acceleration vector fields (10^{-5} m s^{-2})(→=50 x 10^{-5} m s^{-2}). Convection is scalloped and actual wind streamlines are superimposed.

Fig. 31. Same as Fig. 29 except for 600 mb.

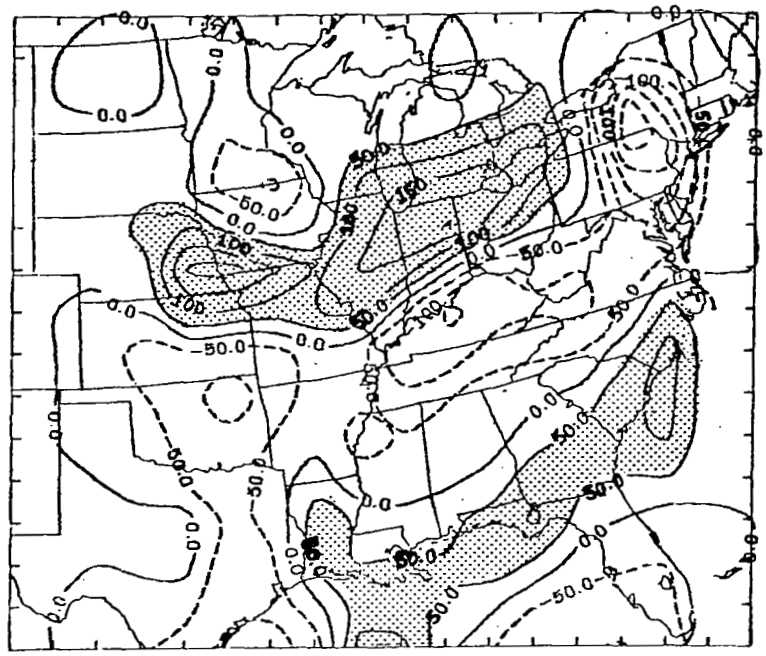

0600 GMT, 24 April

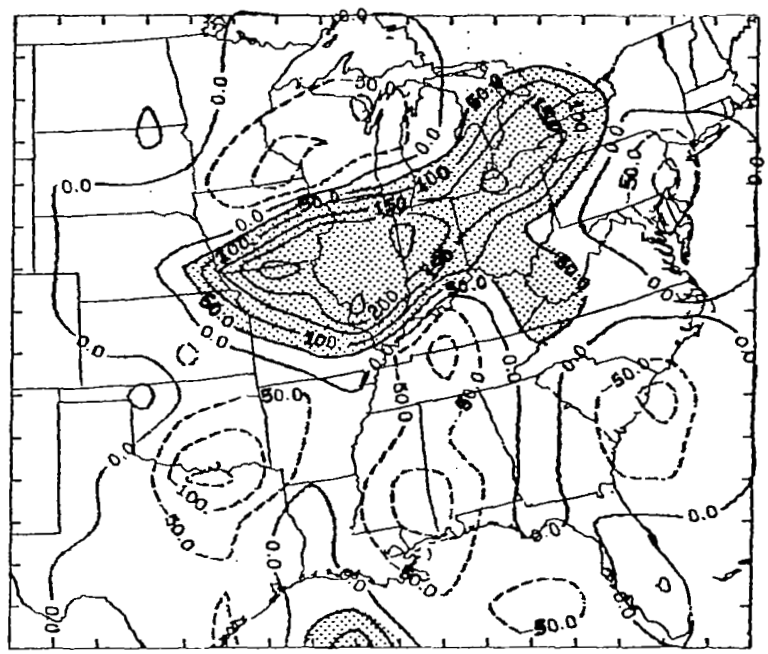

1200 GMT, 24 April

b. Horizontal curl of acceleration vector fields in (a)(10^{-11} s^{-2}). Values greater than 50 are shaded.

Fig. 31. (Continued)

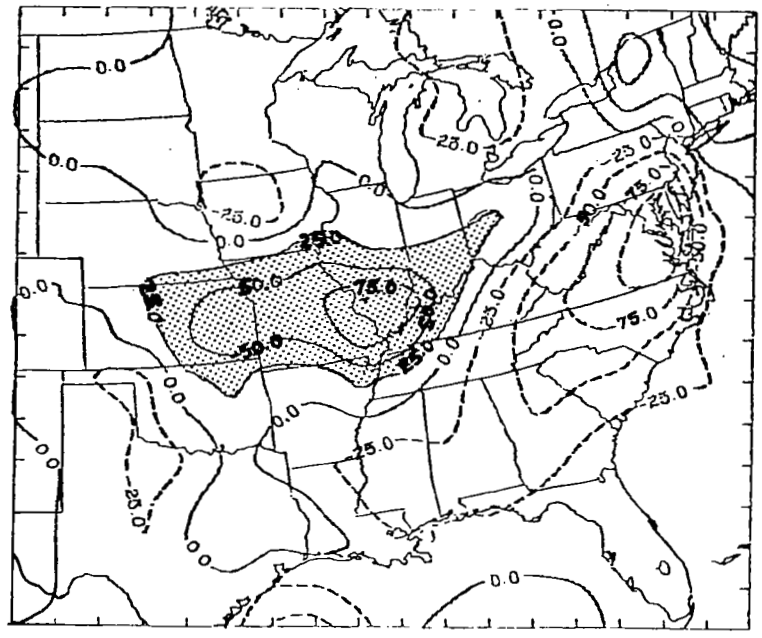

0600 GMT, 24 April

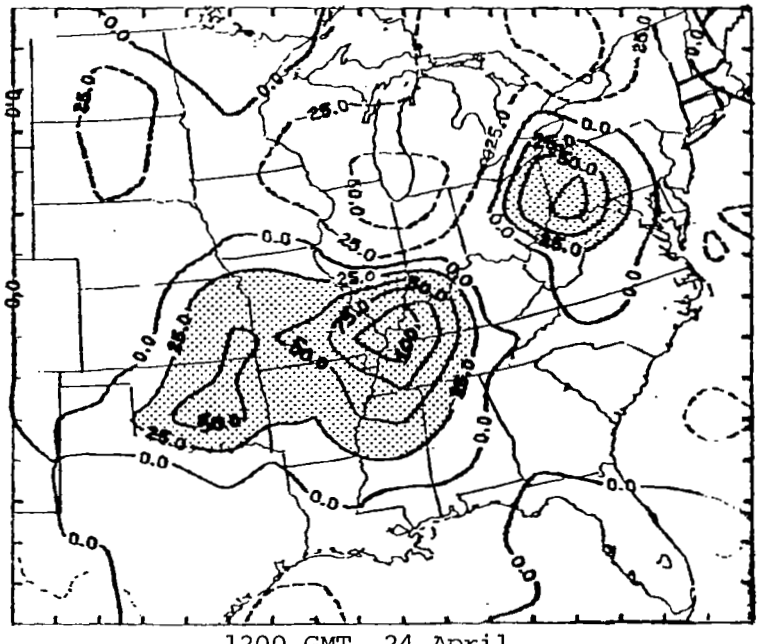

1200 GMT, 24 April

c. Rate of change of parcel kinetic energy $(\frac{d(KE)}{dt})$ (ergs g^{-1} s^{-1}). Values greater than 25 are shaded.

Fig. 31. (Continued)

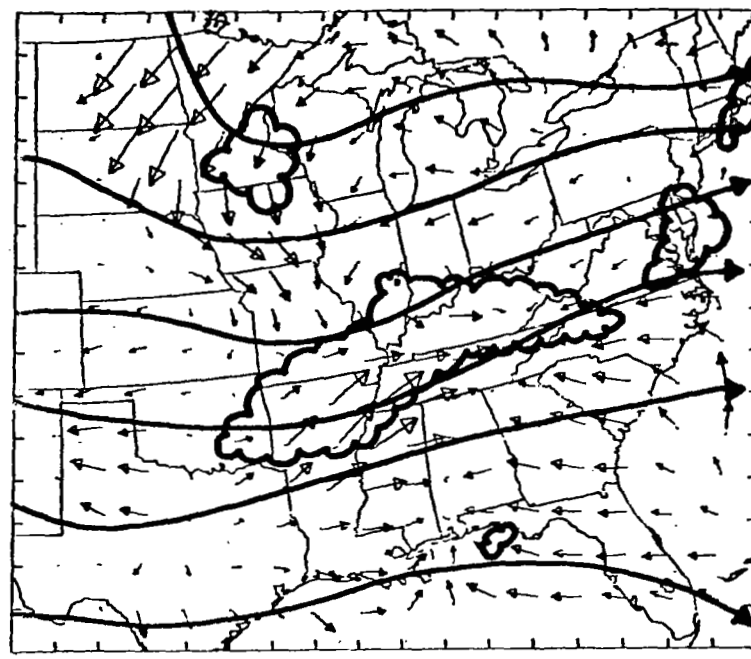

0600 GMT, 25 April

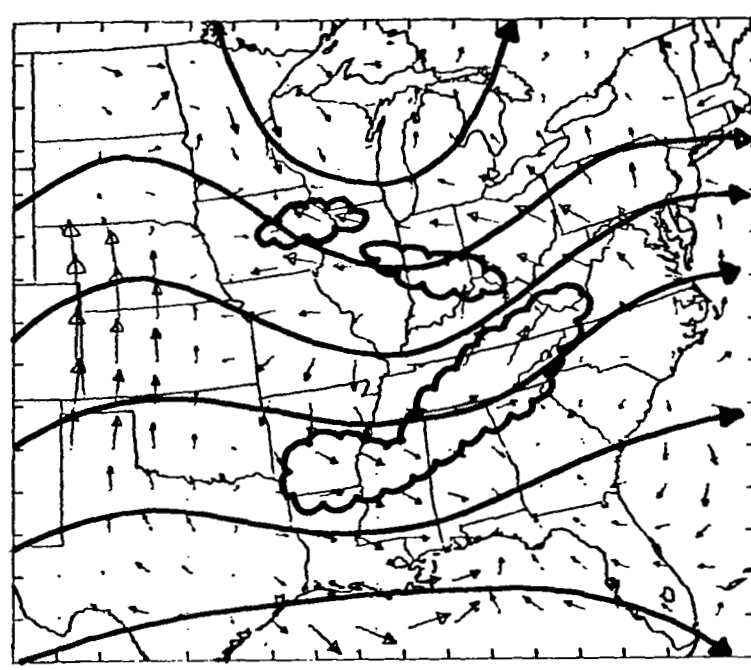

1200 GMT, 25 April

a. Horizontal acceleration vector fields (10^{-5} m s^{-2}) ($\rightarrow$=50 x 10^{-5} m s^{-2}). Convection is scalloped and actual wind streamlines are superimposed.

Fig. 32. Same as Fig. 30 except for 600 mb.

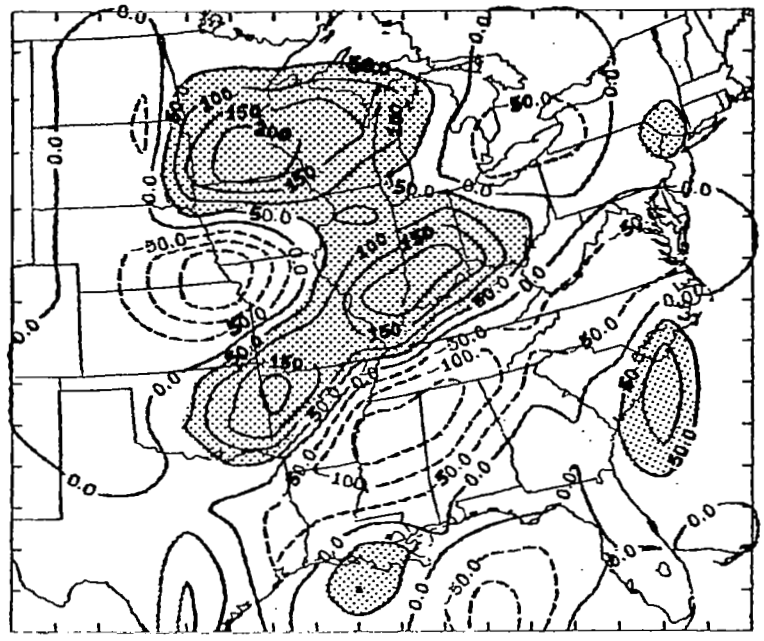

0600 GMT, 25 April

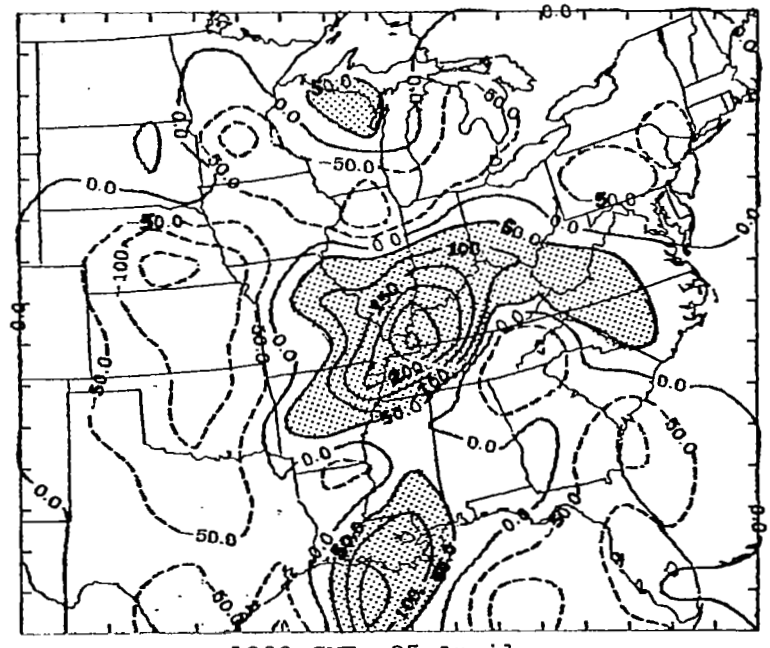

1200 GMT, 25 April

b. Horizontal curl of acceleration vector fields in (a)(10^{-11} s^{-2}). Values greater than 50 are shaded.

Fig. 32. (Continued)

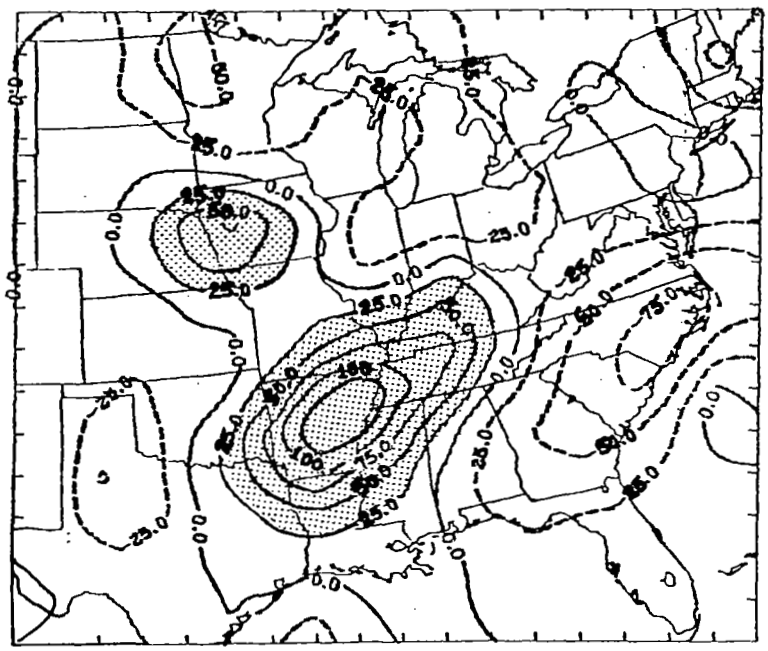

0600 GMT, 25 April

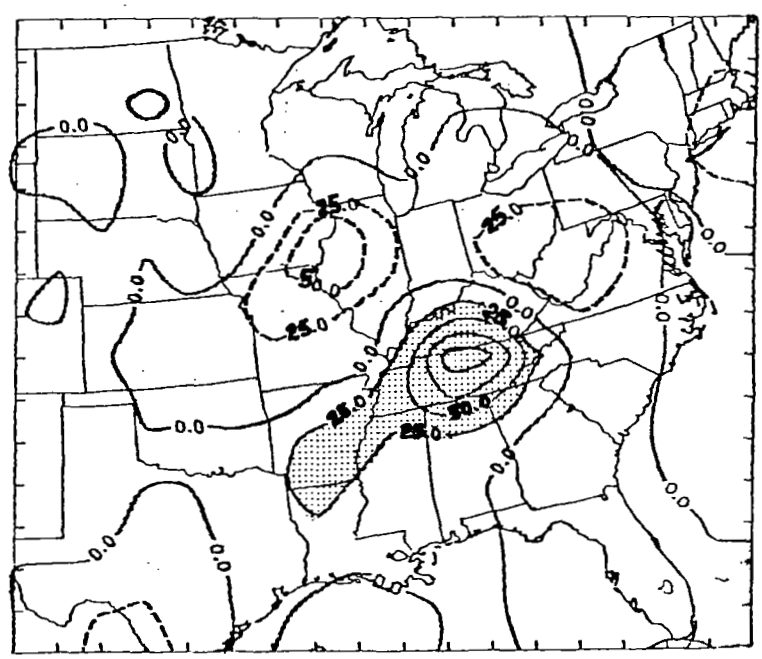

1200 GMT, 25 April

c. Rate of change of parcel kinetic energy $(\frac{d(KE)}{dt})$ (ergs g^{-1} s^{-1}). Values greater than 25 are shaded.

Fig. 32. (Continued)

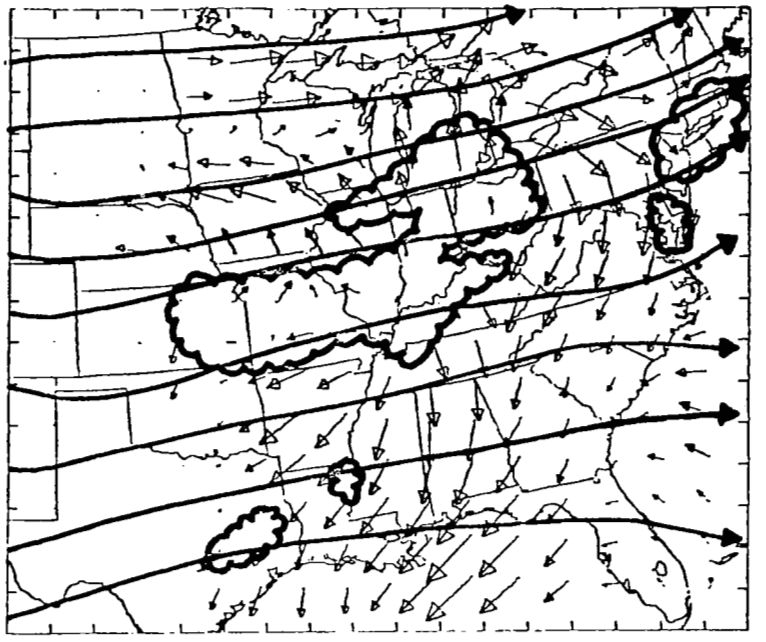

0600 GMT, 24 April

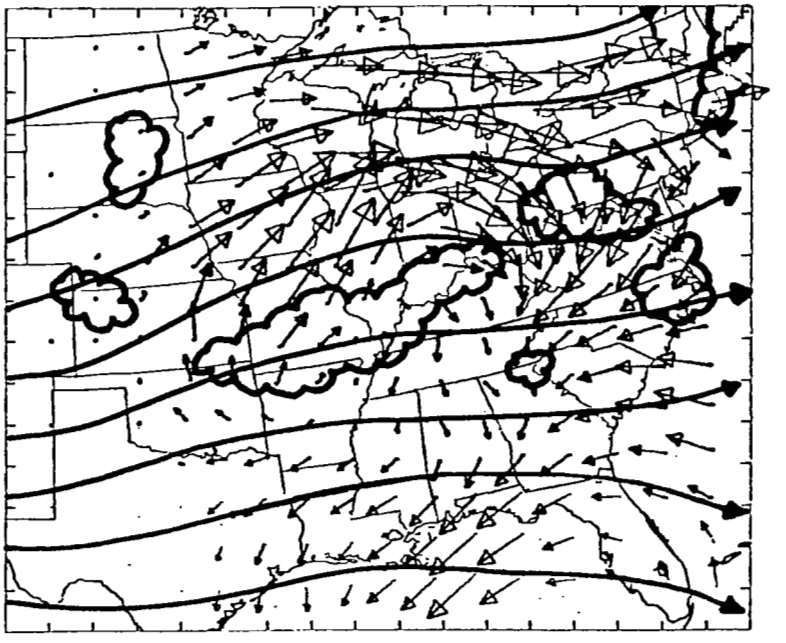

1200 GMT, 24 April

a. Horizontal acceleration vector fields (10^{-5} m s^{-2}) ($\rightarrow$=50 x 10^{-5} m s^{-2}). Convection is scalloped and actual wind streamlines are superimposed.

Fig. 33. Same as Fig. 29 except for 300 mb.

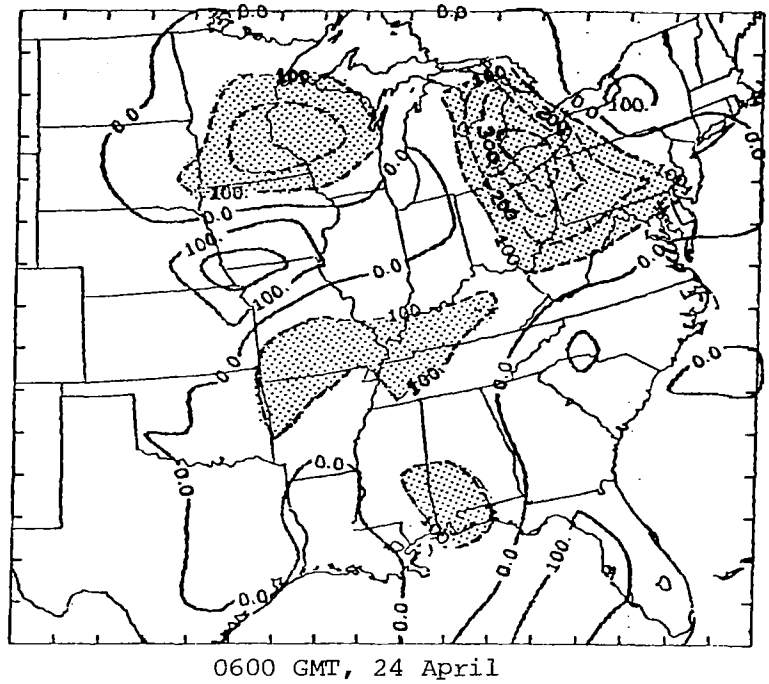

0600 GMT, 24 April

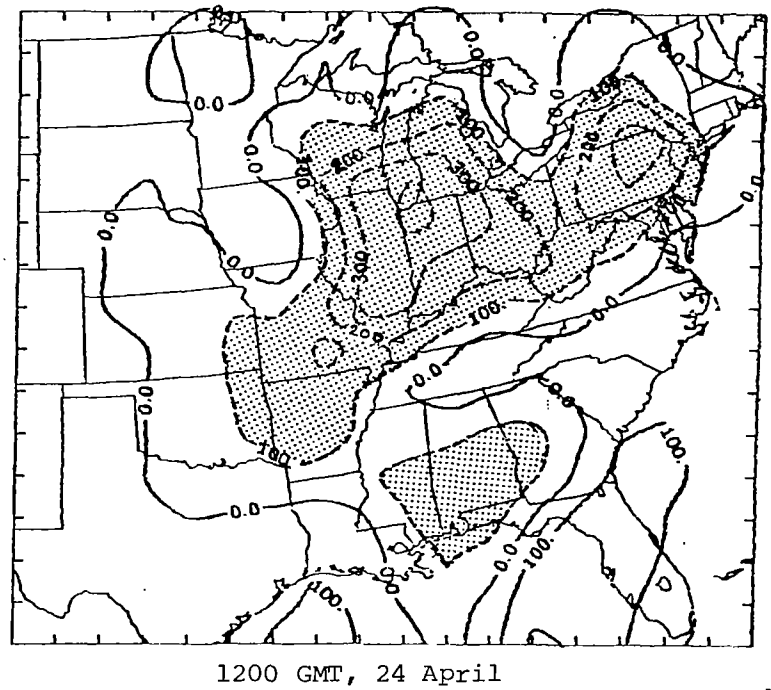

1200 GMT, 24 April

b. Horizontal curl of acceleration vector fields in (a) (10^{-11} s^{-2}). Values greater than 100 are shaded.

Fig. 33. (Continued)

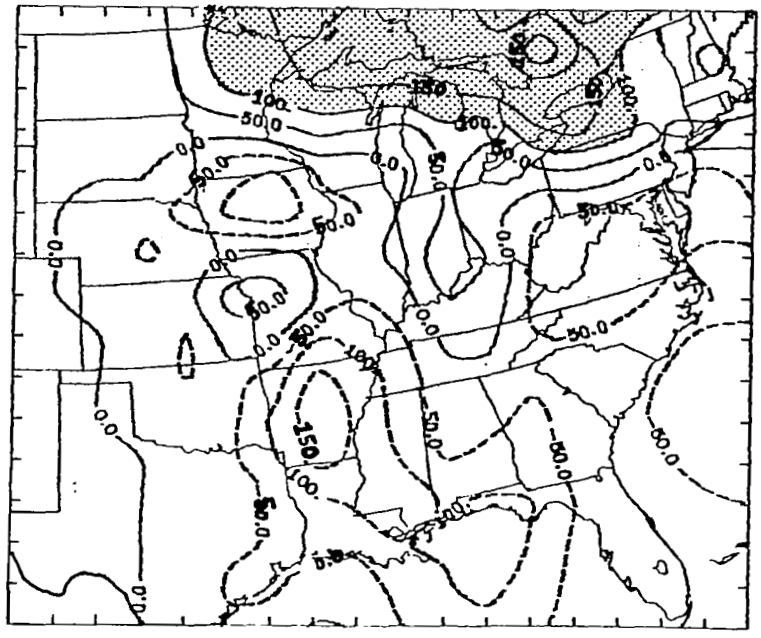

0600 GMT, 24 April

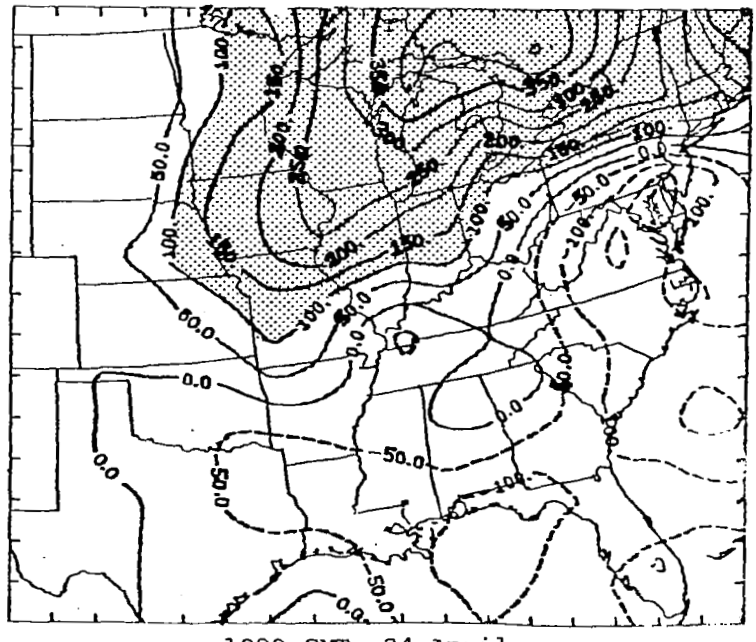

1200 GMT, 24 April

c. Rate of change of parcel kinetic energy ($\frac{d(KE)}{dt}$)(ergs g^{-1} s^{-1}). Values greater than 100 are shaded.

Fig. 33. (Continued)

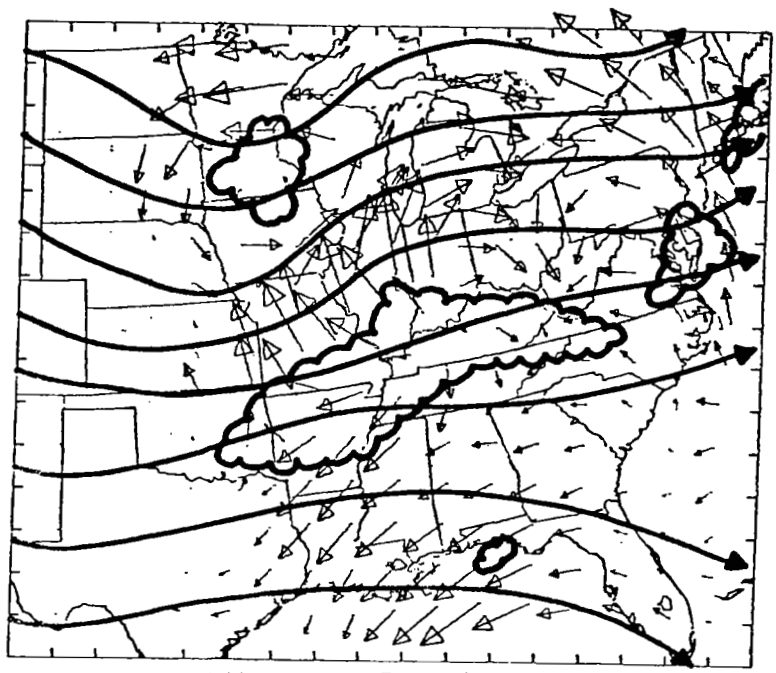

0600 GMT, 25 April

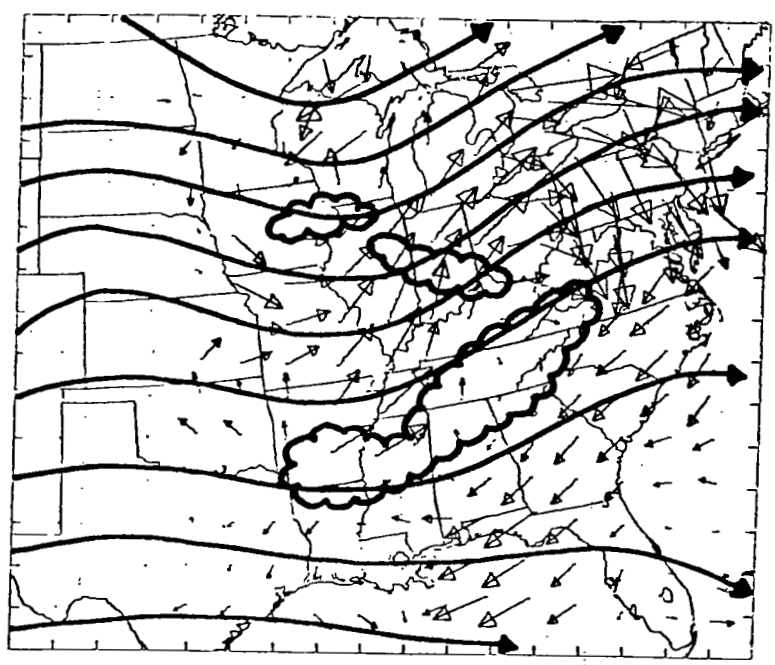

1200 GMT, 25 April

a. Horizontal acceleration vector fields (10^{-5} m s^{-2}) (→=50 x 10^{-5} m s^{-2}). Convection is scalloped and actual wind streamlines are superimposed.

Fig. 34. Same as Fig. 30 except for 300 mb.

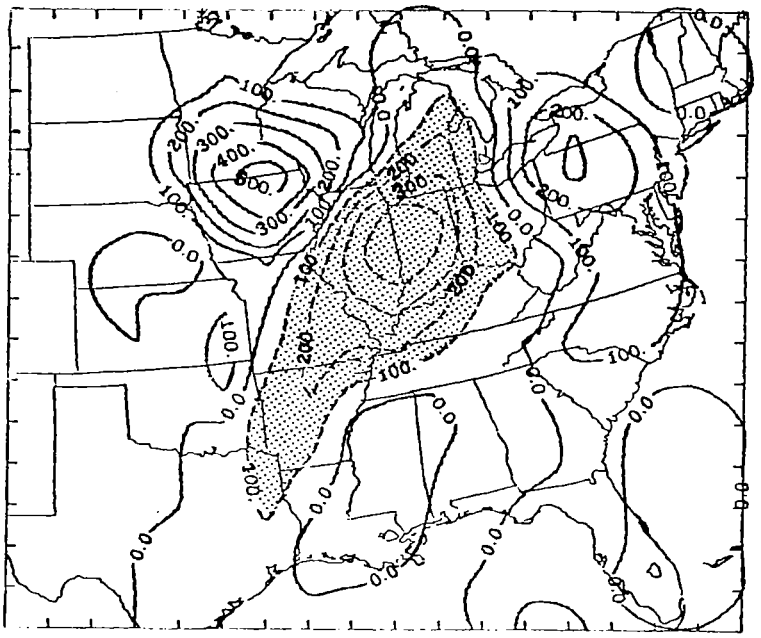

0600 GMT, 25 April

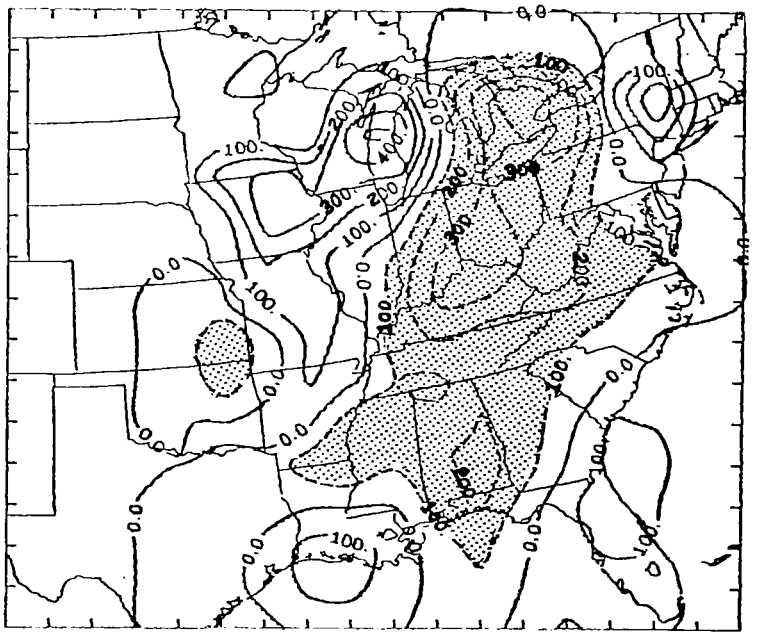

1200 GMT, 25 April

b. Horizontal curl of acceleration vector fields in (a) (10^{-11} s^{-2}). Values greater than 100 are shaded.

Fig. 34. (Continued)

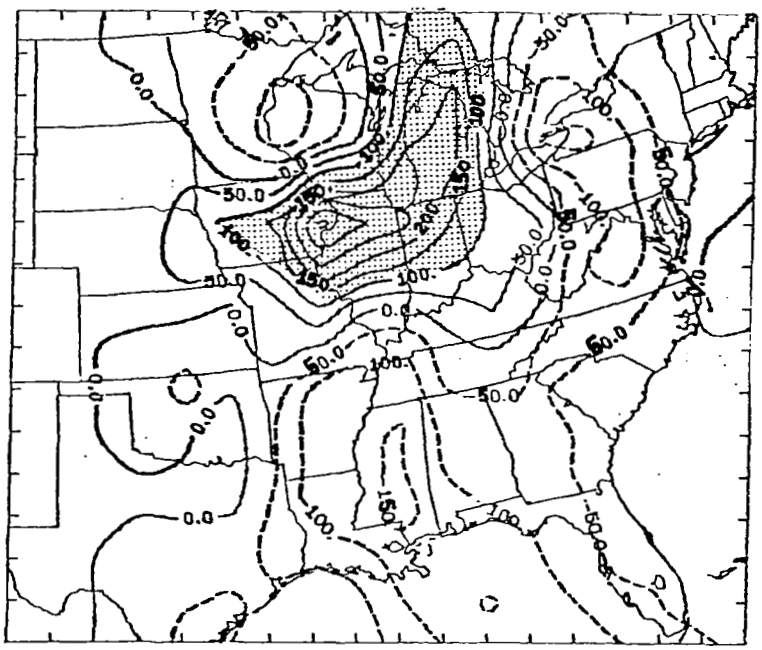

0600 GMT, 25 April

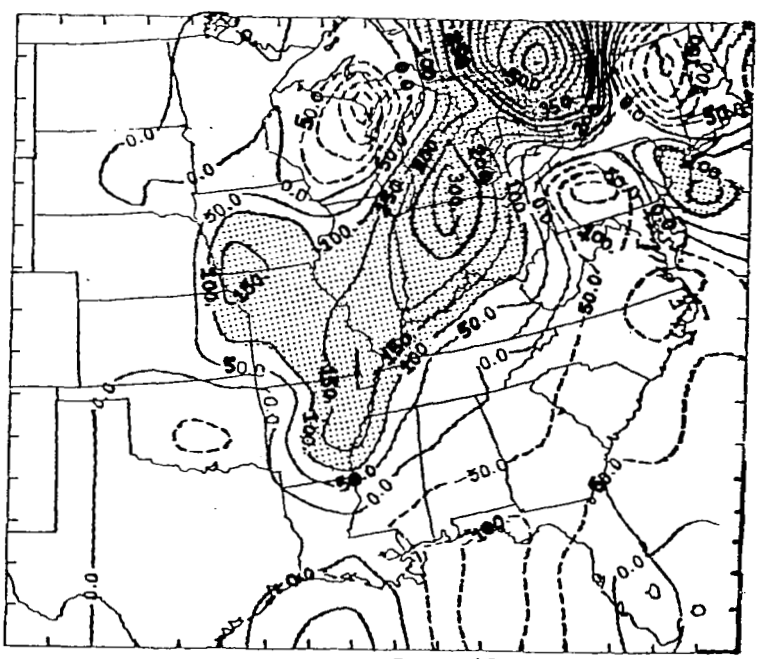

1200 GMT, 25 April

c. Rate of change of parcel kinetic energy $(\frac{d(KE)}{dt})$ (ergs g^{-1} s^{-1}). Values greater than 100 are shaded.

Fig. 34. (Continued)

horizontal acceleration vector fields (10^{-5} m s^{-2}) at 900 mb, 600 mb, and 300 mb, respectively. Each figure pair presents results for the first and last two consecutive times of AVE IV used in trajectory calculations since these periods correspond to the development and movement of severe storm Systems A and E. Convective activity is scalloped in each chart and the magnitude of each acceleration vector is proportional to its length (the length between tick marks on the borders, one grid distance, corresponds to 50 x 10^{-5} m s^{-2}).

These acceleration vector fields reveal remarkably well-defined systems including cyclonic and anticyclonic rotation centers and zones of acceleration maxima and minima, ($>|10^{-4}|$m s^{-2}) some of which show definite relationships to the convective activity. Since these horizontal accelerations represent net forces per unit mass acting on the synoptic-scale flow, changes in the flow characteristics (divergence, vorticity, or air speed and direction) are occurring.

In considering more closely the relationships between the circulation patterns of horizontal accelerations and the two major convective systems in the center of the network, cyclonic areas or centers of rotation can be qualitatively seen "over" the thunderstorms at both the 900- and 600-mb levels (see figure pairs 29a-30a and 31a-32a). At the 300 mb level, Figs. 33a and 34a show anticyclonic rotation over the storms.

A more objective analysis of these circulation patterns and a dynamic understanding of their relationships to convective activity is accomplished by taking the horizontal curl of the vector acceleration fields. After carrying out this operation, analyses of the results are shown directly after each of the acceleration fields (in units of 10^{-11} s^{-2}) in figure pairs 29b-30b, 31b-32b, and 33b-34b for the 900-, 600-, and 300-mb levels, respectively. All positive areas ($\propto$ convergence) greater than 50 x 10^{-11} s^{-2} are shaded in Figs. 29b-32b and negative areas ($\propto$ divergence) less than -100 x 10^{-11} s^{-2} are shaded in Figs. 33b and 34b to clearly show low- and mid-level convergence and divergence aloft.

These scalar fields represent $\frac{d\zeta}{dt}$ where, for synoptic-scale flow, positive (negative) vorticity tendencies are created mostly by convergence (divergence) (see Read and Scoggins (1977) for spatial fields of the divergence term in (8)). At the 900- and 600-mb levels, positive centers ($\propto$ convergence) are closely associated with the superimposed MDR observation of convection, while at 300 mb large negative values ($\propto$ divergence) were calculated over the intense convective activity. The reverse pattern is generally observed outside precipitation. However, the exact contribution of the turbulent frictional force to the acceleration vector cannot be determined here, although the momentum exchange between convective systems and the environment is large (Fuelberg, 1977 and Read and Scoggins, 1977) and, as seen later, alters the existing synoptic-scale acceleration field around the storms.

The average vertical profiles (from all AVE IV periods) of $\{\hat{k} \cdot (\vec{V}_p \times \frac{d\vec{V}}{dt})\}$ are shown in Fig. 35 as a function of pressure and MDR category and reveal that more intense thunderstorm activity occurs with increasingly larger positive values ($\propto$ convergence) in the lower and middle troposphere while large divergence (negative values) occurred above 400 mb. Very small values were computed in "no precipitation" areas.

When net forces act upon air parcels, work is performed and energy transformation occurs. Of particular interest in the atmosphere is the development of kinetic energy within the various size circulation systems.

The rate of change of horizontal kinetic energy following an air parcel can be measured from trajectory calculations by simply measuring $d(\frac{|\vec{V}^2|}{2})/dt \simeq \Delta(\frac{|\vec{V}^2|}{2})/\Delta t$. From a Langrangian point of view, horizontal kinetic energy changes occur when the net horizontal accelerations ($\frac{d\vec{V}}{dt}$ in Figs. 29a-34a), acting upon air parcels, have components along the velocity vectors. Interpretation of the results may be obtained from (9) where parcels change their horizontal kinetic energy during cross-contour flow and from kinetic energy imparted to or removed from the synoptic flow through "scale interaction". The last term in (9) may, in the vicinity of thunderstorms, be important in determining d(KE)/dt.

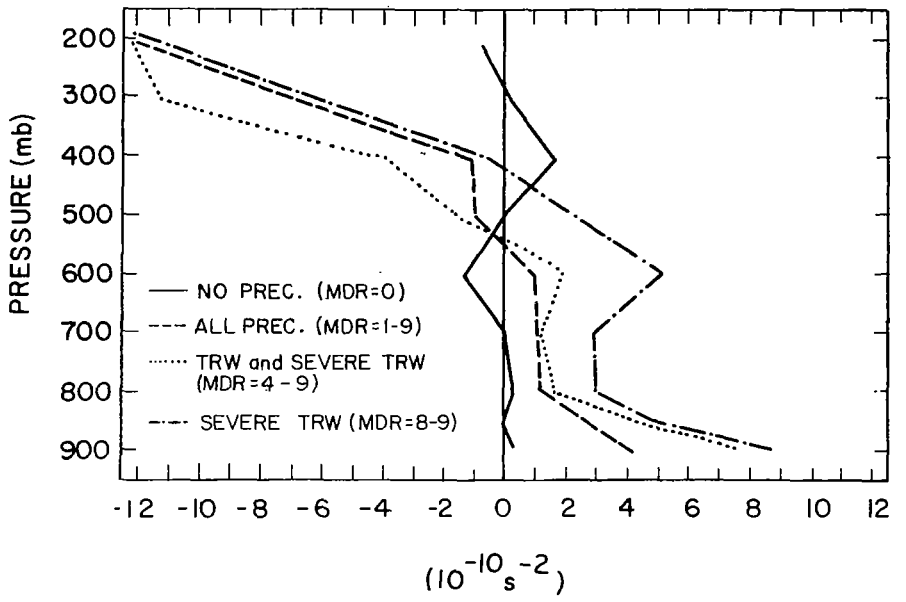

Fig. 35. Average profiles of $\{\hat{k} \cdot (\vec{V}_p \times \frac{d\vec{V}}{dt})\}$ as a function of pressure and MDR coded precipitation intensity. (Maximum MDR value was assigned to a grid point within 1/2 grid distance (≈80 km) from MDR 3-h composite charts).

Figure 36 presents the average vertical profiles (from all AVE IV time periods) of the rate of change of parcel horizontal kinetic energy (ergs $g^{-1}s^{-1}$) plotted as a function of pressure and MDR coded precipitation intensity. In precipitation areas, increasing KE is seen from 900 to 400 mb reaching a maximum about 600 mb, while large negative d(KE)/dt occurs above 400 mb. Small decreasing parcel KE was measured outside precipitation areas. Also, more intense convective activity was accompanied by larger $\frac{d(KE)}{dt}$ values (60 ergs $g^{-1}s^{-1}$ at 600 mb with severe thunderstorms) in the mid-troposphere and larger negative $\frac{d(KE)}{dt}$ values (-70 ergs $g^{-1}s^{-1}$ at 200 mb with severe thunderstorms) in the upper troposphere. Similar results were obtained by Fuelberg and Scoggins (1977) and Fuelberg (1977) where they actually calculated the terms in (9). They reported that the large positive

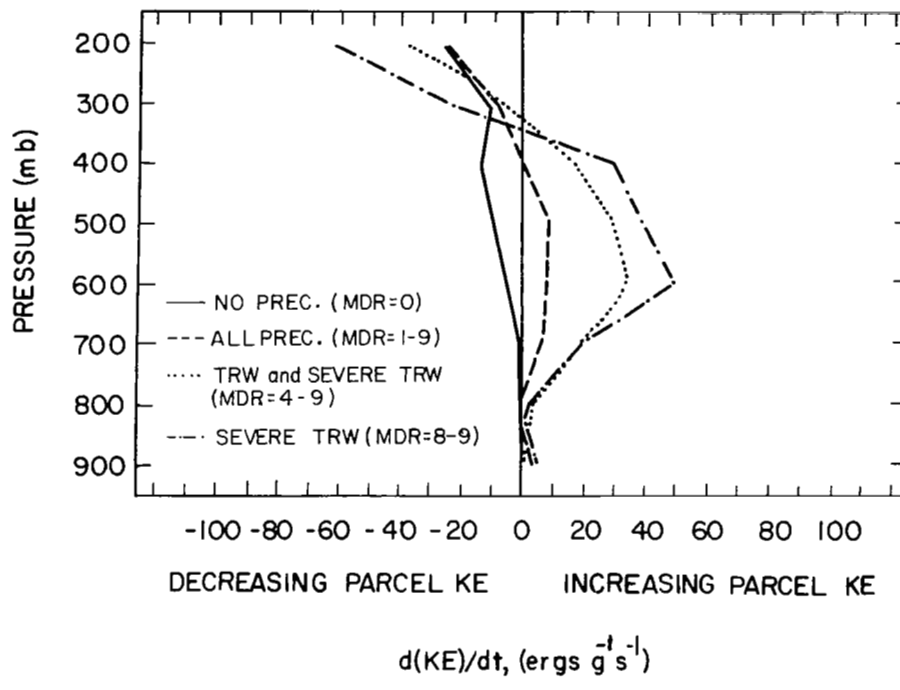

Fig. 36. Average profiles of d(KE)/dt as a function of pressure and MDR coded precipitation intensity. (Maximum MDR value was assigned to a grid point within 1/2 grid distance (≈80 km) from MDR 3-h composite charts).

$\frac{d(KE)}{dt}$ in the mid-troposphere was primarily created by the $\vec{V}\cdot\vec{F}$ term since the cross-contour flow was small.

The three pairs of Figs. 29c-30c, 31c-32c, and 33c-34c show the spatial fields of $\frac{d(KE)}{dt}$ (ergs $g^{-1}s^{-1}$) at 900 mb, 600 mb, and 300 mb, respectively. Positive $\frac{d(KE)}{dt}$ areas greater than 20, 25, and 100 ergs $g^{-1}s^{-1}$ are shaded in each of the three figure pairs.

Similar to results shown by Fuelberg (1977), generation of KE in excess of 75 ergs $g^{-1}s^{-1}$ was calculated at the 600-mb level immediately over each of the storm Systems A and E in Figs. 31c and 32c, indicating the importance of thunderstorm-environment interactions in increasing parcel KE in this region. However, large positive centers were also calculated at 900 mb (values >40 ergs $g^{-1}s^{-1}$) and 300 mb (values

>300 ergs $g^{-1}s^{-1}$) slightly southeast and northwest of these thunderstorm areas in figure pairs 29c-30c and 33c-34c, respectively. This vertical orientation of increasing parcel KE centers suggests an axis of maximum values that slopes northwestward over the thunderstorm areas from about 400 km ahead at 900 mb to directly over the storms at 600 mb (where Fig. 36 shows maximum KE production), to 400 km behind the activity at 300 mb. Therefore, decreasing parcel KE was calculated directly over the area of severe convection in the upper troposphere above 300 mb and near zero production occurred close to the ground in the immediate storm area.

This three-dimensional configuration of kinetic energy production and dissipation is necessary for the maintenance of the large scale vertical circulation that releases potential instability and helps maintain the thunderstorms. Consider the acceleration fields in Figs. 29a-34a where the actual wind streamlines have been superimposed at each level. Over the thunderstorm systems A and E, cyclonic circulation (positive curl of $d\vec{V}/dt$) of the acceleration vectors can be seen in the lower troposphere (Figs. 29a-32a), while anticyclonic circulation (negative curl of $d\vec{V}/dt$) of the acceleration vectors occurs at 300 mb (Figs. 33a and 34a). As explained, this acceleration pattern produces low-level upward vertical velocities and negative NVD's (see Figs. 15b, 16b, 21b, and 22b) which maintain the squall line. Since the actual wind streamlines generally point west to east over the storm systems at all levels, positive (negative) d(KE)/dt occurs in the southern (northern) part of the cyclonic acceleration centers where the acceleration vectors have a component along (against) the direction of the streamlines or wind vectors. The reverse occurs in the anticyclonic acceleration centers so that the observed pattern of d(KE)/dt in Figs. 29c-34c is explained.

The turbulent frictional force is important in the convective storm environment in that it contributes to the net horizontal acceleration in (1), especially in the mid troposphere directly over the storms. Since the positive d(KE)/dt over the thunderstorms in the middle troposphere (Figs. 31c and 32c) is primarily caused by the term $\vec{V}\cdot\vec{F}$ in (9), the turbulent frictional force contributes significantly to the horizontal vector acceleration field to produce larger positive

curl and larger mid-level convergence. This convergence further enhances the macroscale vertical circulation by increasing the upward vertical velocities over the squall line and acts as a "self-propagating" mechanism for the thunderstorm systems.

The centers of positive d(KE)/dt are frequently regions of developing wind maxima. As a result, the commonly observed low-, mid-, and upper-level jet zones associated with severe convective systems are also partially explained above (see Figs. 6c, 7c, 12c, and 13c for wind jet maxima associated with systems A and E). In addition, the diabatic heating calculated in the middle- and upper-troposphere (Figs. 26 and 27) over the thunderstorms further increases the large-scale horizontal temperature gradient and enhances parcel KE and jet stream development (Ninomiya, 1971b). The accelerations, created indirectly by diabatic heating of the synoptic flow, add to the already increasing parcel KE to further strengthen the large-scale vertical velocity field since the cyclonic "circulation" of the acceleration field (or convergence) is increased and extends as high as 400 mb (see Fig. 35), producing larger negative NVD values. This process also acts as a "self-propagating" mechanism for the thunderstorm system but the macroscale must still supply potential instability into the path of the storms through the differential advection of moisture and heat shown in the trajectory plots.

f. Temporal and spatial cross-section analysis of a severe area of thunderstorms (System E)

This section consists of a specific case study analysis of the development and movement of severe thunderstorm System E that spawned the Neosho tornado and was accompanied by over 30 reports of severe weather at the surface.

Figures 37 and 38 are the SMS infrared satellite pictures at 0000 GMT, 25 April 1975 and 0600 GMT, 25 April 1975, respectively, showing the development and movement of this storm system (from Whitney, 1977). Concurrent severe storm reports at the surface and the synoptic features of jet streams and surface fronts are superimposed. Severe storm symbols are identified in the figure inset.

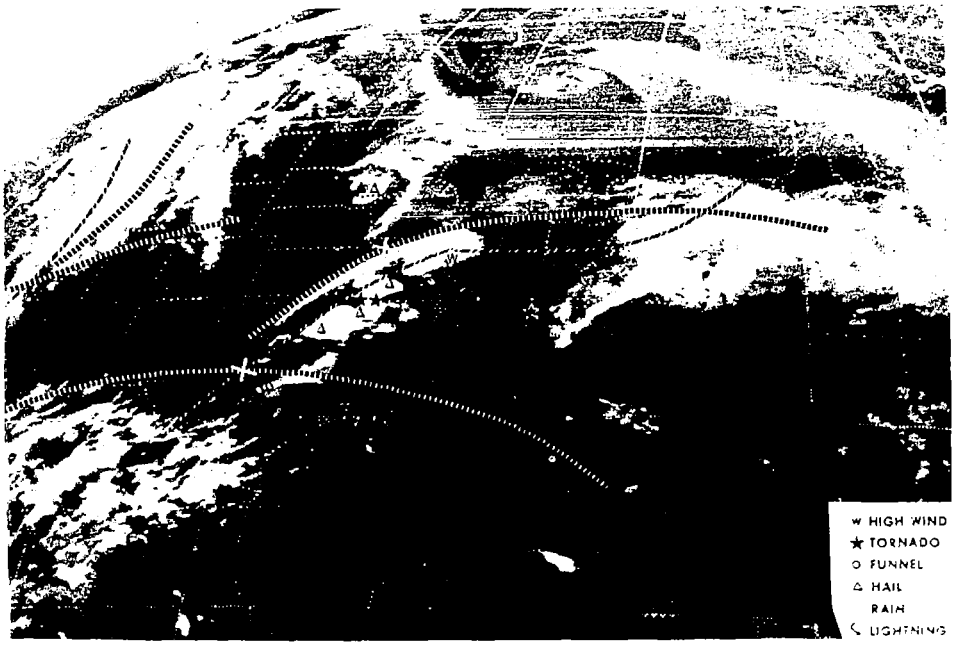

Fig. 37. SMS infrared picture at 0000 GMT, 25 April 1975 showing concurrent severe storms and the synoptic features of jet streams and surface fronts. Severe storm symbols are shown in the inset. The axes of the jet streams are shown as the bold dashed lines with associated wind maxima appearing as heavy X's. The speed of the subtropical wind maxima is given in knots. Surface fronts are shown as thin candy striped lines. The dotted lines are the geographical and political grid overlay. The Neosho tornado occurred at 0040 GMT. (from Whitney, 1977)

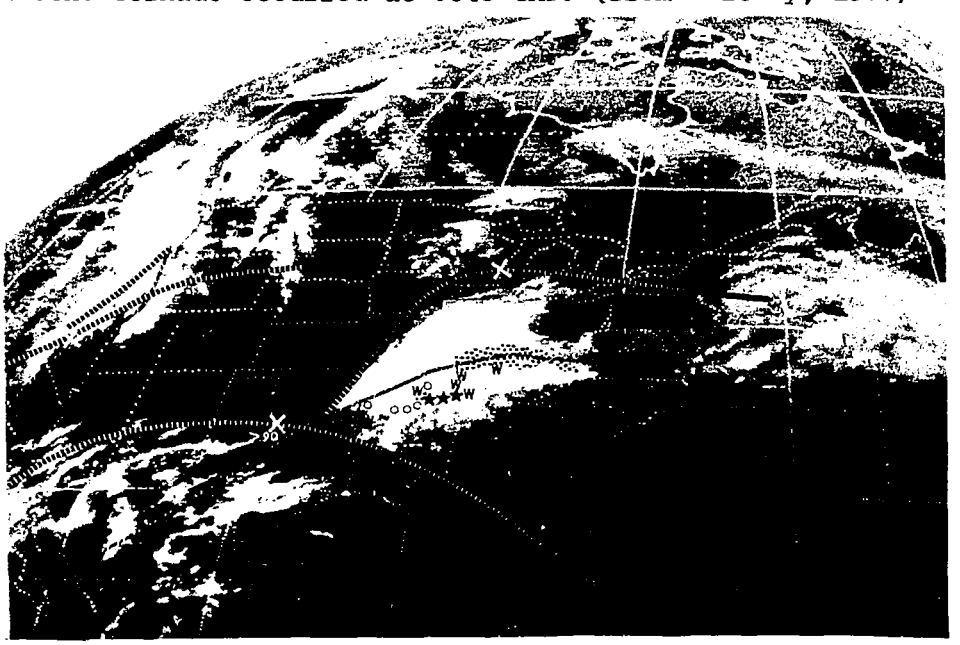

Fig. 38. Same as Fig. 37 except for 0600 GMT, 25 April 1975.

By focusing on this specific storm, many of the previously discussed relationships between convective storms and their synoptic-scale environment can be clarified. Time cross-section analyses are presented to show the temporal variation in atmospheric structure that was associated with severe thunderstorm formation at 0000 GMT, 25 April in Fig. 37. Results from trajectory calculations reveal the hydrodynamic and thermodynamic processes responsible for the structural changes that accompanied storm development. The three-dimensional spatial structure of the atmosphere, at the height of the storm system's intensity (0600 GMT, 25 April in Fig. 38), was analyzed using space cross-sections through the storm area. This produced a detailed view of the instantaneous atmospheric structure in the immediate storm environment. Results from trajectory calculations revealed the processes producing changes in this structure as well as the feedback and scale-interaction processes previously discussed.

Figures 39a, 39b, and 39c are separate time cross-sections of NVD (mb/3h), $\frac{d\theta}{dt}$ (^{o}C/3h), and $\frac{d(KE)}{dt}$(ergs $g^{-1}s^{-1}$) including the AVE IV periods between 1800 GMT (or Z), 24 April and 1200 GMT, 25 April. Trajectory data at each time period and vertical pressure level in the charts are average grid point values of the variable inside the indicated grid boxes surrounding System E in Figs. 9a-13a.

Figure 39a shows that upward NVD's occurred, within the storm environment, throughout the storm's development period at levels below 800 mb. The planetary boundary layer was therefore undergoing dynamic lifting. However, before the system organized into a long line of severe thunderstorms, subsidence was occurring between 800 and 200 mb, reaching a maximum value of 25 mb/3h at 500 mb at 2100 GMT, 24 April. By suppressing convective cloud development, this feature may have been essential to the subsequent formation of the line of severe thunderstorms 3 h later. At 0000 GMT, upward NVD's extended throughout the entire atmosphere coincident with the storm organization and severe weather occurrence (the Neosho tornado was on the ground just after 0000 GMT. This pattern intensified

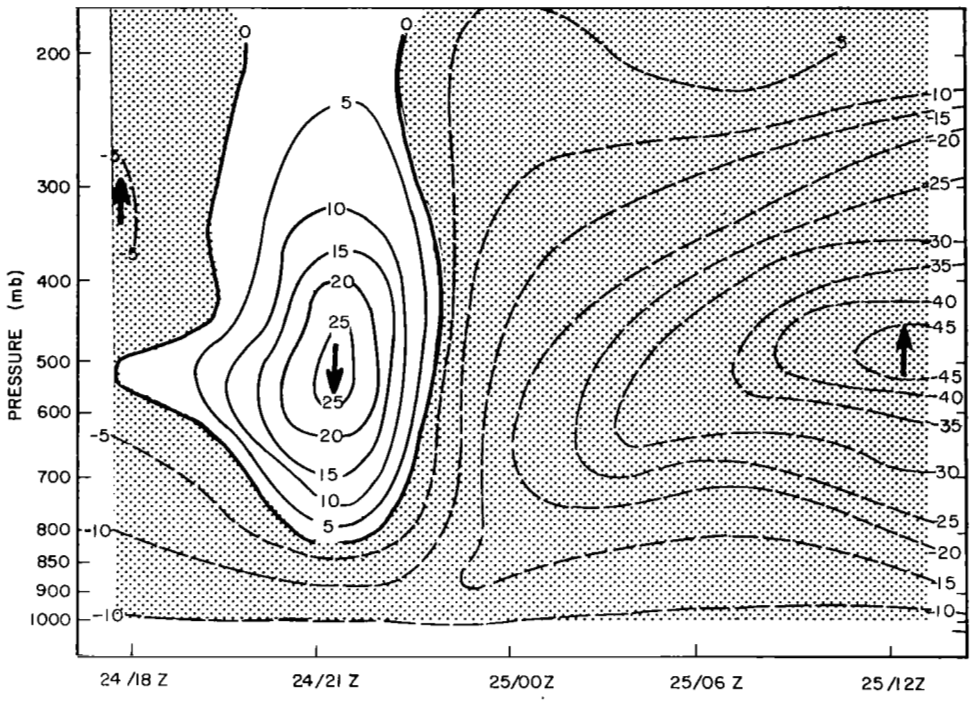

a. Net vertical displacements (NVD) (mb/3h) (upwards shaded).

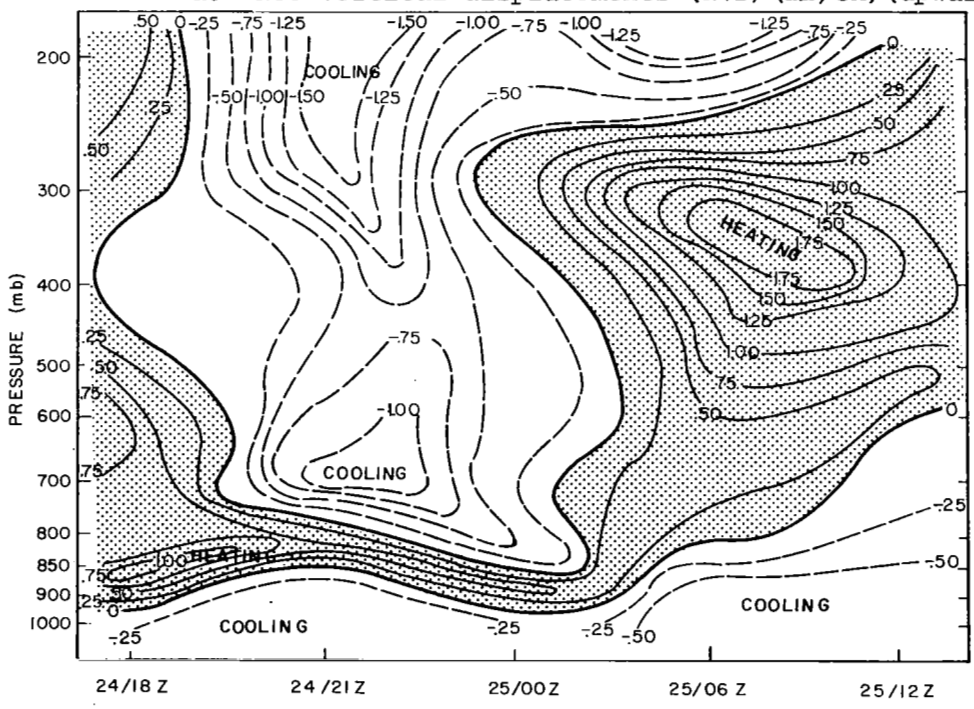

b. $d\theta/dt$ ($^{o}C/3h$) (heating shaded).

Fig. 39. Time cross-sections of NVD, $\frac{d\theta}{dt}$, and $\frac{d(KE)}{dt}$ for System E between 1800 GMT (Z), 24 April and 1200 GMT (Z), 25 April.

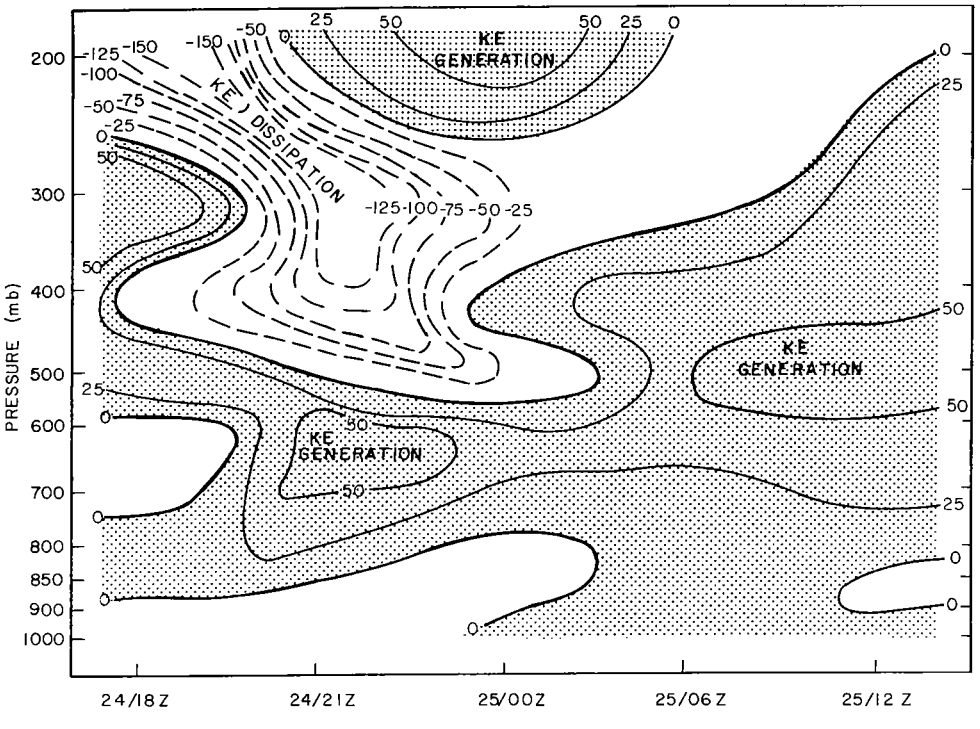

c. d(KE)/dt (ergs $g^{-1}s^{-1}$) (generation shaded).

Fig. 39. (Continued)

in time and by 1200 GMT upward NVD's less than -45 mb/3h were occurring, on the average, within the synoptic-scale storm environment.

The diabatic effects during the storms life are shown in Fig. 39b. The important features to notice between 1800 GMT and 0000 GMT are the diabatic warming (>1°C/3h) occurring in a 100-mb thick zone within the boundary layer and the cooling (<-1°C/3h) taking place immediately above the warming zone that extended to 200 mb. This pattern is extremely consistent with the NVD distribution in Fig. 39a in that upward displacements in the boundary layer were causing both stratiform and cumuliform cloud formation, releasing latent heat. In the mid- and upper-troposphere, existing clouds were evaporating under subsiding conditions, creating diabatic cooling.

This distribution of heating below and cooling aloft, from diabatic processes, added to the destabilizing boundary layer lifting processes already occurring to create smaller static stability (smaller NBE and larger PBE) prior to the thunderstorm system organization. After 0000 GMT strong heating (>1.5°C/3h) occurred in the mid- and upper-troposphere as the realized latent heat within the organized thunderstorm system "warmed" the synoptic flow. Strong diabatic cooling calculated above 300 mb and below 800 mb was associated with radiational cooling over the storm's cirrus shields (see Figs. 28 and 38) and precipitation evaporation below cloud bases, respectively.

Parcel kinetic energy changes (ergs $g^{-1}s^{-1}$) during the development of System E are shown in Fig. 39c where generation has been shaded. Between 1800 GMT and 0000 GMT parcel KE generation (>50 ergs $g^{-1}s^{-1}$) occurred between 850 and 500 mb over the developing storm system, while above 500 mb very strong parcel KE dissipation (<-125 ergs $g^{-1}s^{-1}$) occurred. This pattern indicated that the synoptic flow was highly accelerated during the early stages of the storm system formation with high momentum air aloft descending into the mid- and lower-troposphere within the subsiding region in Fig. 39a. For given air parcels, the resulting accelerations created flow toward lower pressure (or heights) (negative $\vec{V}\cdot\vec{\nabla}\phi$ and KE production from (9)) in the layer from 850 to 500 mb, while flow toward higher pressure resulted in KE dissipation

aloft. The vector orientation of the acceleration fields must have also forced low-level convergence (from flow toward lower pressure and $\frac{d\zeta}{dt}>0$) and upper-level divergence (flow toward higher pressure and $\frac{d\zeta}{dt}<0$) over the developing storm since strong upward vertical velocity and negative NVD's quickly formed at 0000 GMT in place of strong subsidence at 2100 GMT.

After 0000 GMT KE production increased throughout the entire low- and mid-troposphere with weak KE dissipation present above 300 mb. This pattern resembles that found in Fig. 36 with KE production in the middle troposphere resulting from momentum exchange between the convective clouds and the environment, and the increased baroclinity in this region created by the diabatic heating seen in Fig. 39b. Cross-contour flow was very small in the middle troposphere as shown by Fuelberg (1977).

Figures 40a-40f are space cross-sections of various variables, including trajectory parameters, at 0600 GMT 25 April along the line XY of Fig. 12a. This line passes NW-SE through the severe weather areas containing reported tornadoes (see Fig. 38) at the location marked "severe thunderstorms" along the bottom of each chart.

Figures 40a and 40b are the cross-sections of relative humidity (values >50% shaded) and NVD (mb/3h with downward motion shaded), respectively. Of particular interest is the vertical protrusion of relative humidity values >50% extending out of the lower atmosphere into the mid- and upper-troposphere in the severe storm area. Otherwise, relative humidity was <40% at all levels above 700 mb while values exceeded 60% in the moist planetary boundary layer and reached 90% in the immediate storm area. The NVD cross-section partially explains this moisture distribution since very large upward NVD's (<-90 mb/3h) occurred over the storm and some water vapor was "drawn" aloft out of the planetary boundary layer (Scott and Scoggins, 1977). Both southeast and northwest of the convective activity, subsidence was occurring with NVD's >30 mb/3h in the middle troposphere. Within these subsiding areas, relative humidities were low and sometimes fell below 20% both ahead and behind the storm in the middle and

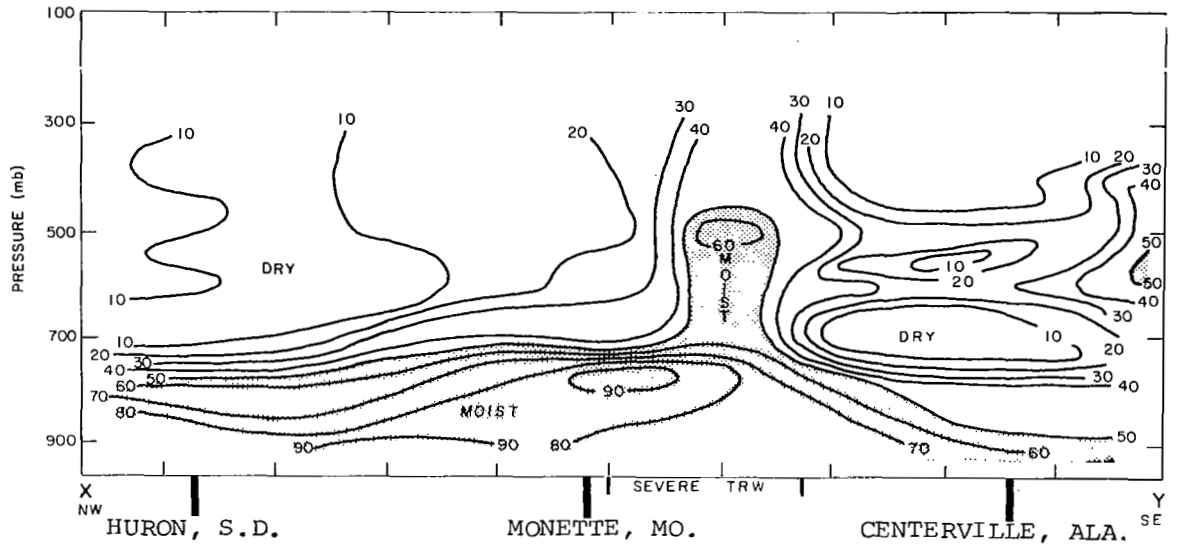

a. Relative humidity (values>50% shaded)

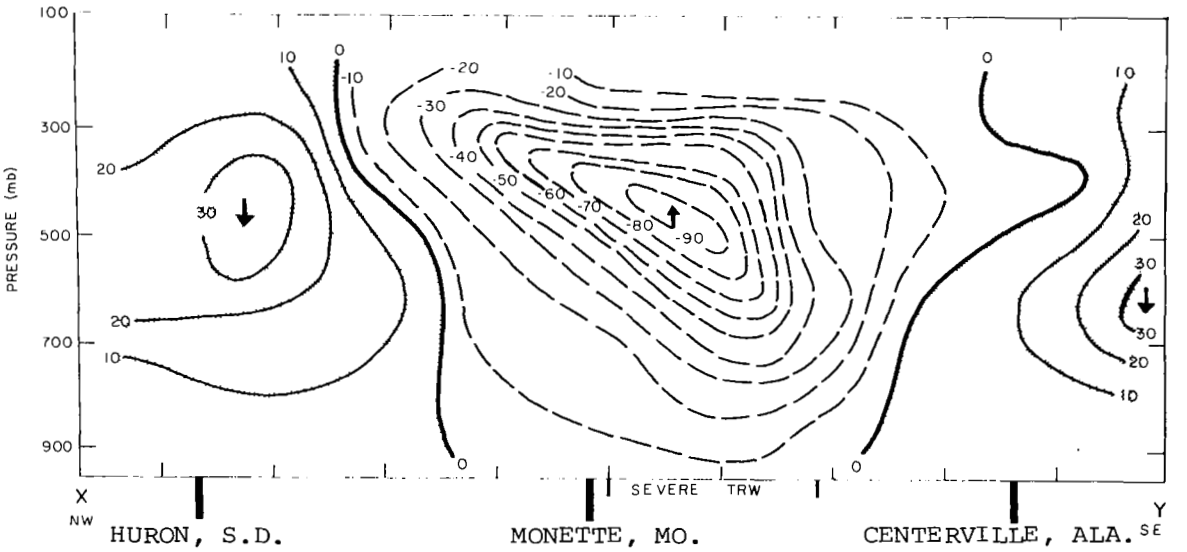

b. Net vertical displacements (NVD) (mb/3h with subsidence shaded)

Fig. 40. Space cross sections of various basic gridded variables and trajectory parameters at 0600 GMT, 25 April along the line XY of Fig. 12a (p.51) that passes through severe thunderstorm System E.

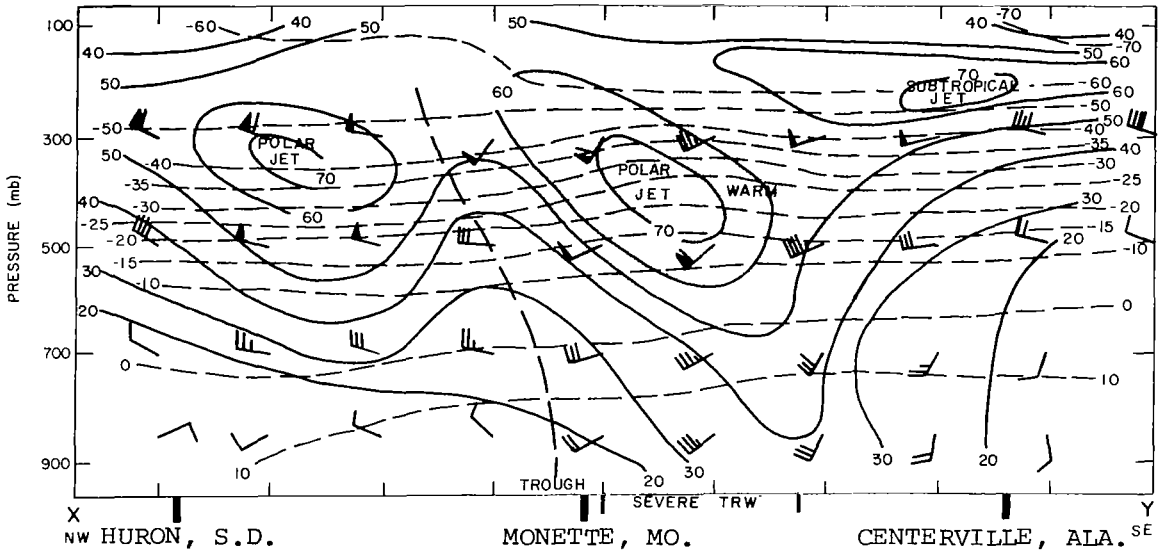

c. Vector wind and isotachs (kts) and temperature (°C).

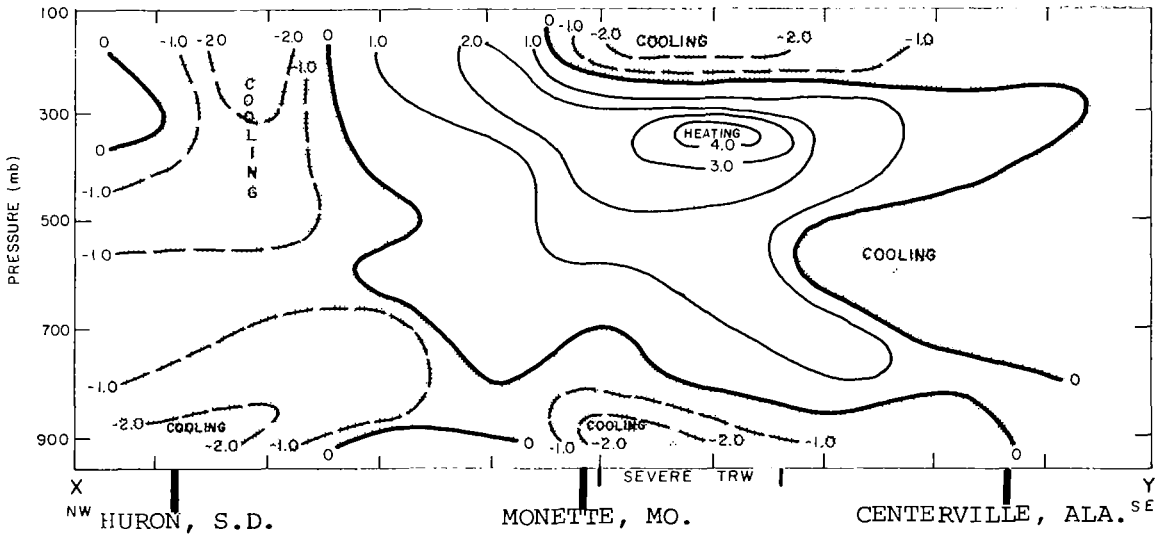

d. $d\theta/dt$ (°C/3h with cooling shaded).

Fig. 40. (Continued)

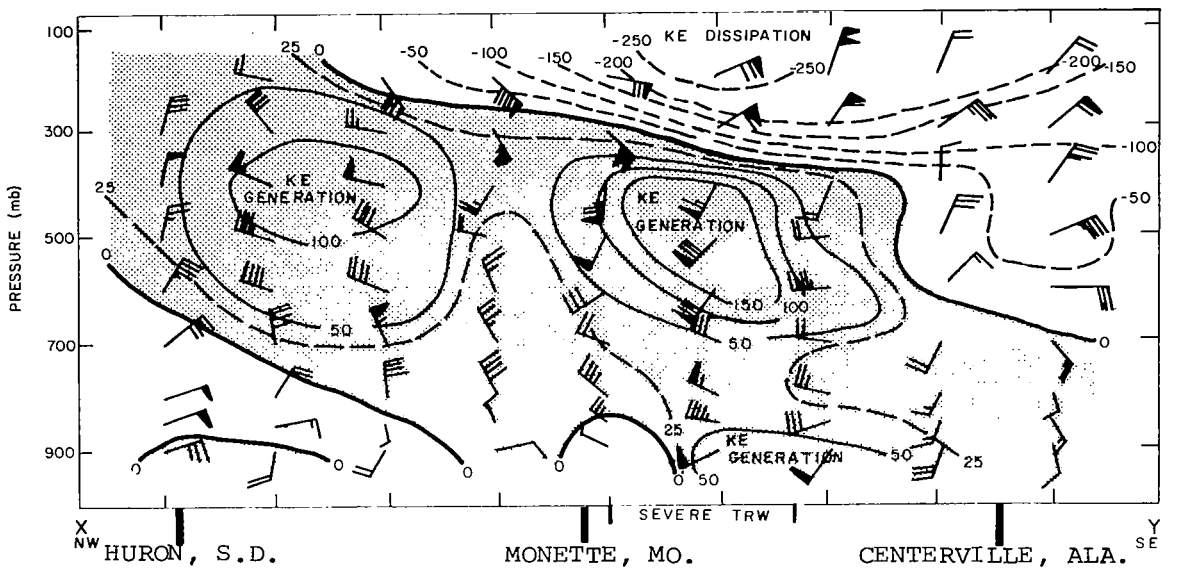

e. d(KE)/dt (ergs $g^{-1}s^{-1}$ with positive areas shaded) and horizontal vector accelerations plotted as wind vectors where 1 barb= $10 \times 10^{-5} m\ s^{-2}$.

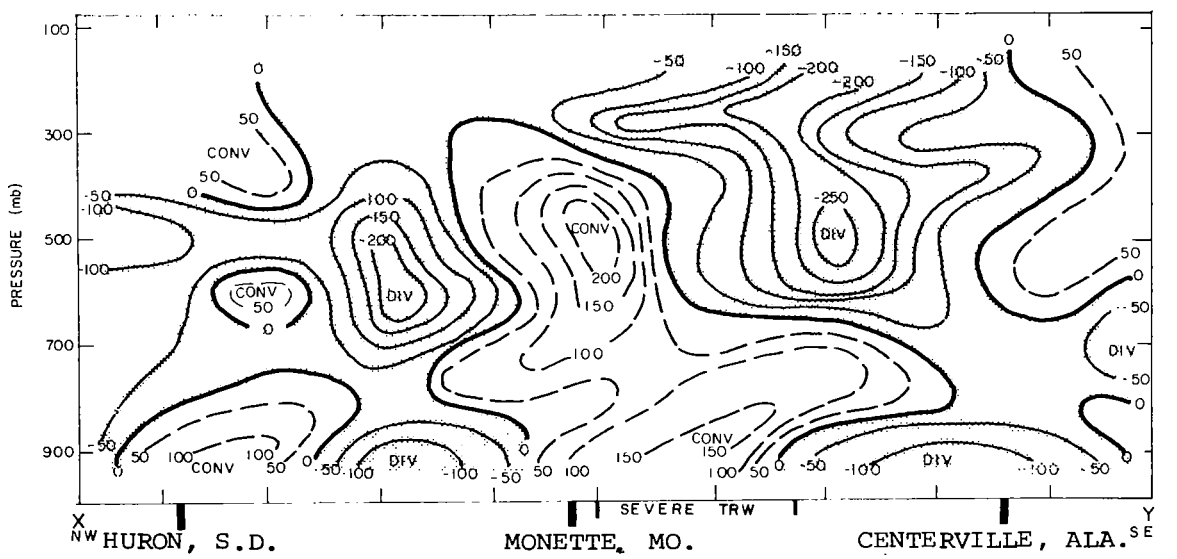

f. Horizontal curl of the acceleration vector field (in units $10^{-11}s^{-2}$ where negative is shaded) in Fig. 40e.

Fig. 40. (Continued)

upper-levels (Fig. 38 also shows the absence of high level clouds in these areas). These dry areas were positioned directly above the moist boundary layer air so that convective instability was large ahead and behind the storm system. As the large upward NVD field moved southeastward, the convective instability was released under dynamic lifting and stretching so that thunderstorm formation occurred and upper levels increased their environmental moisture content.

Figure 40c is the cross section of vector wind (in kts including isotach analysis) and temperature (°C), while Fig. 40d shows the diabatic heating ($d\theta/dt$ in °C/3h) distribution. A trough in the wind field was located just northwest of the storm area and sloped northwestward with height. Both ahead and behind the trough, wind speed maxima (>70 kts) identify the polar jet stream while the subtropical jet was located farther southeast and above the polar jet. All severe weather occurred between the southwesterly polar jet and subtropical jet as shown by Whitney (1977) (see Fig. 38). In addition, the temperature cross-section shows a weak baroclinic zone in the low- and mid-troposphere between the two polar jets. Of particular interest, however, is the warm wedge (lightly shaded) positioned southeastward of the southern polar jet above the 500-mb level. This relatively warm area is located directly over the thunderstorms and increases the atmospheric baroclinity northwest of the convection since the slope of the isotherm pattern with respect to pressure surfaces is increased. Therefore, the southern portion of the polar jet stream lies between the wind and thermal troughs and the thermal ridge.

The diabatic heating cross-section (Fig. 40d) suggests strongly that the warm zone was created mostly by diabatic warming since a zone of positive $d\theta/dt$ (>4°C/3h) lies directly over the thermal ridge. Since environmental relative humidities were <60% above 700 mb (Fig. 40a) within the convective storm area, latent heating within the mean synoptic-flow was non-existent so that the large diabatic heating and resulting thermal ridge formation was caused by turbulent eddy transfer of heat from the convective storms into the environmental flow at mid- and upper-levels. Radiational cooling (<-2°C/3h) over the cirrus shield (see Figs. 28 and 38) is also

seen in the cross-section at levels above 200 mb while, below 800 mb, evaporation of hydrometeors (and possibly some radiational cooling since it was nighttime) resulted in cooling exceeding -2°C/3h under the storm system. Boundary layer relative humidities were highest (>90%) directly under the storm area where evaporation was taking place. Both southeast and northwest of the thunderstorms, diabatic cooling was occurring in the subsiding air in Fig. 40b, possibly caused by cloud water evaporation after storm passage and weak nocturnal radiational cooling.

Figure 40e is the cross-section of d(KE)/dt (ergs $g^{-1}s^{-1}$ where generation is shaded) and the horizontal vector acceleration field ($d\vec{V}/dt$ plotted as wind vectors where 1 barb = 10 x 10^{-5} m s^{-2}). Figure 40f is the cross-section of the horizontal curl of the acceleration field in Fig. 40e {negative (positive) values $\propto$ divergence (convergence)}. The d(KE)/dt pattern can be interpreted physically since generation (dissipation) occurred when the superimposed acceleration vector had a component along (against) the corresponding wind vectors in Fig. 40c. Two centers of large d(KE)/dt production (>100 ergs $g^{-1}s^{-1}$) are located over the two polar wind jets in Fig. 40c where air parcels were accelerated (acceleration vectors were pointing in the same general direction as wind vectors) through the wind maxima. An axis of positive d(KE)/dt, as suggested earlier, was present in the storm vicinity that sloped from slightly ahead of the storm area at 900 mb to behind at 300 mb, with maximum generation (>150 ergs $g^{-1}s^{-1}$) present in the storm environment between 600 and 400 mb. Very strong negative d(KE)/dt (<-250 ergs $g^{-1}s^{-1}$) occurred over the severe thunderstorms above 300 mb where large acceleration vectors pointed west or southwest and actual wind flow was toward the northeast.

The sloping axis of positive d(KE)/dt over the storm area also lies along an axis of maximum southwest-northeast winds shown in the isotach analysis of Fig. 40c and explains, in part, the existence of low-, middle-, and upper-level wind jets frequently measured in the vicinity of severe thunderstorm systems. Moreover, this pattern is dynamically necessary if the synoptic scale is to maintain a favorable

dynamic lifting environment (low-level convergence and divergence aloft) for continued release of potential instability and thunderstorm formation. This follows from the argument given in the last section and is further explained as follows.

Given the strong southwesterly wind flow in the storm environment resulting from a vector acceleration field that points in the same general direction (excluding levels above 300 mb) as the vector wind field (producing positive d(KE)/dt and wind jet formation), the horizontal rotational field or curl of the vector winds should resemble closely that of the acceleration vectors. Since a trough in the wind field was located west of the storm area, the curl of the wind vectors is positive (cyclonic with positive relative vorticity) over the storm area. Therefore, the curl of the acceleration vectors in the storm vicinity is positive (cyclonic) below 300 mb as shown in Fig. 40f (also see Figs. 29a-32a). Since the horizontal curl of $d\vec{V}/dt$ is $\frac{d\zeta}{dt}$ (in units of 10^{-11} s^{-2} where positive areas are shaded), positive (negative) values are nearly equal to (f) times the velocity convergence (divergence) for synoptic-scale flow. The final result is an axis of maximum convergence (see Fig. 40f) that slopes from directly over the storm center at 900 mb to slightly behind at 400 mb. The upper troposphere is highly divergent under large anticyclonic rotation (negative $d\zeta/dt$) of the acceleration vectors and negative d(KE)/dt.

This pattern of horizontal wind divergence creates strong upward vertical velocities and NVD's (see Fig. 40b) over the storm which continuously releases the available buoyant energy (PBE) to maintain the convective storm system. After storm passage, the vector accelerations produce divergence throughout the entire troposphere (see Fig. 40f) resulting in downward vertical velocities and NVD's that suppress the release of potential instability.

The above discussion demonstrates the hydrodynamical processes produced by the synoptic-scale flow, in combination with existing convective activity that support development and maintenance of severe convective storm systems. The remaining question concerns the influences of the severe storms themselves on the synoptic circulations. The momentum and heat, exchanged between the storms and the environmental flow,

could conceivably add to or subtract from the dynamic control exerted by the synoptic flow over thunderstorm formation. However, these scale-interaction processes appear to augment rather than suppress the synoptic control in such a manner that the severe convective storm system actually "self-propagates" itself to a limited extent. This process amounts to an intensification of the kinematic-dynamic control exerted by the synoptic flow over thunderstorm development as described below.

Any accelerations that produce larger positive d(KE)/dt and resulting jet stream intensification along the positive d(KE)/dt axis that slopes over the storm system (see Fig. 40e) will result in larger positive curl (convergence) along the convergence axis. As a result, upward vertical velocities and NVD's are increased in the storm environment so that release of available instability is assured. If this process results from scale-interaction between the convective storms and the environmental flow, accelerations must be produced by sub-grid scale or turbulent processes that have large components along the existing vector wind field surrounding the convective storm system. These forces (per unit mass) result from momentum and heat exchange between the clouds and the immediate environmental flow around the storms and augment the synoptic-scale circulations that maintain the storm system.

Increasing baroclinity of the synoptic structure over the storm environment has already been shown to be directly related to large diabatic heating in the mid-troposphere (see Figs. 40c and 40d). This heating, resulting from net positive heat flux from cloud to environment, produced a thermal ridge over the storm area and increased the horizontal temperature gradient northwest of the storms. This feature accelerated the synoptic flow along the direction of the wind vectors, increasing the wind speed in the jets and the positive curl of the acceleration vectors ($\propto$ convergence) creating a stronger vertical circulation within the storm environment.

In addition, the large kinetic energy production at the synoptic scale (>75 ergs $g^{-1}s^{-1}$) over the storm area in the layer from 600

to 400 mb, has been shown by Fuelberg (1977) to result from kinetic energy transfer (or momentum exchange) from sub-grid scale systems (primarily convective activity) to the synoptic flow. The accelerations associated with the momentum exchange, together with those produced by diabatic heating, extend the zone of low-level convergence (and positive curl of $\frac{d\vec{V}}{dt}$) up to heights greater than 500 mb as seen in Figs. 35 and 40f. The magnitudes of upward vertical velocities and NVD's are therefore increased above those normally produced by the synoptic-scale system without convective activity. The overall effect is one in which the severe convective system "self propagates" itself as scale-interaction processes between the storms and the environment create accelerations in the synoptic flow that supplement the hydro- and thermo-dynamic processes responsible for continued convective cloud formation within the storm system itself.

5. CONCLUSIONS

Three-dimensional diagnostic trajectories have been used successfully to reveal some of the scale interactions that occur between convective storms and their environment using data from NASA's AVE IV Experiment. The availability of 3- and 6-h synoptic-scale data enabled temporal resolution of important systems and features that made this study possible.

Listed below are some of the conclusions drawn from the present research.

1) The existence of convective systems with good temporal and spatial continuity (identified using Manually Digitized Radar data) is related to the development and movement of short-wave (λ<1500 km) wind, height, and thermal perturbations embedded and moving within a zonal mid-tropospheric pattern. The convective storms are located ahead of these systems where horizontal advection of temperature and moisture supplies potential instability, resulting in small NBE and large PBE. Well-defined centers of upward vertical velocities and NVD's are associated with the release of available buoyant energy that results in convective storm formation.

2) The four-dimensional environmental flow pattern, relative to convective storm systems, shows that large upward air parcel movements (>50 mb/3h) occur only in the immediate vicinity of the convective clouds. The air undergoing strong lifting originates as potentially unstable low-level air (below 700 mb) that continuously moves toward and slowly rises (>20 mb/3h) into the storm path from southern and southwestern directions. Rapid destabilization of this air occurs when large vertical displacement and vertical stretching release the instability to produce new convective clouds. Low-level trajectory convergence and large upper-level trajectory divergence maintain the vertical circulation as air parcels pass through and around the storm environment.

3) Total derivatives of pressure (dp/dt or NVD), potential temperature (θ), and vector wind ($d\vec{V}/dt$) from the trajectories can successfully define the thermo- and hydrodynamical processes that lead

to changes in atmospheric structure before, during, and after convective storm formation. During periods before storm formation, the total derivatives appear to result primarily from processes occurring in the mean synoptic flow leading to a favorable environment for storm formation. This can include upward NVD's within potentially unstable air in the boundary layer evolving from a horizontal vector acceleration field ($d\vec{V}/dt$) that produces low-level convergence and upper-level divergence through $d\zeta/dt$. In addition, diabatic heating ($d\theta/dt \neq 0$) in the lower atmosphere and cooling aloft (from both water substance phase changes and radiation) can lead to destabilization of the atmosphere, producing small NBE and larger available (positive) buoyant energy (PBE).

4) By combining NVD's with a measure of static stability (PBE and NBE), using multiple linear regression, convective activity of various intensities can be spatially determined with a 50% accuracy. However, convective and non-convective areas can be delineated with 80% accuracy, demonstrating the high degree of scale interaction between synoptic- and convective-scale systems.

5) The severe thunderstorm environment contains large horizontal accelerations ($>|10^{-3}|$ m s^{-2}) that result in strong low-level convergence and upper-level divergence and partially explain the low-, mid-, and upper-tropospheric jets associated with severe thunderstorms (through $d(KE)/dt$).

6) Interactions between severe convective systems and the environment enhance the synoptic-scale vector acceleration field in the mid-troposphere (through the turbulent frictional force) in such a manner that the storm "self-propagates" itself by increasing the large-scale vertical motion field. This process results from a net momentum and heat exchange between the storm and the environment where large diabatic heating (>2.0 ^{o}C/3h) and momentum exchange within the storm environment increases the horizontal temperature gradient and accelerates the environment flow, producing stronger convergence and divergence patterns, wind jets, and vertical velocities.

6. RECOMMENDATIONS FOR FURTHER RESEARCH

Further studies of this type can provide a more definitive understanding of the interaction processes that occur between convective storms and their environment during different synoptic patterns and seasons. The AVE-SESAME and HIPLEX experiment data should be especially useful in extending these results to include information about the interactions that occur between thunderstorms and mesoscale environmental circulations.

REFERENCES

Aubert, E. J., 1957: On the release of latent heat as a factor in large-scale atmospheric motions. J. Meteor., 14, 527-542.

Barnes, S. L., 1964: A technique for maximizing detail in numerical weather map analysis. J. Appl. Meteor., 3, 396-409.

Barr, S., W. K. Widger, Jr., I. A. Miller, and R. Stanton, 1971: Objective subsynoptic upper level analysis. J. Appl. Meteor., 10, 410-417.

Bonner, W. D., R. M. Reap, and J. E. Kemper, 1971: Preliminary results on severe storm prediction by screening regression using forecast predictors. Preprints of Papers, Seventh Conf. on Severe Local Storms, Kansas City, 36-41.

Brousaides, F. J., 1975: The radiosonde hygristor and low relative humidity measurements. Bull. Amer. Meteor. Soc., 56, 229-233.

Chien, H., and P. J. Smith, 1973: On the estimation of kinematic parameters in the atmosphere from radiosonde wind data. Mon. Wea. Rev., 101, 252-261.

Collins, R. W., 1970: AFGWC multilevel cloud model. AFGWC Tech. Mem. 70-10, 35 pp.

David, C. L., 1973: An objective method for estimating the probability of severe thunderstorms using predictors from the NMC (PE) numerical prediction model and from observed surface data. Preprints of Papers, Eighth Conf. on Severe Local Storms, Denver, 223-225.

Djuric, Dusan, 1961: On the accuracy of air trajectory computations. J. Meteorol., 18, 597-605.

Endlich, R. M., and R. L. Mancuso, 1968: Objective analysis of environmental conditions associated with severe thunderstorms and tornadoes. Mon. Wea. Rev., 96, 342-350.

Fankhauser, J. C., 1969: Convective processes resolved by a mesoscale rawinsonde network. J. Appl. Meteorol., 8, 778-798.

Foster, D. S., and R. M. Reap, 1973: Archiving of manually-digitized radar data, Techniques Development Laboratory Office Note 73-6, National Weather Service, Silver Springs, Md., 12 pp.

Fritsch, J. M., C. F. Chappell, and L. R. Hoxit, 1976: The use of large-scale budgets for convective parameterization. Mon. Wea. Rev., 104, 1408-1418.

Fucik, N. F., and R. E. Turner, 1975: Data for NASA's AVE IV experiment: 25-mb sounding data and synoptic charts. NASA TM X-64952, George C. Marshall Space Flight Center, Alabama, 458 pp.

Fuelberg, H. E., 1974: Reduction and error analysis of the AVE II pilot experiment data. NASA CR-120496, George C. Marshall Space Flight Center, Alabama, 131 pp.

_____, 1977: Atmospheric energetics in regions of intense convective activity. NASA CR-2826, NASA Marshall Space Flight Center, Huntsville, Alabama, 136 pp.

_____, and J. R. Scoggins, 1977: Relationship between the kinetic energy budget and intensity of convection. Preprints of Papers, Tenth Conf. on Severe Local Storms, Omaha.

Godske, C. L., T. Bergeron, J. Bjerknes, and R. C. Bundgaard, 1957: Dynamic Meteorology and Weather Forecasting. Boston, Amer. Meteor. Soc. and Carnegie Inst. Washington, 800 pp.

Haltiner, G. J., and F. L. Martin, 1957: Dynamical and Physical Meteorology. McGraw-Hill Book Company, 470 pp.

Holton, J. R., 1972: An Introduction to Dynamic Meteorology. Academic Press, 319 pp.

Hudson, H. R., 1971: On the relationship between horizontal moisture convergence and convective cloud formation, J. Appl. Meteor., 10, 755-762.

Kaplan, M. L., and D. A. Paine, 1977: A multiscale synoptic-dynamical model of tornado genesis. Preprints of Papers, Tenth Conf. on Severe Local Storms, Omaha.

Kung, E. C., 1973: Note on design of an optimized computation scheme for kinematic vertical motion fields. Mon. Wea. Rev., 101, 685-690.

Lenhard, R. W., 1973: A revised statement of radiosonde accuracy. Bull. Amer. Meteor. Soc., 54, 691-693.

Lumley, J. L., and H. A. Panofsky, 1964: The Structure of Atmospheric Turbulence. New York, John Wiley Interscience, 239 pp.

Miller, R., 1972: Notes on analysis and severe-storm forecasting procedures of the Air Force Global Weather Central, Air Weather Service, Tech. Report No. 200 (REV)., 102 pp.

Newton, C. W., 1963: Dynamics of severe convective storms. Meteorol. Monographs 5, No. 27, 33-58.

Newton, C. W., 1969: The Role of Extratropical Disturbances in the Global Atmosphere. In Global Circulation of the Atmosphere, Salisbury Press, London, 137-158.

Ninomiya, K., 1971a: Dynamical analysis of outflow from tornado-producing thunderstorms as revealed by ATS III pictures. J. Appl. Meteor., 10, 275-294.

_____, 1971b: Mesoscale modification of synoptic situations from thunderstorm development as revealed by ATS III and aerological data. J. Appl. Meteor., 10, 1103-1121.

O'Brien, J. J., 1970: Alternate solutions to the classical vertical velocity problem. J. Appl. Meteor., 9, 197-203.

Ogura, Y., and H. Cho, 1973: Diagnostic determination of cumulus cloud populations from observed large-scale variables. J. Atmos. Sci., 30, 1276-1286.

Paine, D. A., and M. L. Kaplan, 1974: The linking of multiscaled energy sources leading to atmospheric development, National Science Foundation Report No. GA-35250, Washington, D.C.

_____, 1977: A multiscale numerical study into the cascade of kinetic energy leading to severe local storms. Preprints of Papers, Tenth Conf. on Severe Local Storms, Omaha.

Read, W. L., and J. R. Scoggins, 1977: Vorticity budget and stability in relation to convection. NASA CR-2819, NASA Marshall Space Flight Center, Huntsville, Alabama, 111 pp.

Reap, R. M., 1972: An operational three-dimensional trajectory model. J. Appl. Meteor., 11, 1193-1202.

Reed, R. J., and E. E. Recker, 1971: Structure and properties of synoptic-scale wave disturbances in the equatorial Western Pacific. J. Atmos. Sci., 28, 1117-1133.

_____, and M. A. Alaka, 1969: An objective quasi-lagrangian index for predicting convective weather outbreaks. Preprints of Papers, Sixth Conf. on Severe Local Storms.

_____, and D. S. Foster, 1975: New operational thunderstorm and severe storm probability forecast based upon model output statistics (MOS). Preprints of Papers, Ninth Conf. on Severe Local Storms, Norman, 58-63.

Scoggins, J. R., and O. E. Smith, 1973: Data for the first NASA atmospheric variability experiment (AVE I), Part I: Data tabulation. NASA TM X-2938, George C. Marshall Space Flight Center, Alabama, 681 pp.

Scott, R. W., and J. R. Scoggins, 1977: The moisture budget in relation to convection. NASA CR-2817, NASA Marshall Space Flight Center, Huntsville, Alabama, 88 pp.

Shuman, F. G., 1957: Numerical methods in weather prediction: II. Smoothing and filtering. Mon. Wea. Rev., 85, 357-361.

Smith, P. J., 1971: An analysis of kinematic vertical motions. Mon. Wea. Rev., 99, 715-723.

Thomas, D. S., 1971: AFGWC forward trajectory model. AFGWC Tech. Mem. 71-4, 9 pp.

Vincent, D. G., K. E. Bossingham, and H. J. Edmon, Jr., 1976: Comparison of large-scale vertical motions computed by the kinematic method and quasi-geostropic ω-equation. Preprints of Papers, Sixth Conf. on Weather Forecasting and Analysis, Amer. Meteor. Soc., Albany, 357-364.

Whitney, L. F. , 1977: Relationship of the subtropical jet stream to severe local storms. Mon. Wea. Rev., 105, 398-412.

Wilson, G. S., 1976: Large-scale vertical motion calculations in the AVE IV experiment. Geophys. Res. Letters, 3, 735-738.

_____, and J. R. Scoggins, 1976: Atmospheric structure and variability in areas of convective storms determined from 3-h rawinsonde data. NASA CR-2678, NASA Marshall Space Flight Center, Huntsville, Alabama, 118 pp.

Zack, J. W., and J. T. Moore, 1977: An integrated scale-interaction theory with applications to the operational forecasting of severe convective storms. Preprints of Papers, Tenth Conf. on Severe Local Storms, Omaha.

1. Report No. NASA RP-1054	2. Government Accession No.	3. Recipient's Catalog No.
4. Title and Subtitle Thunderstorm-Environment Interactions Determined with Three-Dimensional Trajectories		5. Report Date January 1980 6. Performing Organization Code
7. Author(s) Gregory Sims Wilson*		8. Performing Organization Report No.
9. Performing Organization Name and Address George C. Marshall Space Flight Center Marshall Space Flight Center, Alabama 35812		10. Work Unit No. M-294 11. Contract or Grant No.
12. Sponsoring Agency Name and Address National Aeronautics and Space Administration Washington, D. C. 20546		13. Type of Report and Period Covered Reference Publication 14. Sponsoring Agency Code

15. Supplementary Notes

* Universities Space Research Association
Present Address: Space Sciences Laboratory, NASA Marshall Space Flight Center, AL 35812

16. Abstract

Diagnostically determined three-dimensional trajectories were used to reveal some of the scale interaction processes that occur between convective storms and their environment. Data from NASA's fourth Atmospheric Variability Experiment (AVE IV), conducted on 24-25 April 1975, are analyzed. Two intense squall lines and numerous reports of severe weather occurred during the period.

Convective storm systems with good temporal and spatial continuity are shown to be related to the development and movement of short-wave circulation systems aloft that propagate eastward within a zonal mid-tropospheric wind pattern. These short-wave systems are found to produce the potential instability and dynamic triggering needed for thunderstorm formation.

The environmental flow patterns, relative to convective storm systems, are shown to produce large upward air parcel movements in excess of 50 mb/3h in the immediate vicinity of the storms. The air undergoing strong lifting originates as potentially unstable low-level air traveling into the storm environment from southern and southwestern directions. The thermo- and hydrodynamical processes that lead to changes in atmospheric structure before, during, and after convective storm formation are successfully described using total time derivatives of pressure (dp/dt) or net vertical displacement NVD), potential temperature (θ), and vector wind ($d\vec{V}/dt$) calculated by following air parcels.

The high degree of scale interaction between synoptic- and convective-scale systems is demonstrated statistically, using multiple linear regression, by combining NVD's and static stability measurements to successfully locate convective activity of various intensities over the AVE IV network. After storm formation, interactions between severe convective systems and the environment alter the synoptic-scale flow field in the mid-troposphere in such a manner that the storm "self-propagates" by increasing the large-scale vertical motion field. This process results from a net momentum and heat exchange between the storm and the environment where large diabatic heating (>2.0 ^{o}C/3h) and momentum exchange within the storm environment increase the horizontal temperature gradient and accelerate the environmental flow, producing stronger convergence and divergence patterns, wind jets, and vertical velocities.

17. Key Words (Suggested by Author(s))	18. Distribution Statement		
	Category 47		
19. Security Classif. (of this report)	20. Security Classif. (of this page)	21. No. of Pages	22. Price
Unclassified	Unclassified	163	$8.00

For sale by National Technical Information Service, Springfield, Virginia 22151

NASA-Langley, 1980